Experimental feedback control of separated and open-cavity flows with MEMS technologies

Thomas Arnoult

Centrale Lille

THÈSE

présentée en vue d'obtenir le grade de

DOCTEUR

en

Micro et Nanotechnologies, Acoustique et Télécommunications

par

Thomas Arnoult

Doctorat délivré par Centrale Lille

Experimental feedback control of separated and open-cavity flows with MEMS technologies

Contrôle en boucle fermée d'un écoulement décollé et de l'écoulement sur une cavité ouverte à l'aide de technologies MEMS

Soutenue le 14 mars 2023 devant le jury d'examen:

M. Laurent Cordier,	Directeur de Recherche à l'institut Pprime	Président
M. Louis Cattafesta,	Professeur à l'Illinois Institute of Technology	Rapporteur
M. Jean-François Manceau,	Professeur à l'Université de Franche-Comté	Rapporteur
Mme Lilla Koloszar,	Ingénieure de recherche au Von Karman Institute	Examinateur
Mme Cécile Ghouila-Houri,	Maître de Conférences à Centrale Lille Institut	Encadrant
M. Colin Leclercq,	Ingénieur de recherche à l'ONERA	Co-encadrant
M. Philippe Pernod,	Professeur à Centrale Lille Institut	Co-directeur de thèse
M. Abdelkrim Talbi,	Professeur à Centrale Lille Institut	Directeur de thèse

Invités : Franck Hervy, Denis Sipp, François Lusseyran

Thèse préparée dans les laboratoires de l'Institut d'Electronique, de Microélectronique et de Nanotechnologies (IEMN UMR CNRS 8520, F-59000 Lille, France) et de l'Office National des Etudes et Recherches Aérospatiales (ONERA), centres de Meudon et de Lille

Ecole Doctorale ENGSYS 632

Contents

Résumé en français

Le XX^{eme} siècle ainsi que le début du XXI^{eme} siècle sont marqués par une augmentation du niveau de vie des populations. Smartphones, ordianteurs personnels, voitures et avions sont des objets ordinaires de nos vies ou sont des moyens de transport devenus classiques. Cette évolution des modes de vie est liée à une augmentation de l'utilisation des sources d'énergies fossile, comme illustré en Figure 1. Cependant, à cause de l'effet de ces énergies sur le changement climatique et également à cause leur prix croissant, il est admis que nos modes de vie doivent évoluer.

L'industrie des transports fait ainsi des efforts afin de limiter les emissions de gaz à effets de serre comme le CO_2 ou le NO_x et afin de limiter les émissions de bruits. Des objectifs numériques ont alors été fixés au sein de différents programmes de recherches et développement commme le projet ACARE 2020 en Europe [1], ou le projet Clean Aviation, qui est le programme de référence dans le développement d'une aviation durable et neutre en carbone [2]. Les objectifs environnementaux du projet ACARE pour l'année 2020 étaient de réduire la consommation en carburant des avions et leur émission de CO_2 de 50%, de reduire le bruit perçu de 50% et de réduire les émissions de NO_x de 80%. Les objectifs définis dans le cadre du projet Clean Aviation sont pour les années 2050 de réduire de 90% les émissions de CO_2, par comparaison aux émissions du transport aérien des années 2020. Toutefois, comme souligné dans le rapport du projet ACARE 2020, ces objectifs ambitieux ne sont pas réalisables sans des avancées technologiques importantes.

Ces programmes de recherche soutiennent le dévelopemment du domaine du contrôle des écoulements, domaine multidisciplinaire combinant la mécanique des fluides, l'automatisme et la conception technologique. La mécanique des fluides permet de comprendre la physique du système à contrôler et définit les objectifs du contrôle comme l'augmentation de la portance, la diminution de la traînée ou des émissions de bruit ou encore la limitation des vibrations structurelles induites par des interactions fluides-structures [3]. L'automatisme permet de définir la stratégie de contrôle la plus adaptée dans le cas de la mise en place d'un contrôle réactif. La conception technologique, permet, à partir du cahier des charges établi par la mécanique des fluides et l'automatisme, de concevoir des technologies d'actionneurs et de capteurs adaptées.

Dans ce dernier domaine, la conception technologique, les MEMS (Micro Electro Mechanical Systems) constituent une solution intéressante pour les applications de contrôle d'écoulement. Définis par des tailles caractéristiques submillimétriques et produits par des procédés de micro-fabrication, les actionneurs et capteurs MEMS peuvent être utilisés individuellement ou en réseaux. Les petites dimensions des capteurs, associés à des électroniques de con-

ditionnement adaptées, permettent d'obtenir des informations locales sur les structures de petites tailles se développant dans les écoulements turbulents. Les avantages des MEMS ont été mis en avant notamment par l'équipe de recherche de Sheplak [4, 5, 6, 7]. Concernant les actionneurs, utilisés en réseaux, des forçages adaptés à la position des différents actionneurs peuvent être définis suivant une information locale récupérée dans l'écoulement. Une telle approche de contrôle, dite MIMO (Multiple Inputs Multiple Outputs), serait nécessaire pour la mise en place du contrôle réactif d'écoulements se développant sur des géométries complexes. A cet égard, les technologies MEMS offrent des solutions compactes pour le problème du contrôle des écoulements. Ces technologies ont notamment été développées dans le cadre des projets AeroMEMS 1, AeroMEMS 2 et au sein du projet européen FP6 ADVACT, comme expliqué par Warsop [8].

L'objectif principal de cette thèse est, dans ce contexte, de réaliser des expériences de contrôle d'écoulements en boucle fermée en mettant en œuvre des lois de contrôle simples d'une part et de tester les technologies MEMS dans le but de valider leur utilisation dans des applications de contrôle d'écoulements en boucle fermée et d'augmenter leur TRL (Technology Readiness Level) d'autre part. Deux configurations canoniques d'écoulement sont considérées pour les applications de contrôle en boucle fermée : le contrôle du décollement de l'écoulement sur un volet plein et le contrôle de l'écoulement sur une cavité ouverte. Dans les deux cas, des stratégies SISO (Single Input Single Output) sont envisagées. La première configuration est dédiée à l'essai et au développement de deux lois de contrôle et à l'essai de capteurs MEMS de frottement pariétal. L'objectif est alors de rattacher l'écoulement de base séparé, ce qui nécessite des débits massiques importants - puisque cet état n'existe pas sans forçage -, bien au-delà des capacités des actionneurs MEMS considérés dans le présent travail. Le contrôle de l'écoulement en cavité ouverte vise lui à stabiliser l'écoulement, en atteignant l'écoulement de base forcé en cavité ouverte par le contrôle des instabilités. La troisième configuration considérée dans ce travail consiste en un POD placé sur un ULM pour des essais en vol à l'aide des capteurs MEMS de frottement pariétal, permettant une démonstration de leur fiabilité dans des conditions d'écoulement non contrôlé. Cette thèse est réalisée à l'IEMN (Institut d'électronique, de microélectronique et de nanotechnologie) pour le développement de capteurs et d'actionneurs MEMS et en partenariat avec l'ONERA (Office National d'Etudes et de Recherches Aérospatiales) pour les expériences de contrôle d'écoulement. Le manuscrit de la thèse est divisé en 6 chapitres comme expliqué ci-dessous.

Le premier chapitre présente des généralités sur la dynamique des fluides et le contrôle des écoulements. Un aperçu des capteurs et des actionneurs conçus pour les applications de contrôle des écoulements est donné et des détails sur leur utilisation pour deux configurations canoniques sont présentés: le contrôle des écoulements décollés et le contrôle de l'écoulement sur une caivté ouverte. L'accent est mis en particulier sur le fait que les actionneurs pour le contrôle des écoulements décollés doivent fournir des débits massiques élevés. En effet, l'écoulement de base à atteindre n'existe pas sans un forçage externe. En ce qui concerne le contrôle en boucle fermée d'un écoulement sur une cavité ouverte, l'objectif est d'atteindre l'écoulement de base, qui est un point fixe instable sans forçage. La boucle fermée est nécessaire pour cette application afin de stabiliser le point fixe et une fois que celui-ci est atteint, les efforts pour maintenir cet état stable ne sont plus dus qu'à des perturbations externes.

Le deuxième chapitre présente les deux configurations sur lesquelles les expériences de contrôle d'écoulement en boucle fermée ont été réalisées. La première série d'expériences de contrôle d'écoulement vise le contrôle de l'écoulement séparé au-dessus d'un volet plein de type NACA 4412 et s'est déroulée dans la soufflerie L1 de l'ONERA. Réalisée avec des vannes commerciales et des capteurs à film chaud, la campagne d'essais a pour objectif le contrôle de l'écoulement séparé à l'aide de deux lois de contrôle différentes. La première est une loi de contrôle basée-données, conduisant à la synthèse d'un contrôleur intégral linéaire, et la seconde est une approche phénoménologique/basée sur un modèle, conduisant à une loi de contrôle intégrale positive non-linéaire. D'autres expériences sur le volet plein sont réalisées avec des capteurs MEMS de frottement pariétal. La deuxième série d'expériences a été réalisée sur l'écoulement au dessus d'une cavité ouverte, installée dans la soufflerie S19 de l'ONERA. L'objectif de cette deuxième étude est de mettre en œuvre le contrôle en boucle ouverte et en boucle fermée des oscillations de l'écoulement de la cavité, avec des actionneurs MEMS.

Le troisième chapitre détaille les essais de contrôle en boucle fermée réalisés sur le volet plein de type NACA 4412. Pour une vitesse de 34,5 m/s en soufflerie et pour des angles de braquage du volet compris entre 2° et 37°, les deux méthodes de commande en boucle fermée présentées précédemment ont été utilisées pour suivre une valeur de référence, définie par rapport aux mesures des films chauds. Les résultats obetnus avec les deux lois de contrôle sont discutés en comparant les coefficients de portance et de pression des cas contrôlés et non contrôlés. Les expériences ont été réalisées avec des vannes Festo ON/OFF dont le rapport cyclique est modifé en temps réel. Les actionneurs MEMS ne pouvant pas délivrer les mêmes débit que les vannes Festo, ceux-si sont donc intégrés sur une autre configuration, la cavité ouverte, sur laquelle le contrôle des instabilités de l'écoulement est mis en place.

Le quatrième chapitre décrit l'utilisation de microvalves MMMS (Micro-Magneto-Mechanical Systems) dans des expériences de contrôle d'écoulement en boucle ouverte réalisées sur une cavité ouverte. Les jets de sortie des microvalves MMMS sont dans un premier temps caractérisés à l'aide d'un débitmètre et de mesures fil chaud. Les microvalves à actionnement magnétique sont capables de générer des jets quasi-stationnaires et pulsés et se comportent de manière linéaire. Elles sont donc entièrement caractérisées par une fonction de transfert, qui est déterminée expérimentalement. Intégrés en réseau linéaire sur le bord amont de la cavité ouverte, les jets des microvalves interagissent avec la couche de cisaillement et modifient la dynamique de l'écoulement. Une fois que la dynamique de l'écoulement non forcé est caractérisée, les effets des jets quasi-stationnaires et pulsés sont étudiés. Il est démontré que les jets quasi-stationnaires peuvent réduire l'amplitude de l'oscillation fondamentale de la cavité de 20 dB pour une vitesse d'écoulement de 20 m/s, soit un débit de 25 L/min pour l'ensemble du réseau de 15 actionneurs. En ce qui concerne les jets pulsés, les actionneurs ne sont pas assez puissants pour déclencher des non-linéarités dans l'écoulement, de sorte que ces non-linéarités aient des effets sur l'amplitude de la fréquence fondamentale de la dynamique de l'écoulement. Les jets pulsés ne peuvent donc pas être utilisés pour le contrôle en boucle ouverte. Il est alors nécessaire de mettre en place une stratégie de contrôle en boucle fermée de cet écoulement afin de profiter entièrement de la capactié des microvalves magnétiques.

Le cinquième chapitre vise à mettre en œuvre la stratégie de contrôle en boucle fermée de l'écoulement sur la cavité ouverte. L'application du contrôle en boucle fermée est basée sur la synthèse de contrôleurs linéaires, dont le signal de commande de sortie peut être directement envoyé au réseau d'actionneurs. La notion de fonction de transfert est dans un premier temps défini dans le cas du système oscillant que constitue le cas de la cavité ouverte. Les données fréquentielles pour l'identification de la fonction de transfert sont obtenues par l'utilisation de jets pulsés générés par les microvalves. Un modèle pour la fonction de transfert est ensuite identifié afin de concevoir le contrôleur linéaire, défini par une synthèse structurée H_∞. Enfin, les contrôleurs synthétisés sont appliqués. Pour une vitesse en soufflerie de 20 m/s et un débit de 10 L/min pour le réseau d'actionneurs, l'amplitude de la fréquence de résonance de la cavité a été réduite de 9 dB par rapport au cas du contrôle en boucle ouverte pour le même débit.

Le sixième chapitre porte sur l'augmentation du niveau de TRL de 4 à 5-6 des technologies de capteurs MEMS conçues à l'IEMN pour des applications de contrôle d'écoulements. Ce travail se concentre sur l'augmentation de la fiabilité du processus de fabrication des microcapteurs et sur l'intégration non invasive des technologies sur les véhicules terrestres et aériens. En ce qui concerne le processus de fabrication, une optimisation de l'étape de gravure libérant les fils de mesure suspendus, basée sur l'utilisation de SF6, est abordée. En ce qui concerne l'intégration des capteurs MEMS, la fabrication de vias traversants sur les puces des capteurs est proposée. Utilisant à l'origine la technique du wire bonding, la liaison électrique entre les capteurs et leur électronique de conditionnement était basée sur l'utilisation de fils métalliques soudés mais sensibles aux vibrations. Les vias traversants en cuivre permettent à la fois de contourner ce problème et d'avoir une intégration affleurante sur n'importe quelle surface. Formés par électrodéposition, la formation des vias traversants est optimisée par un procédé Pulse Periodic Reverse Plating (PPRP). Les microcapteurs sont ensuite intégrés sur un POD placé sur le train d'atterrissage d'un ULM pour des mesures en vol. Pour démontrer l'augmentation du TRL des technologies d'actionnement, la conception d'une microvalve avec un microcapteur intégré au canal microfluidique est proposée.

Acronyms

AIC	Antithetic Integral Controller
DBD	Dielectric Barrier Discharge
DRIE	Deep Reactive Ion Etching
ERA	Eigensystem Realization Algorithm
FEM	Finite Element Method
L-DDC	Loewner Data-Driven Control
LDV	Laser Doppler Velocimetry
LGP	Linear Genetic Programming
LMS	Least-Mean Square
LPCVD	Low Pressure Chemical Vapor Deposition
LQG	Linear Quadratic Gaussian
LTI	Linear Time-Invariant
MEMS	Micro-Electro-Mechanical Systems
MIMO	Multiple-Inputs Multiple-Outputs
MMMS	Micro-Magneto-Mechanical Systems
PCB	Printed Circuit Board
PDMS	Polydimethylsiloxane
PECVD	Plasma Enhanced Chemical Vapor Deposition
PFA	Pulsed Fluidic Actuators
PID	Proportional-Integral-Derivative
PIV	Particle Image Velocimetry
POD	Proper Orthogonal Decomposition
PPRP	Pulse Periodic Reverse Plating
PRBS	Pseudo-Random Binary Signals
PSD	Power Spectral Density
PWM	Pulsed Width Modulation
SEM	Scanning Electron Microscopy
SISO	Single-Inputs Single-Outputs
SPL	Sound Pressure Level
TRL	Technology Readiness Level

Acknowledgments

After three years of work, I would like to express my thanks to all the people who contributed to the success of this personnal and professional project. This work was carried out at the IEMN (Institut d'Electronique de Microélectronique et de Nanotechnologie) in partnership with the ONERA (Office Nationale des Etudes et Recherches Aérospatiales). I acknowledge the Région Hauts de France and the Agence Innovation Defense (AID), who funded this work.

I would like to thank the members of the jury and the invited people for their participation. Particularly, I would like to thank Dr. Laurent Cordier who accepted to be president of the jury. I sincerely thank Prof. Louis Cattafesta (Professor at the Illinois Institute of Technology) and Prof. Jean-François Manceau (Professor at Université de Franche-Comté) who honored me reporting my work. I also deeply thank Dr. Lilla Kolosazr (Research Engineer at the Von Karman Institute), who accepted to be part of the jury.

I also would like to thank Franck Hervy, AID supervisor who helped me promote results of the thesis work. I address special thanks to Charles Poussot-Vassal, who was significantly involved in the success of the different closed-loop control test campaigns. I also thank François Lusseyran, Onofrio Semeraro and Colin Leclercq, thanks to whom everything started. They, all three, supervised me during an internship and strengthened my will to do a PhD.

I especially would like to thank Abdelkrim Talbi and Philippe Pernod, who both directed these thesis works and Cécile Ghouila-Houri, who supervised my PhD. I am extremely greatfull for their support all along my PhD, for the numerous and various discussions we had and for the knowledge they brought me during these three years (not only in the scientific domains). Thank you for your patience, wise advices and investments in the success of all the test campaigns carried out.

All this work would not have been possible without the precious help of Eric Garnier, Vianney Nowinski, Jérôme Delva, Gwenaël Acher, Denis Sipp, Gilles Peugnier, Thibault Leudiere, Pascal Molton, Pascal Audo, Jean-Pierre Tobeli, Philippe Geffroy, Cédric Illoul and Caroline Goudeau.

I also would like to thank colleagues and friends for their support and caring during these three years, Munique, Romain, Pierre, Vincent, Othmane, Salah, Axel, Linda, Sylvain, Laure, Arthur, Christophe, Ravinder, Jérémy, Aurélien, Manon and Vincent.

Finally and most importantly I would like to thank my family. Constance for your support and wise recommendations regarding formulations of given expressions. Guillaume for the coffee breaks in your office, while I was in Meudon and for the tedious proofreading of the manuscript. My parents who supported me at all steps of the PhD: without you, all this work would not have been possible.

Fundings

This work was funded by the French National Research Agency (ANR) in the framework of the ANR ASTRID MATURATION "CAMELOTT-MATVAL" Project. It is supported by the regional platform CONTRAERO in the framework of the CPER ELSAT 2020 Project. The Innovation Defense Agency (AID) has also financially sustained this work, as did the Région Hauts de France.

Introduction

The XX$^{\text{th}}$ and start of the XXI$^{\text{st}}$ centuries are marked by the evolution of the population standard of leavings in Western countries. Smartphones, personal computers, cars and airplanes have became ordinary objects or means of transportation. This evolution is linked to an increase in the use of fossil energies, as illustrated in Figure 1. However, because of the effects of fossil energies on climate change and because of the increasing cost of energy, it is widely admitted that our way of life has to change.

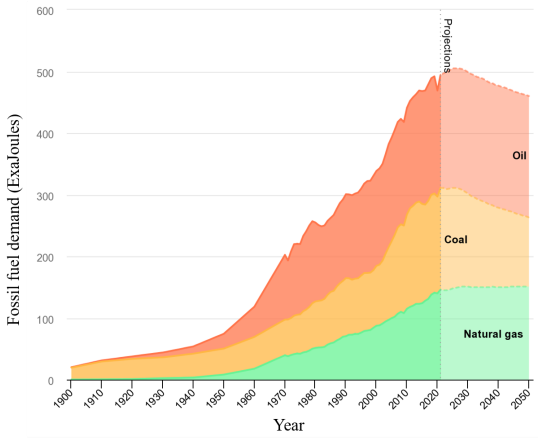

Figure 1: Evolution of the fossil fuel demand (in Exa-Joules) against years from 1900 to 2022 with a projection up to 2050 (from [9]).

The transport industry has therefore made efforts to curb the polluting emissions of CO_2, NO_x and the noise radiations. Numerical objectives regarding these efforts are set within different joint programmes such as ACARE 2020, the Advisory Council for Aviation Research and Innovation in Europe [1] or the Clean Aviation Joint Undertaking (Clean Aviation JU), which is the European Union's leading research and innovation programme for transforming aviation towards a sustainable and climate neutral future [2]. The ACARE 2020 environmental objectives for 2020 were to reduce airplanes fuel consumption and CO_2 emissions by 50%, reduce perceived external noise by 50% and reduce NO_x by 80%. Objectives set by the Clean Aviation JU are to reduce by 2050 net CO_2 emissions by 90% compared to the 2020 state-of-the-art. As emphasized in the ACARE 2020 report, these "objectives are not achievable without important breakthroughs, both in technology and in concepts of operation".

These programmes sustain the development of the multidisciplinary domain of flow control, combining fluid dynamics, control theory and technology design. Fluid dynamics helps un-

derstanding the physics of plants to be controlled and set the objectives to be reached, such as lift enhancement, drag or noise reduction or limiting induced structural vibrations [3]. Control theory helps defining the most adapted control strategy to be employed in the case of reactive control. Technology design, based on fluid dynamics and control theory requirement specifications, helps conceiving adapted actuating and sensing technologies.

Considering this last domain, MEMS (Micro Electro Mechanical Systems) constitute an interesting solution for aerodynamic flow control applications. Defined by submillimetric characteristic sizes and produced using micro-fabrication processes, MEMS sensors and actuators can be used individually or as a network. Regarding sensors, their small size, combined with adapted conditioning electronics, helps getting local information on small scales developing in turbulent flows. MEMS advantages have been strongly put forwards by Sheplak's team [4, 5, 6, 7]. Used as a network, the forcing induced by the actuators in a flow can be defined according to the position of each actuator in the flow and according to the local information fed back to the controller in a MIMO (Multiple Inputs Multiple Outputs) strategy. MIMO approaches might be required on geometries on which non-homogeneous flow dynamics arise. In that sense, MEMS technologies offer a compact and flexible solution for flow control applications and were developed inside successive projects such as AeroMEMS 1, AeroMEMS 2 and the European project FP6 ADVACT, which focused on the control of separated flows, as explained by Warsop [8].

The main objective of this thesis is to perform closed-loop flow control experiments implementing simple but efficient control laws on one hand and testing MEMS technologies in order to validate their use in feedback flow control applications and increase their TRL (Technology Readiness Level) on the other hand. Two canonical flow configurations are considered for flow control applications: the control of flow separation/separated flow over a plain flap and the control of the flow over an open-cavity. In both cases, SISO (Single Input Single Output) strategies are considered. The first configuration is dedicated to the test and development of two control laws and for the test of MEMS wall shear stress sensors. The aim is the reattachment of the separated base flow, requiring large mass flow rates - as this state does not exist without forcing -, much beyond the capacities of the MEMS actuators considered in the present work. The control of the open-cavity flow aims at the stabilization of the flow, by reaching the open-cavity forced base flow through the control of instabilities. The third configuration considered in the present work consists of a POD placed on a microlight aircraft for the real-flight testings of MEMS wall shear stress sensors, providing a demonstration of their reliability against uncontrolled flow conditions. This thesis is carried out at the IEMN (Institute of Electronics Microelectronics and Nanotechnology) for the development of MEMS sensors and actuators and in partnership with ONERA (Office National d'Etudes et de Recherches Aérospatiales) for the flow control experiments. The PhD manuscript is divided into 6 chapters as explained below.

The first chapter recalls generalities on fluid dynamics and flow control. It provides an overview of sensors and actuators designed for flow control applications and provides details on their use on two canonical problems: the control of separated flows and the control of open-cavity flows. It is particularly highlighted that actuators for flow separation control need to deliver high mass flow rates, as the base flow to reach does not exist without an

external forcing. Regarding the closed-loop control of an open-cavity flow, the aim is to reach the base flow, which is an unstable fixed point without forcing. Closed-loop is required for this application to stabilize the fixed point and once it is reached, efforts to maintain this stable state are only due to external noisy disturbances.

The second chapter presents the two configurations on which closed-loop flow control experiments are carried out. The first set of flow control experiments was conducted on a separated flow over a NACA 4412 plain flap and took place in the ONERA L1 wind tunnel. Implemented with commercial valves and hot film sensors, the aim of this study is to control the separated flow through two different closed-loop strategies. The first one being a data-driven control law, leading to a linear integral controller and the second one being a phenomenological/model-driven approach, leading to a non-linear positive integral control law. Further experiments on the plain flap are performed with MEMS wall shear stress sensors. The second set of experiments was carried out on an open-cavity flow and took place in the ONERA S19 wind tunnel. The aim of this second study is to implement both the open- and closed-loop control of the cavity flow oscillations with MEMS actuators based on unsteady pressure measurements.

The third chapter provides details on the closed-loop control experiments carried out on the NACA 4412 plain flap model. For a freestream velocity in the wind tunnel test section of 34.5 m/s and for flap deflection angles between 2° and 37°, the two previously introduced closed-loop control methodologies have been employed to track a reference value, defined with respect to the hot films measurements. Flow control results obtained with both control laws are discussed comparing the lift and pressure coefficients of the uncontrolled and controlled cases. The experiments were carried out with ON/OFF Festo valves with real-time duty-cycle modulation, since MEMS microvalves could not deliver sufficient mass flow rates. The MEMS actuators are therefore integrated on an other flow configuration, the open-cavity, on which control of the flow instabilities is performed.

The fourth chapter describes the use of MMMS (Micro-Magneto-Mechanical Systems) microvalves in open-loop flow control experiments carried out on a subsonic open-cavity flow. MMMS microvalves outlet jets are characterized with a flowmeter and a hot wire measurements. The magnetically actuated microvalves are able to generate both quasi-steady and pulsed jets and behave linearly. They are therefore fully characterized by a transfer function, which is experimentally determined. Integrated as a linear array - driven as a single actuator - on the open-cavity upstream edge, the microvalves jets interact with the developing shear layer to modify the flow dynamics. Once the unforced flow dynamics is characterized, the effects of quasi-steady and pulsed jets are investigated. It is shown that quasi-steady jets could reduce the cavity fundamental oscillation amplitude by 20 dB for a freestream velocity of 20 m/s and for a flow rate of 25 L/min for the full array of 15 actuators. Regarding pulsed jets, actuators do not show enough authority to trigger non-linearities in the flow, such that these non-linearities have effects on the flow dynamics fundamental frequency. Therefore the pulsed jets can not be used for open-loop control. However, the actuators may be efficient during closed-loop control experiments as less power is required to control the flow, as the oscillatory flow dynamics fall into the controllable bandwith of the actuators and as the actuators can be driven with any type of signals.

The fifth chapter aims at implementing the closed-loop control strategy of the open-cavity flow. The application of the closed-loop control is based on the synthesis of linear controllers, whose output signal command can be directly fed to the array of actuators. Indeed, the microvalves command flexibility enables the microvalves to be directly driven by the controllers. It is firstly tried to define the transfer function for the oscillating open-cavity flow. The frequential data for the identification of the transfer function are gathered based on the use of pulsed jets generated by the microvalves. Secondly, a state-space model is identified from the transfer function data to design the linear controller, using a H_∞ synthesis. Finally, synthesized controllers are applied. For a freestream velocity of 20 m/s and a flow rate of 10 L/min for the array of actuators, the cavity resonant frequency amplitude was reduced by 9 dB compared to the open-loop case for the same flow rate.

The sixth chapter focuses on the TRL increase from 4 to 5-6 of the disruptive MEMS sensors technologies developed at the IEMN, designed for flow applications. This work concentrates on increasing the micro sensors fabrication process reliability and on the non-invasive integration of the technologies on terrestrial and aerial vehicles. Regarding the fabrication process, an optimization of the etching step releasing the suspended measurement wires, based on the use of SF6, is explained. Concerning the integration of MEMS sensors, the fabrication of traversing vias on the sensors chips is proposed. Originally using the wire bonding technique, the electrical link between the sensor chips and their conditioning electronics was based on the use of soldered metallic wires sensitive to vibrations. Traversing vias made of copper circumvent this issue and enable a flush mounted integration on any surfaces. Formed by electro-deposition, the traversing via process is optimized by Pulse Periodic Reverse Plating (PPRP). The micro sensors are then integrated on a POD placed on the landing gear of a microlight aircraft for real flight measurements. For a demonstration of the TRL increase of actuators technologies, an in-situ monitoring of a microvalve is proposed through the integration of a MEMS calorimetric sensor.

Chapter 1

Literature review on actuator and sensor technologies designed for flow control applications

Introduction

The first chapter describes the context in which the present work takes place. The partnership between IEMN and ONERA clearly defines the aim of this work: performing closed-loop flow control experiments with MEMS technologies. Two well-known flow configurations are considered in this work for the development and tests of closed-loop control strategies, sensing and actuating technologies.

In a first part, generalities on flow control are recalled. The second part presents both actuator and sensor technologies for active flow control applications. The third and fourth parts respectively focus on closed-loop implementation of separated flow and flow over open-cavities, which constitute the two applications considered in the present work.

1.1 Generalities on flow control

1.1.1 Introduction to flow control

Flow control can be defined, as proposed by MacMynowski and Williams [10], as modifying a flow behavior in order to obtain positive changes. By manipulating a flow, different objectives can be set such as delaying or favoring transition to turbulence, preventing or provoking separation, suppressing or enhancing turbulence. Considering an airplane, these positive changes can result either in drag reduction, lift enhancement, mixing augmentation or aerodynamic noise suppression [3]. First insight into flow control was proposed by Prandtl who introduced in 1904 the boundary layer concept. A physical explanation to flow separation is proposed alongside with a solution to re-attach the separated flow, as highlighted by Tollmien et al. [11].

Flow control can be implemented through different approaches: aerodynamic shape optimization, passive or active control. Considering the first category, it consists in optimizing the system geometry. One common example of flow control through aerodynamic shape optimization is the golf ball, which drag coefficient is reduced compared to a slick ball. Dimples on the surface of a golf ball trigger transition to turbulence of the boundary layer, reducing pressure drag as highlighted by Bearman and Harvey [12], who carried out an experimental study of the flow developing around a cylinder with dimples. Recent examples of flow control approaches consist in the optimization of vehicles aerodynamics using adjoint methods as introduced by Reuther et al. [13]. Figure 1.1 presents the shape optimization results of Papoutsis-Kiachagias et al. [14] of a concept car based on this method.

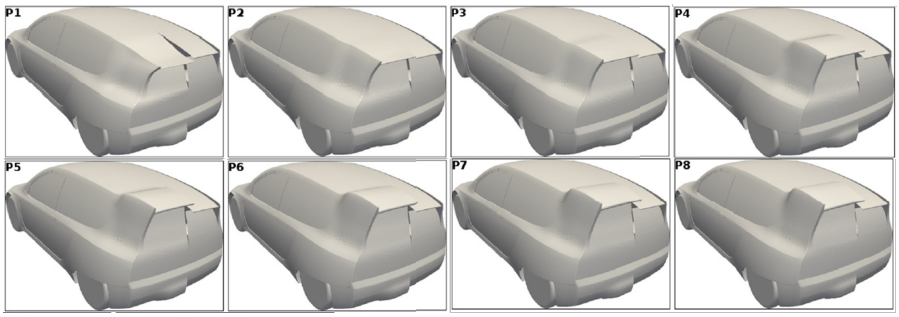

Figure 1.1: Comparison of the optimized geometries (left) to the baseline concept (right). Different optimized shapes are obtained as different objectives have been set by Papoutsis-Kiachagias et al. [14]

The second category is passive flow control. Passive devices modify the flow around an object similarly to the shape optimization approach but with the use of a device added to the considered geometry. Such an approach is used on commercial airliners since the 1940's in the form of vortex generators. As presented in Figure 1.2 and explained by Lin [15], vortex generators often characterized by a height between 10% and 50% of the boundary layer thickness, help re-energizing the boundary layer and prevent flow separation. Another common passive control is the Gurney flap, which consists of a short flat plate attached to the trailing edge of an airfoil and placed perpendicular to the airfoil chord. Depending on the Gurney flap geometry, as presented by Myose et al. [16], it can increase the maximum lift coefficient with a slight effect on drag. Drawbacks of such passive devices lie in the drag

increase they generate at off-point design. Indeed, passive devices act permanently on the flow.

(a) Picture of vortex generators on a flap.

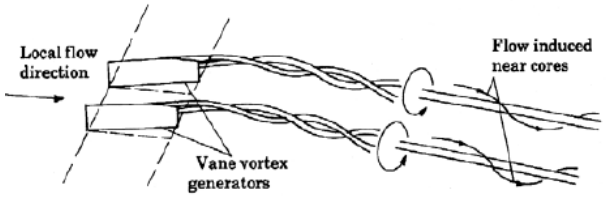

(b) Sketch of the vortices induced by the vortex generators.

Figure 1.2: Illustrations of an array of vortex generators on Boeing 777 flap (a) and sketch of the induced vortices (b) [17].

The third category consists in active flow control. It is based on the use of actuators driven with an external source of energy, which add perturbations in the flow to favorably modify it. Cattafesta and Sheplak [18] proposed a classification of actuators designed for active flow control applications. These devices can be divided into several categories reading moving surfaces actuators, plasma actuators or fluidic actuators. More details on the different technologies are given in Section 1.2. Regarding this third category, Gad-el Hak [3] presented the different methodologies of active flow control, as presented in Figure 1.3.

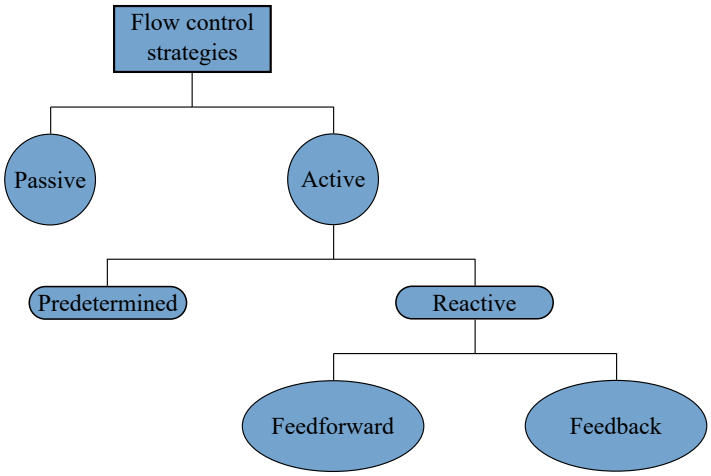

Figure 1.3: Classification of flow control methodologies proposed by Gad-el Hak [3]

Indeed, active flow control is divided between predetermined or reactive methodologies. Predetermined control consists in adding momentum to a flow without monitoring the flow state. This principle defines the open-loop flow control methodology as no sensor information is used to tune the actuators command. Reactive flow control methodology can be further divided into feedforward and feedback. In both reactive control cases, sensor information is used to define the actuators command. The feedforward setup is only feasible in noise-amplifier flows where instabilities are convective. The sensor is placed sufficiently far upstream of the actuator such that it only measures the incoming perturbations, unperturbed by the effect of actuation. On the contrary, in the feedback situation the sensor

observes the consequence of actuation, which provides additional robustness to the control law and is also the only way to stabilize a linearly unstable flow. Sketches of the different reactive flow control methodologies are presented in Figure 1.4. Reactive feedback can be further divided into SISO and MIMO strategies. In the SISO case, the actuator or array of actuators is driven with the same command signal, based on a single flow measurement. In the MIMO case, different command signals are delivered to actuators based on the use of several sources of information in the flow.

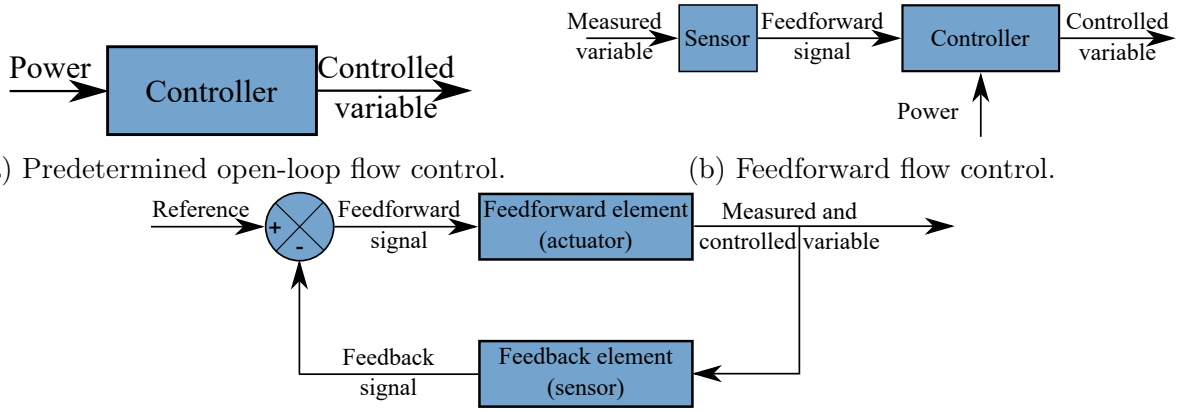

(a) Predetermined open-loop flow control.

(b) Feedforward flow control.

(c) Feedback flow control.

Figure 1.4: Illustrations of the different reactive flow control strategies: predetermined (a), feedforward (b) and feedback (c) strategies [3].

However, as explained by Gad-el Hak [3] and illustrated in Figure 1.5, objectives of flow control are not exclusive. In that sense, reaching a desired effect could degrade another one. This might be described taking the example of a flow around a wing. On the one hand, if the boundary layer is turbulent, it can resist a higher adverse pressure gradient than a laminar one. Therefore, the airplane could be flown at higher angles of attack producing higher lift. On the other hand, the skin-friction drag induced by the turbulent boundary layer is larger than the one induced by a laminar one. Indeed, a laminar boundary layer would generate less skin-friction drag and also limit noise radiation. Achieving a flow control goal adversely affect another aim and trade-offs have to be made.

1.1.2 Controllers design techniques

As presented previously, closed-loop flow control aims at manipulating a flow to reach an objective defined with respect to performance sensor, using a fed back information provided by the estimation sensor. Closed-loop control is particularly relevant to stabilize hydrodynamic instabilities such as the Tollmien-Schlichting waves developing in a transitional boundary layer [19] or the vortex shedding arising in the wake of a cylinder [20] or suppressing the Rossiter modes developing in the flow over an open-cavity [21]. Different ways to implement reactive closed-loop control exist. In the following, widespread controller design techniques are described considering model-free techniques such as extremum seeking, PID (Proportional-Integral-Derivative) controllers, design of control laws based on machine learning and model-based design approaches.

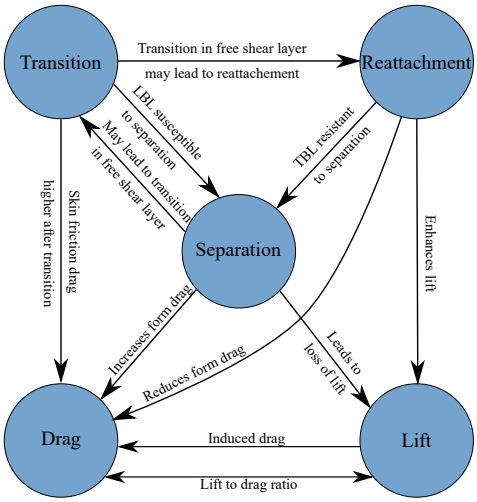

Figure 1.5: Illustration of the flow control objectives and their connections [3].

Model-free design approaches, as explained by Brunton and Noack [22], consists in optimizing a control parameter. Extremum seeking is a common model-free approach, which aims at maximizing (or minimizing) the output variables of a system such as pressure, lift or drag. For instance Pastoor et al. [23] proposed the feedback control of the shear layer of a bluff body based on the use of extremum seeking. In this study, the aim is to maximize the mean pressure coefficients with pulsed jets. Figure 1.6 presents the steady state map derived for the mean pressure coefficient as a function of momentum coefficient induced by the actuators.

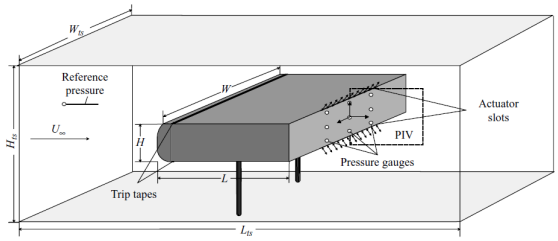

(a) D-shaped body used for the implementation of extremum seeking.

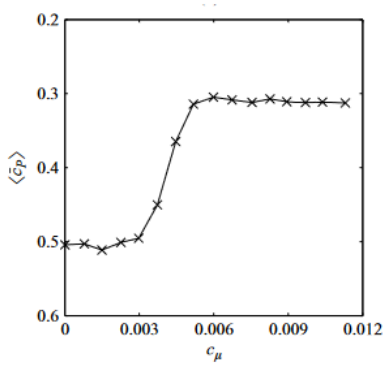

(b) Steady map between the mean pressure coefficient and the actuators momentum coefficient.

Figure 1.6: Sketch of the D-shaped body (a) and steady map (b) derived by Pastoor et al. [23].

Depending on the input parameter (momentum coefficient) c_μ, it can be observed that a maximal value of $< \bar{c}_P >$ can be obtained. In order to implement the extremum-seeking algorithm, it is not mandatory to determine *a priori* the steady map. Also, extremum seeking can be used to minimize a cost function as proposed by Beaudoin et al. [24] who tend to minimize both the drag coefficient of a bluff body and the power consumption of the actuators employed. This first type of closed-loop control is referred in the literature as

"quasi-static" control as it consists in the modification of an open-loop strategy. As explained by Cattafesta et al. [25], the time-scales by which the feed back acts is much slower than the time scales characterizing the flow dynamics. In the following a description of some dynamic controllers used for closed-loop control is presented.
PID controllers are common in the industry and might be employed in flow control applications. For instance Yan et al. [26] used a PID controller, defined in Equation (1.1), to perform closed-loop flow control experiments on an open-cavity flow to damp the flow oscillations. The controller gains and variable ϵ (added for to ensure the controller causality) were manually tuned.

$$C(s) = K_p + \frac{K_i}{s} + \frac{K_d s}{\epsilon s + 1}. \tag{1.1}$$

Despite the controller partially damping of the cavity Rossiter modes, it also included peak-splitting and triggering of nonlinear effects inside the cavity, inducing new frequencies of oscillations in the flow. Nevertheless, advantage of such an approach lies in the simple application of a controller, even though optimization of the parameters might be time-consuming. Tuning of these parameters may be performed within a closed-loop setting, exploiting extremum seeking, as explained in Krstic et al. [27], who tuned a PI controller to stabilize a model of nonlinear acoustic oscillation in a combustion chamber. This method of parameters optimization was generalized to unknown plants by Killingsworth and Krstic [28].

As presented by Brunton and Noack [22], machine learning proposes an alternative to the closed-loop control of complex flows for instance through the optimization of a command law, based on the considered system input-output dynamics. An example of machine learning application is described by Passaggia et al. [29], who performed a real-time feedback control of a stalled airfoil using LGP (Linear Genetic Programming). This method consists in determining the inputs-outputs relation between actuators and sensors that best optimizes a cost function. In this study, aim is to maximize the lift-to-drag ratio. The LGP control is based on the natural selection principle in a population of control laws. The control laws population evolves according to operations defined by the user and only the best individuals are selected to constitute a new generation. Application of such a machine learning program and the control laws population evolution process are described in Figure 1.7. Other examples of machine learning for flow control are presented by Cornejo Maceda and Li [30], Gautier et al. [31], Debien et al. [32] or Efe et al. [33].

Model-based control design techniques obviously rely on the accurate derivation of a model describing the flow dynamics between the inputs (actuators) and the outputs (sensors). As explained by Sipp and Schmid [34], both linear and non-linear models can be derived in order to design a controller law. Several ways to derive linear models can be considered. A classical technique in numerical studies consists in discretizing the linear Navier–Stokes equations, yielding a a state space model with a number of degrees of freedom proportional to the grid size, as for instance presented in [35, 36]. To simplify the obtained model, a reduced-order model can be derived, only keeping information in the flow between the actuators and the sensors. Indeed, the remaining information is neither controllable by the actuators nor observable by the sensors as explained in [34]. Derivation of a linear model can also be performed only using the actuators-sensors data in the frequency domain as proposed

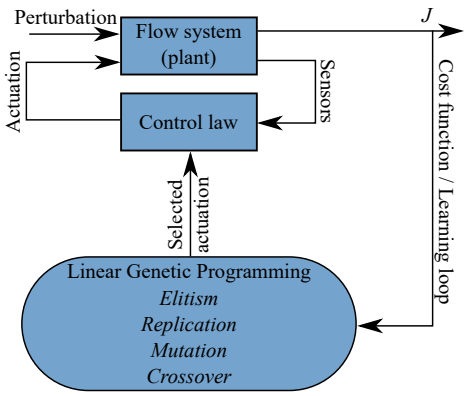

(a) Application of LGP control to a dynamical system.

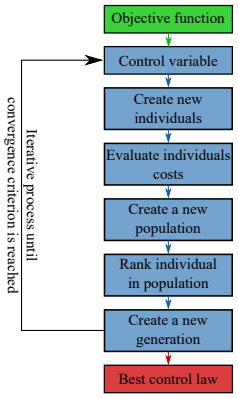

(b) Process of the control laws population growth and selection.

Figure 1.7: Sketch of the application of LGP control to a dynamical system (a) and illustration of the process of the control laws population growth and selection (b) [29].

by Dahan et al. [37]. This method, referred as the derivation of a black-box model, relies on the identification of a state-space model or a transfer function of the considered dynamics. Several ways may be considered for such black-box model identification. For instance, one way consists in exciting the system's dynamics by the considered actuators and derive the frequency response based on the sensors outputs. Different type of signals may be considered, such as harmonic forcings, frequency sweeps (linear or logarithmic), PRBS (Pseudo Random Binary Signals) or white noises. Difficulties encountered with the identification step is the existence justification of such a transfer function, as the plants to be controlled may not be LTI (Linear Time Invariant) systems, as explained in details by Leclercq and Sipp [38].

Based on the model derived, a controller design technique is employed. One model-based control design technique, referred as pole placement, consists in defining a controller such that the closed-loop system poles are placed at desired positions. This approach is the one employed by Joshi et al. [39] to stabilize a plane Poiseuille flow and by Krstic and Banaszuk [40] who implemented an adaptive MIMO pole placement scheme to control instabilities developing in jet engines. A commonly employed designed control technique consists in deriving a LQG (Linear Quadratic Gaussian) controller that minimizes a cost function. As explained by Sasaki et al. [41] considering the Tollmien-Schlichting waves of a transitional boundary layer, the cost functional J to be minimized by the controller takes into account the actuation cost and a quadratic measure of performance. However, as clarified by Brunton and Noack [22], LQG controllers come with no guaranteed stability margin [42] and therefore model-based controller design techniques have evolved towards robust control, such as H_∞ synthesis. For instance, Leclercq et al. [21] used a structured H_∞ synthesis to design a controller and damp the self-sustained oscillations in a quasi-periodic open-cavity flow.

The above presentation of closed-loop design techniques does not aim to be exhaustive but provides commonly used approaches. Furthermore, application examples of such design techniques are given in the following considering the control of separated flows and the control of open-cavity flows.

1.2 Sensors and actuators for reactive flow control applications

The experimental implementation of closed-loop control relies on both sensor and actuator efficient technologies. In the present work, both macro and MEMS technologies are considered. As presented by Löfdahl and Gad-el Hak [43], MEMS are devices with characteristic length less than 1 mm and more than 1 μm, combining electrical and mechanical components, fabricated using micro-machining techniques. In the following, an overview of sensors and actuators used for closed-loop flow control applications is proposed.

1.2.1 Sensors for reactive flow control applications

The information fed back for the implementation of closed-loop control may be a global measurement such as lift [44] or lift-to-drag ratio [45] during wind tunnel experiments or local measurements such as pressure fluctuations [46], wall shear stress [47] or velocity [30]. For global properties, measurements can be performed with balances or by the integration of local measurements alongside the model (e.g. pressure for the derivation of lift). Regarding local measurements, different transduction modes may be explored.

For pressure measurements, widely spread sensors are based on the use of a membrane, which deflection caused by the pressure variations may be detected thanks to piezoresistivity [48, 49, 50, 51], capacitivity [52, 53], optical interference [54, 55] or piezoelectric effects [56, 57]. The MEMS piezoresistive sensor proposed by Berns et al. [48] is based on the use of a silicon membrane which resistivity is a function of the mechanical stress applied to it. The sensor reaches a maximum sensitivity of 3 μmV/Pa for a measurement range of $\pm$ 1 kPa and for simulated frequency bandwith of 160 kHz. Capacitive sensors, as the one proposed by Zagnoni et al. [52] are based on the use of a couple of electrodes. One is fixed and the other one can be deflected by pressure. The distance variation between the two electrodes induces variations in the system capacity. The PCB (Printed Circuit Board) device proposed, reaches a sensitivity of 0.5 to 5 fF/Pa for a pressure range of $\pm$ 2 kPa. Nevertheless, its frequency bandwith is not indicated.

Bae et al. [54] proposed an optical measurement of pressure, using a Fabry-Perot interferometer. The pressure distort a diaphragm, which modulates the optical path difference in the device. Therefore, interference measurements provide a pressure measurement. Such a device reaches a sensitivity of 0.0122 μm/kPa for a pressure range of 27,58 kPa. Piezoelectric effects can also provide a pressure measurements as proposed by Choi et al. [56]. The pressure deflects a piezoelectric membrane and therefore induces a voltage constituting the sensor output. Their sensor reached a sensitivity of 24.7 pC/kPa for a range of 10 kPa. A comparison of the sensor performance is proposed in Table 1.1. The frequency bandwith of the sensors is not always indicated, as the frequency response limitations arise from the associated conditioning electronics.

In a similar way, different transduction modes can be adopted for the measurement of wall shear stress, such as the capacitive mode ([58, 59]) which yields a direct measurement. Chandrasekharan et al. [58] developed a floating-element based sensor associated with comb

fingers suspended by tethers. The comb fingers are used as electrodes, as is the fixed element. A shear stress therefore induces a deflection of the floating elements, modifying the capacitance. Indirect measurements of wall shear stress may also be performed using fluid structure interaction (Von Papen et al. [60], Grosse and Schröder [61]) but the most widely spread indirect techniques is based on thermal transfer between the fluid and a heating element, as used for classical hot films ([62]). Table 1.2 compares some examples of wall shear stress sensors. In the present work, MEMS wall shear stress sensors developed at the IEMN ([63, 64, 65]) are considered for the closed-loop control of the separated flow over a plain flap, as described in Chapter 3. Compared to conventional thermal sensors, these MEMS calorimetric sensors present the advantage of measuring simultaneously the wall shear stress amplitude and the flow direction. Further developments on the sensors fabrication process and use for measurements in uncontrolled flow conditions are given in Chapter 6.

Table 1.1: Comparison of different pressure sensor technologies.

References	Illustration	Transduction mode	Range (Pa)	Sensitivity	Frequency bandwith (kHz)
Berns et al. [48]	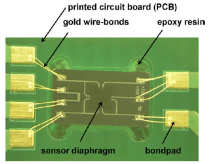	Piezoresistive	± 1 000	3 μV/Pa	160
Sugiyama et al. [49]	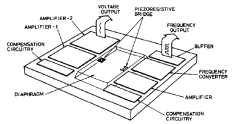	Piezoresistive	± 10 000	30 μV/Pa	210
Lou et al. [50]	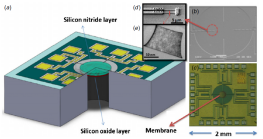	Piezoresistive	330 psi	0.6%/psi	/
Zhu et al. [51]	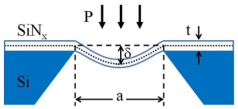	Piezoresistive	70 000	0.85 μV/bar	/
Zagnoni et al. [52]	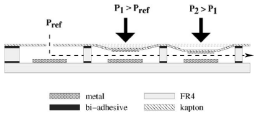	Capacitive	± 1 000	0.5 → 5 fF/Pa	/
Sundararajan and Hasan [53]	/	Capacitive	80 000	4 fF/Pa	/
Bae et al. [54]	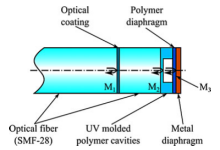	Optical	27 580	0.0122 μm/kPa	/

Eom et al. [55]	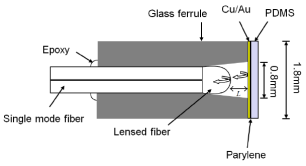	Optical	4 000	1.41 μm/kPa	/
Choi et al. [56]	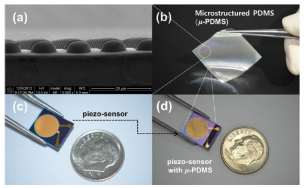	Piezoelectric	4 000	1.41 μm/kPa	/
Horowitz et al. [57]	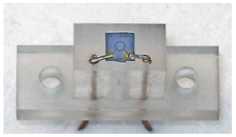	Piezoelectric	5 600	1.66 μV/kPa	59
Kulite XCQ-093-15A	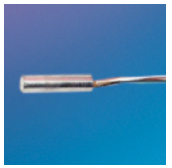	Piezoresistive	100 000	∞	260

Table 1.2: Comparison of different wall shear stress sensor technologies.

References	Illustration	Transduction mode	Range (Pa)	Sensitivity	Frequency bandwith (kHz)
Chandrasekharan et al. [58]	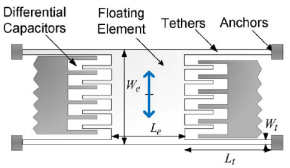	Capacitive	$0 \rightarrow 1.9$	7.66 mV/Pa	6.2 kHz
Von Papen et al. [60]	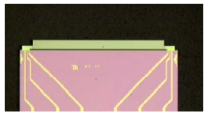	Surface fence	$0 \rightarrow 1.9$	1 mV/Pa	/
Grosse and Schröder [61]	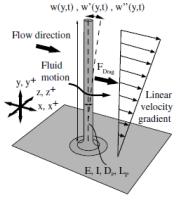	Pillar tip deflection	$0 \rightarrow 2.5$	Pillar height dependent	5 kHz
Haneef et al. [66]	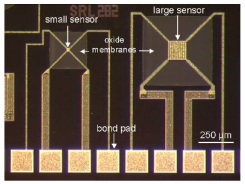	Thermal	$0 \rightarrow 1.5$	/	120 kHz

1.2.2 Actuators for reactive flow control

Different technologies of actuators have been developed and employed in flow control applications. For closed-loop control applications efficient actuators have to meet several requirements as described below:

- Effect on the considered flow dynamics through the induced forcing;
- Ability to follow arbitrary signals;
- Actuators' bandwidth adapted to the flow dynamics to be controlled;
- Small footprint for an easy integration on experimental setups or full scale models;
- Ability to be integrated as an array of actuators for the implementation of a distributed forcing (if a MIMO strategy is employed);
- Easily supplied by electrical power or pressurized air;
- Low cost of fabrication and supply;

The following section sums up some of the widespread actuation technologies and present their specifications. Considering the review of Cattafesta and Sheplak [18] on actuators designed for active flow control applications, devices can be divided between moving surfaces actuators, plasma actuators and fluidic actuators.

Regarding the first category, devices were developed for instance by Seifert et al. [67] or Sarno and Franke [68]. Seifert *et al.* performed flow separation control on an airfoil with piezoelectric unimorph actuators, characterized by a resonant frequency of 170 Hz. For a freestream velocity $U_\infty = 30$ m/s, the actuators deflection can induce velocity fluctuations up to 25% of U_∞. Vortical structures induced by the actuators deflection increased the airfoil maximum lift coefficient of 22%. Considering an open-cavity flow, Sarno and Franke [68] performed open-loop flow control experiments using mechanical fences, affecting the development of the shear layer and damping the flow induced tones. Similar devices were developed by Jeon and Blackwelder [69], Mathew et al. [70] or Cattafesta et al. [71]. The latter author group measured a displacement of 0.4 mm at the actuator tip inducing velocity fluctuations around 10 m/s, for an applied AC voltage with a frequency of 256 Hz. They illustrated the interest of such actuator on an open-loop application on a backward facing-step.

The second category received great attention over the last decades. Plasma actuators in the form of single DBD (Dielectric Barrier Discharge) consists in two electrodes separated by a dielectric layer. The bottom electrode is connected to the ground, while the exposed one is supplied with an AC high voltage in the range of kV with a frequency in the range of kHz. The ambient air is ionized by the electrodes and an electrohydrodynamic force is induced, which can be used to pursue flow control objectives as described by Corke et al. [72] or Durscher and Roy [73]. For instance, Kurz et al. [74] performed boundary layer transition control experiments on an ONERA-D airfoil. The boundary layer transition was then delayed by a distance of 35 % of the airfoil chord length for a freestream velocity of 7 m/s. They also performed active wave cancellation using DBD unsteady forcing in a closed-loop

approach for velocities up to 20 m/s, damping the Tollmien-Schlichting waves characterizing the transition process of the boundary layer. These DBD actuators can be driven with different type of signals as long as a modulation is employed. Indeed a minimum applied voltage to the DBD actuators is required for the ambient air to be ionized. DBD actuators can also be driven by nanosecond pulses and therefore affects the boundary layer developing by an thermal exchange [75].

The third category of fluidic actuators can be decomposed into fluidic oscillators [76, 77], synthetic jets [78, 79, 80, 81, 82] and pulsed jets [83, 84, 85, 86]. Fluidic oscillators were used by Seele *et al* [76, 77] in the form of sweeping jets benefiting from the coanda effect. These actuators were integrated on a wing of the Boeing-Bell V22 to perform flow separation control experiments. The airplane drag was reduced and its lift-to-drag ratio was increased by 60 %. The aerodynamic loads supported by the structure were diminished by 30 % during full scale tests. Another common actuator type is synthetic jet, also referred as zero net mass flux actuators. Synthetic jets alternate blowing and air sucking phases to induce flow velocity fluctuations. Several flow control experiments were carried out such as the one of McCormick [78], who performed boundary layer separation control on an airfoil with directed synthetic jets. For low Mach numbers ranging between 0.03 and 0.05 and an actuation frequency of 50 Hz, the airfoil stall angle was increased by 5 to 6 degrees. Furthermore, the airfoil lift coefficient maximum was increased by 25 %. However, synthetic jets have a limited bandwidth as their actuation frequency must be close to the actuator resonant frequency. Indeed, the induced velocity by synthetic jets is maximum near their resonance and rapidly decays for actuation frequencies away from the resonance. Velocities in To circumvent this issue, pulsed jets can be employed in active flow control experiments as their bandwith is larger, even though they require an external source of fluid. This type of actuator was used in several flow control applications as shown by Bons et al. [83], Lou et al. [84] or Alvi et al. [85]. Bons et al. [83] studied the flow separation control on a low pressure turbine blade with pulsed jets used as vortex generators jets. The two last studies focused on the use of supersonic micro-jets to control impinging jet flows. The micro-jets consist in a submillimetric hole of diameter 400 μm supplied with a pressurized source of air. The on/off pulsating behavior is obtained thanks to solenoid valves placed upstream the actuators. Using these actuators, the impinging jet sound pressure levels were reduced by almost one decade. The microvalve consists of two separated magnets. One is attached to the silicone membrane and closes the microvalve without actuation. The other magnet is surrounded by a coil and helps opening the flow channel when a voltage runs in the coil. These on/off microvalves used with different duty cycles and with frequencies up to 750 Hz delivered velocities up to 100 m/s corresponding to a flow rate of 3 L/min. An array of such microvalves was integrated on an Ahmed body and wind tunnel experiments demonstrated a reduction of the model drag by 4.3 %.

All the previously presented actuators are macro-actuators. Their integration on experimental setups might be limited by their power consumption, supply resources and size. These drawbacks vanish considering MEMS. MEMS actuators of the different types have therefore been developed. For instance, Kilberg et al. [87] designed a MEMS control surface for millimeter-scale rockets. Their device could deliver a maximum torque of 1.6 μNm resulting in a lift force on the rocket of 1.4 mN. Eijo et al. [88] built a pulsed micro-jet with DBD

but no results was reported in the literature on their use for flow control applications. The micro-jet, characterized by PIV (Particle Image Velocimetry) measurements, is pulsed by the DBD burst frequencies ranging from 1 Hz to 80 Hz. MEMS synthetic actuators have also been developed, as highlighted by Gimeno et al. [81], whose synthetic jet relies on magneto-mechanical coupling. The actuator packaging volume is less than 1 cm^3, its outlet hole has a diameter of 600 μm and its actuation bandwith spreads between 400 Hz and 700 Hz. The output velocity characterized with hot wire measurements ranges between 25 m/s and 55 m/s for an electrical power of 500 mW. This work on MEMS synthetic jets has continued, as described by Gerbedoen et al. [89], aiming for a wider bandwidth. Characterized with hot wire measurements these improved actuators design demonstrated a frequency bandwith spreading between 100 Hz and 700 Hz for a maximum outlet velocity of 43 m/s at the resonant frequency of 330 Hz. Considering pulsed jets, Viard et al. [90] designed vertically assembled magneto-mechanical microvalves. Figure 1.8 synthesizes performance of some of the actuators described previously.

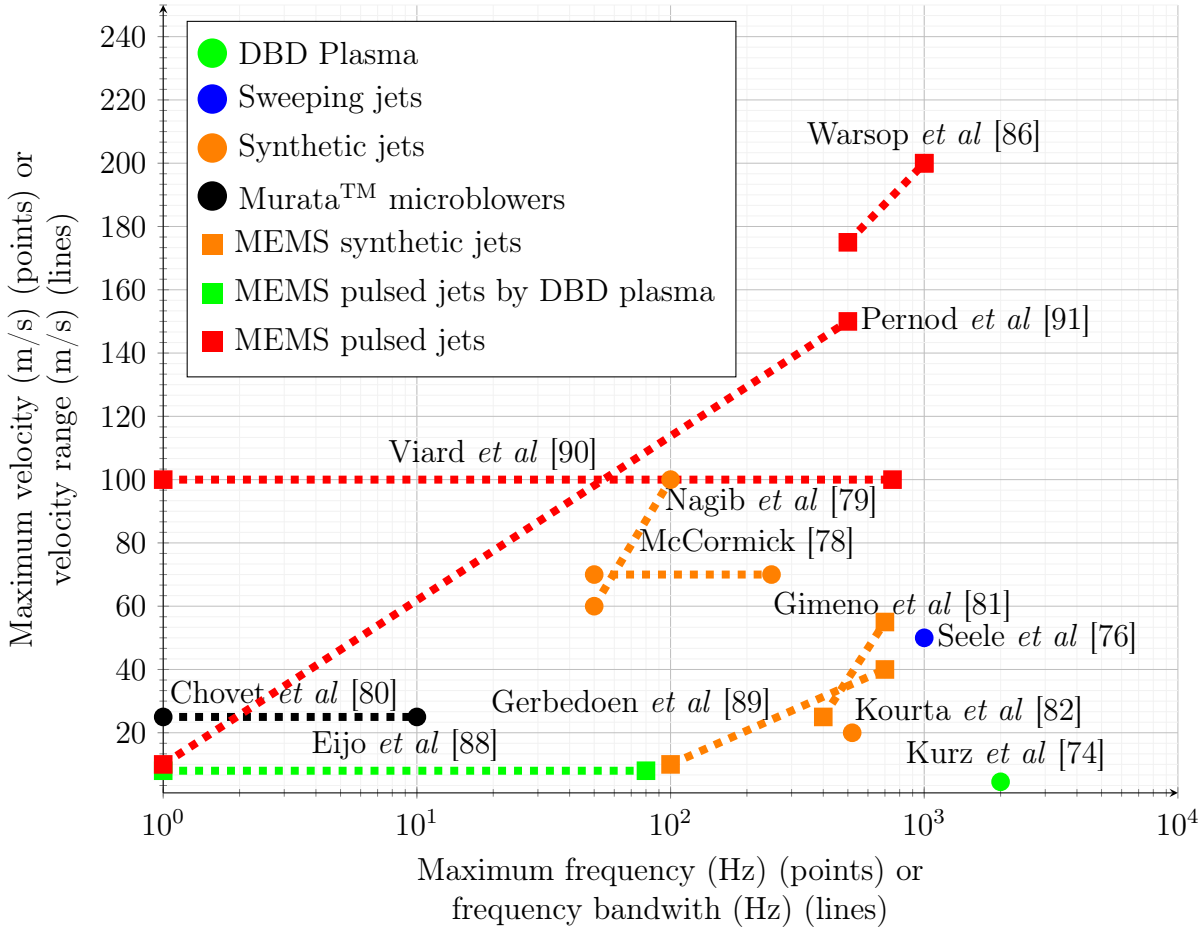

Figure 1.8: Comparison of fluidic actuators performances (inspired from [90]).

As shown above, different ways of generating pulsed jets exist. For instance, Ibrahim et al. [92] used a circular plate with micro-outlets connected to pressure tubes. Driven by an engine, the circular plate is rotated alternating phases during which outlets are aligned with the pressure tubes and phase during which they are not supplied. The engine enable to reach

pulsating frequencies of 6 300 Hz. On their side, Hogue et al. [93] proposed a piezoelectric stack actuator associated with a hydraulic amplifier circuit to produce supersonic microjets. Nevertheless, the most common way of generating pulsed jets is based on the use of solenoid valves ([83, 85, 94, 95, 96]).

Considering the miniaturization of pulsed jets, Frutos et al. [97] proposed the design of hybrid zip valve. The actuator reaches steady outlet velocities of 100 m/s. The outlet jet can be pulsed for frequencies up to 250 Hz with reduced velocities of 15 m/s. MEMS devices have also converged towards the fabrication of pulsed jets. MEMS devices have also converged towards the fabrication of pulsed jets, as proposed by Ducloux [98] and further developed by the IEMN laboratory ([91, 99, 100, 101, 102]). The design enables to reach outlet velocities of 150 m/s for a maximum frequency of 400 Hz. This design of actuator is the one considered in the following for flow control experiments carried out on an open-cavity flow. In addition to the MEMS technology advantages, these actuators can be directly driven with any type of input signals and are characterized by large bandwith. Further details on the fabrication process, steady and dynamics characterization, integration and both open and closed-loop flow control experiments are given in Chapters 2, 4 and 5. Performance of the presented pulsed jets technologies are summed up in Table 1.3.

Table 1.3: Comparison of different pulsed jet technologies.

References	Illustration	Pulsed jet technology	Performance (mass flow rate, velocity, inlet pressure)	Frequency bandwith (Hz)	Application
McManus et al. [95]	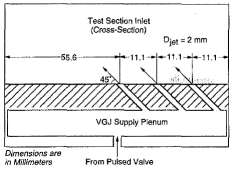	Solenoid valve	0-70 m/s	0-500 Hz	Flow separation
Schaeffler et al. [94]	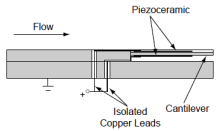	Solenoid valve	0-250 m/s	0-20 Hz	/
Lu and Jensen [103]	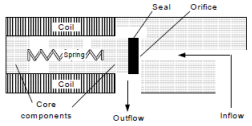	Solenoid valve	700 kPa	50-110 Hz	Fuel injection
Kostas et al. [104]	/	Solenoid valve	0-50 m/s	100 Hz	Separated flow
Kumar and Alvi [105]	/	Solenoid valve	$M_\infty > 1$	/	Supersonic impinging jet
Ibrahim et al. [92]	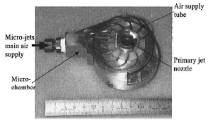	Engine driven microjets	/	6 300 Hz	Fuel injection
Hogue et al. [93]	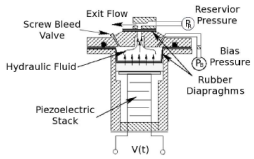	Piezoelectric stack actuator	$M_\infty > 1.5$	1-1 000 Hz	/

Table 1.4: Comparison of different pulsed jet technologies.

Frutos et al. [97]	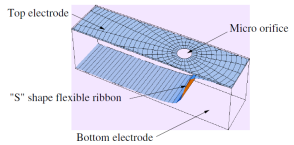	Zip microvalve	15 m/s	0-250 Hz	Boundary layer control
Aider et al. [106]	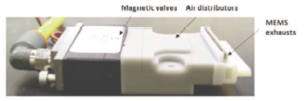	Hybrid MEMS	60 m/s	5-300 Hz	Flow separation
Warsop et al. [86]	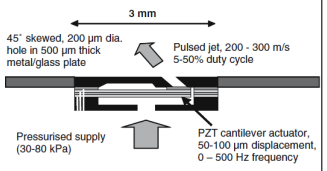	MEMS piezoelectric	200 m/s	500-1 000 Hz	Flow separation
Eijo et al. [88]	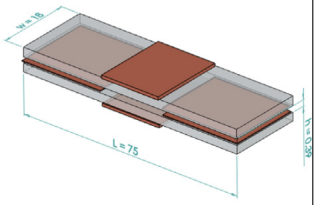	MEMS DBD	8 m/s	1-80 Hz	/
Chovet et al. [80]	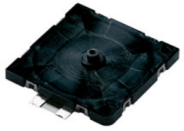	Murata microblowers	25 m/s	1-10 Hz	Flow separation
Pernod et al. [91]	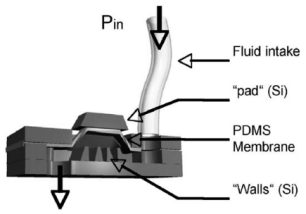	MMMS microvalves	0-150 m/s (outlet dependent)	0-380 Hz	Open-cavity flow

1.3 Active control of flow separation and separated flow

Boundary layer separation over an aircraft flap induces a decrease in the lift coefficient, and an increase in the drag coefficient. It can occur during the critical take-off and landing phases. Most aircraft circumvent this issue using slotted flaps, which however add structural weight and complicate the maintenance. Therefore, one solution would be to simplify these structures into plain flaps with integrated flow control devices to avoid flow separation or reattach a separated flow. For such a control, high mass flow rates are required, as the base flow to reach does not exist without an external forcing and because reattachment is an expensive state to maintain.

1.3.1 Flow separation and boundary layer

Hoerner [107] studied the evolution of the lift increments ΔC_L for several plain flap airfoil sections. Evolution of ΔC_L against the plain flap deflection angle δ is presented in Figure 1.9.

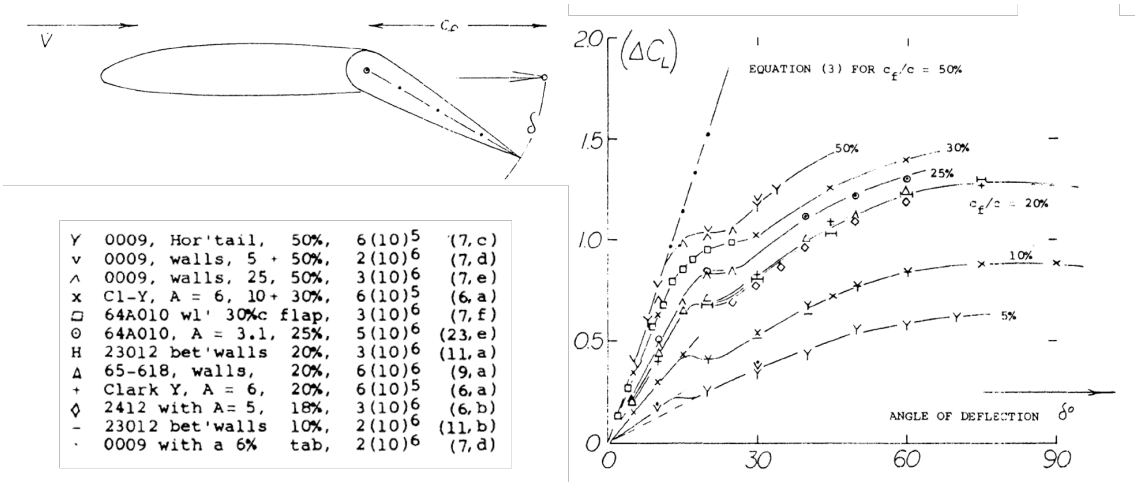

Figure 1.9: Evolution of the lift increment ΔC_L as a function of the plain flap deflection angle δ for different flap airfoil sections [107].

The onset of flow separation is marked by the apparition of plateau in ΔC_L and the flow is fully separated for higher flap deflection angles. The boundary layer developing over the deflected flap is subject to an adverse pressure gradient, which causes the boundary layer to separate. Figure 1.10a depicts the development of such a flow, through the evolution of the wall shear stress defined in Equation (1.2), which characterizes the state of the boundary layer.

$$\tau_w = \mu \left(\frac{\partial u}{\partial y} \right)_{wall} \tag{1.2}$$

Considering a slice of that flow at x_1, the boundary layer is characterized by a positive gradient $\left(\frac{\partial u}{\partial y} \right)_{wall}$. As x is increased, the pressure increases as well and the boundary layer profile flattens until $\left(\frac{\partial u}{\partial y} \right)_{wall} = 0$ at x_2. This point defines the detachment position where

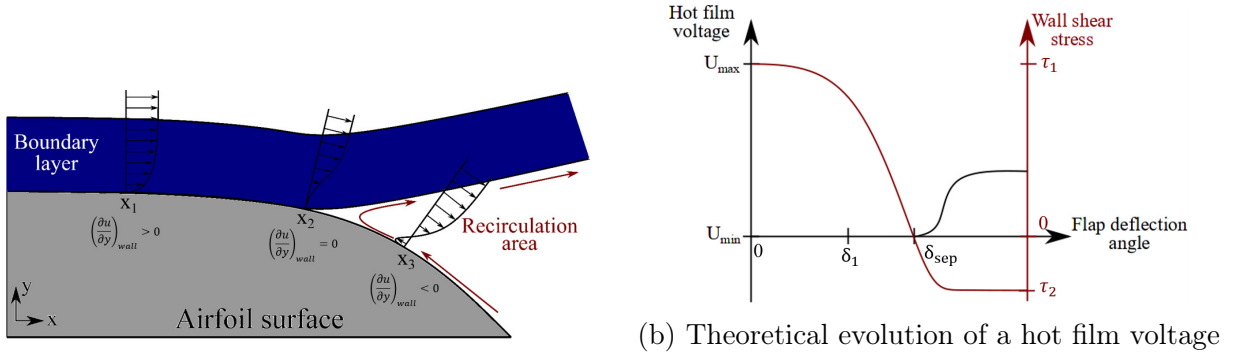

(a) Sketch of the development of flow separation around an airfoil.

(b) Theoretical evolution of a hot film voltage and wall shear stress against the deflection angle of an airfoil.

Figure 1.10: Illustrations of a separated flow (a) and sketch of the theoretical evolution of a hot film wall output in such a flow (b).

the boundary layer separates from the profile. From this point a recirculation bubble with a back flow forms. Also, the gradient $\left(\frac{\partial u}{\partial y}\right)_{wall}$ becomes negative from this point until re-compression occurs. In Figure 1.10b, the evolution of the wall shear stress is presented alongside with the evolution of a hot film measurement. The position of the hot film x_{HF} over the flap is fixed and the deflection angle δ is increased. Between 0° and δ_1, the sensor voltage decreases and similarly does the wall shear stress. As the separation point gets closer to the hot film position, for $\delta_1 < \delta < \delta_{sep}$, the voltage drastically decreases until it reaches a minimum for $\delta = \delta_{sep}$ corresponding to $\tau_w = 0$. For higher deflection angles, the hot film remains in the recirculation zone and its output voltage increases again. The wall shear stress is effectively induced by the back flow, which velocity raises with δ. τ_w becomes negative as the flow direction is reversed compared to the freestream. However, hot films do not deliver information on the flow direction and only provide positive voltages. For flow control application on this study case, hot films are one potential type of measurement for the implementation of closed-loop control, as it is the case in the present work. Nevertheless pressure or lift measurement can also be employed.

As mentioned by Wu et al. [108], post-stall flow control can be divided into two categories: separation control (the flow is partially separated) and separated flow control (the flow is fully separated). In the first case, objectives are to prevent flow separation, reattach the partially separated flow and maintain lift over the considered model. In the second case, aims are to increase lift, reduce drag and reduce the recirculation bubble size. In the following section, studies of post-stall flow control are considered in order to put forwards the different closed-loop control strategies adopted.

1.3.2 Closed-loop control approaches

As discussed by Pastoor et al. [23], closed-loop approaches can be classified depending on their complexity. These different strategies have been used regarding the closed-loop control of flow separation and separated flow. They can rely on triggering, which consists in turning the actuators when a threshold value, related to a predefined criterion of the flow state is exceeded, e.g. onset of flow separation, minimum amount of lift acceptable ([47, 75, 109, 110,

111, 112]) or on the use of PID controllers ([113, 114, 115, 116, 117]), slope and extremum seeking algorithms ([44, 118, 119, 120, 121, 122]) or model-based controller design techniques ([123, 124]) and machine learning approaches ([31, 32, 125]).
A first simple closed-loop approach is the triggering strategy. Poggie et al. [47] employed the triggering method based on hot films sensors rms (root mean square) value for the control of a separated flow. Using DBD actuators, the model sectional lift coefficient was increased of 10% for a freestream Mach number M_∞ of 0.05, when the separation point reached a position defined as the limit. On their side, Rethmel et al. [75] used nanosecond pulse driven DBD actuators placed on a NACA 0015 airfoil to control flow separation. Control is triggered when a threshold power dissipated by the hot film is overcome. The DBD actuators, in this case, do not induce a ionic wind as a forcing but rather set off a thermal exchange with the boundary layer exciting its instabilities. Flow separation control experiments are carried out at Mach numbers up to 0.26. As shown by Tewes et al. [109], Packard and Bons [111] or Lombardi et al. [112], attached flow maintenance requires less power than the control of separated flow with the objective of reattachment. In a similar approach, Benard et al. [110] also highlight the benefits of hysteresis regarded the flow separation control over a NACA 0015 airfoil. The triggering of a single DBD actuator is based on the pressure coefficient rms, used as the flow separation predictor.

PID controllers have also been used for such applications of flow control. Shaqarin et al. [113] and Allan et al. [114] respectively implemented a proportional controller and a PID on a descendant ramp and a hump, both obstacles provoking the flow separation. Allan et al. [114] demonstrated that considering a PID controller, the integral action was the most effective to track the reference value of pressure coefficient, while the proportional or derivative parts amplified the oscillations induced by the flow fluctuations. Troshin and Seifert [115], Lee et al. [116] and Pinier et al. [117] implemented PID controllers on airfoil, respectively with piezoelectric fluidic actuators, synthetic jets and oscillatory jets, targeting either to control lift, the pressure coefficient or delay the onset of separation using pressure measurements. Regarding the study of Garwon et al. [118], both an adaptive integral controller and an extremum seeking algorithm are implemented on a backward facing step for a freestream velocity of 3 m/s. Control is performed using a loudspeaker placed a the step leading edge and pressure measurements are realized to determine the length of the re-circulation area. The extremum seeking implementation is based on the use of a high- and low pass filters, an integrator and a signal generator supplying the actuator. With both type of controls, Garwon et al. [118] showed the ability of both strategies to reduce the re-circulation bubble size.

Slope seeking and extremum seeking algorithms have been widely used for the control of both flow separation and separated flows. Benard et al. [44] and Chabert et al. [119] both used a slope seeking algorithm respectively on a NACA 0015 airfoil for Reynolds numbers between $1.3.10^5$ and 4.10^5 and on a NACA 4412 plain flap for $Re_c = 2.10^6$. Benard et al. [44] aim at maximizing the airfoil lift based on the use of a single DBD and a balance for the measurements. The controller robustness is also shown through dynamics closed-loop experiments, despite a long loop time due to the balance. Slope seeking is based on the presence of a gradient of the static map in the controlled value. An improved version of slope seeking is proposed by Dandois and Pamart [126], who integrated an adaptive gain to

the algorithm ensuring an optimal performance of the gradient estimation. This numerical study, implements the method on a rounded ramp with synthetic jet for a freestream Mach number $M_\infty = 0.31$. This improved methodology was used by Chabert et al. [119], with the loop gain adapted by a fuzzy-logic regulator. This technique enables a faster convergence of the control resulting in less power consumption by the actuators. Using extremum seeking on a high lift configuration, Becker et al. [121] implemented a MIMO approach. Compared to the SISO method also employed in this study, the MIMO scheme achieved the best lift gains. The control is implemented using pulsed jets induced by solenoid valves, while the lift is derived from pressure measurements. Another adaptive control method of separated flow is proposed by Tian et al. [122], who considered a NACA 0025 airfoil for $Re_c = 10^5$ equipped with synthetic jets. The control is performed using a quasi-static adaptive non-linear control scheme based on the downhill simplex algorithm. In this study, despite the non linear of the actuators driven with modulated signals, it is shown that the maximization of the lift to drag ratio depends on the forcing of the non linear interactions between the shear layer and the wake instabilities.

Model-based controller design techniques have also been used for the control of separated flow. Henning and King [123] used the robust H_∞ design technique to control the re-circulation flow length behind a backward facing step characterized by $Re_H = 25000$. An array of pressure sensors (microphones) is used in combination with slot hose loudspeakers for the MIMO closed-loop implementation. The black box model is identified during step experiments, yielding linear time-continuous multi-variable models. The designed controller is then employed to impose the re-circulation flow length and for disturbance rejection. Using the similar controller design technique, King et al. [124] on an airbus half-size model and on a Stemme S10 glider. Both the model and the glider were equipped with pulsed jets driven by solenoid valves and pressure measurements for the monitoring of lift. Both SISO and MIMO controls are implemented. For both the wind tunnel and in-flight experiments, models of the flow dynamics are derived using PRBS as input for the actuators. The controllers then designed were used to both reject disturbances and control lift.

More recently, further model-free approaches have been considered based on machine learning. Gautier et al. [31] and Debien et al. [32] both used genetic programming for the control of separated flows, respectively considering a backward facing step with $Re_H = 1350$ and a sharp edge ramp for $Re_\theta = 3500$. Both studies aimed at the minimization of the re-circulation flow area. Gautier et al. [31] controlled the flow using slotted jets based on on-line PIV measurements, determining the re-circulation bubble size, while Debien et al. [32] used vortex generators supplied by solenoid valves coupled with wall shear stress measurements. Use of deep reinforcement learning was achieved by Shimomura et al. [125] on a NACA 0015 airfoil with $Re_c = 63000$. The control is based on the use of a single DBD actuator and on pressure measurements with the aim of reattaching the separated flow.

Table 1.5 sums up the previously presented flow separation and separated flow control studies. The different configurations presented above constitute a benchmark for the use of new closed-loop control strategies. In the present work, a plain flap configuration, composed of a flat plate and a NACA 4412 airfoil is considered for the closed-loop implementation of flow separation control through two different control approaches: a data-driven strategy, leading

to a linear (integral) controller and a phenomenological/model-driven strategy, leading to a non-linear positive (integral) controller. While the former benefits of a tuning simplicity, the latter prevents undesirable effects and formally guarantees closed-loop stability.

Table 1.5: Comparison of different closed-loop approaches for post-stall configuration flow control (adapted from [127]).

References	Setup illustration	Model	Actuators	Sensed property	Control objective	Closed-loop method
Poggie et al. [47]	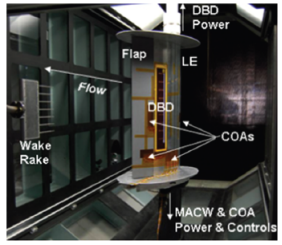	Flex Sys. Inc. Mission Adaptive Compliant Wing + Trailing edge morphing flap for $M_\infty = 0.05 - 0.10$	Nanosecond pulse driven DBD	Wall shear stress	Hot films rms	Triggering
Rethmel et al. [75]	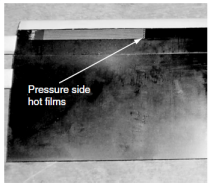	NACA 0015 $M_\infty = 0.26$	Single DBD	Wall shear stress	Hot films rms	Triggering
Tewes et al. [109]		Elliptical airfoil $Re_c = 150000 \rightarrow Re_c = 500000$	Two control valves for suction	Pressure	Pressure coefficient	Triggering
Benard et al. [110]	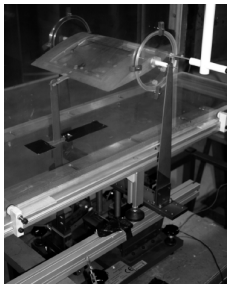	NACA 0015 $Re_c = 1.9.10^5$	Single DBD	Pressure	Pressure coefficient rms	Triggering
Packard and Bons [111]	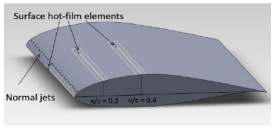	NACA $64_3 - 618$ $Re_c = 6.4.10^4$	Pulsed jets (solenoid valves)	Wall shear stress	Hot films rms	Triggering

Lombardi et al. [112]	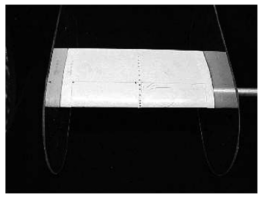	NACA 0015 $U_\infty = 10$ m/s	Single DBD	Pressure	Pressure rms	Triggering
Shaqarin et al. [113]	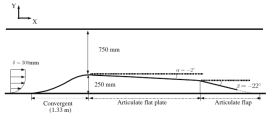	Descendant ramp $U_\infty = 5 \rightarrow 10$ m/s	Vortex generators (solenoid valves)	Wall shear stress	Hot film voltage	Proportional regulator
Allan et al. [114]	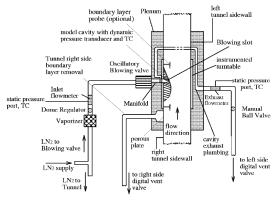	Hump model $M_\infty = 0.25$	Siren type valves	Pressure	Pressure gradient	PID controller
Troshin and Seifert [115]	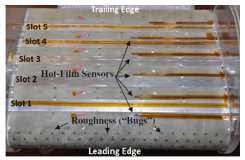	Modified AHW 93 300 $Re_c = 5.10^5$	Piezoelectric fluidic actuators	Wall shear stress and pressure	Lift	PID controller
Lee et al. [116]	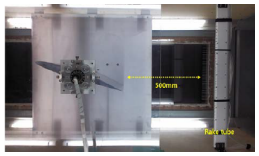	NACA 64A20 $U_\infty = 20 \rightarrow 30$ m/s	Synthetic jets	Pressure	Pressure coefficient	PID controller
Pinier et al. [117]	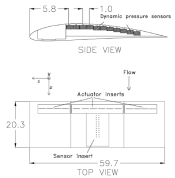	NACA 4412 $U_\infty = 10$ m/s	Oscillatory jets	Pressure	Delay separation	Proportional controller
Garwon et al. [118]	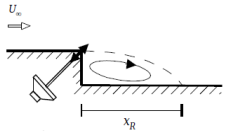	Backward facing step $U_\infty = 3$ m/s	Loudspeaker	Pressure	Re-circulation area minimization	Integral controller and extremum seeking

Benard et al. [44]	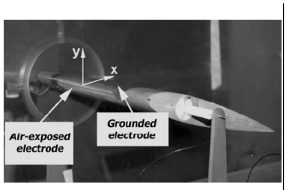	NACA 0015 $Re_c = 1.3.10^5 \rightarrow 4.10^5$	Single DBD	Lift	Maximizing lift	Slope seeking
Chabert et al. [119]	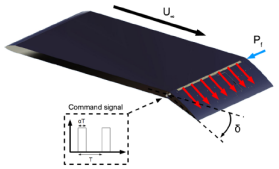	NACA 4412 plain flap $Re_c = 2.10^6$	Pulsed jets (solenoid valves)	Wall shear stress	Maintain flow attached	Slope seeking
Feingesicht et al. [120]	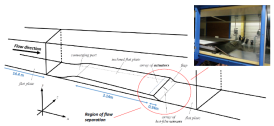	Ramp $U_\infty = 10$ m/s	22 co-rotating round jets	Wall shear stress	Hot film voltage	Sliding mode
Becker et al. [128]	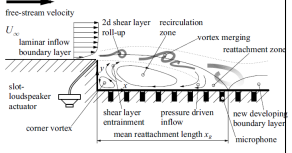	NACA 4412 + NACA 4415 $Re_c = 0.5.10^6$	Pulsed jets (solenoid valves)	Pressure	Pressure gradient	Extremum seeking
Becker et al. [121]	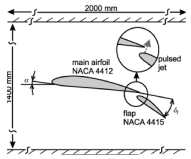	Backward facing step $Re_c = 0.5.10^6$	Pulsed jets (solenoid valves)	Pressure	Pressure gradient	Extremum seeking
Tian et al. [122]	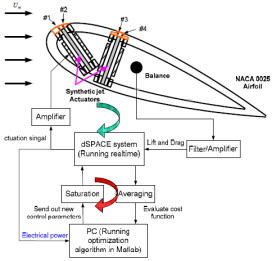	NACA 0025 $Re_c = 10^5$	Synthetic jets	Pressure	Reattachment	Downhill simplex algorithm
Henning and King [123]	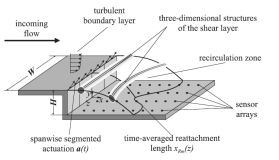	Backward facing step $Re_H = 25000$	Slot hose loudspeakers	Pressure	Disturbances rejection	H_∞ designed controller

King et al. [124]	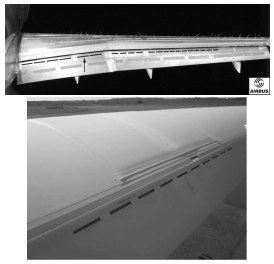	Airbus model and Stemme S10	Pulsed jets (solenoid valves)	Pressure	Lift	H_∞ designed controller
Gautier et al. [31]	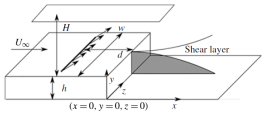	Backward facing step $Re_H = 1350$	Slotted jets	Online PIV	Re-circulation area minimization	Genetic programming
Debien et al. [32]	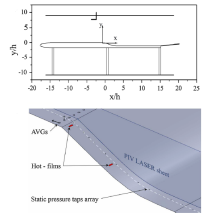	Sharp edge ramp $Re_\theta = 3500$	Vortex generator (solenoid valves)	Wall shear stress	Re-circulation area minimization	Genetic programming
Shimomura et al. [125]	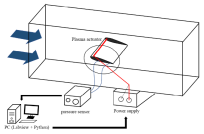	NACA 0015 $Re_C = 63000$	Single DBD	Pressure	Reattachment	Deep re-inforcement learning

1.4 Active control of open-cavity flows

The open-cavity is a commonly studied geometry in fluid dynamics, as it has many practical applications. In the aeronautical domain, weapon bays or airplanes landing gear doors have cavity shapes [129]. These shapes can also be found on vehicles such as cars or trucks, considering wheel wells or trains between two carriages [25]. Flows over open-cavities are responsible for noise radiation and structural vibrations, which could damage structures, hinting at a practical interest of damping the oscillations arising in such flows. Furthermore, the open-cavity has became a convenient test bed in the flow control domain. It can be used for the test of new control strategies, of sensors or of actuators as considered in the present work with MEMS microvalves.

1.4.1 Open-cavity flow

Open-cavity flows are a case of impinging shear flows. The flow dynamics is constrained by the boundary conditions imposed by the solid edges. The flow behaves as an acoustic resonator enhancing particular oscillation frequencies growing in the shear layer, as pointed out in the early studies of Roshko [130] and Krishnamurty [131]. Extensive studies of the open-cavity impinging shear flow was conducted by Plumblee et al. [132], Rossiter [133] or Rockwell and Naudascher [134] highlighting the aeroacoustic feedback mechanism of the self-sustained oscillations. As depicted in Figure 1.11, the laminar or turbulent boundary layer developing upstream the cavity, characterized by a thickness δ and a momentum thickness θ, separates at the cavity upstream border. It results in a shear layer developing over the cavity of length L, depth D and span W. This shear layer undergoes hydrodynamic instabilities over the cavity, reattaches near the cavity downstream corner for deep open-cavities as observed by Rossiter [133]. The vortices growing in the shear layer impact the trailing edge, generating acoustic waves which propagate upstream and excite the shear layer instabilities at the upstream corner, which closes the feedback loop.

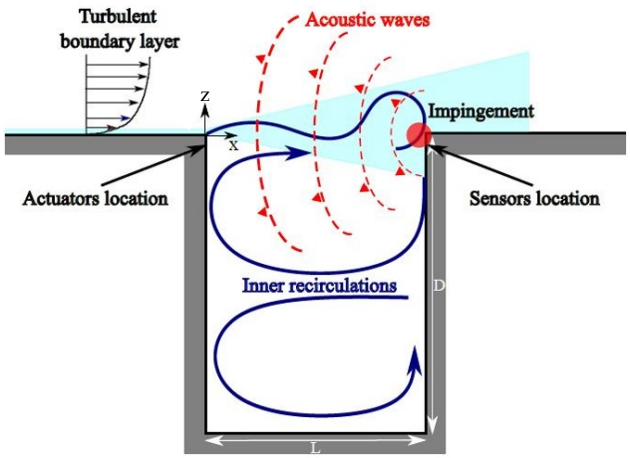

Figure 1.11: Illustration of the developing flow over an open-cavity with an upcoming turbulent boundary layer

Rossiter proposed a semi-empirical expression for the prediction of oscillation frequencies f of an open-cavity with subsonic and transonic flows, such that:

$$f = \frac{U}{L}\frac{(m-\gamma)}{(\frac{1}{\kappa}+M)}, \tag{1.3}$$

where U, L and M respectively denote the freestream velocity, the cavity length and the flow Mach number. The quantities m, κ and γ stand for the mode number, the ratio between the convection speed of the vortices in the shear layer and the freestream velocity and model of a time delay between the vortex impact and the emission of an acoustic wave. Originally, κ and γ were set respectively to 0.57 and 0.25. Considering incompressible cases of flow past open-cavities, Rockwell [135] and Rockwell and Naudascher [136, 134] adapted the semi-empirical Rossiter mode equation according to Equation (1.4):

$$f = \frac{U}{L}(m-\gamma)\kappa. \tag{1.4}$$

For deep open-cavities, the feedback mechanism can be coupled with an acoustic resonance mechanism due to the cavity normal acoustic modes. This particular mechanism was investigated by East [137], who proposed the following equation to predict the fundamental resonance frequency f:

$$\mathrm{f} = \frac{\mathrm{a}}{\mathrm{D}}\frac{0.25}{1+\mathrm{A}(\frac{\mathrm{L}}{\mathrm{D}})^{\mathrm{B}}}, \tag{1.5}$$

with A, B empirical coefficients and a the speed of sound. In this formula, the freestream velocity does not play a role but only the cavity dimensions and the speed of sound indicating a purely acoustic mode. Both Rossiter and East modes can interact with each other, yielding a local maximum in the global modes growth rate of instabilities of the base flow. For low Mach numbers the latter mechanism can be seen as enhancing the former mechanism response, as shown by Yamouni et al. [138]. Both mechanisms result in the generation of flow-induced noise radiation and structural vibrations, which could damage structures. Therefore damping these flow oscillations through control strategies is of interest. This control relies on the suppression of the flow feedback mechanisms by interactions of actuators with the upstream boundary layer ([139]) or by interactions of induced flow perturbations with the shear layer at the upstream edge of the open-cavity ([140, 46, 141, 68, 142]). Some of these open-loop control results are compared with the open-loop test campaign in Chapter 4. In the following section, the focus is on the closed-loop control of open-cavity flows.

1.4.2 Closed-loop control of open-cavity flow

Different closed-loop control approaches have been employed targeting the suppression of the cavity flow oscillations. The first experiments consisted in tuning open-loop forcing parameters in a quasi-static fashion, based on the information fed back from a performance sensor ([143, 144, 145, 146]). With promising results, as described in the following, control of open-cavity flows then moved to closed-loop control from estimation sensors, requiring less power to control the flow than quasi-static approaches. Closed-loop methods can rely on black bock models of the input-output dynamics using adaptive filters approaches ([147, 148, 149, 150, 151, 152, 153, 154]) or using the frequency response of the sensors to an excitation of the actuators ([21, 142, 155, 156, 157, 158, 159, 160]) or be model-free as this

is the case concerning machine learning approaches ([33, 161]).

One of the first closed-loop control study of the flow over an open-cavity was proposed by Gharib [143], who studied the case of an axisymmetric open-cavity for a freestream velocity U_∞= 0.22 m/s in an hydrodynamic tunnel. Control is performed using a heated strip placed upstream the open-cavity leading edge, exciting the boundary layer Tollmien-Schlichting waves. The closed-loop control is quasi-static and consists in a manually tuned forcing gain and phase. With such an approach, Gharib reduced the velocity fluctuations by 40%, based on LDV (Laser Doppler Velocimetry) measurements. Similarly, in a slow tuning approach of open-loop parameters, Shaw and Northcraft [144] presented the closed-loop control of an open-cavity flow characterized by a length-to-depth ratio $L/D = 6.46$ for Mach numbers varied between 0.6 and 0.95. Pulsed fluidic actuators are used with different outlet designs to suppress the cavity resonance despite the apparition of new tones due to the actuation. In the two previous studies, the forcing is performed at the cavity leading edge. Micheau et al. [145] proposed to drive a vibrating surface placed at the trailing edge of an open-cavity of $L/D = 1$ for $M_\infty = 0.11$, based on pressure measurements performed at the bottom of the cavity. The active control employed relies on the use of an envelope controller and completely damped the open-cavity Rossiter mode. Debiasi and Samimy [146] also implemented a quasi-static control of an open-cavity flow characterized by $L/D = 4$ and for Mach numbers between 0.25 and 0.5. The logic-based controller tunes the forcing frequency of the synthetic to get the best peak suppression in the pressure measurements. Despite the emergence of new peaks in pressure spectra due to actuation, Rossiter modes are damped or attenuated on the entire range of Mach numbers tested.

Model-based "dynamic" closed-loop control approaches rely on an accurate identification of the input-output dynamics in the open-cavity flow. Filter-based control methods aim at tuning a filter parameters in order to minimize the error between the filter and the data. Kestens and Nicoud [147] implemented the numerical adaptive control of an open-cavity $L/D = 2$ using a LMS (Least-Mean Square) algorithm, based on a loudspeaker driven to minimize the pressure fluctuations. In a similar way, Williams et al. [150] performed the closed-loop control of several modes using pass-bands filters. The control performed using a synthetic jet reached an attenuation of 7 dB in the two targeted modes, while a smaller attenuation was observed in the other mode. Kegerise et al. [148] and Cattafesta et al. [154] proposed filter-based adaptive closed-loop control of open-cavity flows. While Kegerise et al. [148] reported damping up to 7 dB in several modes, Cattafesta et al. [154] observed a slight damping of mode with the disturbance rejection algorithm. However, the limitation of this last result was due to the piezoelectric flap actuator limitations.

In their study, Rowley et al. [151], who implemented the closed-loop control of an open-cavity flow with $L/D = 5$ and $M_\infty = 0.34$ using a band-pass filter and a phase shifter, proposed a linear modeling of the open-cavity flow giving insight into peak-splitting effects observed during the closed-loop control implementation. The linear model proposed is presented in Figure 1.12. The derivation of such a model of the open-cavity dynamics either based on black-box models (experimental input-output identification) or on linear descriptions as proposed Rowley et al. [151], who considered the open-cavity flow to have slightly amortized modes excited by noise.

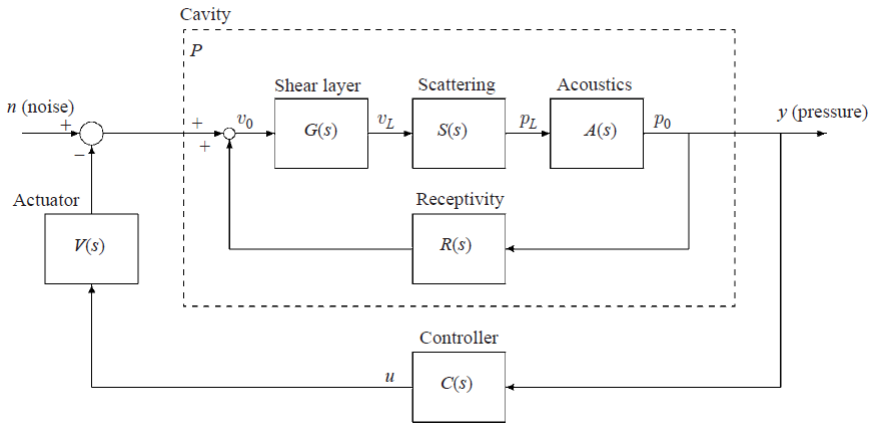

Figure 1.12: Block diagram of the linear stable cavity model proposed by Rowley et al. [151].

From input-output experimental data, Cabell et al. [156] derived a state-space model of the open-cavity dynamics using an ERA (Eigensystem Realization Algorithm) and employed a reduced order model for the controller synthesis. A linear quadratic design method is used in combination with a frequency shaping approach. This way, the synthetic jet actuator driven based on the fed back pressure achieved tone reduction of the open-cavity ($L/D = 5$) for flow Mach numbers between 0.275 and 0.45. LQG controllers were also employed as shown by Cattafesta et al. [142], who reached a reduction of 20 dB in open-cavity tone for a geometry characterized by an aspect ratio $L/D = 0.5$ and 2 and for freestream velocities respectively of $U_\infty = 40$ m/s and 45 m/s. Based on the linear model introduced by Rowley et al. [151], Illingworth et al. [162] proposed the design of a LQG controller for the control of a compressible flow ($M_\infty = 0.6$) over an open-cavity ($L/D = 2$) in a 2D Direct Numerical Simulation (DNS). Based on pressure measurements and on the simulation of a forcing term near the open-cavity leading edge, oscillations in the flow were suppressed. In their numerical study, Barbagallo et al. [157] implemented the closed-loop control of a quasi-periodic flow developing over a 2D square cavity. The forcing term consists in a parabolic velocity field in the streamwise direction placed at the cavity leading edge. Normal wall shear stress measurements are performed at the downstream edge of the cavity, closing the loop with a LQG controller. Barbagallo *et al* show that the use of reduced order models, based either on POD (Proper Orthogonal Decomposition) or balanced modes efficiently represent the input-output behavior for the design of a controller stabilizing the flow. Samimy et al. [159] performed model reduction based on POD modes derived from PIV snapshots. The designed LQG controller combined with pressure measurements and a synthetic jet used an open-cavity of $L/D = 4$ for a freestream Mach number of 0.3 yielded damping of the flow tone.

Loop-shaping design techniques have also been employed for the synthesis of a controller. For instance, Mongeau et al. [163] proposed a robust loop-shaped controller for the suppression of open-cavity pressure fluctuations, using a spoiler driven by a loudspeaker. The controller, shaped using Nichols chart, provided reduction up to 20 dB in the pressure level. H_∞ loop-shaping design technique was also used by Leclercq et al. [21], who considered the same open-cavity study case as Barbagallo et al. [157]. In this FEM (Finite Element

Method) study, it is proposed to iteratively design and apply linear controllers to retrieve the open-cavity base flow. On the contrary to Barbagallo et al. [157], at $t = 0$ of the simulation Leclercq et al. [21] considered the flow in its quasi-periodic state, therefore away from the unstable fixed points. It is shown than an application of 5 controllers is required for the control of the quasi-periodic flow. In this 2D numerical simulation, the volumic forcing term used has a Gaussian shape and is placed at the cavity leading edge, while measurements are performed at the cavity downstream edge.

Model-free approaches have also been considered regarding the closed-loop control of open-cavity flows through machine learning. Based on the use of neural networks, Efe et al. [33] implemented the control of an open-cavity flow characterized by an aspect ratio of 4 and for freestream Mach numbers of 0.25 to 0.5. In a recent study, Maceda et al. [161] employed a gradient enriched machine learning method to perform the closed-loop control of an open-cavity flow. Control experiments were carried out on open-cavities of aspect ratio 1.5 and 1.75 for a freestream velocity of 2.13 m/s. The flow is forced at the leading edge by a single DBD actuator based on the fed back information provided by a hot wire, placed at the open-cavity downstream edge. Implementation of the genetic programming algorithm resulted in the flow stabilization.

Table 1.6 summarizes the previous open-cavity flow closed-loop control studies. The application of the different closed-loop control strategies on the different flow configurations showed some limitations. Application of the control may result in a damping of the cavity tones but may also result in peak-splitting or in the triggering of non linear effects due to too strong forcings. Furthermore as stated by Cattafesta et al. [25], for model-based approaches using data-based frequency response, it is assumed that the plant behaves as a Linear Time Invariant system for the derivation of a transfer function, despite this assumption is not justified. In the present work, the aim is to perform the closed-loop control of a deep open-cavity flow with MEMS actuators, based on the strategy proposed by Leclercq et al. [21]. It is also tried to defined and justify the existence of a transfer function for the considered open-cavity flow. This closed-loop control study aims also at demonstrating the interest of the MEMS actuators fro such an application. Details on the open-cavity geometry are given in Chapter 2, Chapter 4 and Chapter 5 present results respectively of the open- and closed-loop test campaigns.

Table 1.6: Comparison of different closed-loop approaches for open-cavity flows (adapted from [25]).

References	Setup illustration	Model	Actuators	Sensed property	Closed-loop method
Gharib [143]	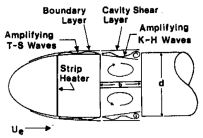	Axi-symmetric cavity (hydrodynamic tunnel) $U_\infty = 0.22$ m/s	Heated strip	LDV	Manual gain and phase adjustment
Shaw and Northcraft [144]	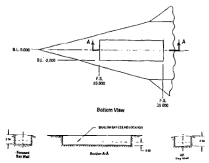	$L/D = 6.46$ $M_\infty = 0.6 \rightarrow 0.95$	Pulsed jets	Pressure	Quasi-static of open-loop parameters
Micheau et al. [145]	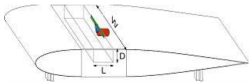	$L/D = 1$ $M_\infty = 0.11$	Vibrating surface at trailing edge	Pressure	Envelope control
Debiasi and Samimy [146]	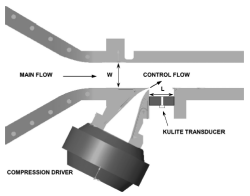	$L/D = 4$ $M_\infty = 0.25 \rightarrow 0.5$	Synthetic jet	Pressure	Logic-based controller
Kestens and Nicoud [147]	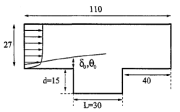	$L/D = 2$ $Re_\delta = 1000$	Loudspeaker at cavity bottom	Pressure	Adaptive control based on LMS filter
Kegerise et al. [148]	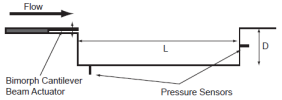	$L/D = 5$ $M_\infty = 0.275 \rightarrow 0.6$	Piezoceramic bimorph flap	Pressure	Self tuning regulator using IIR filters

Williams et al. [150]	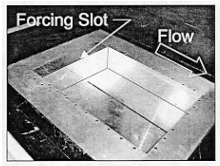	L/D =2,4 and 5 $M_\infty = 0.2 \rightarrow 0.55$	Synthetic jet	Pressure	Analog output feedback with bandpass filters
Rowley et al. [151]	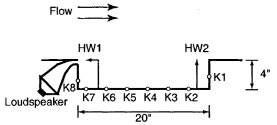	$L/D = 5$ $M_\infty = 0.34$	Loudspeaker	Pressure	Band-pass filters with adjustable gain and time-delay
Kegerise et al. [152],[153]	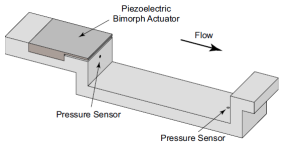	$L/D = 5$ $M_\infty = 0.275 \rightarrow 0.38$	Piezoelectric flap	Pressure	Adaptive generalized predicitve controller
Cattafesta et al. [154]	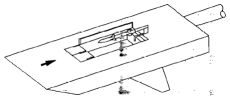	$L/D = 5$ $M_\infty = 0.4$ and 0.6	Piezoelectric flap	Pressure	Adaptive disturbance rejection algorithm
Rowley et al. [155]	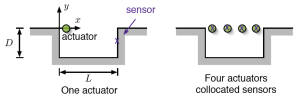	$L/D = 2$ $M_\infty = 0.6$ (2D DNS simulation)	Velocity forcing	Pressure	Heuristic feedback law
Cabell et al. [156]	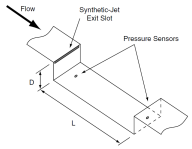	$L/D = 5$ $M_\infty = 0.275 \rightarrow 0.45$	Synthetic jet	Pressure	LQ controller
Cattafesta et al. [142]	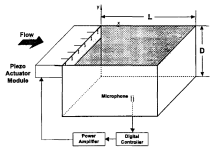	$L/D = 0.5$ and 2 $U_\infty = 40$ and 45 m/s	Piezoelectric segmented flap	Pressure	LQG and pole placement

Barbagallo et al. [157]	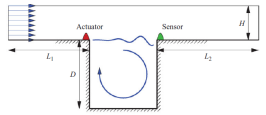	$L/D = 1$ 2D incompressible simulation	Synthetic jet	Pressure	LQG controller
Illingworth et al. [158]	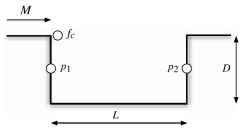	$L/D = 2$ and $M_\infty = 0.6$ 2D compressible DNS	Leading edge forcing	Pressure	LQG controller
Samimy et al. [159]	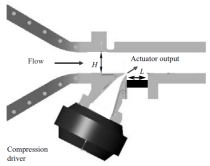	$L/D = 4$ $M_\infty = 0.3$	Synthetic jet	Pressure	LQG controller
Mongeau et al. [163]	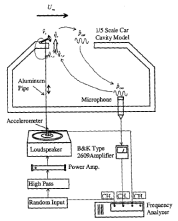	$L/D =$ not indicated $U_\infty = 15 \rightarrow 19$ m/s	Spoiler driven by loudspeaker	Pressure	Robust loop-shaping controller
Yan et al. [160]	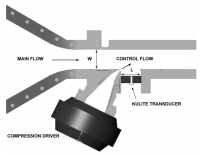	$L/D = 4$ $M_\infty = 0.25 \rightarrow 0.5$	Synthetic jet	Pressure	Smith predictor, PID controller and H_∞ synthesis
Leclercq et al. [21]	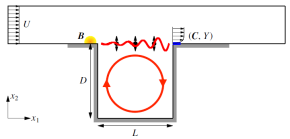	$L/D = 1$ Uniform inlet velocity FEM simulation	Gaussian shape volumic forcing	Downstream edge sensor	Iterative H_∞ synthesis

Efe et al. [33]		$L/D = 4$ $M_\infty = 0.25 \rightarrow 0.5$	Synthetic jet	Pressure	Machine learning neural network
Maceda et al. [161]		$L/D = 1.5$ and 1.75 $M_\infty < 10^{-2}$	Single DBD	Velocity	Machine learning genetic programming

Conclusion

This first chapter introduces the multidisciplinary domain of flow control which consists of a combination of fluid dynamics, control theory and technology design.

The first part of this chapter presents the different approaches that can be considered in flow control. The focus is put on controller design strategies for closed-loop application through an overview of commonly used design techniques. In the present work, the control of flow separation is implemented with two simple but efficient closed-loop control approaches: a data-driven strategy and a phenomenological/model-driven strategy originating from the biological domain.

As described in the second part, sensors and actuators have to meet several requirements for the efficient implementation of closed-loop control strategies. Indeed, actuators technology must be adapted (forcing type, bandwith, controllability, small footprint) to the flow control configuration considered. For the plain flap configuration, the aim is the reattachment of the separated base flow, requiring large mass flow rates, much beyond the capacities of the MEMS actuators considered in the present work. Therefore, the MMMS microvalves are integrated on an open-cavity to control the flow instabilities in both open and closed-loop experiments.

Chapter 2

Experimental facilities for separated flow and shear flow control

Introduction

Chapter 1 presented two well-known flow control problems, respectively the control of separated flows and the control of an open-cavity flow. Both problems constitute a convenient test bed for the use of new technologies and methodologies designed for active flow control applications, which have to meet the requirements pointed out by the literature on each study case. In that sense, actuators for flow separation control need to deliver high mass flow rates, while actuators for open-cavity flow control need to be able to follow arbitrary signals and induce flow velocity perturbations. Sensors and real-time controller used to implement the control strategies also must have time resolution in compliance with the flow dynamics to be controlled.
The present study mainly focuses on the investigation of closed-loop flow control on two experimental configurations. The first set of flow control experiments are conducted on a separated flow over a NACA 4412 plain flap and take place in the L1 wind tunnel of the ONERA. The aim of this first study is to control the flow separation/separated flow developing over the model with conventional actuators and sensors. Two control laws are implemented. The first one being a data-driven control law, leading to a linear integral controller and the second one being a phenomenological/model-driven approach, leading to a non-linear positive integral control law. The second set of experiments is carried out on a low-speed open-cavity flow installed in the S19 wind tunnel of the ONERA. The aim of this second study is to implement the closed-loop control of the cavity flow oscillations with MEMS actuators based on unsteady pressure measurements. Regarding this study, linear controllers are designed based on a structured H_∞ synthesis.

In the present chapter, the two experimental setups are described. For each flow configuration studied, the wind tunnel and model geometry characteristics are introduced. Measurement devices and actuation setups are then described.

2.1 L1 wind tunnel: plain flap model for separated flow control

2.1.1 Plain flap model

Flow separation control experiments were carried out in the L1 wind tunnel facility of the ONERA Lille. This wind tunnel is characterized by a test section diameter of 2.40 m and by a turbulence level of 1.3 %. The model is composed of a flat plate of length $c_{fp} = 867$ mm, stabilizing the boundary layer, followed by a plain flap of chord length $c_{flap} = 220$ mm. The model has therefore a total length $c_{tot} = 1087$ mm. The plain flap design is based on a NACA-4412 airfoil. The model is 800 mm long in the spanwise direction. As depicted in Figure 2.1, two vertical panels are installed at the model extremities to ensure the development of a bi-dimensional flow over the model. Reference axes are sketched in Figure 2.2. The X-axis and Z-axis correspond respectively to the flow streamwise direction and to the orthogonal axis with respect to flat plate. The Y-axis completes the direct system. A carborundum strip, placed on both the flat plate upper and lower surfaces close to the leading edge triggers the boundary layer transition towards a turbulent state. Velocity measurements upstream the model are performed with Pitot tubes. During the experiments, the freestream velocity U_∞ is fixed to 34.5 m/s, yielding a Reynolds number Re based on the model total length of 2.39×10^6. The model is placed inside the test section with a 2° angle of attack. The motorized flap can be deflected downward at an angle δ varied between 2° and 37°.

(a) Picture of the L1 wind tunnel test section with the model.

(b) Picture of the flap and hot films on its upper surface.

Figure 2.1: Pictures of the L1 wind tunnel test section setup (a) and close view of the motorized flap (b).

2.1.2 Measurement setup for flow separation detection and control

To monitor the flow separation over the flap and implement the control laws, eight Senflex® hot films are placed on the flap upper surface, along the chord-wise direction. The hot films locations with respect to the flap leading edge are described in Table 2.1. The hot films outputs are recorded with two Keysight® A/D converters, respectively E1413 and E1433,

with a sampling frequency of 1.25 kHz. Simultaneously, the hot films outputs are sampled at a frequency of 1 kHz via a PXIe-8102 RT from National Instruments and displayed on a LabVIEW Real-Time 2011 interface. The second acquisition system is only used to control the actuators and to implement the closed-loop control laws.

Hot film number	Distance to the flap leading edge (mm)	Dimensionless abscissa x/c_{flap}
HF1	32.6	0.148
HF2	52.6	0.239
HF3	72.6	0.330
HF4	92.4	0.420
HF5	112.4	0.511
HF6	132.4	0.602
HF7	152.5	0.693
HF8	172.5	0.784

Table 2.1: Positions of the hot films with respect to the flap leading edge.

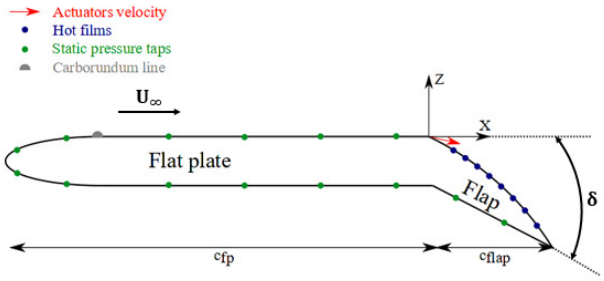

Figure 2.2: Sketch of the plain flap configuration (only few pressure taps are sketched).

Completing the sensor setup, 51 pressure taps are dispatched on both the flat plate and flap upper and lower surfaces. The acquisition of pressure data is performed with a PSI8400 Scanner Digitizer Interface. For each run in this test campaign, an average value of the static pressure at each pressure tap location is stored. The post-processing of these data yield both the pressure coefficient C_p evolution along the model and the global lift coefficient C_L. The pressure coefficient is defined according to the following equation:

$$C_p = \frac{p - p_\infty}{\frac{1}{2}\rho_\infty U_\infty^2} \tag{2.1}$$

where p and p_∞ respectively denote the local static pressure measurement and the freestream static pressure. The lift coefficient is derived from the pressure coefficient computations according to the following formula:

$$C_L = \int_{c_{tot}} (C_{p_{lower}} - C_{p_{upper}})\, d\frac{x}{c_{tot}} \tag{2.2}$$

Both quantities C_p and C_L are used to assess the control effects, comparing cases of uncontrolled and controlled flows.

2.1.3 Integration of Festo valves to the model

The actuation setup is composed of 7 slots spanning along the flap leading edge at a location of $x/c_{flap} = 0.08$. Separated by 7 mm from each other, the actuators slots are 90 mm long and 0.25 mm thick each. They cover 80 % of the flap span and are supplied by on/off Festo MEH2 fast response solenoid valves, fed with pressurized air. Valves driving signals are controlled by the PXIe-8102 RT unit and consist in square signals of frequency f and of duty cycle α. In the present study, the actuation frequency is fixed to 100 Hz, yielding a reduced actuation frequency f^+ such that:

$$f^+ = \frac{f\ c_{flap}}{U_\infty} \cong 0.64 \tag{2.3}$$

with c_{flap} the flap chord and U_∞ the freestream velocity. The duty cycle is therefore the actuators parameter tuned by the controllers and is considered as the system input. The slot outlet velocity is inclined by 30° relatively to the flap local tangent, as illustrated in Figure 2.2. During these experiments the valves are driven with a constant mass flow rate $q_f = 21$ g/s. The fluidic circuit used to supply the valves with that constant mass flow rate is presented in Figure 2.3.

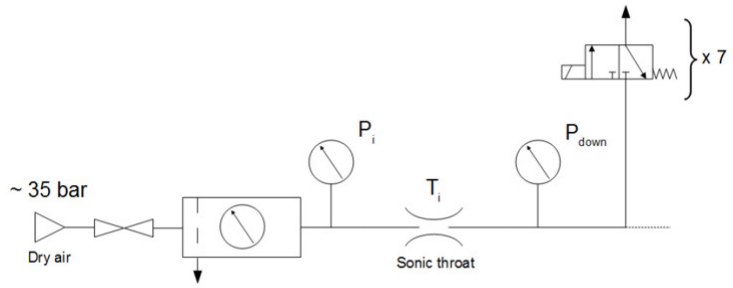

Figure 2.3: Sketch of the air supply circuit for a constant mass flow rate q_f, from Chabert [127]

As described by Chabert [127], the fluidic circuit is connected to a primary circuit of dry air pressurized at 35 bar. The secondary fluidic circuit is composed of a sonic throat, whose outlet supplies the valves. Two pressure sensors are dispatched upstream and downstream the throat to determine the pressure. A thermocouple is placed in the throat to measure the total temperature. Based on this setup, the actuators mass flow rate can therefore be fixed according to Equation (2.4):

$$q_f = 0.404 \frac{A_{throat} P_0}{\sqrt{T_0}} \tag{2.4}$$

where A_{throat}, P_0 and T_0 respectively denote the sonic throat area, the total pressure upstream the throat and the throat total temperature. Equation (2.4) therefore guarantees a constant mass flow rate delivered to the actuators q_{act} such that $q_{act} = q_f$. This result helps characterising the forcing implemented during the control experiments through the calculation of the momentum coefficient C_μ. Considering the case of a steady forcing induced by the valves, it can be defined according to Equation (2.5):

$$C_\mu = \frac{q_{act} U_{act}}{\frac{1}{2}\rho_\infty U_\infty^2 A_{ref}} = \frac{q_f U_{act}}{\frac{1}{2}\rho_\infty U_\infty^2 A_{ref}} = \frac{\rho_{act} U_{act}^2 S_{act}}{\frac{1}{2}\rho_\infty U_\infty^2 A_{ref}} \tag{2.5}$$

where ρ_{act}, U_{act} and S_{act} respectively denote the actuators air density, outlet velocity and outlet total surface. The other terms ρ_∞, U_∞ and A_{ref} stand for the freestream density, velocity and for the reference area chosen as the flap area in the present case. Considering the conditions presented above, the constant blowing momentum coefficient has a value of 1.6%. In the case of pulsed blowing, as in this study, the periodic momentum coefficient is defined by Greenblatt and Wygnanski [164] as:

$$\langle C_\mu \rangle = \frac{\rho_{act} \langle U_{act}^2 \rangle S_{act}}{\frac{1}{2}\rho_\infty U_\infty^2 A_{ref}} \tag{2.6}$$

Given the valves square command signals, the evolution of the outlet velocity with time can be described by Equation (2.7):

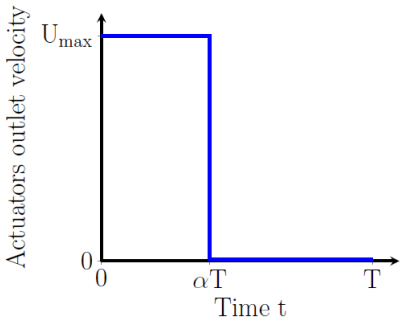

$$U_{act} = \begin{cases} U_{max}, & \text{if } 0 < t \leq \alpha T \\ 0, & \text{if } \alpha T < t \leq T \end{cases} \tag{2.7}$$

Figure 2.4: Sketch of the valves command signal on a period of actuation.

where U_{max}, t and T respectively stand for the valves maximal outlet velocity for the supply conditions considered, the time and the square driving signal period. As $\langle U_{act}^2 \rangle = \alpha U_{max}^2$ and as the actuators average mass flow rate is equal to q_f, Equation (2.6) finally reads:

$$\langle C_\mu \rangle = \alpha \frac{\rho_{act} U_{max}^2 S_{act}}{\frac{1}{2}\rho_\infty U_\infty^2 A_{ref}} = \frac{1}{\alpha} \frac{\rho_{act} \langle U_{act} \rangle^2 S_{act}}{\frac{1}{2}\rho_\infty U_\infty^2 A_{ref}} = \frac{1}{\alpha} \frac{q_f \langle U_{act} \rangle}{\frac{1}{2}\rho_\infty U_\infty^2 A_{ref}} \tag{2.8}$$

During the flow control experiments $\langle C_\mu \rangle$ used reached a maximum value of 4.6%.

2.2 S19 wind tunnel: open-cavity model for shear flow control

2.2.1 Open-cavity model

Experiments of shear flow control were carried out on an open-cavity placed in the S19 wind tunnel at ONERA Meudon. A sketch of the wind tunnel facility is presented in Figure 2.5a. The wind tunnel test section consists in a rectangular test section of span 300 mm, height 150 mm and length 1910 mm. It is characterized by a turbulence level of 0.3% (quantity derived during calibration of a hot-wire), describing a high-quality wind tunnel. Stagnation pressure P_i and total temperature T_i measurements are performed in the wind tunnel plenum chamber respectively with a Pitot tube and a thermocouple. 17 static pressure probes are located along the upper wall of the test section and divergent duct. The boundary-layer transition from laminar to turbulent is forced by a carborundum strip placed 575 mm upstream of the cavity.

The cavity upstream edge is considered as the origin of the reference axes, set in the median plane of the test section. The X-axis is in the streamwise direction (oriented in the direction of

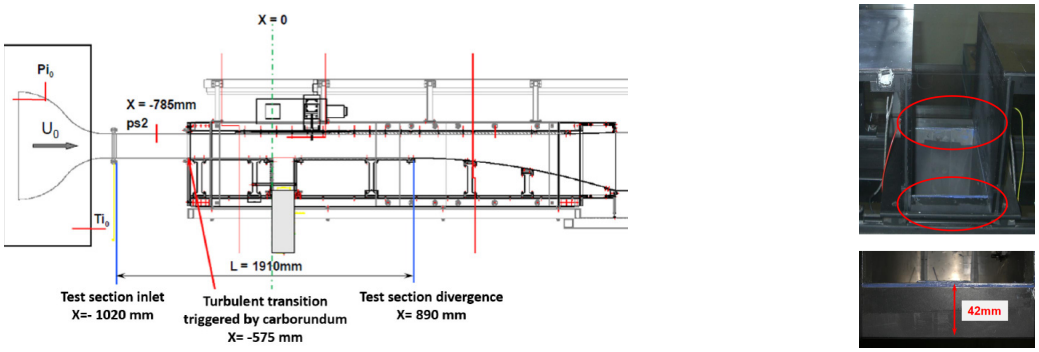

(a) Sketch of the S19 wind tunnel.

(b) Geometry of the open-cavity.

Figure 2.5: Sketch of the S19 wind tunnel (a) and picture of the open-cavity particular geometry (b).

the flow), the Y-axis indicates the span-wise direction (oriented into the page in Figure 2.5a) while the Z-axis is vertical (oriented upwards) and completes the direct system of axes. The cavity of length $L = 134$ mm is inserted on the lower wall of the rectangular test section, as presented in Figure 2.5b. It is composed of two parts with different spans W_1 and W_2. The first part of depth $D_1 = 300$ mm spans over $W_1 = 300$ mm. Below, the second part of depth $D_2 = 600$ mm spans over $W_2 = 216$ mm. Therefore, the cavity total depth D equals 900 mm, yielding a length-to-depth ratio $L/D = 0.15$ The second part of the cavity was added such that the open-cavity flow oscillation frequencies was included in the actuators bandwidth.

2.2.2 Measurement setup for the shear flow characterization and for the investigation of control effects

Data acquisition is performed using a the software Xpert developed by ONERA, which enables synchronized recording of various measurements with a high frequency sampling rate as presented in detail in the following. During the closed-loop test-campaign, the control is implemented with a Dspace MicroLabBox performing both data acquisition and control signal generation.

Boundary-layer characterization

Hot-wire measurements are performed to characterize the boundary layer developing upstream of the cavity. A classical Dantec 55P11 probe associated to a mini-CTA 54T42 is used with a sampling frequency of 10 kHz. The turbulent boundary layer profile is presented in Figure 2.6 describing the evolution of vertical dimensionless distance to the wall against the normalized velocity U/U_∞. Hot wire data are represented by blue points while the inferred Prandtl's profile of Equation (2.9) is described by the thick black line. From these measurements it can be deduced that the boundary layer is characterized by a 99 % thickness $\delta_{99\%} = 14$ mm. The displacement thickness δ^*, momentum thickness θ and boundary layer shape factor H are then inferred based on Prandtl's theory on turbulent boundary layer. Therefore, the normalized velocity distribution inside the boundary layer can be described by Equation (2.9):

$$\frac{U}{U_\infty} = \left(\frac{z}{\delta}\right)^{\frac{1}{n}} \quad \text{with } n = 7.459 \tag{2.9}$$

Values of δ^*, θ and H are respectively 1.655 mm, 1.3051 mm and 1.2681. For freestream velocities ranging from 10 m/s up to 46 m/s, the Reynolds number based on the boundary-layer momentum thickness ranges from 831 to 3 824.

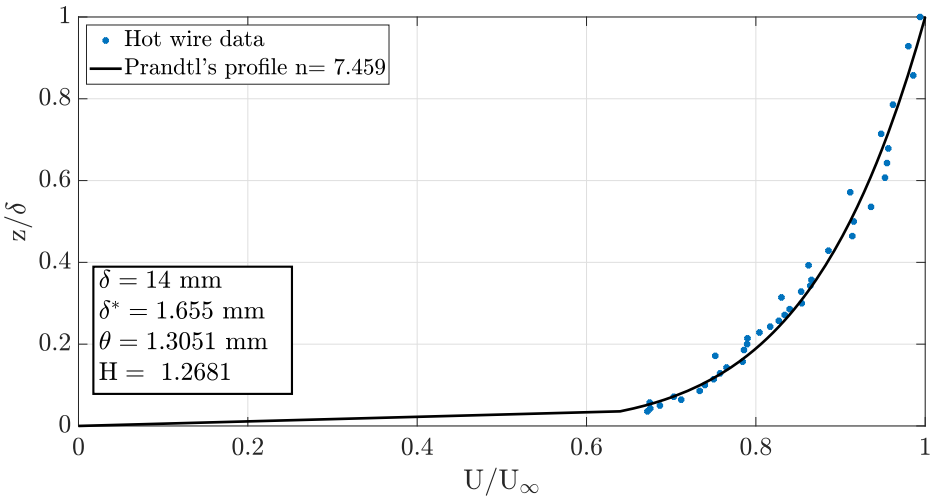

Figure 2.6: Turbulent boundary-layer profile developing upstream the cavity over the flat plate.

Pressure measurements for flow characterization

Characterization of the flow dynamics developing over the open-cavity is performed with unsteady pressure measurements. Static pressure recordings are carried out along the wind tunnel test section and complete the unsteady measurements. It enables to evaluate the effect of the wind tunnel depression on the actuators.

Characterization of the flow dynamics is investigated for several freestream velocities U_∞ ranging between 10 m/s and 42 m/s. The aim of these investigations is to find a flow regime with low frequency oscillations, as discussed in Chapter 4. Unsteady pressure measurements are performed with 4 Kulite XCQ-093-15A (15 PSI) sensors, placed on the open-cavity downstream wall near the edge at Z=0. The SPL (Sound Pressure Level), expressed in dB, obtained from the PSD (Power Spectral Density) of each Kulite sensors are computed based on the following definition:

$$SPL = 20 \log_{10} \left(\frac{\sqrt{PSD}}{P_{ref}} \right), \tag{2.10}$$

where $P_{ref} = 20$ μPa is a reference pressure corresponding to the threshold of human hearing. In the following, unless otherwise specified, unsteady pressure signals are acquired over a duration of 45 s with a sampling frequency $f_s = 10$ kHz. The signal PSD is then computed

with a Welch's algorithm based on 60 Hamming windows and an overlap of 50 %, yielding a frequency resolution of 0.11 Hz. As the 4 Kulite sensors indicate the same resonance frequencies and similar values of SPL within a few dB, results presented in this manuscript are based on one of the 4 unsteady pressure sensors. An example of spectrum derived for a freestream velocity of 20 m/s is presented in Figure 2.7. It is composed of a parasitic peak at 50 Hz due to electrical noise and three peaks characterizing the flow dynamics. The flow spectrum is therefore composed of a fundamental oscillation frequency f_1 at 128.6 Hz and two harmonics f_2 and f_3 respectively at 257.2 Hz and 385.9 Hz. A more detailed analysis of the spectrum is proposed in Chapter 4.

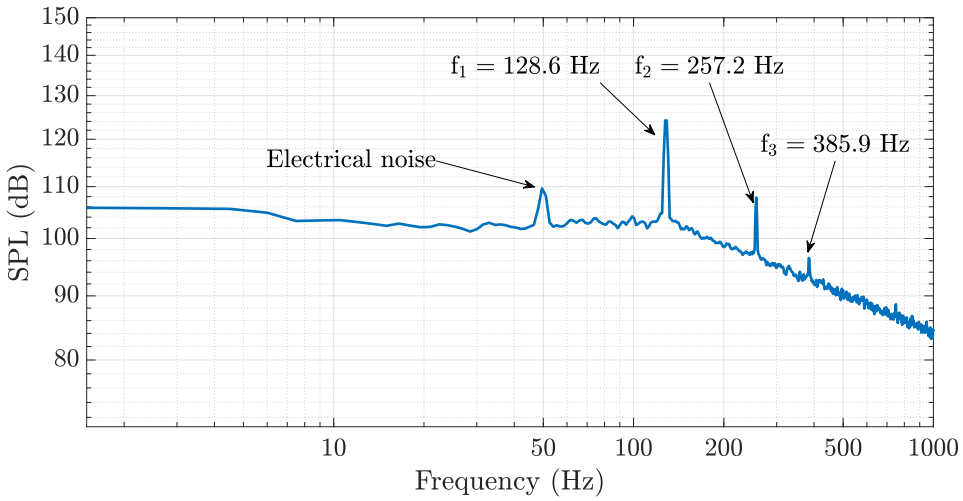

Figure 2.7: SPL (dB) flow spectrum near the downstream edge of the cavity for $U_\infty = 20$ m/s.

Considering the static pressure measurements, 17 pressure taps are distributed along the wind tunnel upper wall from the test section inlet to the divergent. Figure 2.8 illustrates the evolution of static pressure with respect to the atmospheric pressure, along the wind tunnel upper wall for freestream velocities U_∞ of 20 m/s, 30 m/s and 34 m/s. Pressure inside the wind tunnel is lower than the atmospheric pressure. This depression increases at the upstream corner of the cavity up to the starting position of the divergent. From this location, the static pressure increases again.

As observed in Figure 2.8, the depression near the cavity upstream edge is strengthened when the velocity is increased. This might affect the actuators behavior as their supply pressure is set with respect to the atmospheric pressure. The displayed supply pressure of the actuators is therefore lower than the supply pressure actually applied. Additional static pressure measurements realized next to the central actuator (without the actuators working) for several freestream velocities proved that the depression only increased the supply pressure by 2.5 mbar for $U_\infty = 20$ m/s. The supply pressure used being at least of 120 mbar, the error in the estimation of the supply pressure is therefore less than 2 % at 20 m/s. These measurements are presented in Figure 2.9. In the following chapters, reference to ΔP is given without taking into account the correction observed in Figure 2.9 as it is negligible.

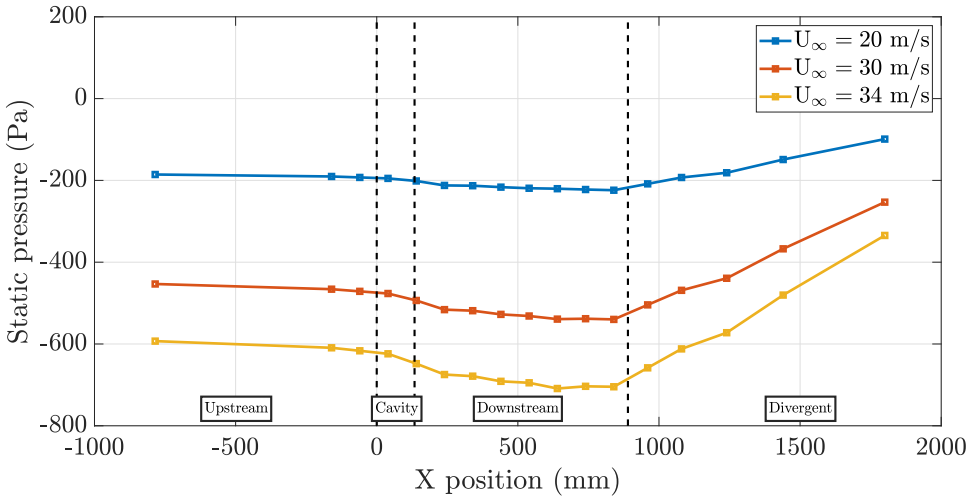

Figure 2.8: Static pressure (Pa) along the wind tunnel upstream wall.

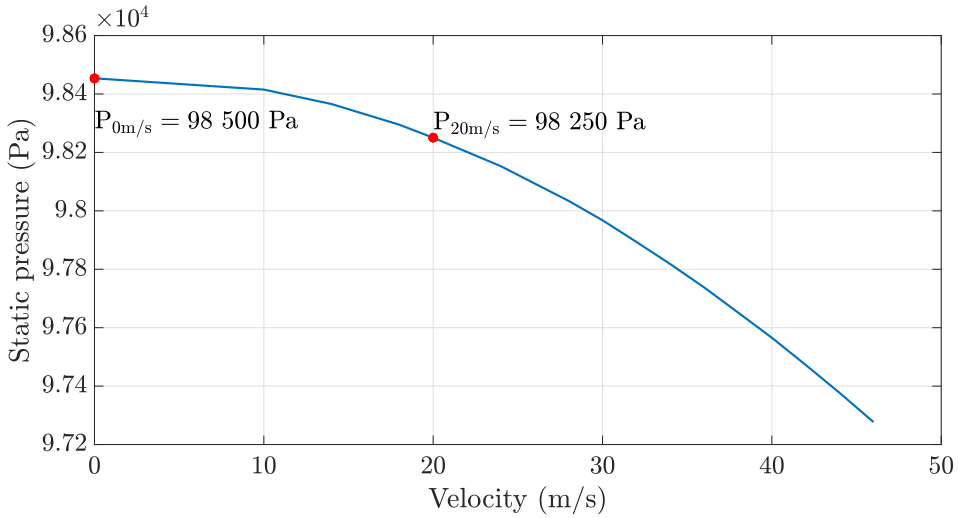

Figure 2.9: Static pressure (Pa) measurements next to the central actuator as a function of freestream velocities (m/s).

2.2.3 Integration of MEMS actuators to the model

The actuation setup is composed of (MMMS) microvalves integrated as a linear array of 15 actuators. The actuators, based on the technology presented by Pernod et al. [91], can generate both quasi-steady and pulsed jets and have the advantage to be able to follow arbitrary command signals, which is a key for closed-loop flow control. To operate the microvalve, a source of pressurized air has to be supplied to the actuators, alongside with an electrical source, if pulsed jets are to be generated.

Design and fabrication process of microvalves

The microvalve is composed of a 240 μm deep silicon micro-channel containing two inner walls and an outlet hole at one of its extremity. A 100 μm thick flexible PDMS (Polydimethyl-

siloxane) membrane surmounts this channel and is fixed to a 350 μm thick silicon pad. A couple of permanent NdFeB magnets of total thickness 2.5 mm is attached to the pad and is surrounded by a coil, contained in the microvalve packaging. This design, schematically presented in Figure 2.10, allows two different actuation types.

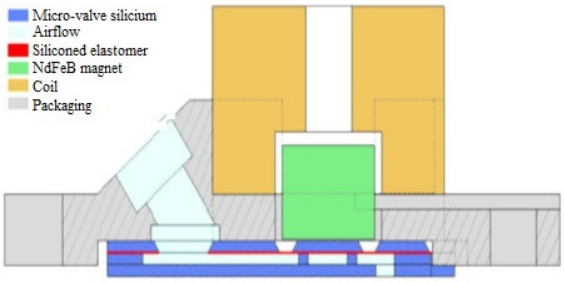

Figure 2.10: Schematic description of a MMMS microvalve.

The first actuation mode consists in generating a quasi-steady jet thanks to a pressure difference applied through the microvalve. Due to the pressure increase inside the micro-channel, the silicon pad and the magnets are lifted up to an equilibrium position. Hence, the air flows from the inlet to the submillimetric outlet. To generate a pulsed-jet, an electrical input signal is applied to the coil surrounding the magnets. Thereby, the silicon pad oscillates around its equilibrium position defined by the inlet pressure. Therefore, the micro-channel height is modulated and a pulsed jet is generated at the microvalve outlet. The silicium pad considered here has an increased size compared to the one presented by Pernod et al. [91]. This limits the apparition of non linearities in the actuation. Furthermore, the actuators have a large frequency bandwith and are not only used at their resonant frequency, which is an advantage regarding the control application of an open-cavity flow.

The fabrication process of the MMMS microvalves associates silicon micro-machining and rapid prototyping. Rapid prototyping was used to process the package of the microvalve that fixes the coil and allows the microvalve assembling. Silicon micro-machining techniques were exploited to realize both the membrane and the micro-channel parts. The membrane is processed (Figure 2.11 (a) and (b)) by first preparing and spin-coating a PDMS solution on a 350 μm thick wafer. After PDMS baking, the wafer is processed on its backside. Photo-lithography defines the silicon pad dimensions and DRIE (Deep Reactive Ion Etching) process is used to etch the silicon wafer. The process, called Bosch process, alternates a passivation phase using C_4F_8 and an etching phase using SF_6 gas to ensure anisotropic etching of silicon. Thereby, the silicon wafer is etched over its thickness and the silicon pad is only maintained by the PDMS layer. This allows the pad to move and proceed to the actuation of the microvalve. It must be noted that at rest (i.e. when no voltage is applied) the microvalve is in the open position.

For the micro-channel part, two DRIE steps are needed (Figure 2.11 (c) and (d)) to manufacture the microfluidic channel and the output. This process is realized on a 500 μm thick double side polished silicon wafer. On one side, the micro fluidic channel is defined by photolithography. DRIE Bosch process etches the silicon by 250 μm which is the wanted depth for the microfluidic channel. Then, backside photo-lithography is needed to align the outlet

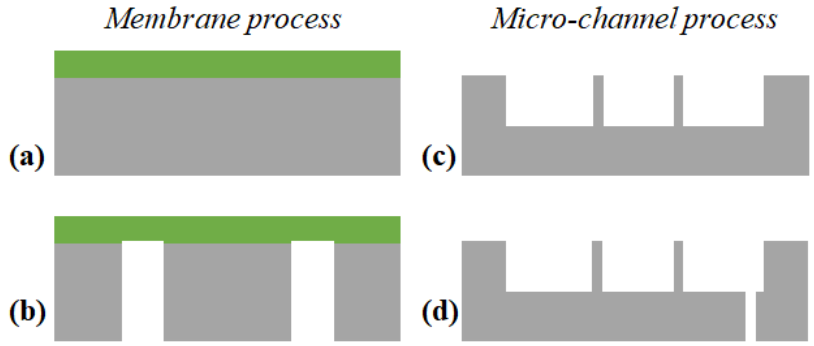

Figure 2.11: Fabrication process of the microvalve. Left: Membrane process with (a) PDMS spin-coating (b) Silicon pad etching. Right Micro-channel process: (c) front side micro-channel etching (d) backside outlet etching

with the front side microfluidic channel. The remaining 250 μm thick silicon is etched again using the Bosch process until the outlet is completely open.

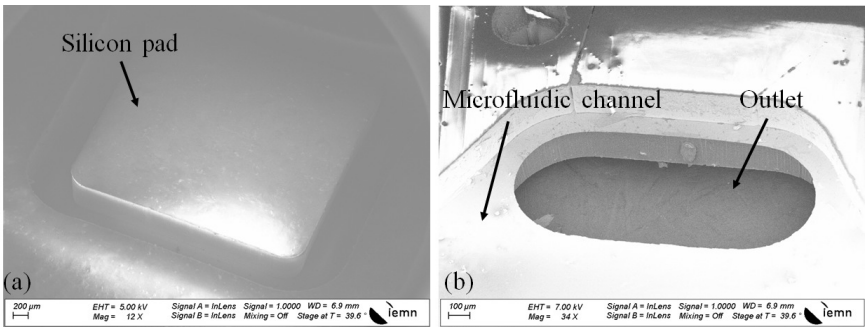

Figure 2.12: SEM (Scanning Electron Microscopy) pictures of the MMMS microvalve: (a) the membrane and the silicon pad (b) the extremity of the microfluidic channel with the outlet

Figures 2.12 (a) and (b) are SEM (Scanning Electron Microscopy) pictures of the realized device parts. Figure 2.12 (a) shows the silicon pad etched over the wafer thickness and maintained by the PDMS layer. Figure 2.12 (b) shows one extremity of the microfluidic channel with the microvalve outlet. This picture shows the two etching steps: the first up to half the wafer thickness for the microfluidic channel and the second step opening the silicon wafer for the fluidic jet outlet.

Microvalves integration to the open-cavity

An example of assembled microvalve is presented in Figure 2.13. The microvalve outlet had to be adapted to the open-cavity geometry. To conduct flow control experiments with the microvalves, their induced jets have to spread over the entire cavity span. Therefore, the submillimetric outlet was adapted towards a slot outlet. For a single microvalve, the slot length and height are respectively 12 mm and 0.2 mm. The adapters were fabricated by stereolithography in a Problack10 resin. It is composed of an upper and a lower part, which brought together induce a jet outlet angle of 45°.

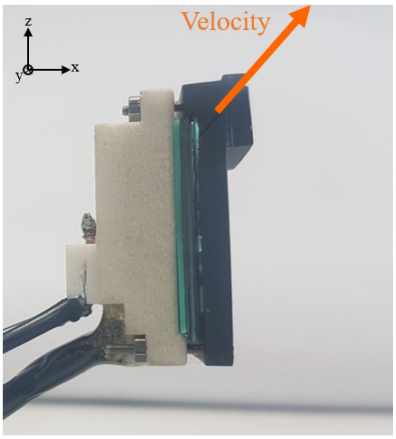

Figure 2.13: Microvalve with the jet adapter. The outlet velocity is indicated by the orange arrow.

A set of 15 microvalves was assembled and mounted as a linear array. It was then integrated on the upstream cavity corner as depicted in Figure 2.14. The actuators are located just below the shear layer at the cavity upstream edge, and out-coming jets interact with the shear layer due to their velocity outlet angle. Despite the following advantage is not exploited in the present work (as the considered open cavity flow configuration presents a relatively invariant dynamics along the spanwise direction.), having an array of 15 individual microvalves enable the implementation of a MIMO control as each microvalve can be driven separately from the others.

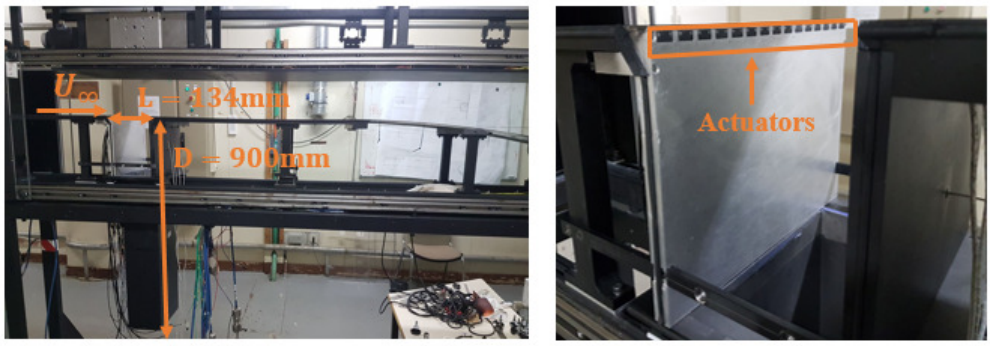

Figure 2.14: Pictures of the wind tunnel experimental setup with the cavity dimensions (left) and integration of the actuator array (right).

Conclusion

This second chapter presented the two flow control configurations. The first experimental configuration consists in a plain flap placed in the L1 wind tunnel of the ONERA. The control aims at avoiding the flow separation over the flap occurring when its angle of attack is increased. The second experimental configuration consists in an open-cavity installed in the ONERA S19 wind tunnel. Aim of the control implemented on this configuration is to damp the self-sustained oscillations developing in the flow.

Regarding the control of flow separation on the plain flap, experiments are carried out with a freestream velocity U_∞ of 34.5 m/s for flap deflection angles δ varied between 2° and 37°. Hot films integrated along the flap chord are used to characterize both the unforced and forced flows dynamics. Furthermore, the hot films output voltages help designing either the data-driven linear controller or the positive non-linear controller and are used to assess the controllers ability to avoid flow separation/ control a separated flow. Pressure taps dispatched on both upper and lower surfaces of the model yield average values of the lift coefficient C_L and the pressure coefficient C_p. The comparison of these coefficients in the uncontrolled and controlled cases help determining the effect of control on the flow dynamics. On this configuration the control is performed with a set of 7 Festo valves placed at the flap leading edge. Implementation of the different tested controllers is performed with a PXIe system of National Instruments, generating the valves command signal based on the hot films measurements.
Considering the control of the open-cavity flow, experiments are carried out for freestream velocities U_∞ of the order of 20 m/s. The boundary layer developing upstream the open-cavity is characterized with hot wire measurements. Both the unforced and forced flow dynamics are investigated through unsteady pressure measurements performed at the cavity downstream edge. The control is implemented with MEMS actuators in the form of magnetically actuated microvalves, generating either quasi-steady jets or pulsed jets. The implementation of the closed-loop control of the open-cavity flow is achieved with a Dspace real time controller using the unsteady pressure measurements to generate the actuators command signal. The closed-loop control strategy considered in this study case is based on the synthesis and application of a SISO linear controller, using a structured H_∞ synthesis.

Implementation of the control strategies on both flow configurations are described in the following chapters of the manuscript. Chapter 3 deals with the control of the plain flap flow separation/separated flow. The flow dynamics is presented alongside with the application of the closed-loop control based on hot films measurements.

Chapter 3

Study of the closed-loop control of flow separation on a plain flap with linear and non-linear controllers

Introduction

The previous chapter presented the flow configurations on which closed-loop flow control experiments are carried out. For both the separated flow and shear flow configurations, wind tunnels, sensors and actuators setups have been described. The Chapter 3 objective is the implementation of the closed-loop control of flow separation/separated flow over a NACA-4412 plain flap. For a freestream velocity in the wind tunnel test section of 34.5 m/s and for flap deflection angles between 2° and 37°, two different closed-loop control methodologies have been employed to track a reference value, defined with respect to the hot films measurements. The first applied control law is a data-driven one, leading to a linear integral controller. The second one is a phenomenological/model-driven law, yielding a non-linear positive integral controller.

In the following, the characterization of the unforced flow developing over the model is introduced. Measurements performed with the hot films indicate the onset of flow separation on the flap and its development for high flap deflection angles. Pressure measurements yield the evolution of the lift coefficient C_L and pressure coefficient C_p in the unforced case and also outline the flow dynamics. Then, the linear and non-linear controllers syntheses based on open-loop measurements are presented. Flow control results obtained with both control laws are discussed afterwards, comparing the lift and pressure coefficients of the uncontrolled and controlled cases. Finally, an experimental protocol to carry out the same closed-loop experiments with MEMS thermal wall shear stress sensors is proposed.

3.1 Unforced flow characterization with pressure and hot films measurements

3.1.1 Lift and pressure coefficients distributions

First measurements focused on the unforced flow characterization. The freestream velocity was fixed to $U_\infty = 34.5\ m/s$ and the flap was deflected downwards from 2° to 37°, by steps of 2°. The evolution of the entire model lift coefficient is presented in Figure 3.1 and similar results to the one presented by Chabert et al. [165] are obtained. Hoerner [107] described 4 zones which are highlighted in this chart. The first zone (I), for δ between 2° and 12°, describes a linear evolution of C_L against δ. The second zone (I)-(II) corresponds to a slower increase in the lift coefficient and spreads between 12° and 20°, indicating the development of flow separation over the flap. The zone denoted (II) corresponds to a plateau of C_L due to the recirculation bubble entirely developed over the flap. The flap is thereby in a stall configuration at this point. Finally, the zone (III) denotes a zone of non-linear increase in the lift coefficient. The non-linear behavior of C_L would be better observed with higher deflection angles, as pointed out by Hoerner [107], who performed measurements with deflection angles down to 90°.

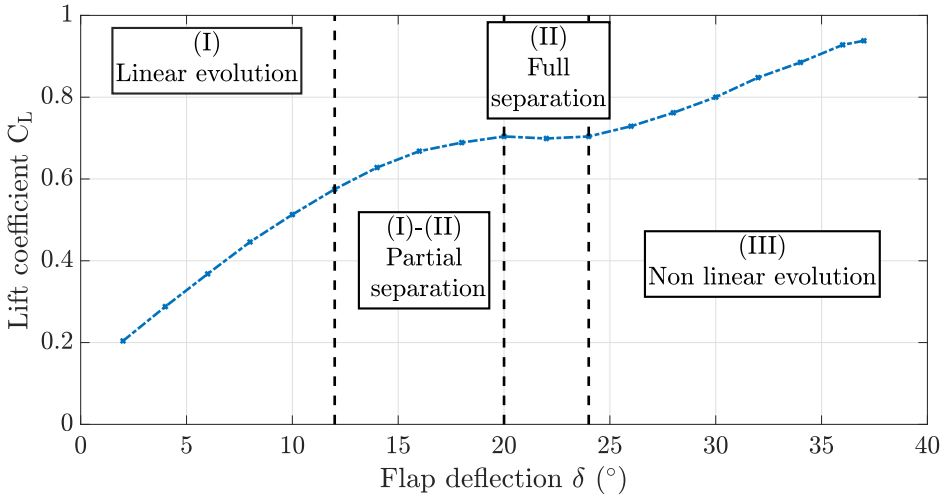

Figure 3.1: Evolution of the unforced flow lift coefficient C_L against the flap deflection angle δ ($U_\infty = 34.5\ m/s$).

The development of the recirculation area over the flap can also be observed in the pressure coefficient measured over the flap. The C_p is plotted against the dimensionless abscissa x/c_{flap} alongside with the airfoil shape to highlight the positions of the pressure taps. It can be observed that pressure taps over the flap spread up to $x/c_{flap} = 0.65$, as beyond this position pressure taps could not be connected. As highlighted in Figure 3.2a, for low deflection angles down to 12°, the flow remains attached to the flap on its entire length, as a pressure gradient is observed. For $\delta = 16°$, a plateau of C_p forms at the flap trailing edge. The length of the plateau reflects the length of the recirculation bubble developed over the flap. For higher deflection angles, as illustrated in Figure 3.2b, the recirculation area tends to extend up to the flap leading edge. For $\delta < 30°$, the flow is not separated on the

entire flap as a pressure gradient still develops at the leading edge. However, for $\delta \geq 30°$, the flow is detached over the entire flap. Based on these measurements, it can be deduced that the separation point position evolves towards the flap leading edge. As presented in the following, this information is confirmed by the monitoring of the 8 hot films outputs.

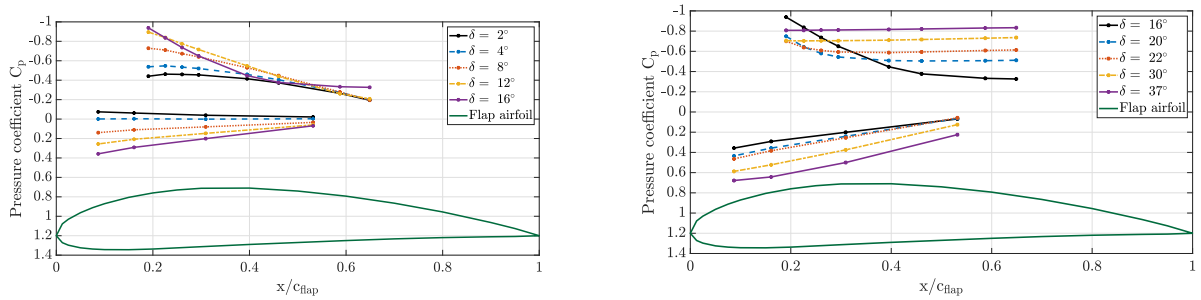

(a) Pressure coefficient for $\delta = 2°, 4°, 8°, 12°, 16°$. (b) Pressure coefficient for $\delta = 16°, 20°, 22°, 30°37°$.

Figure 3.2: Evolution of the unforced flow pressure coefficient over the flap for different deflection angles δ against the dimensionless abscissa x/c_{flap} ($U_\infty = 34.5\ m/s$).

3.1.2 Wall shear stress evolution on the pain flap

To further characterize the unforced flow developing over the flap, hot films voltages are recorded for the same experimental conditions as the one used to derive the unforced C_L and C_p evolution's. For each deflection angle, hot films time series have been averaged and normalized according to the following equation:

$$U^* = \frac{\langle U \rangle - U_{min}}{U_{max} - U_{min}}, \tag{3.1}$$

where U^* is the dimensionless hot film voltage, $\langle U \rangle$ the hot film mean voltage, U_{min} and U_{max} respectively the hot film minimum and maximum outputs. Figure 3.3 depicts the evolution of U^* for the first, fifth and eighth hot films on the flap, which are respectively located at $x/c_{flap} = 0.148$, $x/c_{flap} = 0.511$ and $x/c_{flap} = 0.784$.
For the first hot film in Figure 3.3a, it can be observed that the flow only separates for very high flap deflection angles. This is expected as this hot film is close to the flap leading edge. The fifth and eighth hot films, respectively in Figure 3.3b and Figure 3.3c present the same behavior as expected in Figure 1.10. As the flap angle is increased the hot film normalized voltage decreases. A local minimum is reached for both hot films respectively for $\delta = 20°$ and $\delta = 16°$. These first minima point out the flow separation at the hot films locations. As expected, the onset of separation firstly appears at the flap trailing edge and then spreads towards the leading edge. When the flap is further deflected, the hot films voltages increase due to the flow recirculation bubble. Besides the expected voltages evolution described above, both hot films voltages reach a second minimum respectively for $\delta = 32°$ and $\delta = 28°$. This second minimum may be due to the apparition of a second recirculation zone occurring for high deflection angles as observed by Chabert [127] during flow visualization experiments.

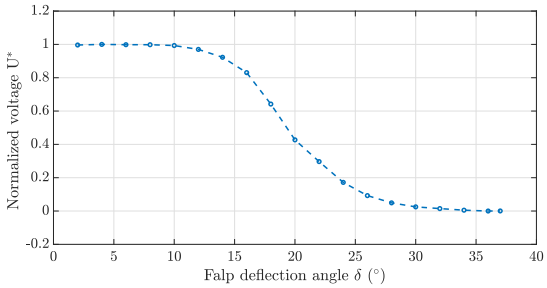

(a) First hot film $x/c_{flap} = 0.148$.

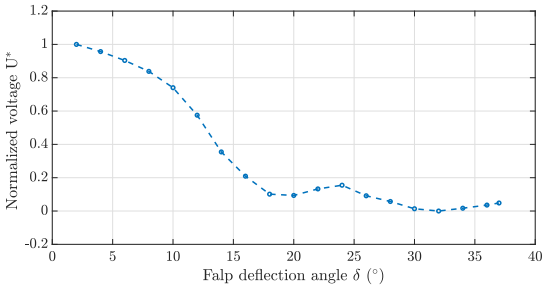

(b) Fifth hot film $x/c_{flap} = 0.511$.

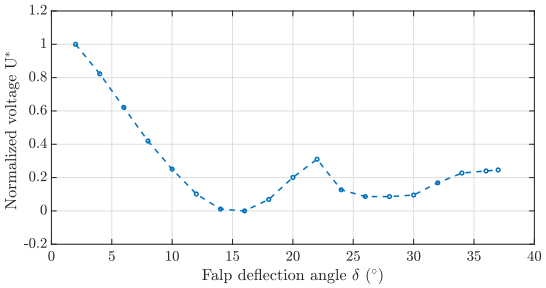

(c) Eighth hot film $x/c_{flap} = 0.784$.

Figure 3.3: Evolution of the normalized voltage for three hot films against the flap deflection angle δ ($U_\infty = 34.5\ m/s$).

3.1.3 Definition of the closed-loop objective based on the detection of flow separation

Based on the previous measurements, a reference signal tracking feedback control architecture can be set up. With reference to Figure 3.4, a h-sampled control law is designed, aiming at ensuring that the output signal $y(t_k)$, measured by the fifth hot film, tracks $r(t_k)$, the reference level defined by the user. Based on the error $e(t_k) = r(t_k) - y(t_k)$, the controller provides a sampled-time continuous order $u(t_k)$, transformed in an on-off one $\overline{u}(t_{k/N})$, leading to the controlled duty cycle α applied by the PFA (Pulsed Fluidic Actuators), sampled N times faster.

Located at the flap mid-chord ($x/c_{flap} = 0.511$), the 5^{th} hot film indicates the onset of flow separation for an angle of 22°, in the middle of the flap deflection angle range. This hot film is therefore chosen as reference and provides the feedback measurement. A reference value for the fifth hot film sensor is defined, such that the flow separation over the flap is avoided. The normalized objective value U^*_{obj} is fixed to 0.3903, so that the hot film voltage remains above its minima.

In Figure 3.5, this reference value is superimposed with the evolution of the fifth hot film normalized voltage. The controller aim is therefore to maintain the hot film normalized voltage to the reference value. Therefore, two different zones are defined in this chart. One for deflection angles δ below 13.8° and the second one for $\delta > 13.8°$. The first one corresponds to deflection angles for which actuators do not add momentum to the flow, as the hot film voltage is above the reference value. The second one defines angles δ for which the Festo

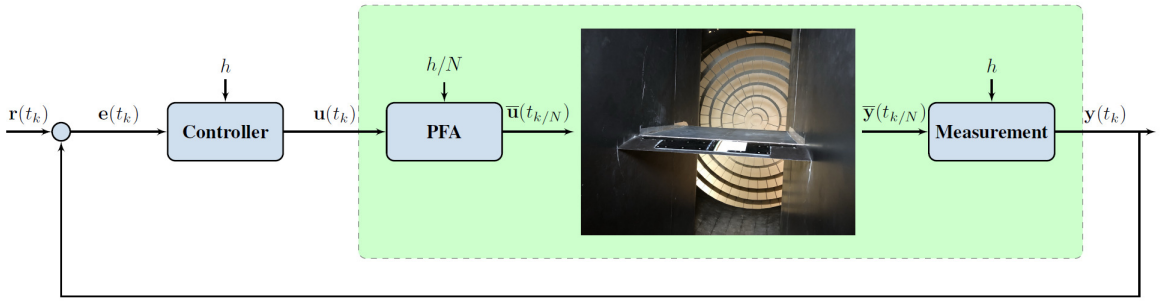

Figure 3.4: Overview of the considered closed-loop architecture. The controller, sampled at frequency h, feeds the seven PFA acting along the wing span. The system is illustrated by the setup photo, and the measurement is achieved by the hot films located along the flap.

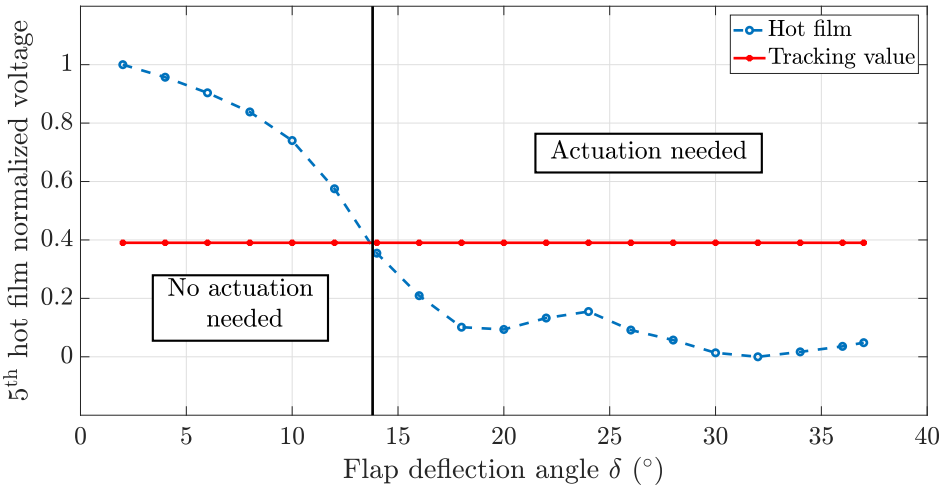

Figure 3.5: Evolution of the normalized voltage of the fifth hot film (blue curve) and the reference value (red curve) against the deflection angle δ ($U_\infty = 34.5$ m/s). The black curve separates areas without and with actuation.

valves are cyclically actuated and the controller aims at maintaining the hot film voltage to the imposed level. Based on this reference value, ability of both control strategies to maintain this value is investigated.

3.2 Linear and non-linear controllers synthesis

Considering the control architecture in Figure 3.4, this section provides details on the design and tuning of the controllers. Two different strategies are implemented and evaluated. Firstly, the linear L-DDC (Loewner Data-Driven Control), as presented by Kergus [166], is described. Secondly, a phenomenological-driven nonlinear positive control, introduced by Briat [167], is considered.

3.2.1 Linear data-driven control (L-DDC) design

Theoretical principle

The L-DDC belongs to the so-called data-driven reference model approaches. DDC methods have a long history dating to the proportional, integral, derivative (PID) tuning method proposed by Ziegler and Nichols [168] in early 40's or the self tuning regulator introduced by Åström [169] in the 90's. The L-DDC procedure boils down to two steps: firstly deriving the ideal controller denoted $\mathbf{K}^\star$ and secondly identifying the controller via an interpolation in the Loewner framework, as proposed by Mayo and Antoulas [170]. The main steps in the SISO case to implement the reference tracking architecture are recalled, referring to Figure 3.6.

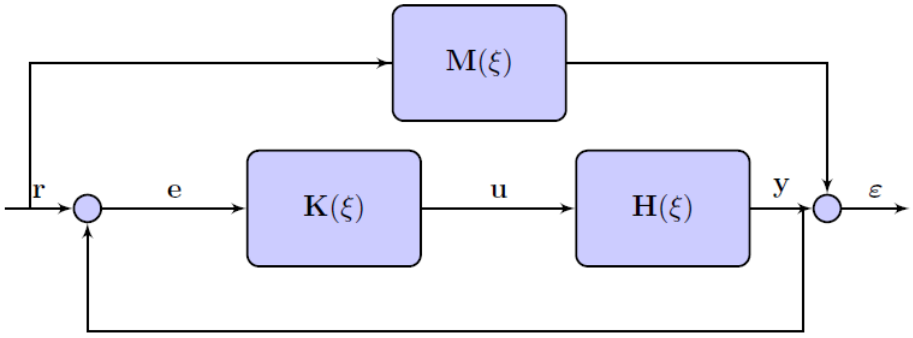

Figure 3.6: Data-driven control problem formulation.

The objective is to find an LTI controller with a transfer function $\mathbf{K} : \mathbb{C}\backslash\Lambda_{\mathbf{K}} \to \mathbb{C}$ that minimizes the transfer difference between $\mathbf{r}$ and $\boldsymbol{\varepsilon}$, i.e. between the resulting closed-loop and a user-defined reference model $\mathbf{M} : \mathbb{C}\backslash\boldsymbol{\Lambda}_{\mathbf{M}} \to \mathbb{C}$. This is made possible through the definition of the ideal controller $\mathbf{K}^\star$, being the LTI controller that would have given the desired reference model behavior if inserted in the closed-loop. The latter is defined as $\mathbf{K}^\star = \mathbf{H}^{-1}\mathbf{M}(I - \mathbf{M})^{-1}$, where $\mathbf{H} : \mathbb{C}\backslash\boldsymbol{\Lambda}_{\mathbf{H}} \to \mathbb{C}$ is the model of the system to control. In the data-driven case, when $\mathbf{H}$ is not explicitly known, but may be evaluated at some values $z_k \in \mathbb{C}$, this definition may be recast as a discrete set of $k = 1, \ldots, N$ equations:

$$\mathbf{K}^\star(z_k) = \boldsymbol{\Phi}_k^{-1}\mathbf{M}(z_k)(I - \mathbf{M}(z_k))^{-1}, \tag{3.2}$$

where $\mathbf{H}(z_k) = \boldsymbol{\Phi}_k \in \mathbb{C}$ is the evaluation of the unknown model at z_k. In an experimental context, one usually considers sampling $\mathbf{H}$ at $z_k = \imath\omega_k$ ($\omega_k \in \mathbb{R}_+$). In this case, $\boldsymbol{\Phi}_k$ is the frequency response at ω_k. Then, the couple

$$\{z_k, \boldsymbol{\Phi}_k\}_{k=1}^N, \tag{3.3}$$

is referred as the raw data. Finding a controller $\mathbf{K}$ that fits Equation (3.3) can be considered to be an identification/interpolation problem which may be solved by many approaches. The Loewner framework allows constructing both a function $\mathbf{K}$ with minimal McMillan degree and realization order n, satisfying conditions Equation (3.2) or constructing an approximation of it with a realization of order $r < n$. L-DDC is a combination of determining the ideal

controller from frequency-domain data via a reference model and of exploiting the Loewner framework to construct a reduced order controller. Such an interpolatory-based data-driven control design solves problems faced by practitioners: the controller design is directly obtained using open-loop raw data Equation (3.3) collected on the experimental setup, without any optimization process (only linear algebra manipulation) and without any prior controller structure or order specification (these latter may be automated by a rank revealing factorization). This approach has proven to be effective on infinite dimensional systems as pointed out by Gosea et al. [171], for digital control as demonstrated by Vuillemin et al. [172] and on experimental application as emphasized by Poussot-Vassal et al. [173].

However, using a linear controller brings drawbacks. One of them is encountered during the experiments and points out that the linear controller does not handle actuator limitations, which is the case with on/off valves only blowing air. In presence of an integral action, this may result in stability issues, as will be discussed in Section 3.2.2.

Application to flow separation control

The frequency-domain response describing the separated flow dynamics over the flap is first assessed. The operating point for this step is a deflection angle $\delta = 24°$ and $U_\infty = 34.5$ m/s, conditions for which the flow is indeed separated at the sensor location, as discussed in Section 3.1.2. For the identification step, the actuators command signal $\mathbf{u}(t_k)$ consists in a logarithmic frequency sweep applied to the duty cycle with frequencies ranging from 0.01 Hz to 10 Hz over 180 s. The valves duty cycle is therefore varied between 0 and 1 with an increasing rate. From this input, the fifth hot film response $\mathbf{y}(t_k)$ is collected. The discrete frequency-domain transfer data from $\mathbf{u}(t_k)$ to $\mathbf{y}(t_k)$ is obtained and denoted $\{\imath\omega_k, \boldsymbol{\Phi}_k\}_{k=1}^N$, where $\omega_k \in \mathbb{R}_+$ is the pulsation and $\boldsymbol{\Phi}_k \in \mathbb{C}$ is the SISO transfer response of the system (green block in Figure 3.4) and $N \in \mathbb{N}$ is the length of the Fast Fourier Transform (FFT).

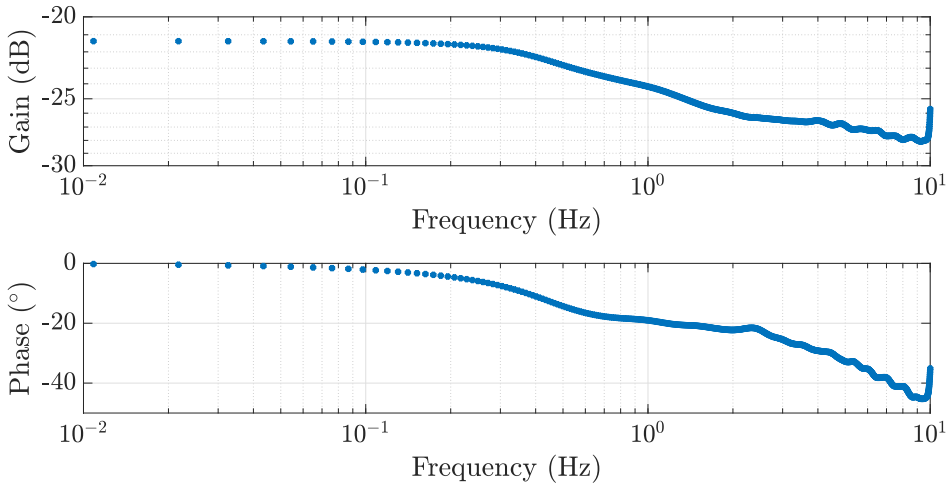

Figure 3.7: Bode diagrams of the frequency data collected with the 5$^{\text{th}}$ hot film ($x/c_{flap} = 0.511$) during the open-loop measurements.

The data-driven Bode-like diagram is presented in Figure 3.7, exhibiting a gain decay around 0.3 Hz and a decay in the phase, characteristic of delayed systems. The objective closed-loop

transfer function $\mathbf{M}$ is defined as a first order model $\mathbf{M(s)} = \dfrac{\mathbf{1}}{\mathbf{s}/\omega_\mathbf{0} + \mathbf{1}}$ where $\omega_0 = 2\pi$ rad/s, is the natural cut-off frequency. $\mathbf{M}$ aims at accelerating the system (three time faster) and ensuring no steady-sate error (static gain to one). With reference to Equation (3.2), the ideal controller $\mathbf{K}^\star$ can now be computed. Its exact interpolation $\mathbf{K}_n$ is also calculated with n=144, a value automatically selected by the rank revealing factorization embedded in the Loewner process. The reduced form of the controller, denoted $\mathbf{K}_r$, is simultaneously derived with an order $r = 1$. Figure 3.8 illustrates the controller gains with $\mathbf{K}_r(z) = 0.7468/(z-1)$, after time-domain discretization with a frequency of 100 Hz.

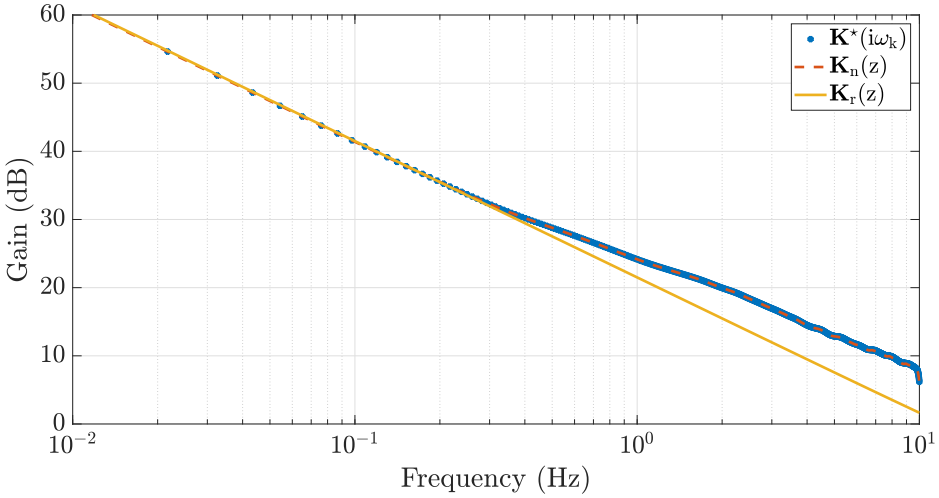

Figure 3.8: Bode gain diagrams of the ideal controller data $\mathbf{K}^\star$ (3.2), its exact interpolated sampled-time controller $\mathbf{K_n}$ and its approximation $\mathbf{K_r}$ with an order $r = 1$.

Figure 3.8 illustrates that the exact interpolation perfectly matches the data and the approximation with an order $r = 1$ preserves the integral term. Such an observation, coupled with the knowledge of the system input-output positivity property (input blows air and output measures positive values only), motivates the use of a more involved control strategy discussed in the next section.

3.2.2 Non-linear positive control design

Theoretical principle

Observing that the considered system is stable and input-output positive (for any non-negative input $\mathbf{u}$, the output $\mathbf{y}$ is non-negative), it seems interesting to exploit this property for control purposes. Although not recent (Farina and Rinaldi [174]), positive systems have recently attracted a lot of attention due to their properties as pointed out by Briat [175] and Ebihara et al. [176]. In particular, the theory of linear positive systems is playing an essential role in the modeling, the analysis and the control of compartmental systems which include biological, physiological, epidemiological and ecological systems as special cases as explained by Haddad et al. [177]. Recently, a novel type of integral controller, the AIC (Antithetic Integral Controller), was introduced by Briat et al. [178] in the context of biological control and chemical reaction networks. The rationale for introducing such a controller was the

derivation of a controller having a positive system representation that could always return a non-negative control input. It was later proved by Briat [167] that this nonlinear integral controller enjoyed certain interesting properties which are absent from its linear non-positive counterpart. It is also worth mentioning that other nonlinear positive integral controllers exist as for example presented by Briat [167], but the AIC exhibits a lot of the desirable behavioral properties of the usual integral controllers. Indeed, Briat [167] provides a stability proof of the closed-loop interconnection if the original underlying model is a linear positive one. In fact, those stability conditions coincide, in the worst-case, with the stability conditions of the standard integral controller, which indicates that using the AIC is not more constraining than using a linear integral controller.

In the L-DDC setting, no stability proof can be guaranteed a-priori. This may be checked afterwards with specific data-driven techniques, as explained by Kergus [166] or Poussot-Vassal et al. [179]. However, one important feature of the positive design by Briat [167] stands in the fact that the interconnection of this law to a stable input-output positive system, ensures global stability, while preserving input signal limitations.

Application to flow separation control

The discretized version using the backward method of Briat [167] controller writes as:

$$\begin{cases} z_1(t_k+h) = z_1(t_k) + h\big(\mathbf{r}(k) - k\eta z_1(k) z_2(k)\big) \\ z_2(t_k+h) = z_2(t_k) + h\big(\mathbf{y}(k) - k\eta z_1(t_k) z_2(t_k)\big) \\ \mathbf{u}(k) = k z_1(t_k) \end{cases} \tag{3.4}$$

Implemented in the real-time application, the operator then tunes the values of $k \in \mathbb{R}$ and $\eta \in \mathbb{R}_+$ according to the desired controller.

3.3 Closed-loop control of the separated flow over a plain flap

Once designed, both linear and non-linear controllers have been applied for the same flow conditions $U_\infty = 34.5$ m/s. As the control is implemented based on the 5^{th} hot film raw measurements, the reference value $U^*_{\text{obj}} = 0.3903$ is converted into a reference voltage, yielding $U_{obj} = 3.4$ V. The closed-loop control effects are firstly investigated for fixed deflection angles of the flap between 2° and 37°. Secondly, the same controllers are applied for continuously varying flap deflection angles.

3.3.1 Closed-loop control with fixed flap deflection angles

Application of L-DDC

The application of L-DDC with the closed-loop transfer function M presented previously as $\mathbf{M}(s) = 1/(s/w_0 + 1))$ with $\omega_0 = 2\pi\ rad/s$, is firstly considered. Figure 3.9 highlights the controller application. As presented during the controller designing phase, valves are not opened for δ values below 13.8°, since the hot film voltage is above the reference value as

observed in Figure 3.9a. When the flap deflection angle is above this threshold of 13.8°, the controller delivers a command signal to the valves, therefore controlling their duty cycle. For instance, for $\delta = 18°$, as depicted in Figure 3.9b, the valves duty cycle varies around a mean value of 18.3 %. As δ is further increased, the duty cycle is raised by the controller, as highlighted in Figure 3.9c for $\delta = 24°$, for which the mean value of α is 34.6%. For higher δ, the controller still maintains the hot film voltage to the reference value voltage, but with a lower duty cycle than the ones presented in Figure 3.9.

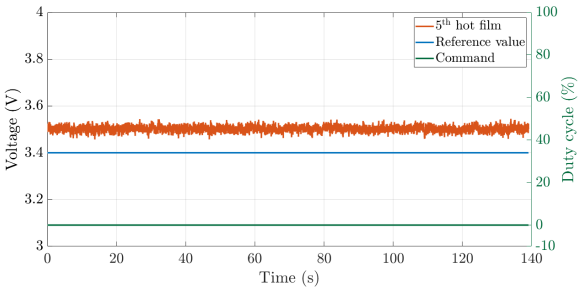

(a) Closed loop L-DDC for $\delta = 8°$.

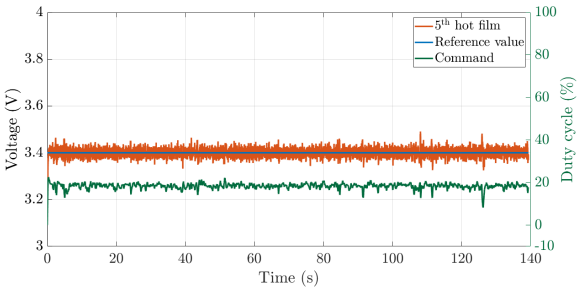

(b) Closed loop L-DDC for $\delta = 18°$.

Figure 3.10a and Figure 3.10b illustrate this case. For $\delta = 30°$ and $\delta = 37°$ the mean duty cycles respectively stand around 8.9 % and 22.7 %, while it remained around 34.6 % for $\delta = 24°$. This phenomenon might be due to the development of flow separation at the flap trailing edge, as for high deflection angles actuators, duty cycle is not high enough to counter its onset and spreading towards the leading edge. Also for $\delta = 37°$, the duty cycle suddenly raises to 54.5 % after 70 s. This might be due to an instability of the recirculation bubble above the considered hot film.
Nevertheless, it is observed that for the entire range of tested deflection angles δ, the linear controller maintains the hot film voltage to the reference value, no matter the phenomena developing in the flow.

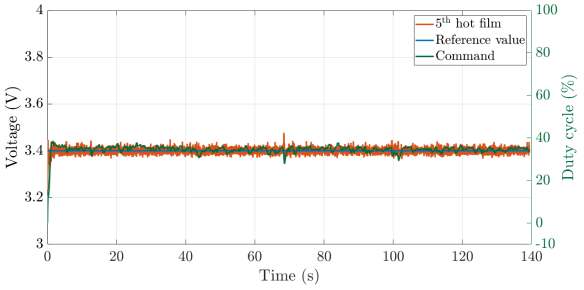

(c) Closed loop L-DDC for $\delta = 24°$.

Figure 3.9: Closed-loop L-DDC application for different flap deflection angles ($U_\infty = 34.5$ m/s). The 5$^{\text{th}}$ hot-film voltage and the reference value are read on the left y-axis. The actuators duty cycle value is presented on the right y-axis.

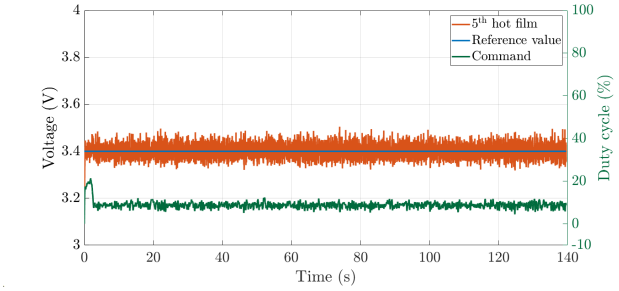

(a) Closed loop L-DDC for $\delta = 30°$.

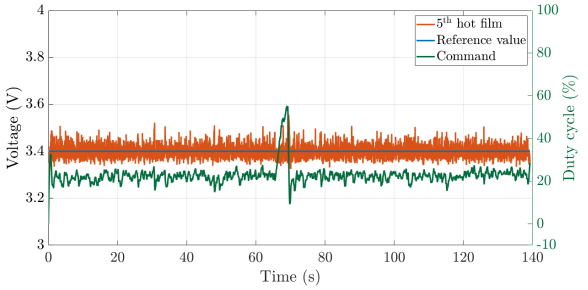

(b) Closed loop L-DDC for $\delta = 37°$.

Figure 3.10: Application of the closed-loop L-DDC for different high flap deflection angles ($U_\infty = 34.5$ m/s).

Application of the non linear positive controller

As Equation (3.4) aims at reproducing the integral action, gain k has been set, in our settings, equal to the integral term obtained with the L-DDC approach, yielding $k = 0.7468$. The coupling parameter $\eta = 300$ is used to tend to a pure integral action. As outlined in Figure 3.11, similar results to those presented previously are obtained with the non linear positive controller.

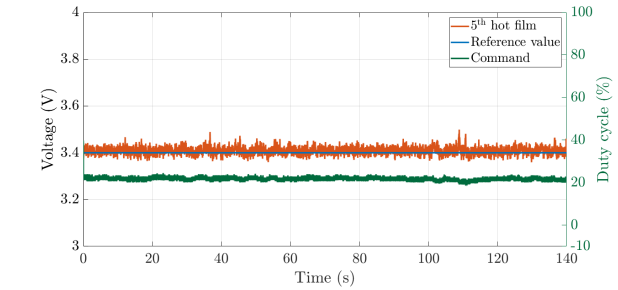

(a) Closed loop non linear positive control for $\delta = 18°$.

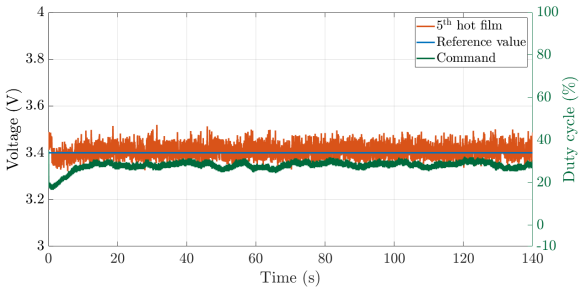

(b) Closed loop non linear positive control for $\delta = 37°$.

Figure 3.11: Application of the non linear positive closed-loop control for different flap deflection angles ($U_\infty = 34.5$ m/s).

For $\delta = 18°$, the duty cycle has a mean value of 21.2 %, while it reaches a mean value of 27.5 % for $\delta = 37°$, slightly above duty cycles used with the linear controller.

Control benefits on the lift and pressure coefficients

Effects of closed-loop flow control results are assessed through the comparison of C_L and C_p in both uncontrolled and controlled cases. As both the linear controller and the non-linear positive controller have been applied with the same reference value on the 5^{th} hot film, both control cases yielded the same results on the lift and pressure coefficients. Figure 3.12 highlights the benefit of control on the lift coefficient C_L increase.
For $\delta < 13.8°$, both uncontrolled and controlled flow present the same lift coefficient, as in both cases valves are not opened by the controller. However, for $\delta > 13.8°$, curves for the two cases do not superimpose anymore. The lift coefficient in the controlled case is higher than

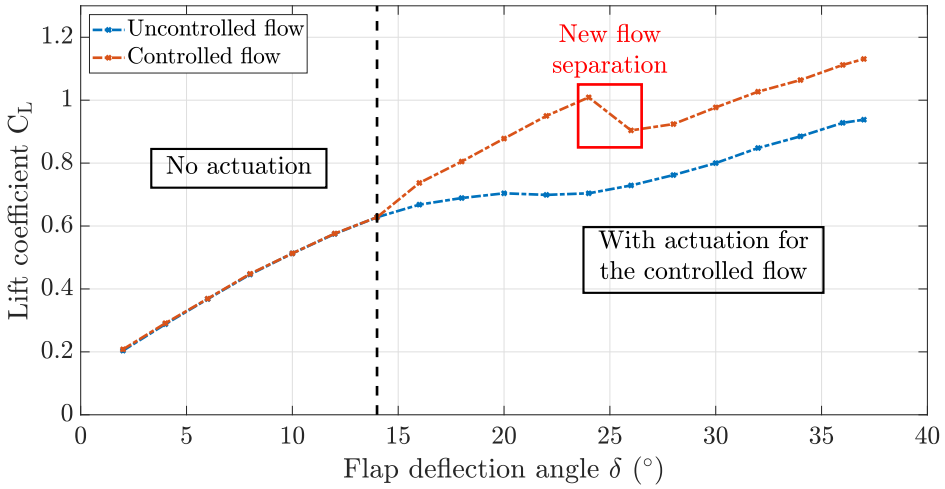

Figure 3.12: Evolution of the lift coefficient C_L without (blue curve) and with (red curve) control against the flap deflection angle δ for $U_\infty =$ 34.5 m/s.

the one of the uncontrolled case. Regarding the controlled case, the linear evolution of C_L is extended up to $\delta = 24°$. Between $\delta = 24°$ and $\delta = 26°$, flow separation develops at the flap trailing edge, as previously assumed considering Figure 3.9 and Figure 3.10. Therefore, C_L drastically reduces. This flow separation does not spread over the entire flap as the control counters it and hold it at the flap trailing edge. These results can also be observed in the analysis of the pressure coefficient evolution in both the uncontrolled and controlled flow cases, as explained in the following.

Considering the pressure coefficient C_p on the flap, similarly to the analysis conducted on C_L, both uncontrolled and controlled flows present the same pressure coefficient distribution on the flap for $\delta < 13.8°$, as shown in Figure 3.13a. For $\delta > 13.8°$, as illustrated in Figure 3.13b, the actuation of valves by the controller induces a pressure gradient on the flap upper surface and delay the onset of flow separation, indicated by the C_p plateau in the uncontrolled case growing at the flap trailing edge. For $\delta = 24°$ in Figure 3.13c, the pressure gradient induced by the valves is maintained on the entire flap, on the contrary to the uncontrolled case as the flow separation spreads almost entirely over the flap.

For deflection angles above 24°, the pressure coefficient distribution over the flap exhibit another behavior than the ones presented in Figure 3.13. Figure 3.14 illustrates the evolution of C_p respectively for $\delta = 30°$ and $\delta = 37°$. As hypothesized based on the hot film measurements in the controlled case, for high flap deflection angles a new separation of the flow develops from the trailing edge. Figure 3.14a illustrates this phenomenon, as in the controlled case a smaller pressure gradient is induced by the forcing compared to the cases of lower δ. In Figure 3.14b a plateau of C_p is observed from the flap trailing edge to $x/c_{tot} = 0.08$. Even though the forcing maintains the hot film voltage up to the reference value, it does not totally avoid flow separation for high δ. These control drawbacks observed in both C_L and C_p could be addressed using a more involved multi input control, based on several sensors, motivating future investigations.
These observations on both C_L and C_p motivate future investigations involving additional

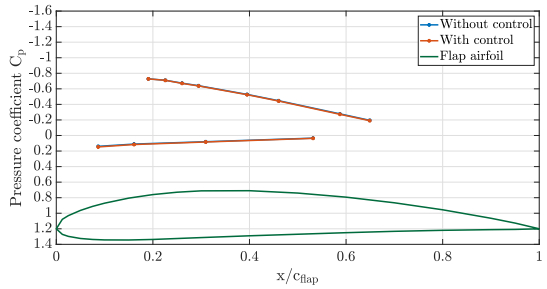

(a) Pressure coefficient comparison for $\delta = 8°$.

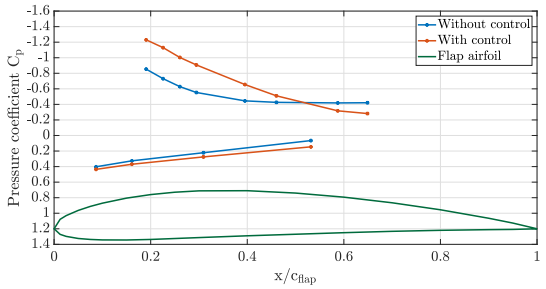

(b) Pressure coefficient comparison for $\delta = 18°$.

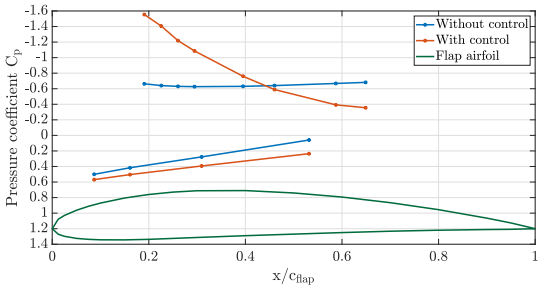

(c) Pressure coefficient comparison for $\delta = 24°$.

Figure 3.13: Comparisons of the flap pressure coefficients distributions in the uncontrolled (blue) and controlled (red) cases for different flap deflection angles ($U_\infty = 34.5$ m/s).

sensors and a more involved multi-input control.

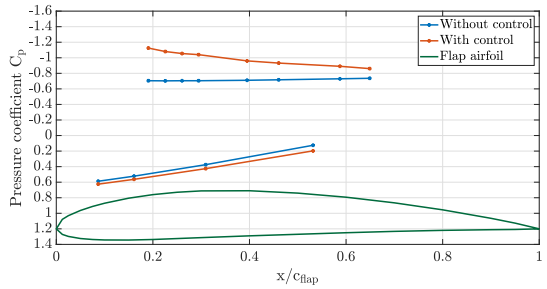

(a) Pressure coefficient comparison for $\delta = 30°$.

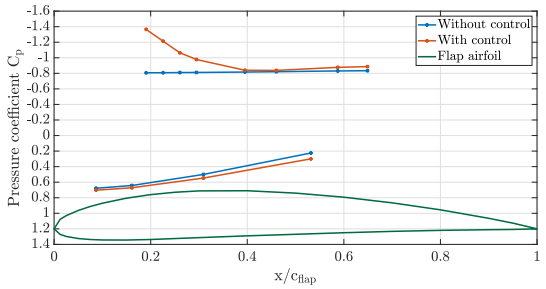

(b) Pressure coefficient comparison for $\delta = 37°$.

Figure 3.14: Comparisons of the flap pressure coefficients distributions in the uncontrolled (blue curves) and controlled (red curves) cases for flap deflection angles above 24° ($U_\infty = 34.5$ m/s).

3.3.2 Controllers robustness towards the flap orientation

In order to test the controllers robustness against the deflection angle, measurements were also performed with continuously varying angles. The flap deflection angle was varied from

$\delta = 8°$ to $\delta = 18°$ and to $\delta = 24°$. The linear controller shows its limits due to its linear integral behavior and the fact that it does not handle the positiveness of the system. As valves are not opened for $\delta = 8°$, the linear controller takes into account the error and therefore accumulates an integral error. Therefore, when the deflection angle increases to $\delta = 18°$ for which valves have to be opened, the controller effect is in the wrong direction. As observed in Figure 3.15a, once the linear controller has overcome the accumulated error, the controller is robust to the deflection angle variation from 18° to 24°.

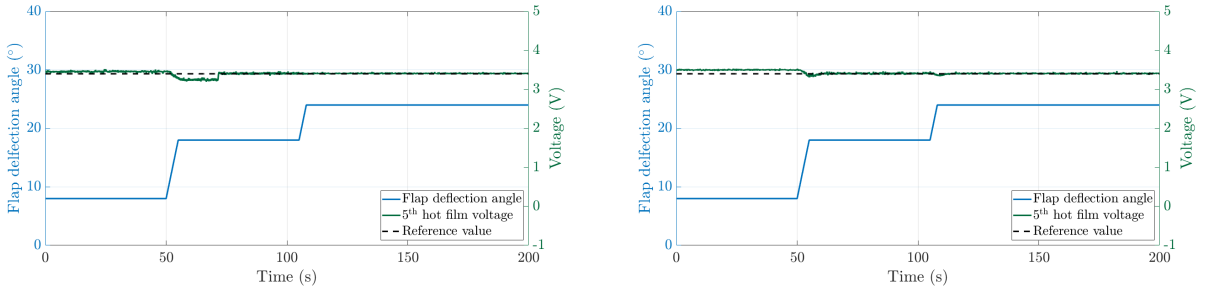

(a) Linear controller.

(b) Positive controller.

Figure 3.15: Evolution of the flap deflection angle against time (left axis) and evolution of both the 5$^{\text{th}}$ hot film voltage and reference value (right axis) against time for the linear (a) and positive (b) controllers ($U_\infty = 34.5$ m/s).

As such an error could not be tolerated in real application, a way to circumvent the delay would be to implement an anti-windup on the linear controller. This may be done at a price of more involved calculus, usually involving a model, while here, the pure data-driven setup is employed. However, it is proved in these experiments than an other simple and efficient way to deal with this integral behavior is to implement a non-linear positive controller instead. As described in Figure 3.15b, the delay resulting from the integral error issue totally vanishes considering this controller. In addition to that, the input output stability is formally guaranteed.

3.3.3 Tracking of a time dependent reference in the L-DDC framework

During the control experiments carried out with the L-DDC, the reference value set with respect to the 5$^{\text{th}}$ hot film measurements was varied with time for fixed flap deflection angles. The aim of these measurements are to find out by experimental identification whether the objective closed-loop transfer function $\mathbf{M}(s) = 1/(s/w_0 + 1))$ is effectively applied with the discretized and interpolated controller.

The first step towards the identification of the closed-loop transfer effectively applied, consists in applying a reference value defined as a sine wave of frequency $1Hz$, amplitude 0.1 V and oscillating around a mean value of 3.4 V, such that $r(t_k) = 3.4 + 0.1\sin(2\pi t_k)$. Figure 3.16 illustrates the measurements over 5 seconds for two different flap deflection angles: $\delta = 18°$ in Figure 3.16a and $\delta = 24°$ in Figure 3.16b. As illustrated in Figure 3.3b, for $\delta = 18°$ in uncontrolled conditions, the flow is not separated yet over the 5$^{\text{th}}$ hot film. Hence, the controller modifies the wall shear stress measurements of the hot film in attached conditions.

The hot film response follows the sine wave pattern set as reference value. The maximum error observed while tracking the reference value is about 1.9 %. The delay observed in the evolution of the hot film measurements is directly due to the phase delay of the considered system and its controller. Considering the case $\delta = 24°$, the flow is separated over the hot film in uncontrolled conditions. As described previously, setting a reference value of 3.4 V on the

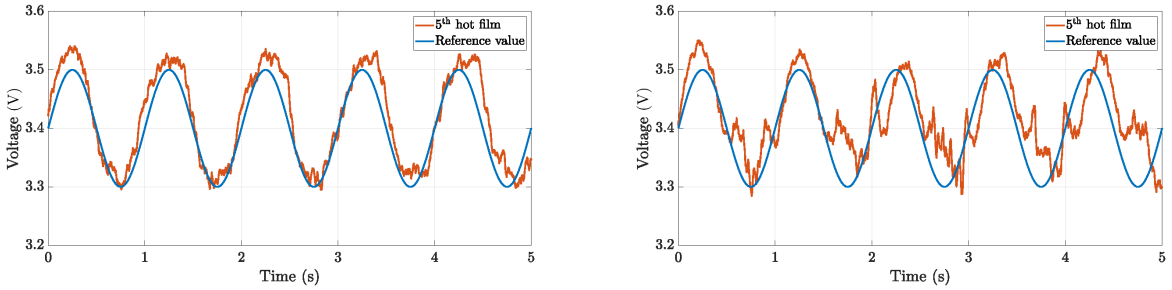

(a) Flap deflection angle $\delta = 18°$.

(b) Flap deflection angle $\delta = 24°$.

Figure 3.16: Evolution of the 5$^{\text{th}}$ hot film measurements during closed-loop L-DDC control with a sine wave as reference value ($r(t_k) = 3.4 + 0.1\sin(2\pi t_k)$) for different flap deflection angles ($U_\infty = 34.5$ m/s).

hot film counters the development of flow separation at this location. Therefore, using a sine wave $r(t_k) = 3.4 + 0.1\sin(2\pi t_k)$ as reference value for $\delta = 24°$ results in alternating phases during which the flow is separated and re-attached to the flap. This changeover, between attached and separated flow, can be observed in the sine wave lower part ($r(t_k) < 3.4\ V$). Therefore, in Figure 3.16b, the hot film measurements do not strictly match the reference value.
Further measurements with time dependent reference value are carried out in order to identify the closed-loop transfer function of the system. Similarly to the L-DDC identification step, a logarithmic frequency sweep applied to the hot film voltage with frequencies ranging from 0.01 Hz to 10 Hz is applied. The voltage lower (respectively upper) limit is defined by the mean voltage recorded on the hot film with the valves completely closed (respectively opened). Measurements are performed for a flap deflection angle of 24°, the same conditions in which the data were gathered to design the controller. The reference signal and the 5$^{\text{th}}$ hot film response are presented in Figure 3.17.

Based on these measurements, the transfer function can be identified through the tfestimate routine in matlab, computing the ratio of the cross power spectral density of the reference signal and the hot film response with the power spectral density of the reference signal. Based on a Welch algorithm, 40 Hamming windows are used for the computation with an overlap of 50 %.
Figure 3.18 presents the Bode diagrams of both the estimated closed-loop transfer function, obtained based on the ideal controller computed during the L-DDC process and the closed-loop transfer function computed based on the identification step proposed above. For low frequencies, below 2.10^{-1}, both estimated and experimental data superimpose. For frequencies above 2.10^{-1} a discrepancy is observed between the curves with a maximal dispersion in the gain of 5 dB at 0.75 Hz.

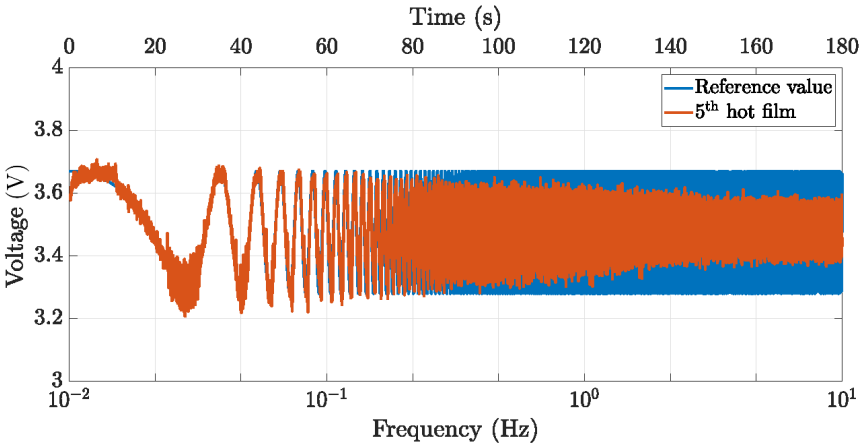

Figure 3.17: Evolution of the reference signal (blue curve) and hot film (red curve) voltages against frequency (Hz - lower axis) and time (s - upper axis) for $\delta = 24°$ ($U_\infty = 34.5$ m/s).

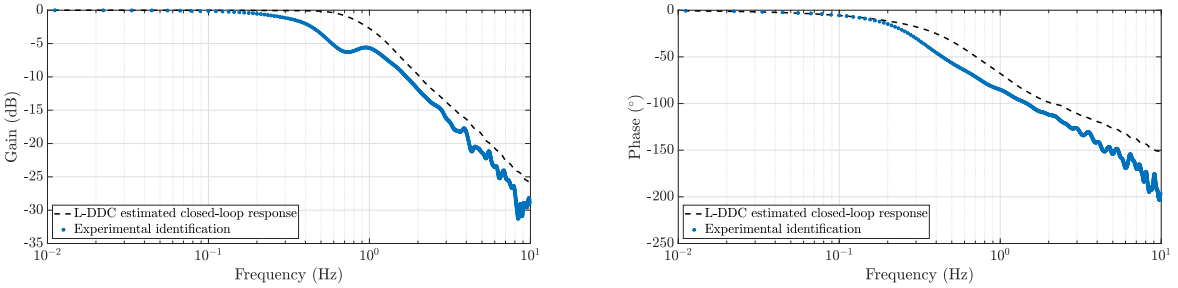

(a) Gain (dB) of the identified closed-loop transfer function against frequency.

(b) Phase (°) of the identified closed-loop transfer function against frequency.

Figure 3.18: Bode diagrams of the estimated L-DDC closed-loop response (black dashed curve) and experimental identification of the closed-loop response (blue points).

3.3.4 Overview of the closed-loop control experiments

Control of flow separation over a plain flap was performed involving two different control approaches. Both strategies, based on a linear data-driven controller or on a phenomenological controller, enabled to maintain a reference voltage value on the objective hot film placed at the flap mid-chord. The latter reference, being calculated based on the flow separation observation. Both controllers efficiency were assessed through lift coefficient calculations derived from pressure measurements. Limiting the development of flow separation on the plain flap, they did not completely avoid it. To do so, a more constraining reference value migth be used in combination with another hot film located closer to the trailing edge. Also a more involved closed-loop MISO control strategy could be implemented.
Both controller robustness to the flap deflection angle was also tested through experiments, during which the flap angle was continuously varied. The most significant advantage of these control techniques lies in the simplicity of their application which is of importance in view of experimentation and implementation, for practitioners. Considering the linear controller, its application relies only on a data identification problem solved via the Loewner framework. Regarding the non-linear positive controller, its application only requires the tuning of the

two constants k and η, for which values obtained in the L-DDC are good starting points. To avoid or counter the development of flow separation, large mass flow rates are required. Furthermore, the definition of the reference value is based on measurements performed with hot films, which do not guarantee that flow separation is avoided over the entire flap. Therefore, another way of characterizing flow separation might be required to perform similar flow control experiments. In that sense, MEMS calorimetric wall shear stress sensors were developed at the IEMN and used to detect the onset of flow separation. The next section provides details on their design and use in similar open-loop experiments and an experimental protocol is proposed to use the MEMS sensors in closed-loop flow control experiments.

3.4 Towards the use of MEMS technologies in flow separation control

3.4.1 MEMS wall shear stress sensors

Calorimetric MEMS sensors were developed at the IEMN by Ghouila-Houri et al. [64] for the measurement of wall shear stress. The sensors are composed of three suspended multi layers wires as presented in Figure 3.19. Similarly to hot film measurements, the central

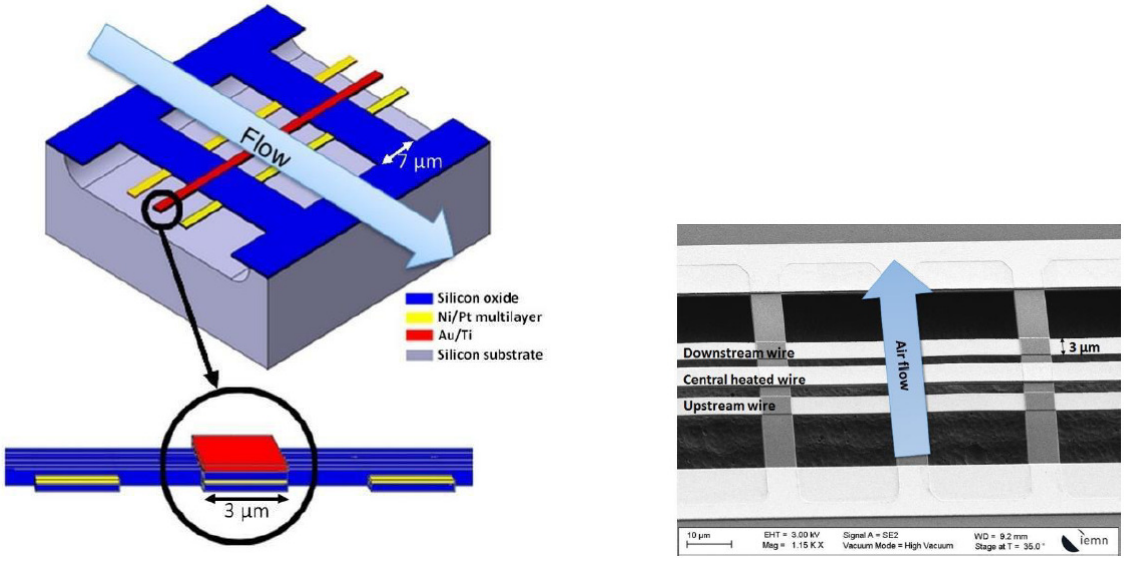

(a) Scheme of the sensor.

(b) SEM picture of the sensor.

Figure 3.19: Scheme (a) and SEM picture (b) of the calorimetric MEMS wall shear stress sensor [180].

wire is heated and its energy losses in the surrounding flow enable a measurement of the wall shear stress amplitude. Cold wires are placed on each side of the central wire. Cooled differently by the flow deflecting the thermal boundary layer induced by the central wire, the differential measure indicates the flow direction. The sensors structure guarantees the mechanical robustness and a non-intrusive measure. Based on micro-machining processes, the fabrication of the sensors consists in depositing a layer of silicon oxide SiO_2 on the substrate by PECVD (Plasma Enhanced Chemical Vapor Deposition) and then manufacturing

the wires by photolithography, metalization by evaporation and lift-off [63]. As presented in Figure 3.19a, measurement wires are composed of a NiPt multilayer, while the heating wire is composed of Au. The latter wire is separated from the central measurement wire by a layer of SiO_2. Finally, a etching step releases the wires from the substrate. More details on the fabrication process can be found in [63]. Manufactured on a 3 inches wafer, hundreds of sensors can be simultaneously produced. Figure 3.20 shows a wafer with the chips and

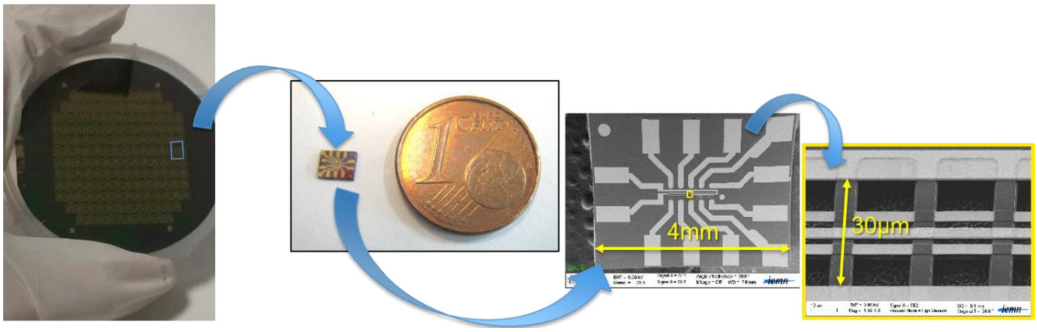

Figure 3.20: Pictures of a wafer with the MEMS wall shear stress sensors and size comparison [180].

illustrates the characteristic lengths of a sensor. Employed with a dedicated electronic, the sensors can be exploited in both constant current (CC) or constant temperature (CT) modes, the latter providing a larger frequency bandwith. Sensors are calibrated in a boundary layer wind tunnel and output voltages are converted in wall shear stress amplitudes using the Coles-Fernholz method [181].

3.4.2 Detection of flow separation with the MEMS sensors

The considered calorimetric sensor design can deliver both the wall shear stress amplitude and sign. Regarding Figure 1.10b, the sensor output voltage therefore follows the theoretical evolution of the wall shear stress. While the flow is still attached to the surface, the sensor delivers a positive wall shear stress measure, as would do a hot film. At the separation point, the sensor delivers a null wall shear stress measure and then provides negative values, once placed in the recirculating flow.

An array of MEMS calorimetric sensors was integrated by Ghouila-Houri et al. [65] on the same configuration as the one presented in this chapter. The flap upper surface was adapted such that the sensors could be flush mounted. Figure 3.21a illustrates the integration along the flap chord. Using multiplexing to record the sensors data, the flap was deflected between $\delta = 2°$ and $\delta = 30°$ for a freestream velocity $U_\infty = 24.5\ m/s$, yielding a Reynolds number $Re = 3.45.10^5$.
Figure 3.21b highlights the normalized wall shear stress response of three sensors at different positions. With a signed normalized wall shear stress measurements, it can be observed that the flow separation point evolves towards the flap leading edge, as pointed out in Figure 3.3. These first measurements proved the ability of the sensors to detect flow separation. They were then used in open-loop flow control experiments.

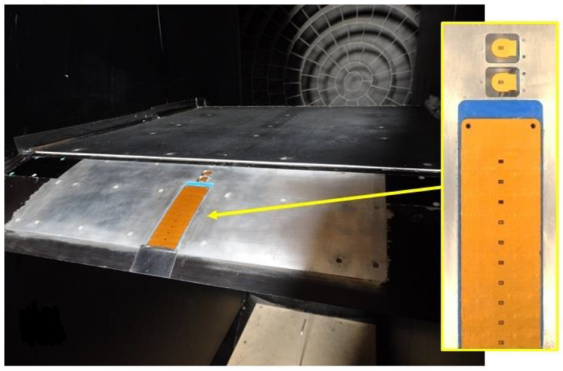

(a) Picture of the model with the MEMS sensors integrated on the flap upper surface.

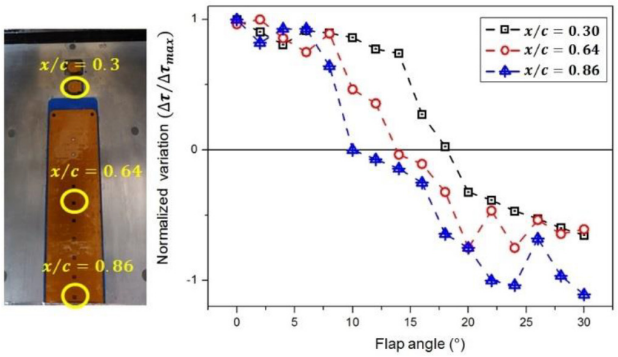

(b) Evolution of three sensors normalized wall shear stress variations against the flap deflection angle.

Figure 3.21: Picture (a) and results (b) of the flow separation detection with MEMS calorimetric sensors [65].

During the open-loop flow separation control measurements, valves were supplied with a constant mass flow rates of 20 g/s, actuated with a frequency of 60 Hz and a duty cycle of 50 %. Aim of these measurements were to observe the effect of the forcing on flow separation thanks to the MEMS calorimetric sensors. Figure 3.22 summarizes the results obtained for the sensor placed at $x/c_{flap} = 0.3$. The blue points correspond to the uncontrolled case

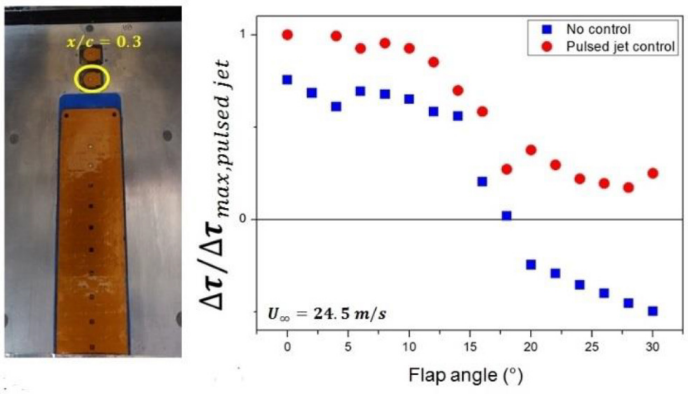

Figure 3.22: Effects of open-loop forcing on flow separation observed with a MEMS calorimetric sensors at $x/c_{flap} = 0.3$ for $U_\infty = 24.5\ m/s$ [65].

and indicate flow separation at this location for $\delta = 18°$. In the open-loop control case, flow separation is avoided for the tested range of flap deflection angles, as wall shear stress measurements remain positive. Based on these measurements, a protocol of closed-loop separation control with the MEMS calorimetric sensor is proposed in the following section.

3.4.3 Towards the closed-loop control of separated flow with MEMS sensors

MEMS calorimetric sensor integration

Similarly to the experiments carried out by Ghouila-Houri et al. [65] on the plain flap, a set of 4 MEMS calorimetric sensors was integrated on the flap upper surface as depicted in Figure 3.23. Electronics of the sensors are placed inside the flat plate, upstream the flap and signals are recorded with the same acquisition chain as the one presented in Section 2.1. Because of issues with the sensors electronics, flow control experiments could not go to the end but some results were still acquired and are presented in the following. A new version of the sensors electronics is under investigations and should be tested in the future.

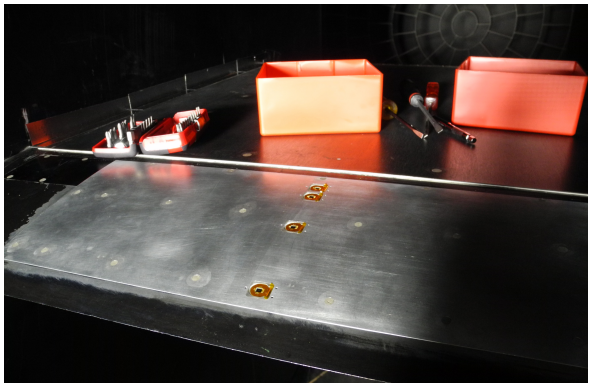

Figure 3.23: Integration of MEMS calorimetric sensors for closed-loop flow separation control.

Flow characterization with the MEMS sensors

For a freestream velocity $U_\infty = 34.5\ m/s$, the flap was deflected for $\delta = 2°,\ 10°,\ 18°,\ 26°$ and $34°$. Data from the central wire combined with the side cold wires indicated similar results to those obtained with the hot films. Figure 3.24 presents the evolution of normalized wall shear stress amplitude τ^* measured by the sensor placed at $x/c_{flap} = 0.5$.
Similarly to U^*, τ^* is defined according to the following relation: $\tau^* = \pm|\frac{\tau - \tau_{min}}{\tau_{max} - \tau_{min}}|$. Therefore τ^* evolves between -1 and 1 and its sign is inferred on the differential measure provided by the lateral wires. As expected, τ^* decays until it reaches its minimum around $\delta = 20°$. Because of the electronics problems mentioned above (making impossible the definition of a reference value to track), τ^* remains close to 0 on a range of deflection angles between 18° and 25°, before it becomes negative, as the sensor stands in the recirculating bubble. Based on the first measurements performed with hot films on the same configuration, it is assumed that the flow separates at $x/c_{flap} = 0.5$ for $\delta = 18°$.

The first step towards the implementation of L-DDC with the MEMS sensors is realized, yielding the discrete frequency-domain transfer data $\{\imath\omega_k, \boldsymbol{\Phi}_k\}_{k=1}^N$. Figure 3.25 shows the Bode diagram of the transfer function identified with the same actuators driving signal as presented in Section 3.2.1. Despite the data gathered, closed-loop control experiments with the MEMS sensors could not go further, as the electronics did not enable the definition of a

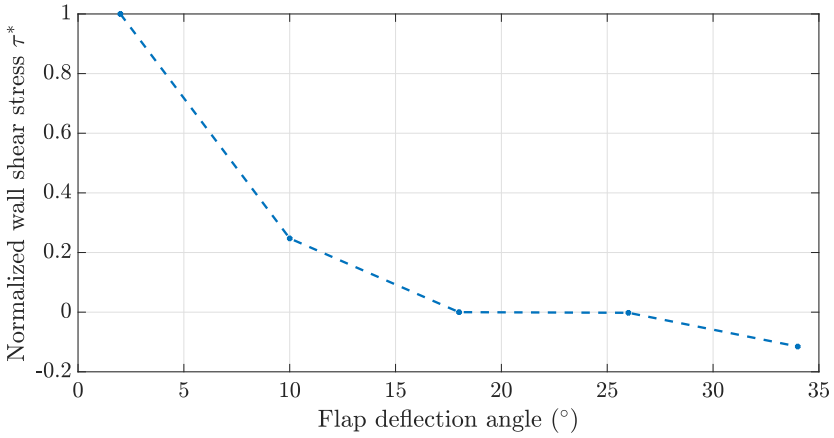

Figure 3.24: Evolution of the normalized wall shear stress measurement against the flap deflection angle.

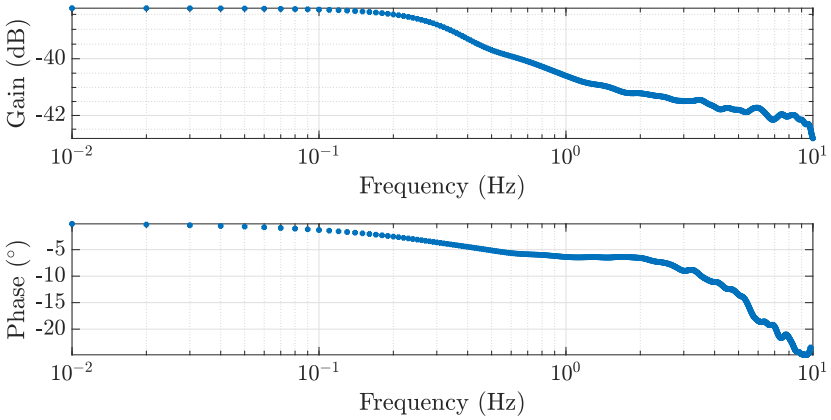

Figure 3.25: Bode diagrams of the frequency data collected during the open-loop measurements.

reference value to track, because of drifting outputs polluting the measurements.

If the closed-loop control experiments in L1 had been done with the MEMS sensors, the reference value chosen for the control would have been slightly positive, considering the measurements presented in Figure 3.24. Advantage of the MEMS sensors relies on providing the signed wall shear stress measurement. Therefore, a slightly positive reference value would have been sufficient to ensure that the flow remains attached above the considered sensor.

Conclusion

This 3rd chapter consisted in the application of the closed-loop control of a separated flow over a NACA 4412 plain flap, for a freestream velocity of 34.5 m/s and for deflection angles varied between 2° and 37°. Two control strategies, one data-driven and one phenomenological/model-driven, handled the flow separation control while tracking a reference value based on the hot films measurements.

To perform the closed-loop experiments, the first step consisted in the characterization of the unforced flow dynamics. Pressure measurements provided the evolution of C_L and C_p for the experimental conditions. Unforced flow hot films measurements also enabled the definition of the reference value to be tracked by the controllers in order to delay flow separation.
Then, open-loop flow control measurements helped designing the linear integral data-driven controller and the non-linear integral positive controller.
Afterwards, both type of controllers have been applied for the same experimental conditions. They both avoided the onset of flow separation on the flap for deflection angles up to 24°. For $\delta > 24°$, both controllers limited the development of the recirculation bubble developing for high deflection angles. Furthermore, the non-linear positive controller, originating from the biological field, circumvents the issues encountered with the linear integral controller.
Finally, the use of MEMS calorimetric wall shear stress sensors in similar flow control experiments is proposed. These sensors yielding both the wall shear stress amplitude measurements and the flow direction could help reducing the tracking value to its minimum such that the flow is kept attached to the flap in all conditions.

The application of a closed-loop control of the separated flow was performed with 7 Festo valves driven with a mass flow rate of 21 g/s. This high mass flow rate is required as it is aimed to modify the flow mean properties to counter the development of flow separation over the flap. For this reason, it is clear that MEMS actuators could not be employed in such experiments, as they could not reach these mass flow rates orders of magnitude. In that sense, Chapter 4 presents the integration of MMMS microvalves on an open-cavity for the open-loop control of the flow instabilities.

Chapter 4

Study of the open-loop control of a subsonic open-cavity flow

Introduction

The control of a separated flow has been presented in Chapter 3 and focused on the application of two closed-loop control methods. Actuators used during these experiments reached mass flow rates of 21 g/s, much beyond the performance range of MEMS actuators. In Chapter 4, the aim is to perform open-loop flow control experiments on an open-cavity flow with MEMS microvalves. The objective consists of the modification of the open-cavity mean flow with both the quasi-steady and the pulsed jets induced by the microvalves.

The first part of the present chapter is dedicated to the MMMS microvalves characterization. Able to generate both quasi-steady and pulsed jets, the magnetically actuated microvalves are characterized with hot wire measurements. Their linear behavior is highlighted in the estimation of the actuators transfer function. The second part provides details on the integration of the actuators to the open-cavity upstream edge in the ONERA S19 low-speed wind tunnel. The unforced flow is characterized with unsteady pressure measurements, such that flow regimes with periodic low-frequency oscillations are identified. The third part is dedicated to the implementation of open-loop forcings with the microvalves. Effects of the actuators quasi-steady jets on the flow dynamics are investigated on the identified periodic flow regimes. Pulsed jets effects are finally considered and are implemented in the form of harmonic forcings with actuation frequencies distant and close to the cavity resonant frequency.

4.1 Characterization of MMMS magnetically actuated microvalves designed for flow control

In order to perform the open-loop flow-control experiments on the open cavity presented in Chapter 2, a set of 15 microvalves is assembled and integrated as a linear array as depicted in Figure 4.1. This setup and the test bench are used to characterize both the microvalves quasi-steady and pulsed jets, as described in the following.

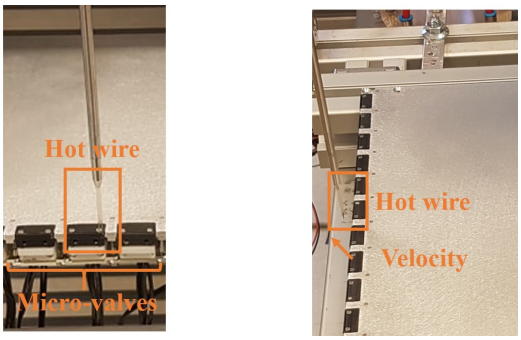

Figure 4.1: Test bench with the integrated microvalves array from two different views.

4.1.1 Quasi-steady jets characterization

Firstly, MMMS microvalves are actuated individually in order to characterize their quasi-steady jet through the measurements of flow rate as a function of supply pressure. Each actuator is supplied with a pressure difference, set up with respect to the ambient pressure, varied between 0 mbar and 200 mbar. The induced flow rate through the microvalves was measured and proved that the mounted microvalves have the same flow rate/pressure difference characteristics. For pressure differences lower than 25 mbar, no flow rate could be measured. However as illustrated in Figure 4.2, for pressure differences higher than 25 mbar the flow rate/pressure difference relation is well fitted by the linear relation in Equation (4.1):

$$D = -0.15 + 0.01\Delta P \text{ with } D \text{ in L/min and } \Delta P \text{ in mbar.} \tag{4.1}$$

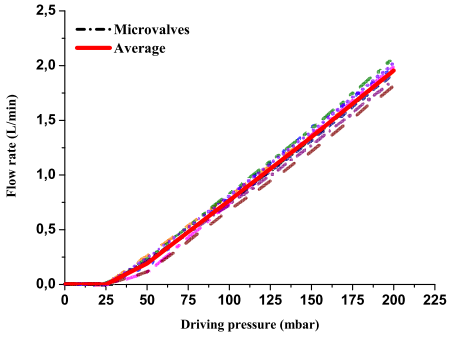

Figure 4.2: Microvalves flow rate/pressure characteristics.

In Figure 4.2, the scattering between the highest and the lowest flow rates measured for a driving pressure above 100 mbar is about 14 %. This scattering can be explained by the manual assembly of each layer composing the microvalves.

Hot-wire measurements completed the quasi-steady jets characterization. A Dantec 55P11 hot wire probe associated to a mini CTA 54T42 is used to perform measurements with a sampling frequency of 20 kHz over 1 s at each considered point. Measurements are carried out in the (YZ) and (XZ) planes, defined in Figure 2.13 where X, Y and Z axes are defined with respect to the actuators outlet. The flow crosses the (XZ) measurement plane with a 45° angle. The hot wire probe is placed parallel to the Y axis. Hence, the velocity measured by the hot wire is a combination of the X and Z velocity components. One microvalve is supplied with a pressure difference of $\Delta P = 150$ mbar, yielding a flow rate D of 1.5 L/min.

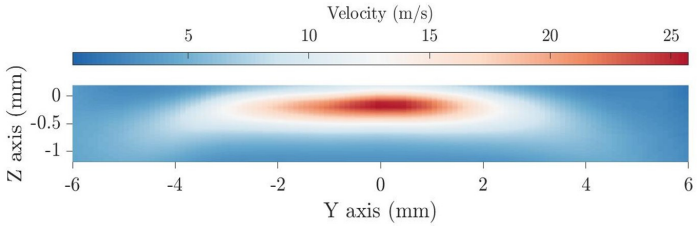

Figure 4.3: Quasi-steady jet mapping in the (YZ) plane for $\Delta P = 150$ *mbar*.

Figures 4.3 and 4.4 respectively present the measurements in the (YZ) and (XZ) planes. As depicted in Figure 4.3, the jet outlet is centered on the slot exit. The maximum velocity reached for $\Delta P = 150$ mbar is about 25 m/s. Figure 4.4 presents the jet velocity mapping for the same parameters in the (XZ) plane. The jet outlet angle of 45° can be measured from this mapping.

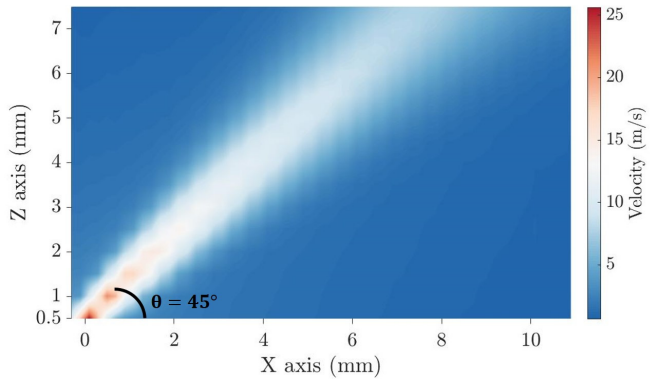

Figure 4.4: Quasi-steady jet mapping in the (XZ) plane for $\Delta P = 150$ mbar.

4.1.2 Pulsed jets characterization

The microvalves pulsed jets are then characterized. The entire array is supplied with a total pressure difference of 250 mbar. One microvalve at a time is fed with an electrical signal. Input signals used are sine waves of the form $A\sin(2\pi ft)$ with amplitude values A of 0.5 V, 1 V, 1.5 V and 2 V and frequencies f ranging from 20 Hz up to 380 Hz. The amplitude

denoted A corresponds to the signal generator amplitude, which is firstly fed to a linear amplifier, before it reaches the actuators. Hot-wire measurements are performed at the microvalve maximum velocity location in the (YZ) plane and for $X = 0.5$ mm. Considering an input signal of frequency 240 Hz and amplitude 2V in Figure 4.5a, the associated velocity measurements are presented in Figure 4.5b. It can be observed that the velocity oscillates around a mean value of 22 m/s. Figure 4.5c presents the raw velocity PSD. Three peaks are clearly identified: one at 240 Hz corresponding to the fundamental frequency of the actuation and two others respectively at 480 Hz and 720 Hz corresponding to harmonics. Harmonics are largely dominated by the fundamental frequency, as their PSD is lower by at least 10 dB, corresponding to time domain amplitude divided by 3. In Figure 4.5d, we therefore consider the output signal filtered at the sinusoidal forcing frequency and four amplitudes A. The velocity modulation depth appears to evolve linearly with A.

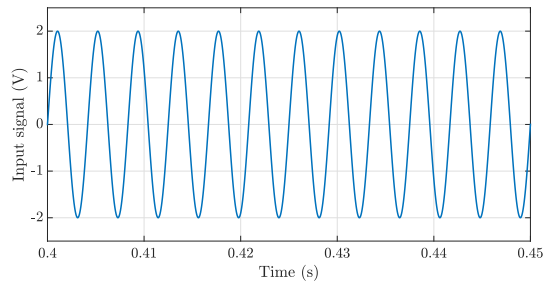

(a) Electrical driving signal.

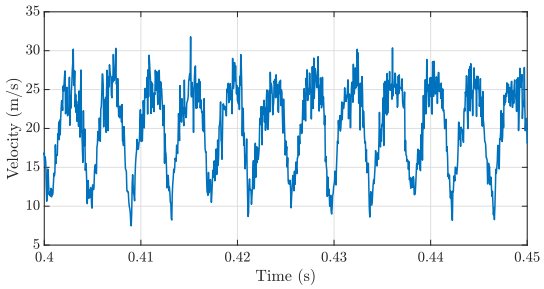

(b) Raw pulsed jet velocity.

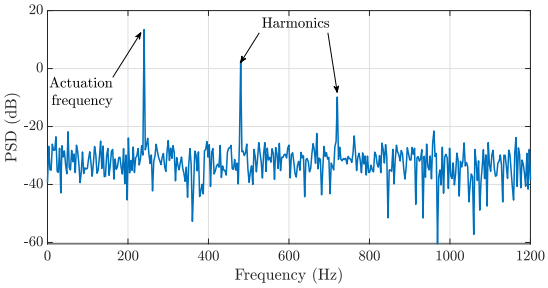

(c) Microvalve velocity spectrum.

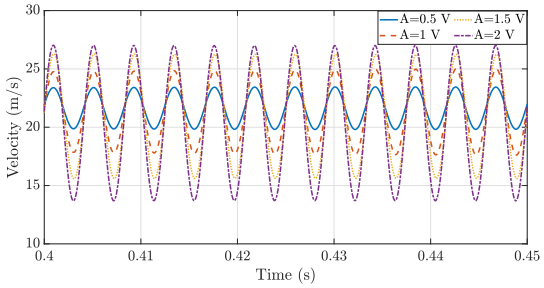

(d) Filtered pulsed jet velocity.

Figure 4.5: Actuator input signal (a), velocity measurement (b), spectrum (c) and comparison of the filtered velocity around the actuation frequency for different amplitudes (d), $f = 240$ Hz and $A = 0.5$ V, 1 V, 1.5 V and 2 V.

The microvalve transfer function is then computed as the ratio between the velocity hot-wire measurements and the signal generator driving signal. The transfer function Bode diagram of one microvalve is presented in Figure 4.6. The gain plot indicates that the actuator behaves linearly as the four curves for the different amplitudes superimpose, except for A =2 V and $f \geq 250$ Hz. Considering the phase plot for a given frequency, whatever the input signal amplitude, the same delay between the signal command and the outlet velocity is induced. Figure 4.7 further shows the linear behavior of the microvalves. An input signal composed of two sine waves respectively with frequencies of 100 Hz and 200 Hz and with the same amplitudes is used. The microvalve response is measured with a hot wire. Both the input and output signals PSD are presented in Figure 4.7. The input signal PSD is obviously composed of two peaks respectively at 100 Hz and 200 Hz with the same amplitude. The

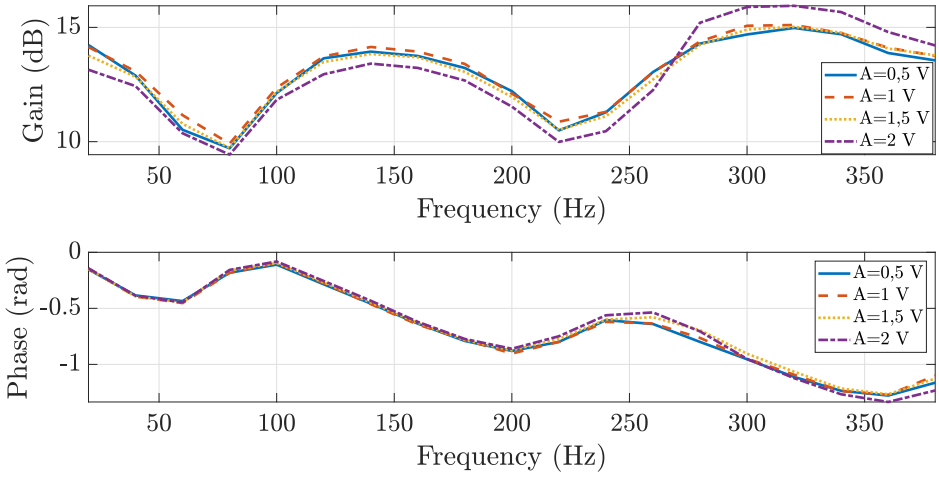

Figure 4.6: Microvalve transfer function Bode diagrams.

output signal PSD is also composed of two peaks at these frequencies pointing out the superposition principle respected by the actuators. The amplitude difference between the two peaks is explained by the transfer function previously presented in Figure 4.6, which does not exhibit a flat gain curve. The linear behavior of such actuators implies their ability to

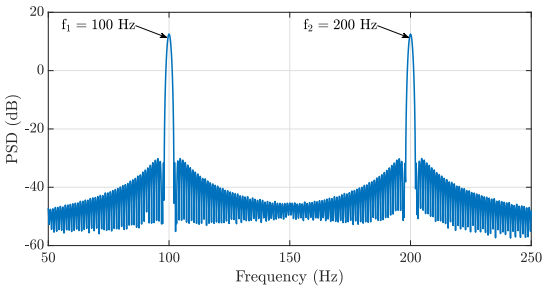

(a) Input signal PSD.

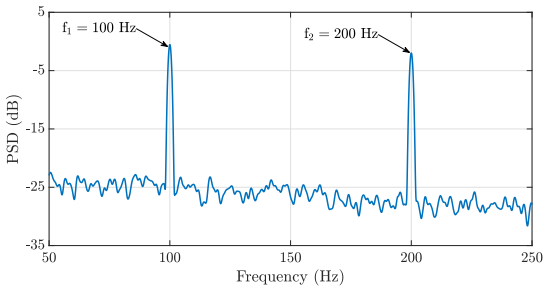

(b) Hot-wire measurement PSD.

Figure 4.7: Illustration of the actuator superposition principle.

be controlled with arbitrary signals and constitutes a first step towards the implementation of closed-loop control strategies of the flow over the open-cavity.

4.2 Unforced open-cavity flow characterization with unsteady pressure measurements

4.2.1 Investigation of the different flow regimes

First measurements in the wind tunnel are dedicated to the flow dynamics characterization without the microvalves jets. Freestream velocities U_∞ ranging from 10 m/s up to 46 m/s are explored. Different flow regimes are identified depending on U_∞, based on the unsteady pressure measurements as explained in detail in Chapter 2. On one hand, flow regimes without particular oscillating frequencies could be found. Figure 4.8 presents two spectra respectively for $U_\infty = 14$ m/s and $U_\infty = 24$ m/s. In each case, the flow does not exhibit

strongly dominant peaks. In Figure 4.8a, only a peak at 100 Hz emerges from the noise, while in Figure 4.8b two broad peaks arise respectively at $f_1 = 94$ Hz and $f_2 = 175$ Hz.

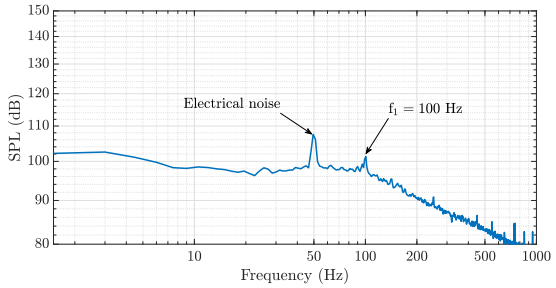

(a) Spectrum for $U_\infty = 14$ m/s.

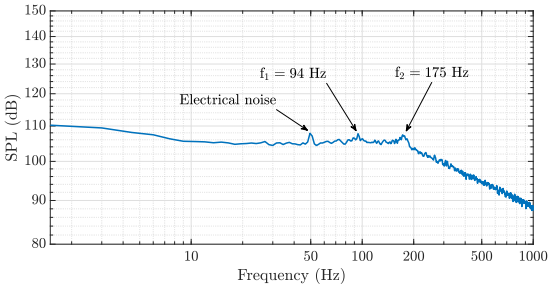

(b) Spectrum for $U_\infty = 24$ m/s.

Figure 4.8: SPL (dB) flow spectrum for several freestream velocities.

On the other hand, several periodic and quasi-periodic flow regimes could be identified. Different periodic flow regimes are identified for freestream velocities of 20 m/s, 30 m/s and 34 m/s. Spectra of these flow regimes are presented in Figure 4.9. The relative amplitude of the higher-order harmonics increases with U_∞, but as $U_\infty = 20$ m/s and 30 m/s, the oscillation is nearly monochromatic. Indeed, the second peak is respectively 16 dB and 14 dB weaker than the fundamental in the two cases.

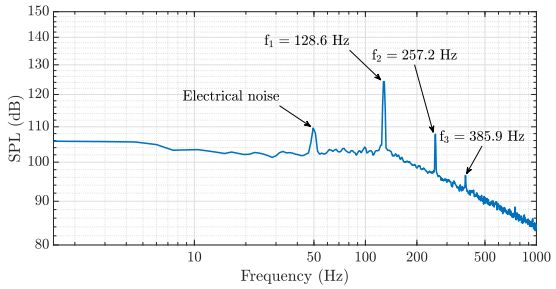

(a) Spectrum for $U_\infty = 20$ m/s.

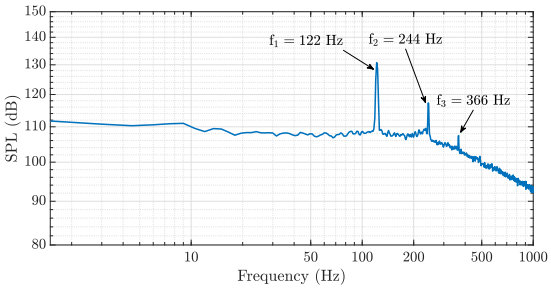

(b) Spectrum for $U_\infty = 30$ m/s.

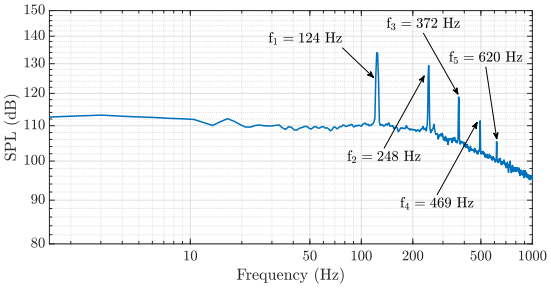

(c) Spectrum for $U_\infty = 34$ m/s.

Figure 4.9: SPL (dB) flow spectrum for several freestream velocities in the periodic case.

For a freestream velocity U_∞ =20 m/s (which is the flow regime considered in the following), the semi-empirical formula proposed by Rossiter (Equation (1.3)) yields a first mode

resonance at 58.6 Hz and a second mode at 136.7 Hz. Given the dimensions of the deep ($L/D = 0.15$) open-cavity considered, the semi-empirical formula proposed by East yields a resonance frequency of 81.7 Hz, while the one observed in the spectrum is of 128.6 Hz. The difference with the experimental observation may be due to the specific geometry of the deep open-cavity considered in the present work, which section varies with depth, as presented in Figure 2.5b. The resonance may be rather acoustic than hydrodynamics as the observed peaks in the different spectra are very sharp (on the contrary to spectra observed by Basley [182]) and as oscillations tend to be quasi-harmonic. Slight change in the resonance frequency from one freestream velocity to another hints aswell at an acoustic resonance.

More complex flow regimes are identified for freestream velocities $U_\infty = 36$ m/s and $U_\infty = 42$ m/s. These quasi-periodic flow regimes are characterized by one low frequency and one high frequency and harmonics arising from self-interactions and cross-interactions between these two incommensurate basic frequencies (2-torus attractor). Figure 4.10 highlights spectra of two quasi-periodic flow regimes. The first one considered in Figure 4.10a is characterized by a low frequency $f_1 = 19$ Hz and a high frequency $f_2 = 126$ Hz. The second one presented in Figure 4.10b is composed of a low frequency $f_1 = 45$ Hz and a high frequency $f_2 = 128$ Hz. In both cases, cross-interactions between the modes can be described by the equation $nf_1 + kf_2$ with n and k two integers.

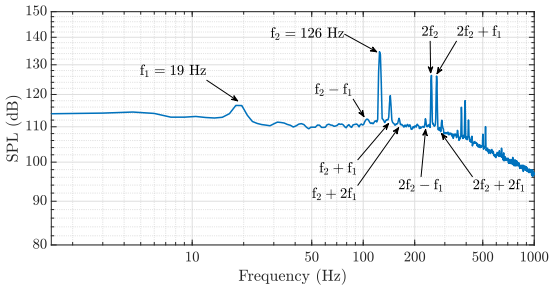

(a) Spectrum for $U_\infty = 36$ m/s.

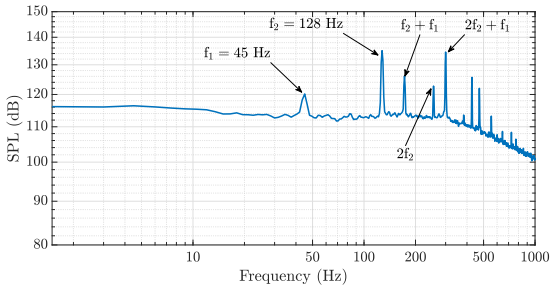

(b) Spectrum for $U_\infty = 42$ m/s.

Figure 4.10: SPL (dB) flow spectrum for several freestream velocities in the quasi-periodic case.

As the MMMS microvalves are tested for the first time on the open-cavity configuration, it is chosen to consider a low frequency oscillatory flow regimes such as the one presented above. This choice is made such that the flow frequencies fall within the actuators bandwidth. Therefore, the following open-loop flow control experiments are carried out with freestream velocities U_∞ of 20 m/s, 30 m/s and 34 m/s.

4.3 Implementation of quasi-steady forcings on the open-cavity flow

For each of the three freestream velocities, effects of quasi-steady jets on the flow dynamics are studied. Actuators driving pressures are varied between 150 mbar and 290 mbar. The pressure differences ΔP used during the measurements are gathered in Table 4.1. Spectra

derived from the open-loop forcings with quasi-steady jets are compared with spectra of the unforced open-cavity dynamics.

Table 4.1: Actuators driving pressure for the open-loop quasi-steady jets flow control experiments.

ΔP (mbar)							
0	150	175	200	225	250	275	290

4.3.1 Effects of the quasi steady-jets on the flow dynamics

As expected based from Chapter 1, it was observed that injection of momentum by the quasi-steady jets in the flow reduce the amplitudes of the peaks at the resonant frequencies. Their effects for a freestream velocity of 20 m/s can be observed in Figure 4.11. As highlighted, the higher the driving pressure, the further the fundamental frequency SPL is reduced. A maximum reduction of 20.4 dB is obtained for U_∞ =20 m/s and ΔP =290 mbar, which compared to the literature is a very good result as shown in the following. Furthermore, the harmonics are completely damped by the quasi-steady jets for ΔP above 250 mbar.

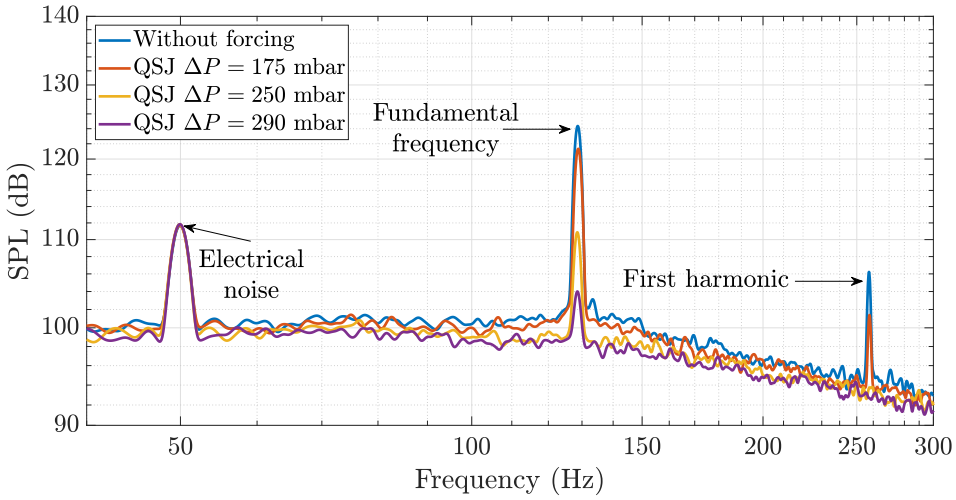

Figure 4.11: Flow spectra for U_∞ =20 m/s and different driving pressure generating quasi-steady jets.

When the freestream velocity is increased to 30 m/s, the quasi-steady jets still affect the cavity dynamics and reduce the cavity fundamental frequency amplitude. However, the reduction is less important with a higher U_∞, than the reduction obtained with U_∞ =20 m/s. As shown in Figure 4.12a, a maximum reduction in the cavity fundamental SPL of 12.6 dB is reached for ΔP =290 mbar, which is still a satisfying result compared to literature. Nevertheless, the cavity harmonics are completely damped by the quasi-steady jets for driving pressures above 250 mbar.

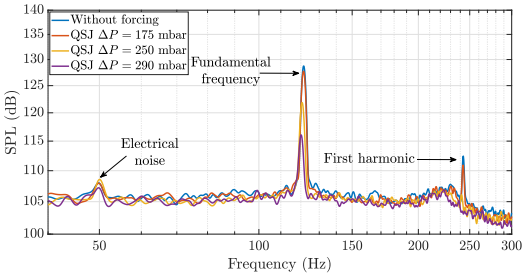

(a) Spectrum for U_∞ =30 m/s.

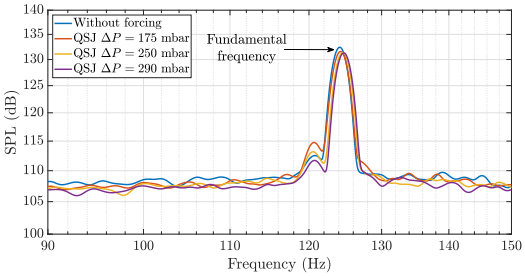

(b) Spectrum for U_∞ =34 m/s.

Figure 4.12: Flow spectra for U_∞ =30 m/s (a) and U_∞ =34 m/s (b) for different driving pressure generating quasi-steady jets.

The reduction of the quasi-steady jets effects is further observed considering a freestream velocity of U_∞ =34 m/s, as presented in Figure 4.12b. Quasi-steady jets do not impact the cavity dynamics anymore, as the cavity fundamental frequency amplitude is constant for the entire set of driving pressures tested. The harmonics are not damped anymore by the quasi-steady jets.
From these different measurements with different freestream velocities, the decrease in amplitude of the cavity fundamental frequency peak was computed. Figure 4.13 sums up the effect of the quasi-steady jets on the cavity fundamental SPL. The amplitude reduction observed can be explained by the interaction of the jets with the shear layer developing over the cavity. The 45° inclined jets might deflect the shear layer to the top, mitigating its interaction with the downstream corner. Effects of the quasi-steady jets on the cavity fundamental frequency is dependent on both the microvalves driving pressure ΔP and on the freestream velocity U_∞. For a fixed value of U_∞, the higher ΔP is, the more effect quasi-steady jets have on the cavity fundamental resonant frequency. In addition, for a fixed value of ΔP, the higher the freestream velocity U_∞ is, the less effect microvalves have on the cavity resonant frequency. From these first measurements it is possible to observe the actuators authority limit on the flow dynamics.

4.3.2 Evaluation of the MMMS microvalves control efficiency

In order to compare results obtained with the quasi-steady jets to those obtained in passed similar studies, the blowing coefficient B_c, firstly proposed by Vakili and Gauthier [139] for rectangular cavities is calculated. This coefficient is defined as the mass flow rate of the actuator normalized by a typical mass flow rate of the cavity, where ρ_∞ denotes the freestream density and $A_{cavity} = LW_1$:

$$B_c = \frac{\dot{m}_{inj}}{\rho_\infty U_\infty A_{cavity}}. \tag{4.2}$$

The results obtained for U_∞ =20 m/s and ΔP =290 mbar are compared in Figure 4.14 to results from different open-loop control studies of a cavity flow. This chart presents the distribution of B_c in % against the SPL reduction in dB.

Depending on the study-cases and the actuators technology used, different SPL reduction in the cavity oscillation were obtained. In the present study, measurements are realized on

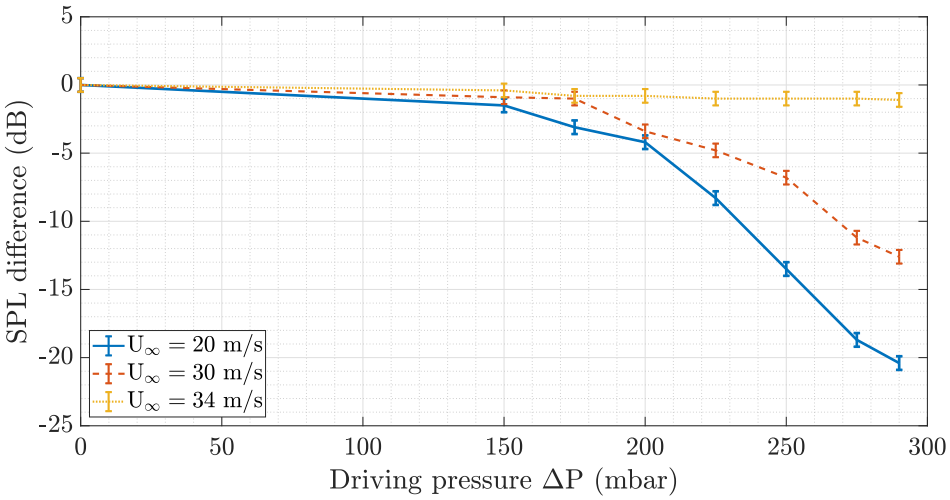

Figure 4.13: Evolution of the fundamental frequency SPL (dB) difference without and with the quasi-steady jets against the actuators driving pressure for different velocities.

an open-cavity of very deep aspect ratio $L/D = 0.15$ and for Mach numbers M varying between 0.06 and 0.1. Results presented in Figure 4.14 were performed on cavities with different aspect ratio, Re_θ and Mach number, implying different flow dynamics. Shaw [46] considered an open-cavity such that $L/D = 6.5$ with M ranging from 0.6 up to 1.05. The control was performed with pulsed jets integrated to the upstream cavity border. The study case presented by Vakili and Gauthier [139] was such that $M = 1.8$ and for a cavity characterized by $L/D = 2.54$. Momentum was added to the flow through perforated plates placed upstream the cavity. This results in modified boundary layer properties affecting the cavity oscillations amplitudes. Stanek et al. [141] used 4 high frequency fluidic actuators to control the flow over a cavity of aspect ratio $L/D = 5$ with M varying between 0.4 and 1.35. Raman and Raghu [183] studied a cavity of length to depth ratio of 6 with Mach flows ranging between 0.4 and 0.7. They performed control experiments with sweeping jets benefiting from the coanda effect placed on the bottom floor of the cavity near the upstream and downstream edges. Bueno et al. [184] focused on a cavity for which L/D was varied between 5 and 9 with a freestream Mach number of 2. Their actuators were commercialized high speed valves (General Valve Series 9) pressurized up to 11 bar. Due to the actuators size, a staggered configuration was employed to integrate the valves to the experimental setup. Zhuang et al. [185] studied a cavity of length to depth ratio of 5.16 with a flow Mach number of 2. The actuators employed simply consist of micro-holes of 400 μm diameter supplied with a pressurized source of nitrogen. On their side, Ukeiley et al. [140] considered a cavity of length to depth ratio of 5.6 or 9 with Mach numbers of 0.6 and 0.75 and the control was performed with powered whistles. In Figure 4.14, low B_c coefficients correspond to low energy consumption control systems, while efficient controllers are represented on this chart with a high SPL reduction value. Therefore, it can be observed that the microvalves provide a satisfying compromise between efficiency and energy cost compared to the other studies.

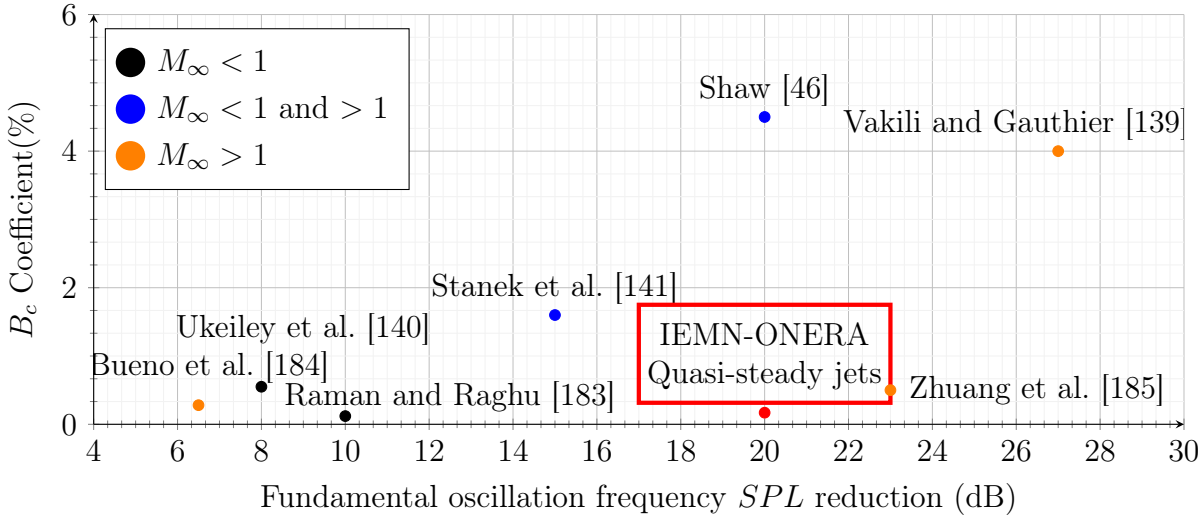

Figure 4.14: Evolution of the B_c coefficient against the fundamental resonant frequency SPL (dB) reduction for different studies and actuation technologies.

4.4 Implementation of harmonic forcings on the open-cavity flow

After characterizing the effects of quasi-steady jets on the cavity dynamics, effects of pulsed jets are investigated for actuation frequencies in the resonant and non resonant cases.

4.4.1 Theoretical framework of harmonic forcing

Sipp [186] proposed a theoretical description and numerical simulations regarding the open-loop control of an open-cavity flow with harmonic forcings. As discussed in the article, the two-dimensional laminar open-cavity flow considered responds to harmonic forcings the same way a forced Van der Pol oscillator does. Based on this, Sipp extended the nonlinear Stuart-Landau equation governing the amplitude of the open-cavity global mode to take into account the effect of harmonic forcings. Another way of reliably replicates the open-cavity flow subject to harmonic forcing, as this is the case in this study, is to directly solve the forced Van der Pol equation as proposed by Li and Juniper [187], who considered the case of a self-excited jet.

The forced Van der Pol equation can be written as:

$$\ddot{z} - \epsilon\omega_0(1 - z^2)\dot{z} + \omega_0^2 z = \omega_0^2 B \sin(\omega_f t) \tag{4.3}$$

In Equation (4.3) z refers to the dynamical variable while ω_0, ω_f, B and ϵ respectively stand for the system oscillating angular frequency, the forcing angular frequency, the forcing amplitude and the feedback parameter defining the degree of nonlinearity.

Given harmonic forcings are implemented for $U_\infty = 20$ m/s, the flow regime considered is periodic and defined by a fundamental resonant frequency $f_0 = 128.6$ Hz. To retrieve ϵ

from the experimental data, a parallel is drown between Equation (4.3) and the differential equation of a damped oscillator defined in Equation (4.4):

$$\ddot{z} + \frac{\omega_0}{Q}\dot{z} + \omega_0^2 z = \omega_0^2 B \sin(\omega_f t) \tag{4.4}$$

The open-cavity quality factor Q, defined as the ratio between the resonant frequency and the bandwith at -3 dB, is therefore linked to ϵ according to: $\epsilon = 1/Q$. Based on the measurements presented in Figure 2.7, $Q = 71$ yielding $\epsilon = 1.4 \times 10^{-2}$. Equation (4.3) is then solved through Matlab/Simulink for harmonic forcings in both the resonant and non-resonant cases. Similarly to the experiments, time series obtained from the numerical resolution are post-processed through a Welch algorithm with Hamming windows and 50% overlap. Spectra derived from the time series are presented in the following sections and compared with the experimental results.

4.4.2 Locking phenomenon in the open-cavity flow

The locking phenomenon is experimentally investigated for harmonic forcings with frequencies varied between 126 Hz and 132 Hz by step of 0.2 Hz. Different forcing amplitudes $(\Delta P, A)$ are implemented such that the capture bandwith dependency with the forcing amplitude can be investigated.

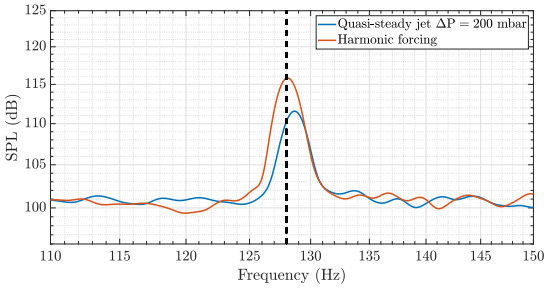

(a) Forcing frequency of 128 Hz.

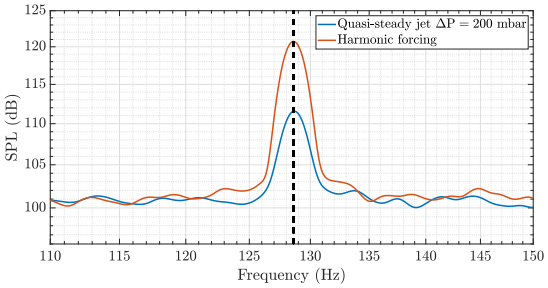

(b) Forcing frequency of 128.6 Hz.

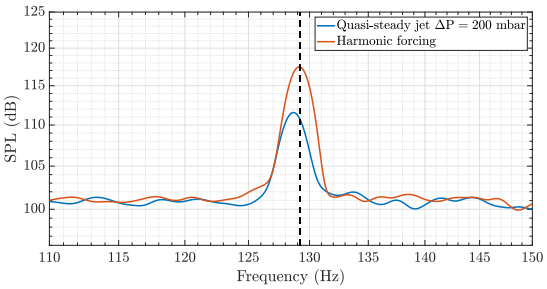

(c) Forcing frequency of 129.2 Hz.

Figure 4.15: Illustration of the locking phenomenon for $\Delta P = 200\ mbar$, $A = 1\ V$ for f_f= 128 Hz (a), f_f=128.6 Hz (b) and f_f=129.2 Hz (c).

Considering the case of harmonic forcings with ΔP =200 mbar and A =1 V, Figure 4.15 presents the spectra for forcing frequencies of 128 Hz, 128.6 Hz and 129.2 Hz. These forcing frequencies are outlined by the black dashed line. In the two first cases the cavity resonant frequency is attracted towards the actuators forcing frequency, as expected based on the

Van der Pol oscillator analogy. For an harmonic forcing at the cavity resonant frequency, the resonance is amplified as highlighted in Figure 4.15b. Spectra inferred on the Van der Pol equation are presented in Figure 4.16 for the same forcing frequencies and $B = 1$.

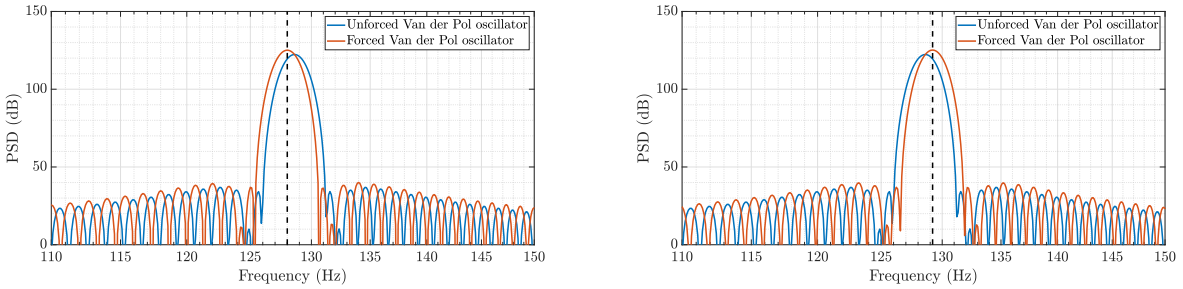

(a) Forcing frequency of 128 Hz. (b) Forcing frequency of 129.2 Hz.

Figure 4.16: Spectra of the forced Van der Pol $\dot{z}$ solution for a forcing frequencies of 128 Hz (a) and 129.2 Hz (b).

Then, harmonic forcings with frequencies more distant from the cavity resonant one are implemented. Figure 4.17 illustrates this case for forcing frequencies of 126.4 Hz and 131 Hz. Spectra derived from the experimental results are presented in Figures 4.17a and 4.17b while those obtained from the forced Van der Pol numerical computation are depicted in Figures 4.17c and 4.17d. As observed, for forcing frequencies outside of the capture bandwith both the resonance and the forcing superimpose in the spectra. These forcings are on the edge of the resonant case.

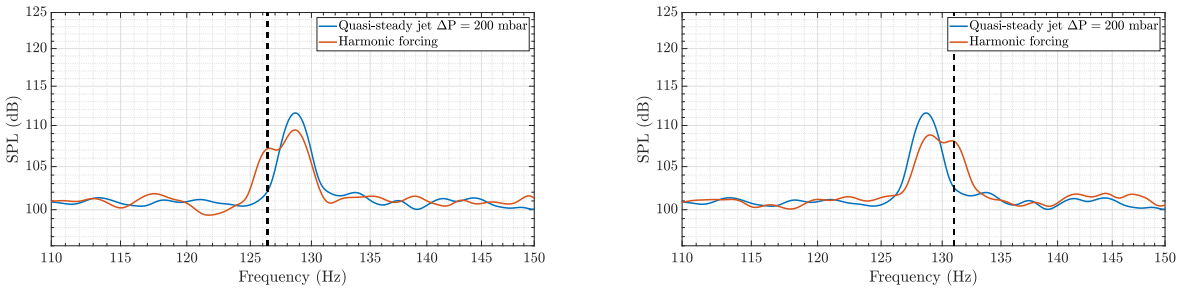

(a) Forcing frequency of 126.4 Hz. (b) Forcing frequency of 131 Hz.

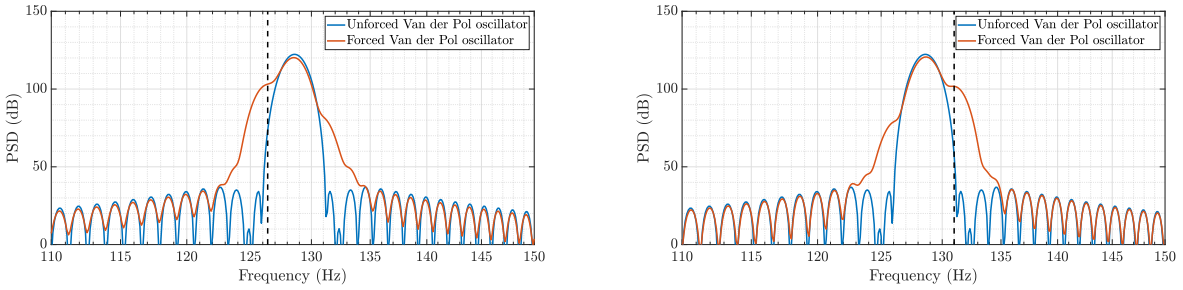

(c) Forcing frequency of 126.4 Hz. (d) Forcing frequency of 131 Hz.

Figure 4.17: Harmonic forcings outside of the locking capture bandwith for the open cavity flow with ΔP =200 mbar, A =1 V, f_f=126.4 Hz and f_f=131 Hz (a,b) and for the forced Van der Pol oscillator with the same forcing frequencies and $B = 1$ (c,d).

Based on the spectra analysis, the capture bandwith of the locking phenomenon for ΔP =200 mbar and A =1 V extends from 128 Hz up to 129.6 Hz. Figure 4.18 represents the evolution of the cavity resonant frequency against the forcing frequency for ΔP = 200 mbar and two electrical signals amplitude A =1 V and A =2 V. The capture bandwith for both forcing amplitudes considered is highlighted by the vertical dashed lines. This bandwith is of 1.6 Hz and 4 Hz respectively for A =1 V and A =2 V. The locking bandwith dependency with the forcing amplitude is experimentally retrieved, as expected and presented by Sipp [186]. Furthermore, it is well-defined in the case of A =2 V between 127 Hz and 131 Hz. Considering A = 1 V, for forcing frequencies between 127 Hz and 128 Hz the resonant frequency is shifted towards the forcing frequency but does not match it. This observation is also valid for forcing frequencies between 129.6 Hz and 130.6 Hz. For forcing frequencies above 130.6 Hz the cavity spectrum is composed of the resonant frequency shifted to 129 Hz and of the forcing frequency, as observed in Figure 4.17b.

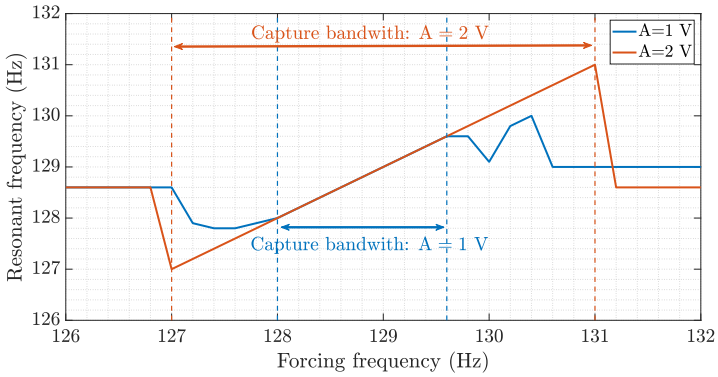

Figure 4.18: Evolution of the cavity resonant frequency against the forcing frequency for U_∞ =20 m/s, ΔP =200 mbar and several amplitudes.

Similar measurements are performed for ΔP =250 mbar and ΔP =290 mbar and are presented in Figure 4.19. As observed for ΔP =200 mbar, the higher A is, the larger the capture bandwith is. For ΔP =250 mbar (respectively ΔP =290 mbar) and A =1 V the capture bandwith spreads over 2.6 Hz (respectively 3 Hz) , while for A= 2V it spreads over 4.4 Hz (respectively 4.2 Hz). The actuators driving pressure does not seem to have an effect on the locking bandwith. Indeed, when ΔP is increased, it only further reduces the cavity resonance amplitude without completely damping it.

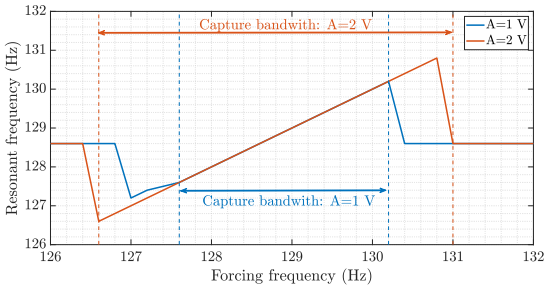

(a) ΔP = 250 mbar.

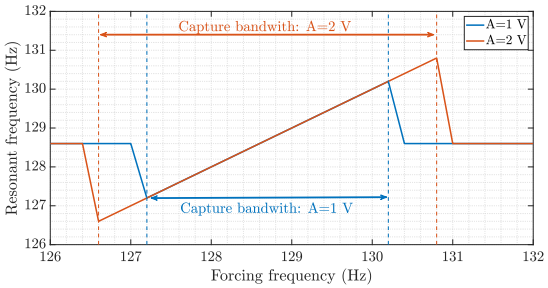

(b) ΔP = 290 mbar.

Figure 4.19: Evolution of the cavity resonant frequency against the forcing frequency for U_∞ =20 m/s, ΔP =250 mbar (a) and ΔP =290 mbar (b).

4.4.3 Harmonic forcings in the non resonant case

Resolution of the forced Van der Pol equation in the non resonant case indicates that the forcing frequency superimposes with the oscillator proper mode without interfering with it. On the contrary, Sipp [186] demonstrated on the open-cavity case that, depending on the forcing amplitude and frequency, in the non-resonant case, the forcing could damp the flow proper mode. Moreover, the Van der Pol oscillator responds to all frequencies used for the harmonic forcings, while it is not the case for the open-cavity regarding the experimental data. The non-resonant case therefore shows the limit of the analogy between the forced Van der Pol oscillator with the harmonically forced open-cavity flow. Figure 4.20 depicts the forcing cases for $f_f = 80$ Hz, $f_f = 160$ Hz and $B = 1$.

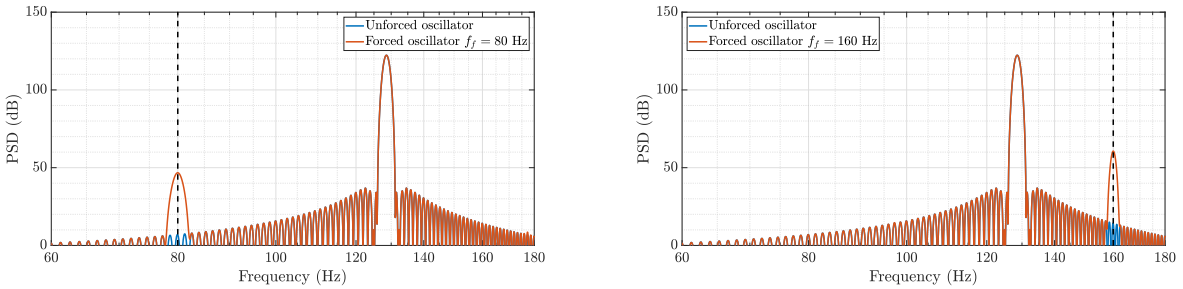

(a) Forcing frequency of 80 Hz.

(b) Forcing frequency of 160 Hz.

Figure 4.20: Spectra of the forced Van der Pol $\dot{z}$ solution for forcing frequencies of 80 Hz (a) and 160 Hz (b).

In the non-resonant case, microvalves are driven with several conditions recalled in Table 4.2. In the following open-cavity spectra, results are shown for forcing amplitudes of $A = 1$ V and $A = 2$ V for the sake of clarity.

Table 4.2: Sets of parameters used for the study of pulsed jets effects.

ΔP (mbar)	200, 250 290
Frequencies (Hz)	80 to 300 (step of 20 Hz)
Amplitudes (V)	0.5 V, 1 V, 1.5 V 2 V

As previously explained, pulsed jets modulate the velocity about a mean value fixed by the driving pressure ΔP. We therefore expect, with the pulsed jets, at least the same amplitude reduction at the fundamental frequency than the one obtained with the quasi-steady jets. In Figure 4.21b, cavity spectra for U_∞ =20 m/s are compared for quasi-steady jets and pulsed jets with a driving pressure of ΔP =250 mbar. The unsteady forcing highlighted in this Figure is characterized by a frequency of 160 Hz. Two phenomena can be observed. Firstly, a peak at the pulsating frequency appears in the spectrum, which SPL depends on the forcing amplitude and on the actuation frequency. For a frequency of 160 Hz and an amplitude of $A = 1$ V, the SPL reaches 102.8 dB, while for A =2 V the SPL reaches 107.7 dB, yielding a difference of 4.9 dB between the two cases, instead of 6dB in the linear case. Secondly, a further reduction in the cavity fundamental frequency amplitude of 3.5 dB is observed due to the pulsed jets. This second observation varies with the forcing frequency and also with the

forcing amplitude as presented in Figure 4.21a, for which the cavity fundamental frequency amplitude is reduced of 3 to 5 dB respectively for $A = 2$ V and $A = 1$ V. The way the open-cavity responds to pulsed jets for f_f =140 Hz or f_f =160 Hz spreads over a bandwith of 160 Hz starting at 120 Hz and ending at 280 Hz. Outside this range, the open-cavity flow is insensitive to the open-loop harmonic forcings induced with the microvalves. Therefore, the open-cavity flow behaves similarly to a band-pass filter, as observed in Leclercq et al. [21].

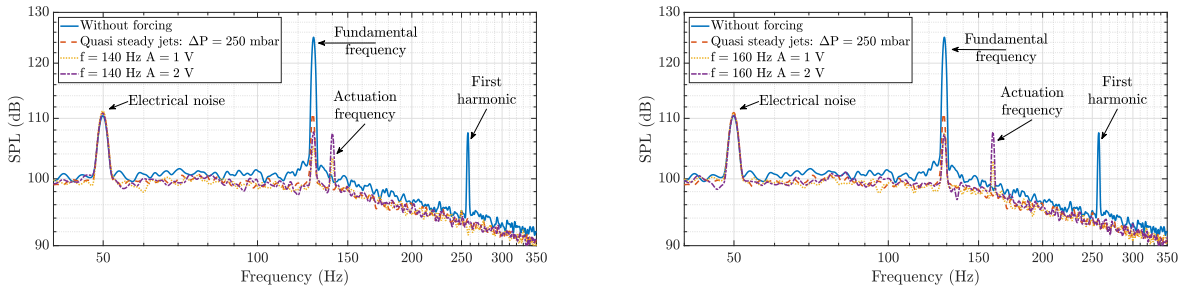

(a) Forcing frequency of 140 Hz. (b) Forcing frequency of 160 Hz.

Figure 4.21: SPL (dB) spectra comparison with U_∞ =20 m/s for a quasi-steady jets case and two different pulsed jets cases: 140 Hz (a) and 160 Hz (b).

Figure 4.22 illustrates this behavior for forcing frequencies $f_f = 100$ Hz and $f_f = 300$ Hz. For both cases, the forcing frequency does not appear in the cavity spectrum, even though the cavity resonant frequency amplitude is further damped by a few dB. In Figure 4.22b, further peaks appear at 150 Hz, 250 Hz and 350 Hz. However, these peaks are due to electrical noise originating from a power supply added in the wind tunnel room during the experiments. These peaks can therefore be ignored. Effects of the pulsed jets on the open-cavity resonance amplitude are summed up in Figure 4.23 for all the tested frequencies, amplitudes and for ΔP =250 mbar.

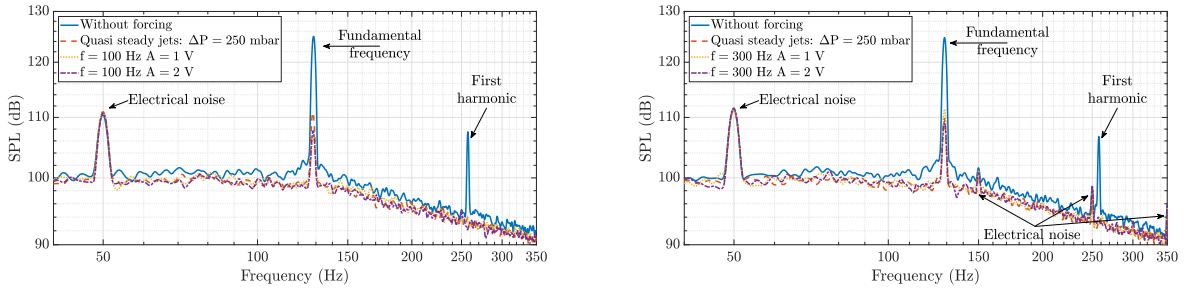

(a) Forcing frequency of 100 Hz. (b) Forcing frequency of 300 Hz.

Figure 4.22: SPL (dB) spectra comparison with U_∞ =20 m/s for a quasi-steady jets case and two different pulsed jets cases: $f_f = 100$ Hz (a) and f_f =300 Hz (b).

As observed in the previous spectra, the further reduction in the open-cavity resonance depends on the forcing frequency and on the forcing amplitudes. This non linear phenomenon characterizes a part of the pulsed jet effects. Most important is the flow dynamics response

at the forcing frequency considered. As discussed above, for forcing frequencies between f_f =120 Hz and f_f =280 Hz, the forcing frequency superimposes with the open-cavity dynamics, without triggering non-linear effects and without significantly damping the cavity resonance. Despite, pulsed jets can not be used for the open-loop control of the open-cavity flow, less power is required for the implementation of the closed-loop control.

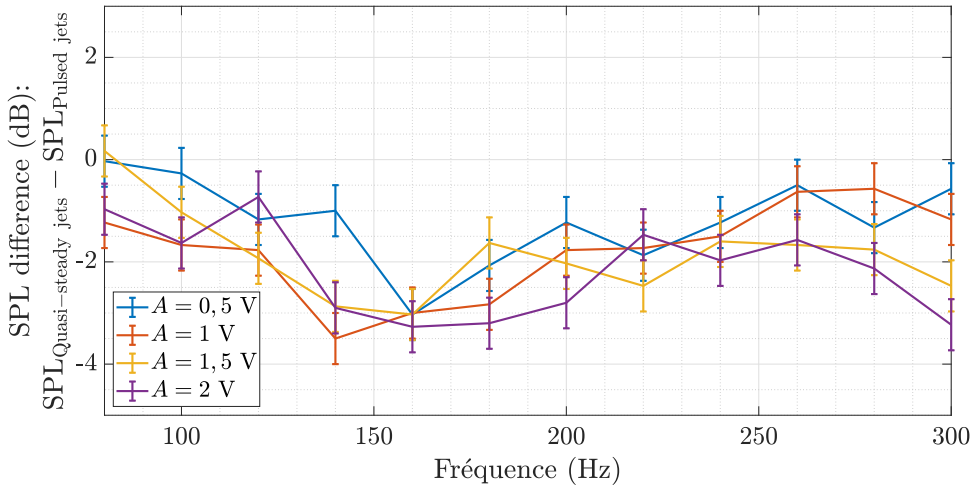

Figure 4.23: SPL (dB) difference between the forced flow with quasi steady jets ($\Delta P = 250$ mbar) fundamental resonance and the forced flow with pulsed jets.

Conclusion

Chapter 4 puts forward the use of MMMS microvalves in open-loop flow control experiments carried out on a subsonic open-cavity flow. Integrated as a linear array - with synchronized actuation as if it were a single actuator - on the open-cavity upstream edge, the microvalves jets interact with the shear layer to modify the flow dynamics.

Microvalves performances have been investigated. The flow rate/pressure characteristic has been investigated for a set of microvalves, indicating an affine evolution of the flow rate with respect to the pressure. The actuators outlet velocity was measured for both quasi-steady and pulsed jets. Considering pulsed jets, the actuators linear behavior on a large frequency band up to 370 Hz was characterized. Actuators, therefore respecting the superposition and proportionality principles of linearity, have then been integrated in the wind tunnel with the open-cavity model.
Once the experimental setup installed, first measurements were dedicated to the unforced flow characterization. Open-cavity flow for velocities between 10 m/s and 42 m/s have been investigated. Unsteady pressure measurements helped defining a range of freestream velocities at which oscillatory flow dynamics fall into the controllable bandwidth of the actuators. These velocities of 20 m/s, 30 m/s and 34 m/s constitute the flow velocities for which open-loop control experiments have been carried out.
Effects of both quasi-steady and pulsed jets have been investigated. It was demonstrated that quasi-steady jets could reduce the cavity fundamental oscillation amplitude down by 20 dB for a freestream velocity of 20 m/s and for a driving pressure of 290 mbar. For a low B_c coefficient a high reduction on the cavity fundamental frequency SPL. Regarding pulsed jets, a locking phenomenon was highlighted for harmonic forcing frequencies close to the cavity resonant frequency. It was outlined that the capture bandwith on which the cavity resonant frequency is shifted towards the actuators frequency depends on the forcing driving pressure ΔP and on the amplitude of the electrical driving signal. Nevertheless, the capture bandwidth only spreads over few Hz, showing the authority limit of the pulsed jet on the flow in open-loop experiments. Harmonic forcings with actuation frequencies away from the cavity resonant frequency were only able to further reduce the cavity resonant frequency amplitude by few dB. Effects of the pulsed jets do not enable to perform open-loop flow control experiments on the open-cavity flow as actuators do not show enough authority to trigger non-linearities in the flow, such that these non-linearities have effects on the flow dynamics fundamental frequency.

However, the actuators may be efficient during closed-loop control experiments as less power is required to control the flow, as the oscillatory flow dynamics fall into the controllable bandwith of the actuators and as the actuators can be driven with any type of signals. Chapter 5 provides details on the implementation of the closed-loop control of the open-cavity flow with the MMMS microvalves.

Chapter 5

Study of the closed-loop control of an open-cavity flow with linear controllers

Introduction

Chapter 4 demonstrated the ability of MMMS microvalves to damp a subsonic open-cavity flow oscillations based on the use of the quasi-steady jets but effects of the pulsed jets do not enable to perform open-loop flow control experiments. Nevertheless, as the oscillatory flow dynamics fall into the controllable bandwith of the actuators and as the actuators can be driven with any type of signals, authority of the actuators on the flow in closed-loop may be sufficient as less power is required than in open-loop. Chapter 5 aims at implementing the closed-loop control of the open-cavity flow. The application of closed-loop control is based on the identification of a transfer function and on the synthesis of a linear controller, which output signal command can be fed to the array of actuators. Indeed, the microvalves command flexibility enables the array of actuators to be directly driven by the controller output, unlike ON/OFF Festo valves which require the implementation of a PWM (Pulsed Width Modulation).

To complete the aim of closed-loop control, the first part of this chapter focuses on the identification of a transfer function between the actuators command and the selected Kulite sensor output. It is firstly tried to define the transfer function for the oscillating open-cavity flow, as the notion of transfer function is only clearly defined for LTI plants. The frequential data for the identification of the transfer function are gathered based on the use of pulsed jets generated by the microvalves. The second part provides details on the identification of a state-space model from the frequential data, later used to design a linear controller. Using a H_∞ loop-shaping synthesis, an optimized controller is derived. The third part of this chapter discusses the application of the closed-loop control strategy on the flow and specifies the controller effects on the flow dynamics.

5.1 Identification of a transfer function between the microvalves and the pressure sensors

The closed-loop control implementation of the open-cavity flow can be sketched as presented in Figure 5.1. Variables $d(t)$, $y(t)$ and $u(t)$ respectively denote the input disturbances, the unsteady pressure measurements and the command signal to the microvalves determined by the controller. $\langle\hat{H}\rangle(s)$ stands for the open-cavity transfer function, while $K(s)$ refers to the controller and $W_{\hat{H}S}$, W_S and W_K respectively designate the weighting functions involved in structured H_∞ loop-shaping approach. The first step for the closed-loop control of the open-cavity flow consists in the identification of $\langle\hat{H}\rangle(s)$, which determines the following steps of the controller design and implementation.

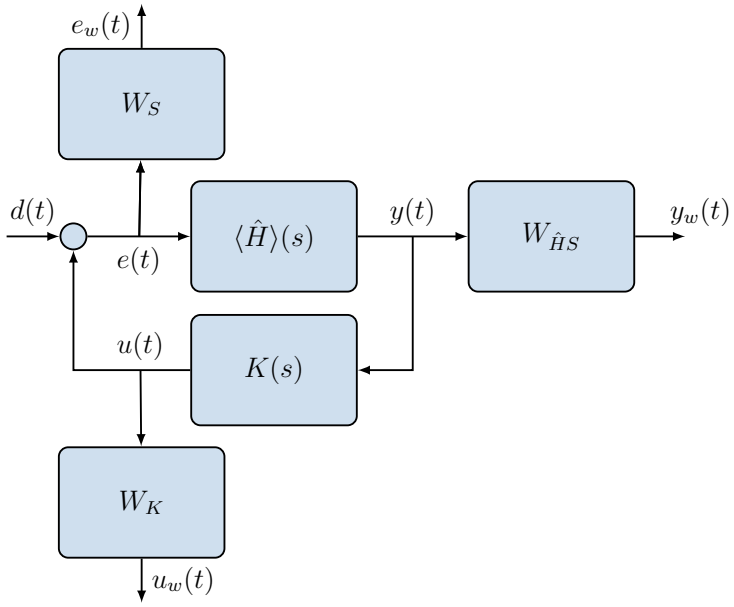

Figure 5.1: Closed-loop scheme of the control design synthesis in the open-cavity.

5.1.1 Definition of a transfer function for the open-cavity

As discussed by Leclercq and Sipp [38], the linear response of unsteady flows to a given external forcing $\mathbf{f}(t)$ is not unique, as infinitesimal perturbations interact with a *time-evolving* base flow. Therefore, it is necessary to justify the existence of a transfer function for a time-varying plant such as the open-cavity oscillatory flow of the present work. To highlight the time-evolving aspect of the considered open-cavity flow regime, the Probability Density Function (PDF) based on the pressure measurements is computed and presented in Figure 5.2. The PDF is composed of two peaks indicating that the system is in a limit cycle, as discussed by Rowley et al. [188]. As sketched in Figure 5.3, three options exist in the literature for the definition of the transfer function, in the situation where the time-invariance hypothesis is violated. In this Figure, $\mathbf{f}(s)$ and $\mathbf{y}(s)$ stand for the linear forcing term and for the corresponding linear system output, both in the frequency domain (s being the Laplace variable). The resolvent operator about the mean flow and the mean resolvent operator

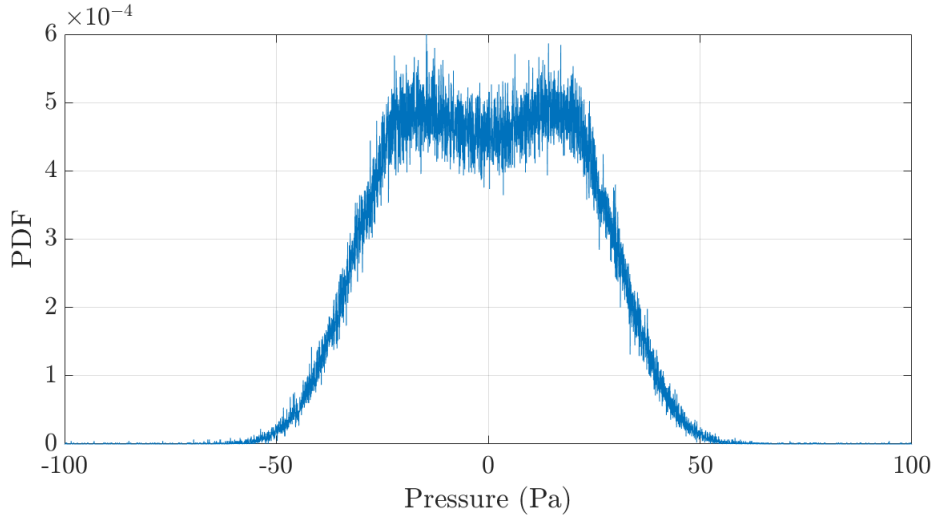

Figure 5.2: PDF of the pressure measurements for the open-cavity flow regime considered.

are respectively denoted $\mathbf{R}_{\bar{\mathbf{U}}}(s)$ and $\mathbf{R}_0(s)$ in the following. The operator $<>_{\Phi}$ defines an ensemble average with respect to Φ, the phase of the limit cycle at the time when forcing is initiated. More precisely, $\phi = \omega_0 \tau_0 \pmod{2\pi}$, where ω_0 is the fundamental frequency of oscillation of the unforced flow and τ_0 is the instant when forcing is started. This time is defined relative to an arbitrary origin of time $\tau = 0$ where the flow is already oscillating in a periodic fashion (i.e. the dynamics is already post-transient).

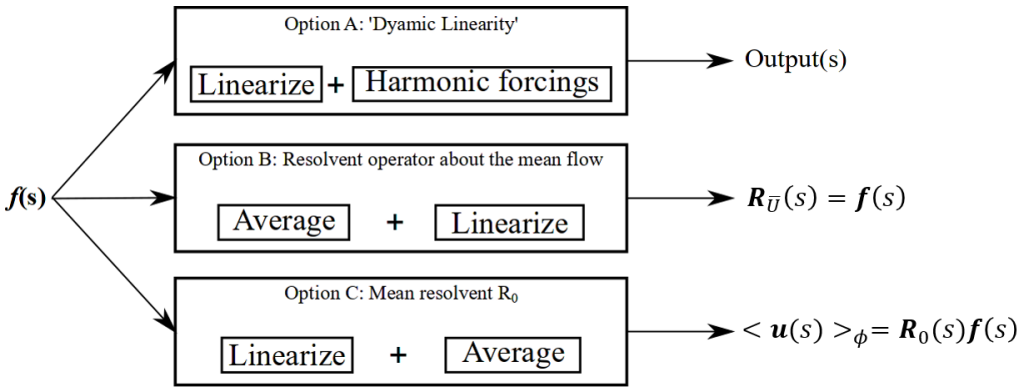

Figure 5.3: Options for the definition of a transfer function in the case of a time varying system (from [38]).

Option A, referred as "Dynamic linearity" by Dahan et al. [37], consists in the use of harmonic forcings for the identification of transfer functions. Small amplitude forcing ensuring a linear response of the considered flow, a frequency response can be built by computing the ratio between the complex amplitudes of the output and input at the forcing frequency. This method hints at the existence of transfer functions in the case of time-varying plants, because the computed ratio does not appear to depend on the phase ϕ, as later pointed out by Leclercq et al. [21].

Option B is based on the use of the resolvent operator about the mean flow $\mathbf{R}_{\bar{\mathbf{U}}}(s)$. The resolvent operator is derived from the linearized Navier–Stokes equations about the mean

flow **U**. The input-output model yielded by this method has been used in the context of closed-loop control of open-cavity flow by Leclercq et al. [21]. However, as stated by the authors themselves, the reason for the relevance of the resolvent operator about the mean flow is not clearly understood.

Option C uses the mean resolvent operator $\mathbf{R}_0(s)$, assuming again linear response to infinitesimal forcing. The mean resolvent operator $\mathbf{R}_0$ is defined according to the following equation:

$$< \mathbf{y}(s) >_{\Phi} = \mathbf{R}_0(s)\mathbf{f}(s), \tag{5.1}$$

as the operator predicting, in the frequency domain, the mean (with respect to ϕ) linear response to any forcing. It is therefore, by definition, the statistically optimal time-invariant approximation of the linear time-varying dynamics. It was shown in [38] that the resolvent operator about the mean flow is a finite-order approximation of $\mathbf{R}_0$ when unsteadiness is small. The mean resolvent, on the other hand, has an infinite number of poles, as it is related to the Koopman operator (averaged with respect to ϕ). It was also shown that using harmonic forcings always leads to the same response, regardless of the phase ϕ, and this response is predicted by the mean resolvent $\mathbf{R}_0$. This property, called "dynamic linearity" by Dahan et al. [37], is specific to harmonic forcings. However, for frequency-rich inputs, the output signal $y(s)$ obtained by performing a Laplace transform of the timeseries $y(t)$ is phase-dependent. Therefore, in order for the time-invariant approximation of the linear input-output dynamics to be valid, one needs to check that the variance of the output signal $y(s;\phi)$ is indeed small with respect to the module of the mean $\langle y(s)\rangle_\phi$, predicted by the mean resolvent.

Instead of characterizing this variance-to-mean ratio globally, it is quantified for the specific scalar input u and output y of our control problem. We can introduce time-invariant actuator and measurement fields $\mathbf{B}$ and $\mathbf{C}$ such that $\mathbf{u} = \mathbf{B}u(t)$ and $y(t) = \mathbf{C}^T\mathbf{y}$ in discretized form. For any given input signal $u(t)$ and frequency s Leclercq and Sipp [38] defines the ratio $\eta(s,u) = Var_\phi y/|\langle y\rangle_\phi|$. At any given complex frequency s, the time-invariant approximation is valid if $\eta << 1$ for any input signal f. Harmonic inputs at the frequency $s = i\omega$ are a very specific case of input for which $\eta = 0$, at the forcing frequency.

The mean transfer function $\langle\hat{H}\rangle_\phi = \langle y(s)\rangle_\phi / f(s)$ between f and y is related to the mean resolvent operator through $\hat{H} = \mathbf{C}^T\mathbf{R}_0\mathbf{B}$. The ratio η can also be used to characterize the convergence of the mean estimate $\langle\hat{H}\rangle_{\phi,N_s}$ to the true mean $\langle\hat{H}\rangle_\phi$ from N_s samples (i.e. N_s linear responses to the same forcing signal $f(t)$ at different phases $0 \leq \phi < 2\pi$).

In the following, the identification of the mean transfer function $\langle\hat{H}\rangle$ is performed on the open-cavity flow for a periodic flow regime with small-amplitude forcings of different types. For all exciting signals tested, the frequency responses are computed based on the Matlab tfestimate routine, presented in Section 3.2.

5.1.2 Transfer function identification based on harmonic forcings

Important note: Flow control experiments on the open-cavity have been divided into two different test campaigns: a first one focused on the open-loop control of the flow and a second one dedicated to the closed-loop control implementation. Previous results regarding the flow dynamics characterization have been obtained during the first test campaign. The following measurements, performed during the second test campaign, have been acquired 6 months after the first test campaign. In-between the two tests campaigns, the open-cavity in the S19 wind tunnel had to be removed before its second installation. Therefore, at the beginning of the second test campaign, new flow characterization measurements have been carried out.

The low periodic oscillating flow dynamics considered here, corresponds to a freestream velocity of $U_\infty = 18$ m/s. The open-cavity resonance occurs at a frequency of 124 Hz, as presented in Figure 5.4.

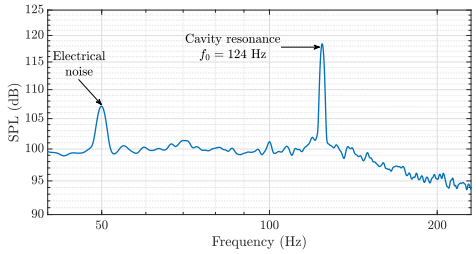

Figure 5.4: SPL (dB) flow spectrum of the open-cavity for $U_\infty = 18$ m/s.

For the first identification investigations, the microvalves are driven with $\Delta P = 120$ mbar and with a voltage amplitude $A = 2$ V, inducing a forcing to which the open-cavity responds almost linearly, as presented in Chapter 4. Frequencies of the harmonic forcings are varied between 120 Hz and 140 Hz with a step of 2 Hz. For each frequency considered, measurements are repeated five times. The acquisition of the microvalves signal $u(t)$ and the pressure signal $y(t)$ is synchronized. The transfer function is then computed by taking the ratio between the $y(s)$ and $u(s)$, yielding five frequency responses for each forcing frequency. In the following, for one forcing frequency, each response is denoted "Trial i" ($\mathrm{i} \in [\![1; 5]\!]$). Figure 5.5 presents the frequency response gain and phase for the different triplets.
For a given frequency, considering either the gain or the phase of the frequency response, a negligible variability in the results is observed, which confirms the theoretical result on dynamic linearity from Leclercq and Sipp [38]: the response to linear harmonic forcing is independent on the phase ϕ, even though the base flow is not time-invariant but periodic. The residual dispersion observed is not due to the time-varying character of the unforced flow, but to additional factors (weak non-linearity, measurement noise, etc.).

The phase-independence of the response, at the forcing frequency, to harmonic forcing, makes this input signal a suitable choice for identification of the mean transfer function. Indeed, a *single realization* suffice to identify a given frequency, and no averaging is in fact required. However, $N_\omega = O(10-100)$ are required to correctly estimate the transfer function, and repeating the process over such a large number of frequencies may be tedious. In the following, it is sought if a frequency-rich input signal containing at least N_ω frequencies, can

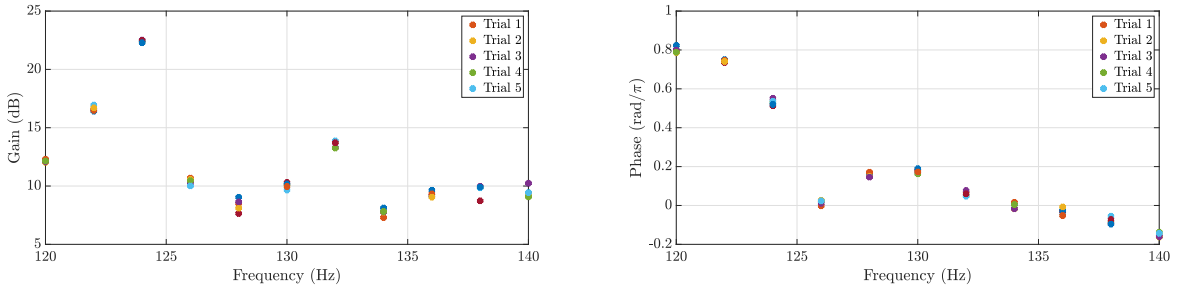

(a) Frequency response gain.

(b) Frequency response phase.

Figure 5.5: Gain and phase of the frequency response estimated from harmonic forcings for $U_\infty = 18$ m/s and for the microvalves driving conditions $\Delta P = 120$ mbar, $f_f = 120$ Hz $\rightarrow$ 140 Hz and $A = 2$ V.

be used to converge the mean transfer function from only N_s samples, with $N_s \ll N_\omega$. By evaluating the ratio η for various frequency-rich signals, we will also evaluate the validity of the time-invariant approximation of the time-varying input-output dynamics (i.e. is $\eta << 1$ for any input u and any frequency s ?).

5.1.3 Transfer function identification based on multi-frequency forcings

Linear frequency sweeps

First multi-frequency signals considered are linear frequency sweeps of duration $\Delta t = 315$ s and amplitude $A = 2$ V with a frequency varying between $f_{start} = 120$ Hz and $f_{stop} = 240$ Hz and for $\Delta P = 120$ mbar. These signals can be described by the following equation:

$$f(t) = A \sin\left(2\pi\left(f_{start} + \frac{f_{stop} - f_{start}}{\Delta t} t\right) t\right). \tag{5.2}$$

Figure 5.6 presents both the spectrograms of the input and output. The input signal is repeated 99 times such that a mean response of the cavity to the forcing is computed. The sensor spectrogram is dominated by the open-cavity resonance at 124 Hz. The cavity response to the linear frequency sweep corresponds to the straight line, which slope is induced by the actuators command.

The gain and phase of the 99 identified frequency responses are presented in Figure 5.7, alongside with the gain and phase of the average frequency response represented by the black line.

The 99 frequency responses all exhibit a resonance at the cavity natural frequency of 124 Hz. For higher frequencies, the frequency responses present the same trend. Dispersion in the gain may be due to the time-varying aspect of the system. Regarding the phase though, very little dispersion is observed. The phase linearly decreases with frequency. Considering the phase of the average frequency response based on the 99 trials, the slope is related to a delay τ associated to the advection of the flow perturbations along the cavity in the shear layer with a mean velocity κU_∞. Therefore, the relationship between τ and κ can be written as:

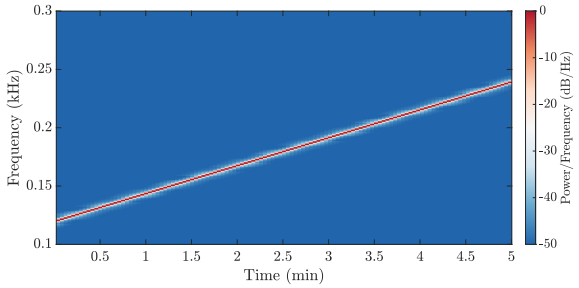

(a) Actuators command spectrogram.

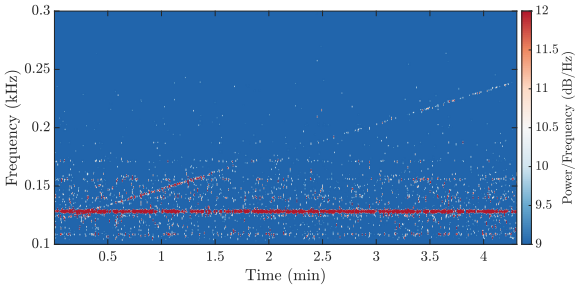

(b) Sensor output spectrogram.

Figure 5.6: Spectrograms of the actuators command (a) and sensor output (b) for a linear frequency sweep forcing.

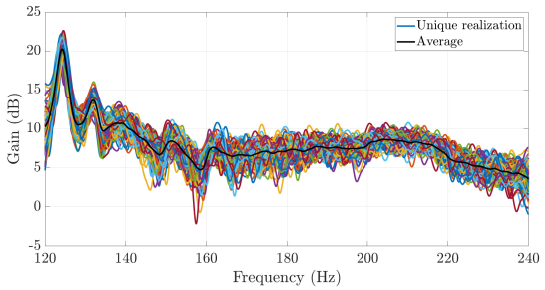

(a) Gain of the 99 frequency responses and gain of the average frequency response.

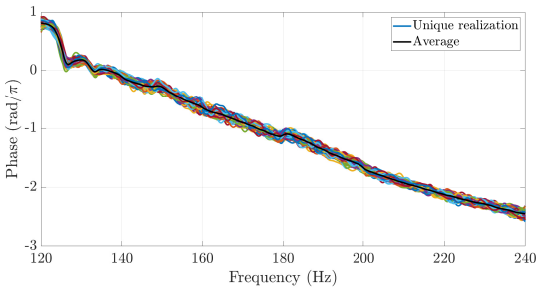

(b) Phase of the 99 frequency responses and phase of the average frequency response.

Figure 5.7: Frequency responses gain (a) and phase (b).

$$\tau = \frac{L}{\kappa U_\infty} \iff \kappa = \frac{L}{U_\infty \tau}. \tag{5.3}$$

Based on the measurements presented in Figure 5.7b, $\tau = 0.0118$ s, yielding $\kappa \approx 0.57$. Hence, the perturbations induced by the actuators are convected inside the flow with a mean velocity of $0.57U_\infty$. This result is of the same order as the one in the numerical study of Leclercq et al. [21], who proposed the numerical closed-loop control of a 2D-square open-cavity and found $\kappa = 0.73$.

The ratio η, characterizing the ratio between the standard deviation (with respect to ϕ) of the response to the module of the mean response, is computed with the linear frequency sweeps considered here for $N_s = 3$ and $N_s = 99$. Figure 5.8 compares, for the frequencies between 120 Hz and 240 Hz, the values of η for $N_s = 99$ and $N_s = 3$ realizations to 1 and $\sqrt{N_s}$. For a given frequency s, the system is nearly LTI if $\eta \ll 1$ for any type of input u. As explained in [38], the ratio η also helps evaluating the convergence of the mean estimate $\langle \hat{H} \rangle_{\phi,N_s}$ to the true mean $\langle \hat{H} \rangle_\phi$, based on the use of N_s realizations. The convergence criterion can therefore be expressed as $\eta \ll \sqrt{N_s}$. In Figure 5.8a for $N_s = 99$, the blue curve is well-below the red threshold of convergence of the estimate of the mean transfer. This is nearly the case too for only $N_s = 3$ samples in Figure 5.8b, but there is not an order of magnitude difference between the blue and red curve for all frequencies so it is estimated that 10 samples are

required to reach satisfactory convergence. By examining the position of the converged blue

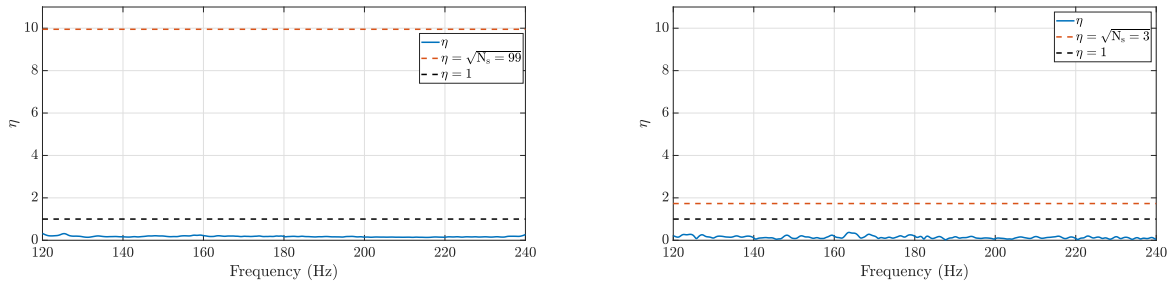

(a) η for 99 realizations. (b) η for 3 realizations.

Figure 5.8: Ratio η for the linear frequency sweep between 120 Hz and 240 Hz for 99 realizations (a) and 3 realizations (b). The black dashed line stands for the threshold $\eta = 1$ and the red line stands for the threshold $\eta = \sqrt{N_s}$.

curve with respect to the black threshold $\eta = 1$, it is noticed that the standard deviation is well-below the module of the mean transfer at all frequencies (although not an order of magnitude difference). It is hypothesized that the variability is so low because the sweep is extremely "slow", with slow being defined as $\Delta t \times f_{min} = 315 \times 120 = 3.8 \times^4 \gg 1$. Indeed, the frequency varies at a quasi-static rate and at any given time, the flow is approximated forced by a purely harmonic input. This type of signal is therefore ideal for identification because the entire frequency range 120-240Hz may be identified using less than 10 realizations to converge the mean response to a good precision. This is indeed much more economical than using purely harmonic forcings.

PRBS

Similar measurements of frequency response are performed with PRBS signals. PRBS signals consist of a signal varying between two values in a random fashion. The considered PRBS signal is characterized by a clock period of 20 time steps, with a time step of 1 ms. Therefore, the signal value can change from 1 V (respectively -1 V) to -1 V (respectively 1 V) every 20 time steps. Figure 5.9a presents a time evolution of such a PRBS.

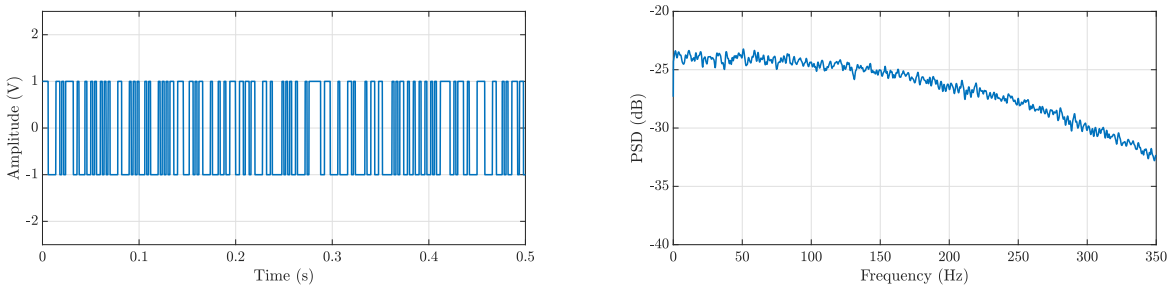

(a) PRBS against time between 0 s and 0.5 s. (b) PSD of the PRBS.

Figure 5.9: PRBS against time (a) and its PSD (b).

The entire set of computed frequency responses between 120 Hz and 240 Hz is presented in Figure 5.10a. The average frequency response (black line) is computed with $N_s = 30$.

Evolution of the quantity η against frequency for $N_s = 30$ is presented in Figure 5.10b. The blue curve is below the red threshold $\eta = \sqrt{N_s}$ but not even by an order of magnitude so the mean estimate is not quite converged yet with only 30 samples. Clearly, convergence is slower than with the slow linear sweeps. For most of the frequency range, the blue curve is not well below the black threshold, which means that the standard deviation about the mean is not negligible with respect to the mean module. These observations are not surprising according to Leclercq and Sipp [38]: indeed, greater dispersion of the response is expected for frequency-rich signals, as there are more opportunities for phase-dependent cross-frequency transfers to be excited. The fact that η is not small compared to 1 means that if the control signal u happens to be far from harmonic in closed-loop, then the input-model provided by the mean transfer function will be very poor. And the larger eta, the larger the uncertainty. We see that typically in the high-frequency range $f > 210Hz$, the model is more inaccurate and robustness to model uncertainties should therefore be enforced at such frequencies when shaping the closed-loop. Fortunately though, the input signal will never be very far from a harmonic input because the linear controller will be driven by the measurement y, which is itself nearly harmonic at all times. Therefore, the estimation of model uncertainty (due to neglected time-varying aspects) from a PRBS signal may be considered very conservative in the present case.

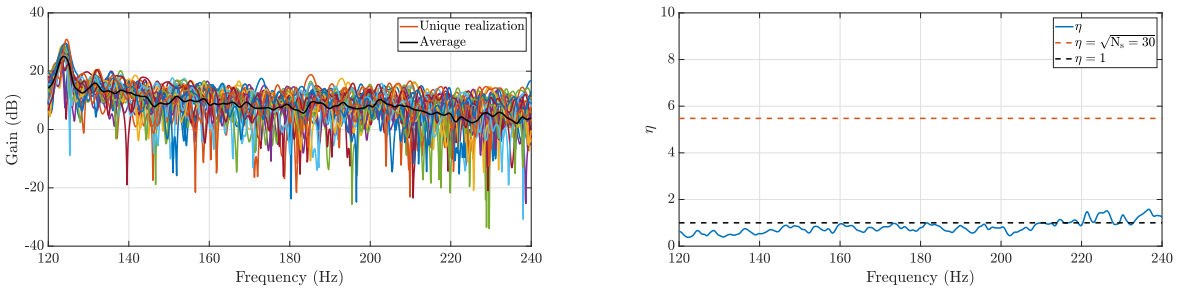

(a) Gain of the frequency responses and gain of the average frequency response for $N_s = 30$.

(b) Ratio η for the PRBS signals computed with $N_s = 30$.

Figure 5.10: Gain of the frequency responses and gain of the average frequency response for $N_s = 30$ (a) and ratio η (b).

For all the following closed-loop experiments, the identification step of a mean frequency response is performed using the repetition of 3 linear frequency sweeps and considering the average response. Robustness to high-frequency uncertainties will be enforced by choosing a strictly proper controller architecture, which gain naturally decays at high frequencies.

5.2 Design of a linear controller based on the average frequency response

The identification step presented previously yields a frequency data sets. The aim is therefore to construct a proper transfer function $\langle \hat{H} \rangle$ consisting in an approximation of the data set. Based on mean estimate of the transfer function $\langle \hat{H} \rangle$, a continuous-time linear controller K

is sought using the H_∞-norm minimization criteria and implemented in the real-time Dspace MicroLabBox controller.

5.2.1 Construction of the interpolated transfer function

The construction of the interpolated transfer function is based on the use of the Matlab routine "n4sid" estimating a discrete-time state-space model using the frequency data previously identified. In the time domain, the state space-model of order n can be described by the following system of equations:

$$\begin{cases} \dot{\hat{x}}(t) = \hat{A}\hat{x}(t) + \hat{B}f(t) \\ y(t) = \hat{C}\hat{x}(t) \end{cases} \tag{5.4}$$

where $\hat{x}(t) \in \mathbb{R}^n$ stands for the internal variables, $A \in \mathbb{R}^{n\times n}$, $B \in \mathbb{R}^{n\times 1}$ and $C \in \mathbb{R}^{n\times r}$ denote the model constant matrices. For the freestream velocity $U_\infty = 18$ m/s and $\Delta P = 120$ mbar, the considered average frequency response computed with $N_s = 3$ (based on linear frequency sweeps) is presented in Figure 5.11.

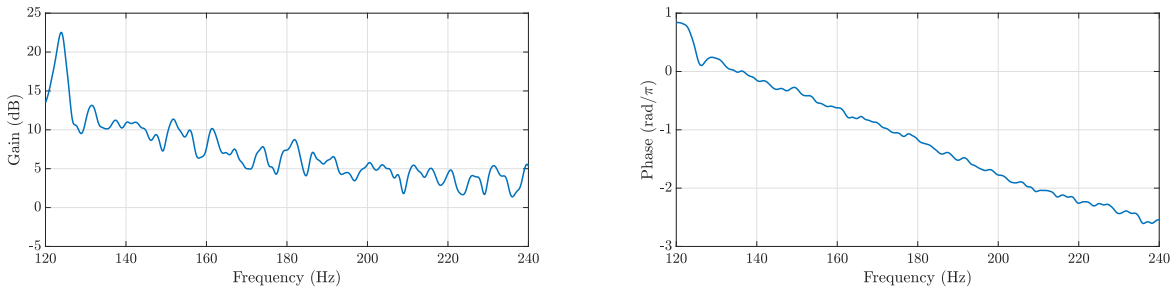

(a) Gain of the average frequency response.

(b) Phase of the average frequency response.

Figure 5.11: Average frequency response gain (a) and phase (b) for $U_\infty = 18$ m/s and $\Delta P = 120$, computed with linear frequency sweeps and $N_s = 3$.

For the purpose of the closed-loop control implementation, the most important information in the average frequency response is located around the open-cavity resonance. Therefore, it is decided before the definition of the transfer function $\langle \hat{H} \rangle$, to use a modified frequency data set. Data for frequencies between 120 Hz and 140 Hz are kept, while for frequencies above 140 Hz a moving average is applied to the elements to reduce the oscillations observed in the gain and due to the residual noise. This moving average is applied because the choice of $N_s = 3$ leads to oscillations in the almost not converged estimate of the mean transfer. Figure 5.12 compares the gain and phase of both the initial and modified data sets.
The transfer function is then computed using the "n4sid" routine and using an order $n = 7$. In Figure 5.13, the transfer function $\langle \hat{H} \rangle$ gain follows the gain trend of the average frequency response.
The phase is matched with an even greater precision. The transfer function fit is estimated at 73.3%, according to the normalized RMS error. This transfer function $\langle \hat{H} \rangle$ is then used for the synthesis of a linear controller, as presented in the following.

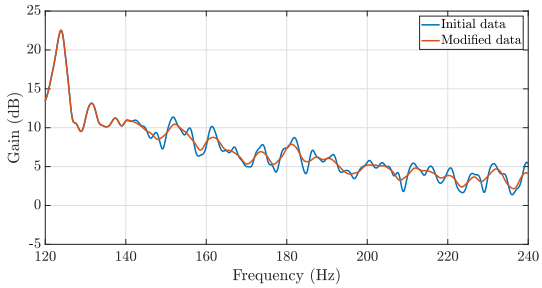

(a) Initial and modified data sets gain.

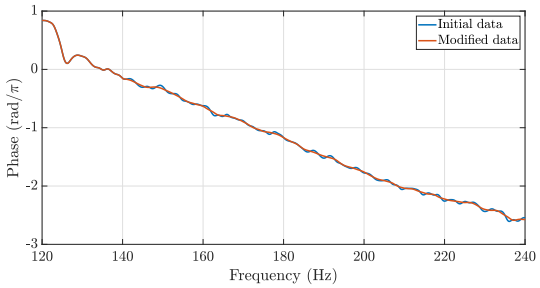

(b) Initial and modified data sets phase.

Figure 5.12: Comparison of the initial and modified data sets gain (a) and phase (b).

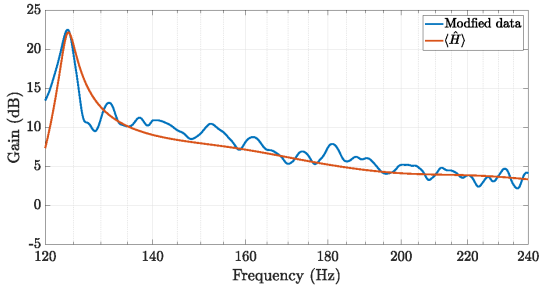

(a) Frequency response and $\langle \hat{H} \rangle$ gain.

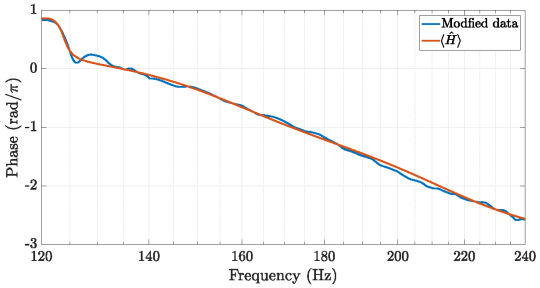

(b) Frequency response and $\langle \hat{H} \rangle$ phase.

Figure 5.13: Frequency response and transfer function gain (a) and phase (b).

5.2.2 Structured H_∞ loop-shaping synthesis for the design of a linear controller

Based on the transfer function $\langle \hat{H} \rangle$, the aim is to design a controller, which closed-loop performance is defined by the user. The design process is based on the mixed-sensitivity formulation of a H_∞ loop-shaping approach. A set of weighting functions W_S, $W_{\langle \hat{H} \rangle S}$ and W_K is defined. These functions, connected to $\langle \hat{H} \rangle$ as illustrated in Figure 5.1, constitute the basis of the control optimization process.

Considering the open-cavity system presented in Figure 5.1, four key transfer functions fully characterize the system closed-loop dynamics. The first one considered is $S(s)$, the sensitivity function, connecting the input disturbance $d(t)$ to the error $e(t)$ according to equation Equation (5.5):

$$S(s) = \frac{1}{1 - \hat{H}(s)K(s)}. \tag{5.5}$$

The second one, $\langle \hat{H} \rangle(s)S(s)$, corresponds to the system closed-loop transfer function and is defined as the ratio between the system output measurement $y(t)$ with the system input disturbance $d(t)$ in Equation (5.6):

$$\langle \hat{H} \rangle S(s) = \frac{\langle \hat{H} \rangle(s)}{1 - \langle \hat{H} \rangle(s)K(s)} \tag{5.6}$$

The previously introduced weighting functions are employed to limit undesired dynamics outside the considered frequency bandwith and to constrain the maximum gain of the characteristic transfer functions. Hence, templates are applied to the three transfer functions $S(s)$, $\langle\hat{H}\rangle S(s)$ and $K(s)$ the controller.

The H_∞ loop-shaping control design approach amounts to minimizing the cost function γ bounding the H_∞ norm of the previous four transfer functions based on the chosen weighting functions. Solved through the "hinfstruct" routine in Matlab, the controller $K(s)$ is sought, such that Equation (5.7) is satisfied and such that the internal dynamics of the system is stabilized.

$$\begin{cases} \|W_S S\|_\infty \leq \gamma \\ \|W_{\hat{H}S}\hat{H}S\|_\infty \leq \gamma \\ \|W_{KS}KS\|_\infty \leq \gamma \end{cases} \tag{5.7}$$

Shaping of the three transfer functions aims at different objectives. Shaping of the $\langle\hat{H}\rangle S$ transfer aims at attenuating the main resonance peak. Regarding the sensitivity S, the constraint guarantees the closed-loop system stability robustness with a modulus margin of 6 dB. Finally, shaping KS achieves a performance robustness of the controller to modeling errors at high frequency. Another constraint is imposed to the controller static gain $K(0)$. The aim of the closed-loop control is to reach the open-cavity base flow, which is unstable and which only exists without quasi-steady forcing. Therefore, to reach that base flow the static gain of the controller has to be canceled. If the base flow is not reached and if the controller command has a non-negligible mean value, effects of the control may be attributed to the open-loop forcing (modification of the mean outlet velocity of the microvalves) instead of the closed-loop forcing. Therefore, the condition $K(0) \ll \dfrac{\bar{V}(\Delta P)}{h_0 y_0}$ has to be observed, with $\bar{V}(\Delta P)$, h_0 and y_0 the mean outlet velocity of the microvalves, the microvalves static gain and the mean pressure measurement. It is chosen to have $K(0) = \dfrac{\bar{V}(\Delta P)}{100 \times h_0 y_0}$, yielding in dB a value of -70.2 dB.

The controller structure consists in a SISO controller with ten internal states. The first weighting function considered is $W_{\langle\hat{H}\rangle S}$ defined as a bell-shaped frequency template:

$$W_{\langle\hat{H}\rangle S}(s) = \frac{1}{\|\hat{H}\|_\infty} \frac{s^2 \ + \ 2m\omega_0 s \ + \ \omega_0^2}{\left(\dfrac{s}{\alpha}\right)^2 \ + \ 2m\omega_0 s \ + \ \left(\dfrac{\omega_0}{\alpha}\right)^2}, \tag{5.8}$$

where $\|\hat{H}\|_\infty = \max_{\omega\in\mathbb{R}} |\langle\hat{H}\rangle(i\omega)|$, as for a SISO system the infinity-norm of a stable transfer function $\langle\hat{H}\rangle$ is given by the maximum of the modulus of the frequency response. The variable ω_0 stands for the open-cavity fundamental resonant frequency. Other parameters are fixed by the user and are defined in the considered case such that: $m = 5$ and $\alpha = 2$. The second weighting function W_S is defined as a constant, $W_S(s) = 2$, and ensures the stability robustness through the modulus margin. The third weighting function W_K consists in a low pass first order filter, satisfying the constant gain constraint at low frequencies previously described.

Running the hinfstruct routine with the previous weighting functions yields $\gamma = 0.954$ after 143 iterations. Figure 5.14 presents the closed-loop controller performance. It can be observed in Figure 5.14a that the weighting function forces the controller gain to reach a minimum value of -90 dB for low frequencies below 10^{-4} Hz. Considering Figure 5.14b, the weighting function $W_{\hat{HS}}$ damps the open-loop resonance by 1.1 dB. The sensitivity function presented in Figure 5.14c lies below γ/W_S by 6 dB.

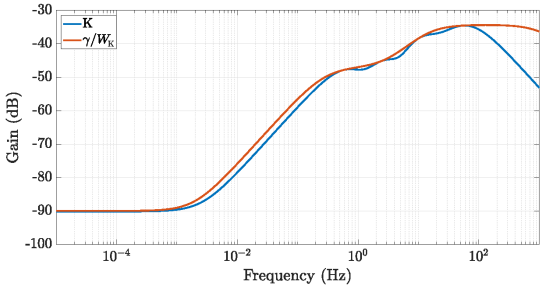

(a) Gain of the controller K.

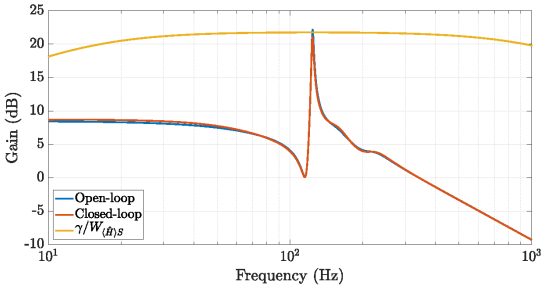

(b) Gain of the closed-loop system.

Once designed, the controller state-space matrices are implemented in the real-time controller software as described in the following.

5.2.3 Implementation of controllers in the real-time software

The closed-loop control is implemented on a Dspace MicroLabBox. Written in Matlab Simulink, the code is then interpreted in C++ and transferred to the MicroLabBox. The Kulite sensor measurements are used as inputs and the driving signal from the controller is supplied to the microvalves. Figure 5.15 shows the different Simulink blocks needed for the closed-loop application.
The "Analog-to-Digital Converter" block uses the Kulite sensor voltage as input and outputs its digital conversion $U_{Kulite}(t)$. This signal is then converted into pressure through the "Calibration" block. $P_{Kulite}(t)$ is then fed to the "Controller State-space model". The controller outputs the actuators command signal $U_{Cont}(t)$ which passes through a "Saturation"

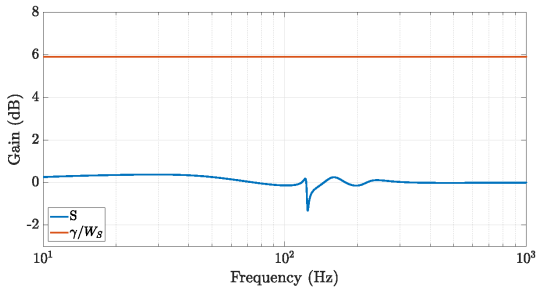

(c) Gain of the sensitivity function S.

Figure 5.14: Gains of the weighting functions used in the H_∞ loop-shaping process for $U_\infty = 18$ m/s and $\Delta P = 120$ mbar.

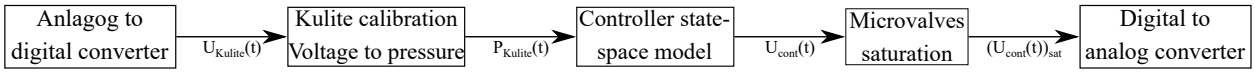

Figure 5.15: Sketch of the Simulink program used for the closed-loop implementation.

block limiting $U_{Cont}(t)$ between -2 V and 2 V, in order to protect the microvalves. Finally, $(U_{Cont}(t))_{sat}$ is converted to an analog signal through the "Digital to Analog Converter". This final output constitutes the microvalves driving signal.

5.3 Application of the closed-loop controller on the open-cavity flow

In this section, results regarding the closed-loop control of the open-cavity flow are discussed. Results obtained for the study case $U_\infty = 20$ m/s and $\Delta P = 120$ mbar are firstly presented, as they highlight the successful implementation of the control. Then, different study cases results are presented alongside with different measurements investigating the closed-loop performance (robustness, iterative application of controllers and effects of reducing the number of micro-valves used), including the previously study case on which the identification and the controller synthesis steps were described.

5.3.1 Closed-loop control application

The identified transfer function for U_∞=20 m/s and ΔP=120 mbar is presented in Figure 5.16 alongside with the frequency response data. The transfer function fit is estimated at 80%.

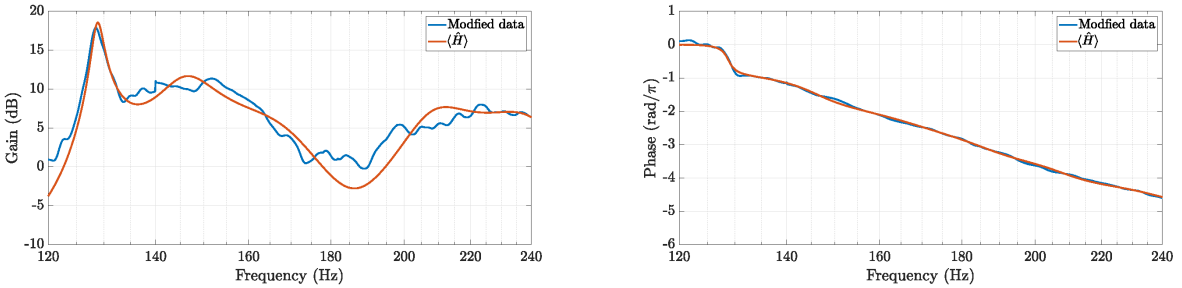

(a) Frequency response and $\langle \hat{H} \rangle$ gain.

(b) Frequency response and $\langle \hat{H} \rangle$ phase.

Figure 5.16: Comparison of the frequency response and transfer function gain (a) and phase (b) for $U_\infty = 20$ m/s and $\Delta P = 120$ mbar.

Running the hinfstruct routine, with similar weighting functions as previously, yields $\gamma = 0.801$ after 58 iterations. Figure 5.17 presents the closed-loop controller performance.
Figure 5.18 compares the cavity spectra for $U_\infty = 20$ m/s and $\Delta P = 120$ mbar in the closed-loop case. The cavity dynamics without forcing corresponds to the blue curve, which exhibits the resonance at $f = 128.6$ Hz for a SPL of 117 dB. The red curve corresponds to the open-loop forcing of the cavity with the quasi-steady jets for $\Delta P = 120$ mbar. In this case, the cavity resonance is only damped by 1 dB. This low damping of the resonance in open-loop is chosen in order to highlight the effect of the closed-loop control. The yellow

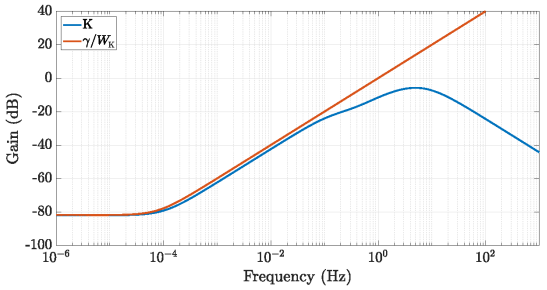

(a) Gain of the controller K.

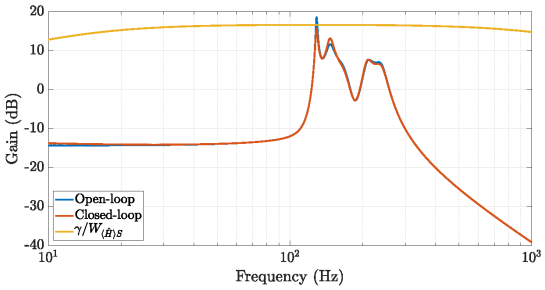

(b) Gain of the closed-loop system.

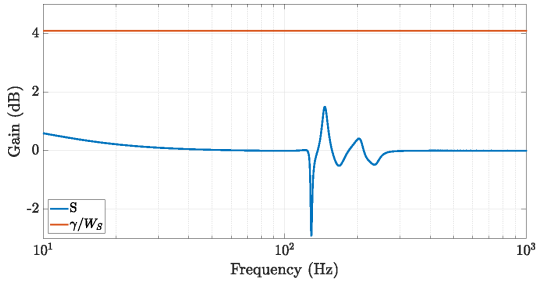

(c) Gain of the sensitivity function S.

Figure 5.17: Gains of the inverse of the weighting transfer functions and transfer functions for: the controller (a), the system in open and closed loop (b) and the sensitivity (c).

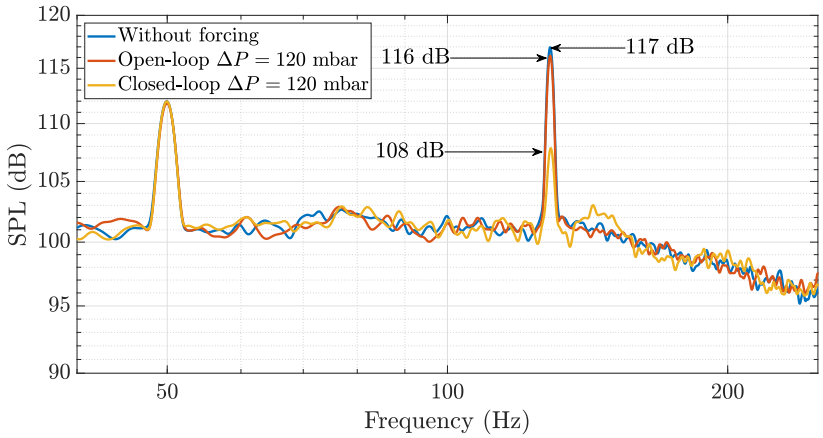

Figure 5.18: SPL (dB) flow spectrum of the open-cavity for $U_\infty = 20$ m/s and $\Delta P = 120$ mbar in the unforced case (blue), open-loop case (red) and closed-loop case (yellow).

curve describes the closed-loop case for which the cavity resonance is damped by 8 dB compared to the open-loop case.

The closed-loop control strongly dampens the cavity resonance as expected from the controller synthesis, although the linear theory underestimates the damping of the resonance by 5 dB. In the closed-loop spectrum, a frequency bump around 143 Hz can be observed. These frequencies are expected in the spectrum as they also appear in the theoretical closed-loop

response of the cavity presented in Figure 5.17b. During the experiments the command signal delivered to the microvalves is recorded, as is the supplied intensity. Figure 5.19 illustrates the microvalves command and power consumption over 2 s and exhibits the command signal spectrum.

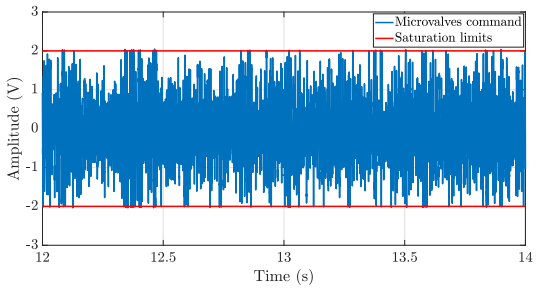

(a) Microvalves closed-loop command.

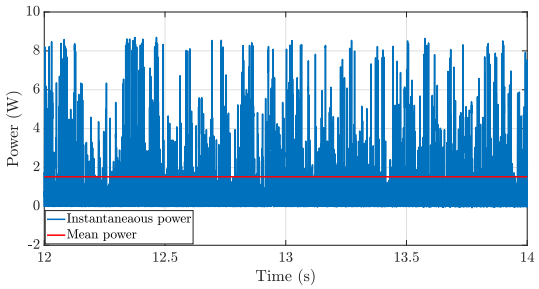

(b) Microvalves power consumption.

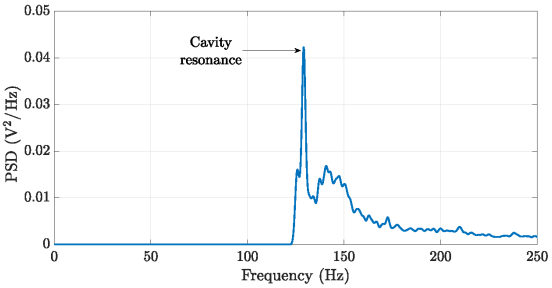

(c) Microvalves command spectrum.

Figure 5.19: Microvalves command signal (a), power consumption (b) and command spectrum (c) for the closed-loop control case $U_\infty = 20$ m/s and $\Delta P = 120$ mbar.

As expected during the H_∞ synthesis, the controller command mean value is negligible (about -0.05 V). Also the saturation imposed to the command signal are seldom overcame, ensuring a linear actuation of the microvalves. The electrical power consumption derived from the microvalves command and intensity records indicates a mean consumption of 1.5 W for the array of 15 microvalves, yielding an average consumption of 0.1 W per actuator.

Further measurements are performed on this study case with the progressive implementation of open-loop and closed-loop control. During an experiment of 180 s, the cavity natural dynamics is recorded over 45 s for $U_\infty = 20$ m/s. Then, open-loop forcing is applied for $\Delta P = 120$ mbar over the next 45 s. Finally for a duration of 90 s, the closed-loop control is finally applied. Figure 5.20 illustrates qualitatively this measurement through the pressure spectrogram. Times of the different control application are outlined by black vertical lines. The cavity natural resonance is outlined during the first 45 s by the red line, which intensity slightly changes once the open-loop forcing is applied. This observation corresponds to the small cavity resonance SPL reduction as noted in Figure 5.18. As the closed-loop control is implemented, the cavity resonance is damped as shown in the spectrogram by the resonance intensity decaying. This is the observation seen also in Figure 5.18, considering the closed-loop curve.

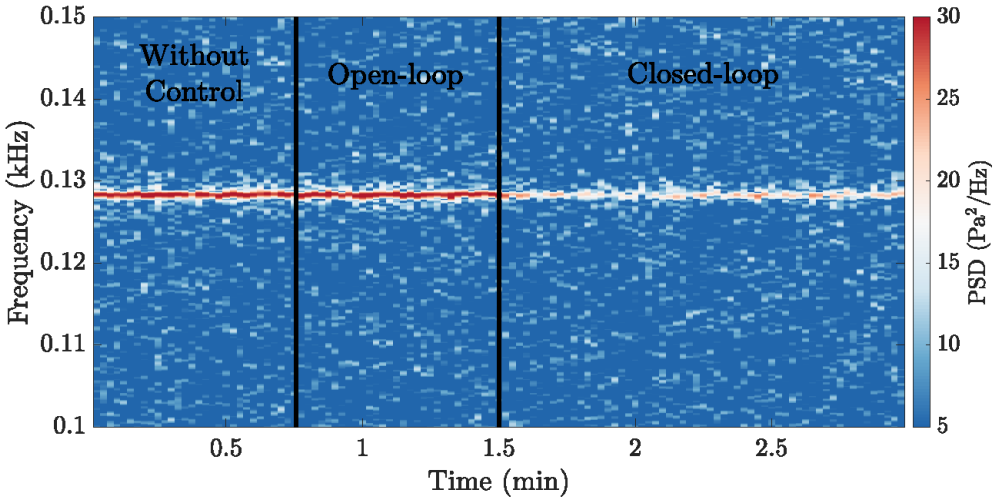

Figure 5.20: Spectrogram of the cavity pressure measurements for an incremental application of control for $U_\infty = 20$ m/s and $\Delta P = 120$ mbar.

Transfer functions identification, controller synthesis and closed-loop control application are also performed for several microvalves driving pressures of 140 mbar, 160 mbar, 180 mbar and 200 mbar. Cavity spectra for the closed-loop implementation of these study cases are presented in Figure 5.21. As highlighted in Chapter 4, the higher the quasi-steady jet component is, the further the cavity resonance is damped in open-loop. Nevertheless, the effect of closed-loop control is still observed in the different spectra. Also, as seen in Figure 5.18, the frequency bump around 143 Hz, inherited from the closed-loop controller designs, remains in the spectra. Furthermore, the closed-loop control is only due to the fluctuating part of the command signals as for 140 mbar, 160 mbar, 180 mbar and 200 mbar, mean values of the actuators command are respectively 0.048 V, -0.005 V, 0.034 V and 0.0493, all negligible

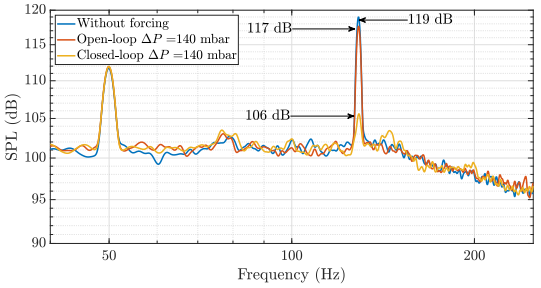

(a) Closed-loop control $\Delta P = 140$ mbar.

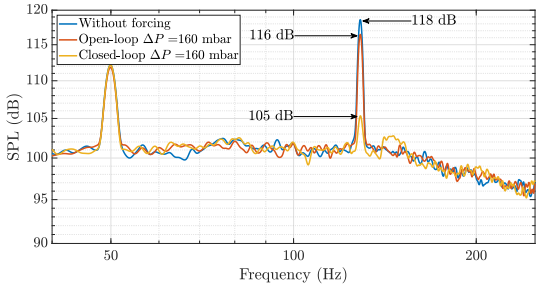

(b) Closed-loop control $\Delta P = 160$ mbar.

Further investigations on the closed-loop are carried out for $U_\infty = 20$ m/s and $\Delta P = 200$ mbar. It is firstly verified that the feedback information is crucial in the closed-loop control implementation. For this measurement, the control signal delivered by the controller during the closed-loop experiment presented in Figure 5.21d is recorded and used to drive the actuators during an open-loop test. Therefore, the microvalves follow the closed-loop command signal without using the sensor feedback information. Figure 5.22 presents these measurements.

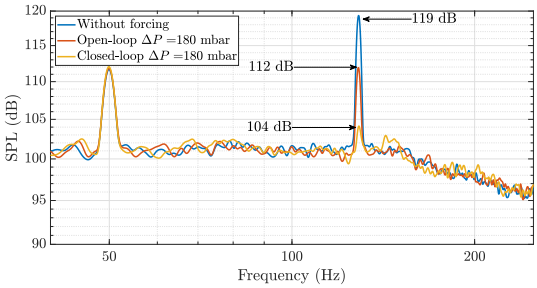

(c) Closed-loop control $\Delta P = 180$ mbar.

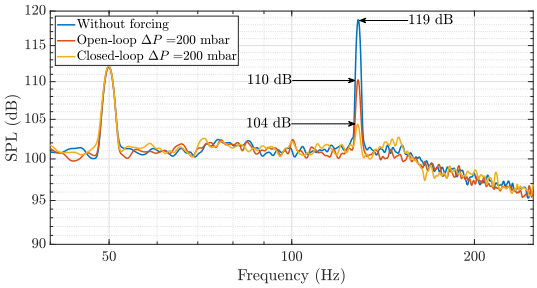

(d) Closed-loop control $\Delta P = 200$ mbar.

Figure 5.21: SPL (dB) flow spectra of the open-cavity in the closed-loop case for $U_\infty = 20$ m/s, $\Delta P = 140$ mbar (a), 160 mbar (b), 180 mbar (c) and 200 mbar (d).

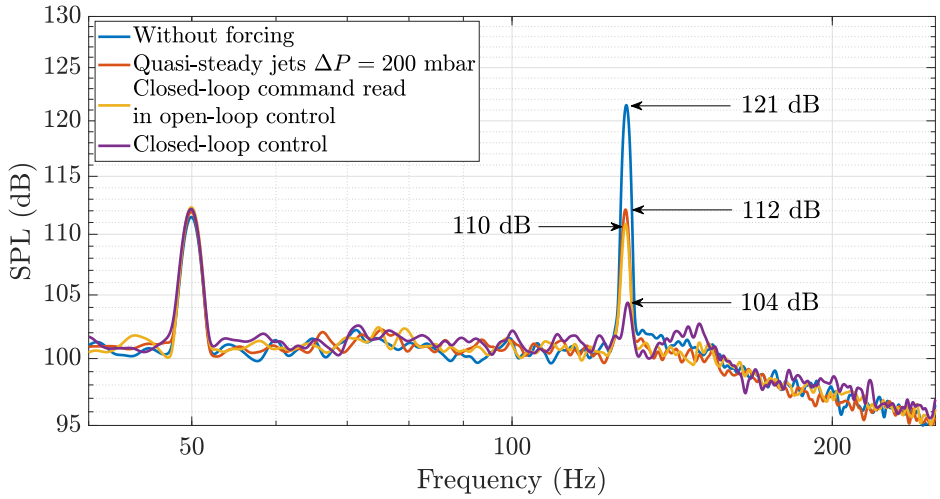

Figure 5.22: SPL (dB) flow spectra of the open-cavity for $U_\infty = 20$ m/s and $\Delta P = 200$ mbar during open and closed-loop measurements verification.

The blue curve stands for the open-cavity unforced dynamics, showing the cavity resonance at 128.6 Hz and 121 dB. The red curve corresponds to the effect of the effect of the open-loop quasi-steady forcing for $\Delta P = 200$ mbar. As already observed several times, the quasi-steady jets reduce the cavity resonance. In this case, the reduction observed reaches 11 dB. The yellow curves corresponds to the use of the closed-loop control signal read in open-loop. The cavity resonance, compared to the open-loop quasi-steady jets, is only further reduced by 1 dB. The comparison with the purple curve clearly indicates that this reduction is only due to the pulsed jets induced by the command signal. Indeed, the real closed-loop application, corresponding to the purple curve, enable to damp the cavity resonance by 8 dB compared to the quasi-steady jets. These measurements show the importance of the feedback pressure measurement, which encloses the essential phase information, used to control the actuators during the closed-loop applications.

Further measurements investigate the controller robustness to freestream velocity variations. The controller designed for a freestream velocity of $U_\infty = 20$ m/s is therefore applied for $U_\infty = 19$ m/s and $U_\infty = 21$ m/s, yielding variations of $\pm 5\%$ in U_∞. For these two velocities,

the open-cavity resonance is shifted respectively to 127 Hz and 130 Hz, instead of 128.6 Hz. As observed in Figure 5.23, for both flow regimes, the controller still manages to damp the resonance.

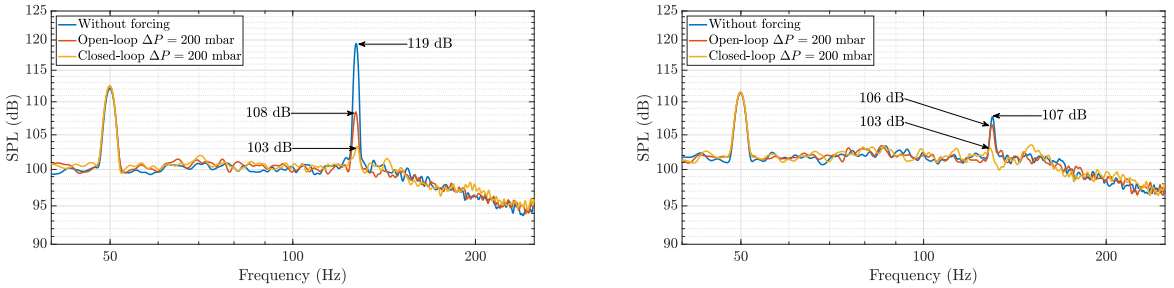

(a) Closed-loop control $U_\infty = 19$ m/s.

(b) Closed-loop control $U_\infty = 21$ m/s.

Figure 5.23: SPL (dB) flow spectra of the open-cavity for robustness measurements for $U_\infty = 19$ m/s (a) and $U_\infty = 21$ m/s (b) and $\Delta P = 200$ mbar.

Considering the firstly presented flow regime for $U_\infty = 18$ m/s and $\Delta P = 120$ mbar, further investigations focused on the number of required actuators to have an effect on the flow dynamics during closed-loop control experiments. Closed-loop control is performed with the synthesized controller presented in Section 5.2.2 and for different numbers of microvalves effectively actuated.

The first measurements presented in Figure 5.24a are performed with the entire set of microvalves actuated. The cavity dynamics without forcing exhibits resonance at 124 Hz and 113 dB. In open-loop, the quasi-steady jets only reduce the resonance SPL by 1 dB. In closed-loop the cavity resonance is attenuated by 4 dB compared to the open-loop case. Figure 5.24b shows the same closed-loop implementation but with only one microvalve every two microvalves actuated. Therefore, the use of only 7 microvalves provide the same control results as the one obtained with the entire array of actuators. Further reducing the number of actuators to only 5 microvalves (1 every 3 microvalves), regulerly distributed along the cavity upstream edge, lowers the closed-loop control effect on the cavity dynamics, as illustrated in Figure 5.24c. The cavity resonance is only damped by 1 dB compared to the open-loop case. Obviously, decreasing again the number of actuated microvalves totally cancel the interest of both open and closed-loop control as observed in Figure 5.24d.

5.3.2 Iterative applications of linear controllers

Considering Figure 5.24a, despite resonance damping by closed-loop control, the peak does not entirely vanish. Based on this observation, further measurements explored the iterative application of a second controller as numerically proposed by Leclercq et al. [21]. The first controller output signal mostly oscillates between -1 V and 1V at a frequency of 124 Hz, as shown in Figure 5.25.
Therefore, the iterative identification process can be performed using frequency sweeps of amplitude 1 V. In this study case, let $\langle \hat{H}_1 \rangle(s)$ denotes the iterative transfer function identified. For this new identification process, the closed-loop control with the first controller must be implemented while excitation signals are also generated. Therefore, the closed-loop control signal and the frequency sweeps superimpose. Based on the assumption of the open-cavity

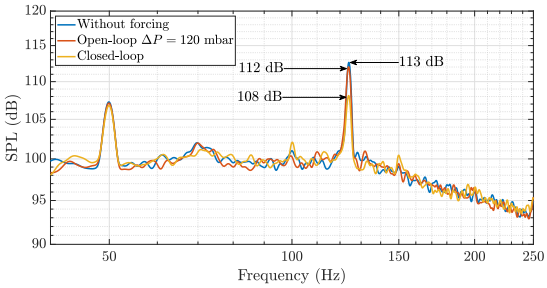

(a) Closed-loop implementation with the 15 microvalves.

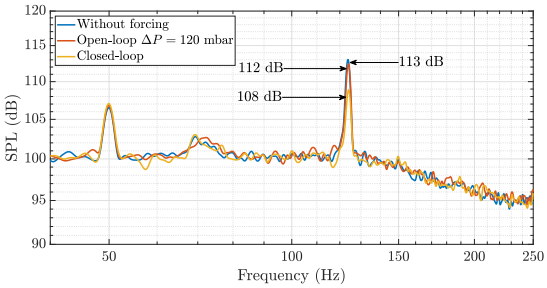

(b) Closed-loop implementation with 7 microvalves.

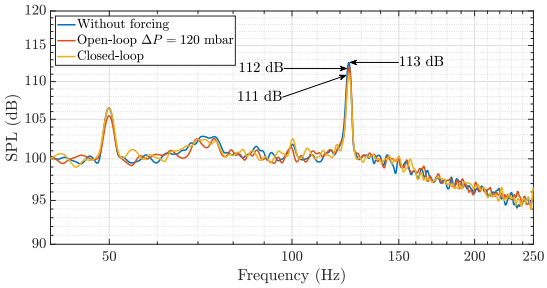

(c) Closed-loop implementation with 5 microvalves.

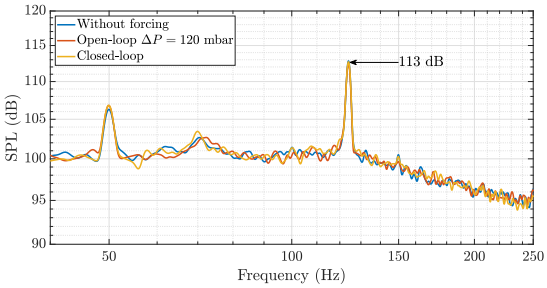

(d) Closed-loop implementation with 1 microvalve.

Figure 5.24: Closed-loop implementation for $U_\infty = 18$ m/s and $\Delta P = 120$ mbar for different number of actuated microvalves: 15 microvalves (a), 7 microvalves - 1 out of 2 - (b), 5 microvalves - 1 out of 3 (c) and only one actuator (d).

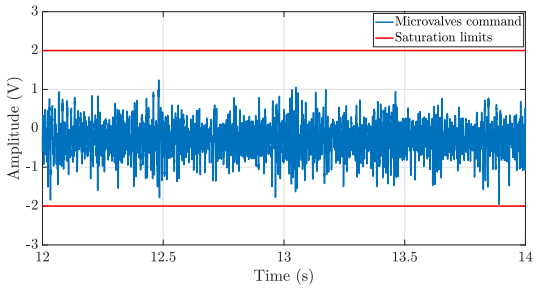

(a) Microvalves closed-loop command.

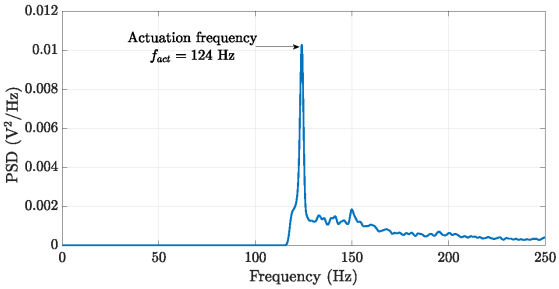

(b) Microvalves command spectrum.

Figure 5.25: Microvalves command signal (a) and command spectrum (b) for the closed-loop control case $U_\infty = 18$ m/s and $\Delta P = 120$ mbar.

linear behavior in this case, it is then expected to identify $\langle \hat{H}_1 \rangle$ from the measurements. The implementation of this identification step is sketched in Figure 5.26. The transfer function $\langle \hat{H}_1 \rangle$ is therefore defined as the ratio in the frequency domain between the input perturbation superimposed with the controller command, with the downstream pressure measurements. The identified transfer function is presented in Figure 5.27. Considering the phase, the linear decrease trend is still observed, with the open-cavity flow resonance highlighted by the change in phase around 124 Hz. The transfer function fit reaches 67.9%.
A controller similar to the one presented in Section 5.2.2 is designed. Figure 5.28 illustrates

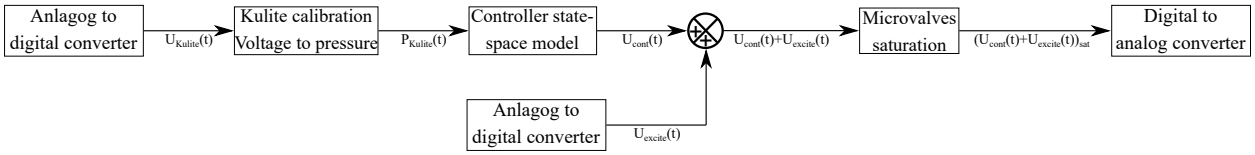

Figure 5.26: Sketch of the Simulink program used for the iterative identification step.

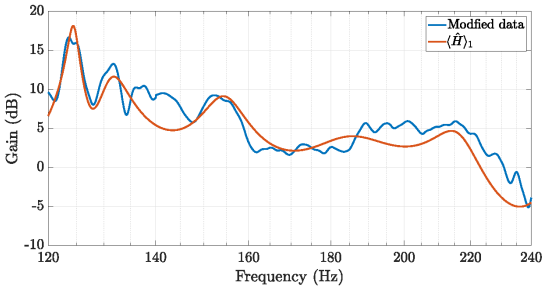

(a) Frequency response and $\langle \hat{H}_1 \rangle_1$ gain.

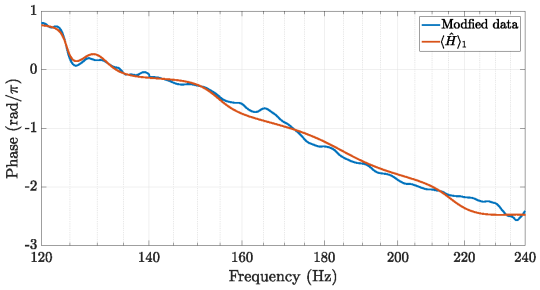

(b) Frequency response and $\langle \hat{H}_1 \rangle_1$ phase.

Figure 5.27: Frequency response and transfer function $\langle \hat{H}_1 \rangle_1$ gain (a) and phase (b).

the controller performance.

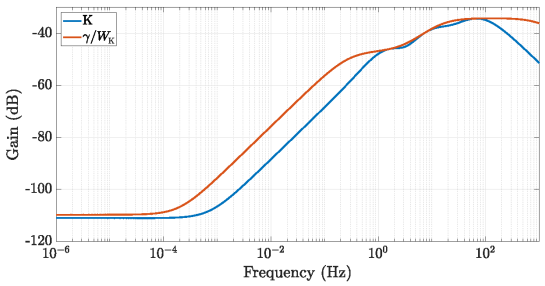

(a) Gain of the controller K.

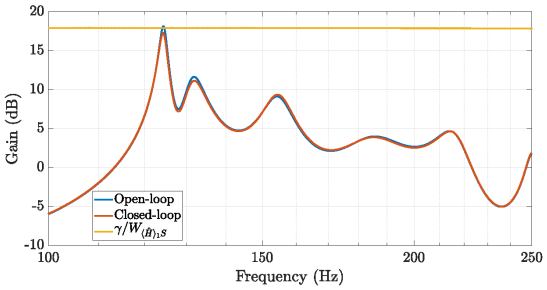

(b) Gain of the closed-loop system.

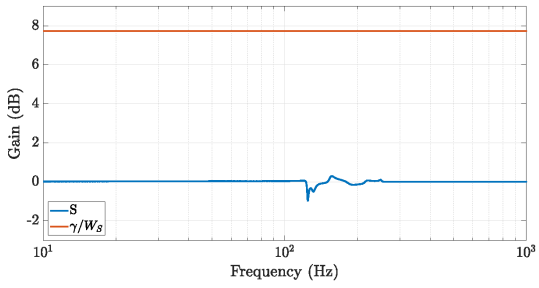

(c) Gain of the sensitivity function S.

Figure 5.28: Gains of the inverse weighting functions and transfer functions used in the H_∞ loop-shaping process for the second controller derivation for $U_\infty = 18$ m/s and $\Delta P = 120$ mbar.

Considering the linear theory, the application of the second controller should result in a

damping of the resonance by 0.9 dB. Once the second controller is designed, the Simulink program for the iterative closed-loop implementation is built, as illustrated in Figure 5.29. The Kulite sensor voltage is recovered by the ADC block and then converted into pressure. The pressure signal $P(t)$ is then supplied to both controller K and K_1, whose outputs are added by the summation block. The command signal $u_1(t) + u_2(t)$ then goes through the saturation block, whose output is then transformed into an analog signal supplied to the microvalves.

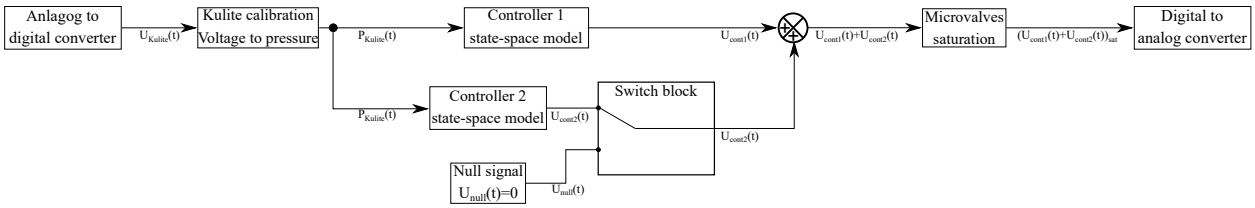

Figure 5.29: Sketch of the Simulink program for the iterative application of two controllers.

Indeed, for the iterative application of the second controller, $u_2(t)$ must be added to $u_1(t)$ once the first controller already modified the flow dynamics. Therefore, the second controller output reaches a switch block. During the first 100 s of the measurements, the switch block delivers a null output signal, such that the flow dynamics converges towards the equilibrium imposed by the first controller. After these 100 s, the switch block provides the second controller command signal $u_2(t)$, which is then added to $u_1(t)$ and delivered to the microvalves. Measurements for the iterative application of the two controllers are presented in Figure 5.30.

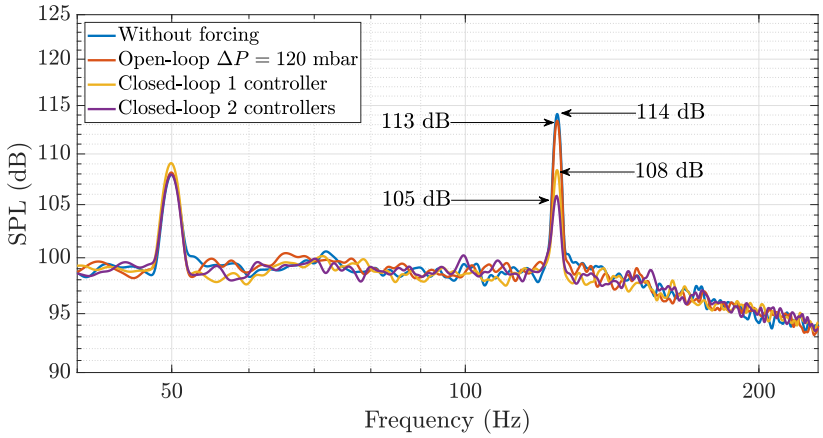

Figure 5.30: SPL (dB) flow spectra of the open-cavity for $U_\infty = 18$ m/s and $\Delta P = 120$ mbar during the iterative closed-loop application of two controllers.

The blue curve which corresponds to the open-cavity natural dynamics presents a resonance peak at 124 Hz and 114 dB. The quasi-steady jets, red curve, reduce the resonance by 1 dB, while the first controller, yellow curve, induces a reduction of 5 dB compared to the open-loop case. The application of the second controller, illustrated by the purple curve indicate a further reduction of the resonance of 3 dB compared to the application of the first controller.

Figure 5.31 presents the time series of $u_1(t)$ and $u_1(t) + u_2(t)$ and their spectra. Regarding the time series, it is observed that applying the second controller decreases the mean value

from -0.3 V to -0.6 V. Considering the signals spectra it is observed that the PSD at 124 Hz increases from 0.011 V^2/Hz to 0.018 V^2/Hz. Despite the increase in the actuation frequency power and because the controller static gain is not properly enforced to 0, reduction of the open-cavity resonance SPL may be due to the command mean value induced by the controller.

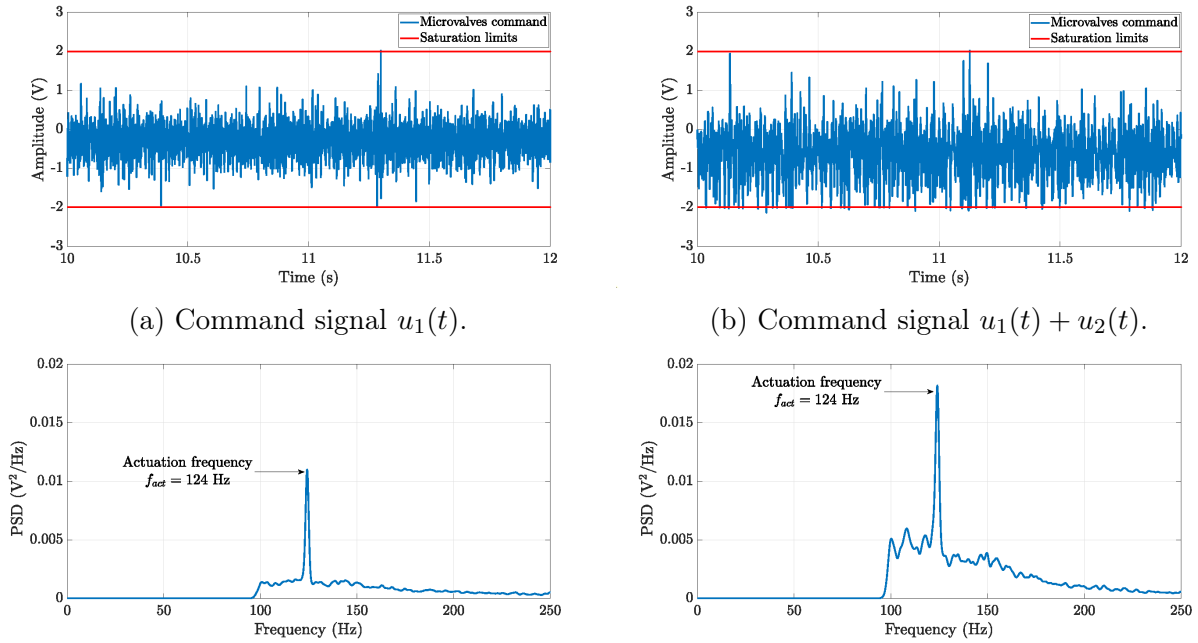

(a) Command signal $u_1(t)$.

(b) Command signal $u_1(t) + u_2(t)$.

(c) Spectrum of $u_1(t)$.

(d) Spectrum of $u_1(t) + u_2(t)$.

Figure 5.31: Time series and spectra of the command signals $u_1(t)$ of the first controller (a,c) and of the iterative application of the second controller $u_1(t) + u_2(t)$ (b,d) for $U_\infty = 18$ m/s and $\Delta P = 120$ mbar.

Conclusion

This 5$^{\text{th}}$ chapter presented the closed-loop control of an open-cavity flow. The notion of transfer function for the oscillating open-cavity flow is firstly addressed. Frequential data are then gathered based on the use of frequency-rich signals used to drive the microvalves. A state-space model is then derived from the gathered data and a linear controller is synthesized based on the H_∞ loop-shaping approach. Application of the controller is then discussed through different experiments.

To obtain the frequency response of the open-cavity flow, different input signals are used. First measurements are carried out with harmonic inputs showing that the response to linear harmonic forcing is independent on the phase ϕ, even though the base flow is not time-invariant but periodic. Second measurements are performed with multi-frequency signals consisting in frequency linear sweeps. Variability in these measurements is low because the frequency in these input signals varies at a quasi-static rate and at any given time, the flow is considered as forced by a purely harmonic input. This type of signal is therefore ideal for identification because the entire frequency range $120 - 240$ Hz may be identified using less than 10 realizations to converge the mean response to a good precision. This is indeed much more economical than using purely harmonic forcings.
Based on the frequential data, a state-space model is derived and used for the design of a linear controller, based on a H_∞ loop-shaping approach.
Closed-loop flow control experiments are carried out for different freestream velocities and for different driving pressures applied to the array of microvalves. For each study cases, a transfer function identification step and a synthesis of a controller were performed. The controllers were then compiled on the Dspace real time software and applied. For a freestream velocity of 20 m/s and for a driving pressure of 120 mbar, the cavity resonant frequency amplitude was reduced down by 9 dB compared to the open-loop case for the same driving pressure. Further experiments show the controller robustness towards modification of the freestream velocity by $\pm 5\%$ and indicate that a reduced number of microvalves can be used to reach the same reduction in the open-cavity resonance SPL.

This study shows the straightforward use of the MMMS microvalves (with the ability to be driven with any type of signal, as required in closed-loop) in the closed-loop control of a periodic open-cavity flow and constitutes a first step towards the closed-loop control of more complex flows such as quasi-periodic open-cavity flows or the control of different flow configurations such as the jet flows, as will be considered in future studies.

Chapter 6

Development and tests of improved MEMS technologies for flow control applications

Introduction

In this chapter, the focus is brought onto the TRL increase from 4 to 5-6 of the disruptive MEMS sensors technologies developed at the IEMN, designed for flow control applications. The work is concentrated on increasing the micro sensors fabrication process reliability and on the non-intrusive integration of the technologies on aerial vehicles. In that sense, the micro sensors are integrated on a POD placed on the landing gear of a microlight aircraft, for real flight measurements. For a demonstration of the TRL increase of actuators technologies, an in-situ monitoring of a microvalve is proposed through the integration of a MEMS calorimetric sensor.

This chapter first part deals with the improvement of the MEMS calorimetric wall shear stress sensors and integration on an aerial vehicle for real flight measurements. An optimization of the etching step releasing the suspended measurement wires, based on the use of SF_6, is discussed alongside with the fabrication of traversing vias in the micro sensors chips. Originally using the wire bonding technique, the electrical link between the sensor chips and their conditioning electronics was based on the use of soldered metallic wires sensitive to vibrations. Traversing vias made of copper circumvent this issue and enable a flush mounted integration on any surface. The traversing via process, performed by electro-deposition, is optimized by PPRP. In addition, development of the MMMS microvalves are discussed. It is proposed to integrate a micro machined hot film sensor inside a microvalve microchannel. Closed-loop control of the microvalve is performed with the in-situ sensor in order to flatten the gain curve which would be relevant for future open-loop flow control experiments. The closed-loop control is implemented thanks to the data-driven approach considered on the plain flap configuration.

6.1 Real flight tests of calorimetric micro sensors

Calorimetric micro sensors presented in Chapter 3 constitute a disruptive sensor technology designed for integration on terrestrial and aerial vehicles, for real flow sensing applications. In the following, improvements of the fabrication process are proposed, as well as the integration of a calorimetric micro sensor on a microlight aircraft is described alongside with the real flight measurements. Aim of these experiments is to prove the reliability of the micro sensors and their electronics against uncontrolled atmospheric conditions.

6.1.1 Calorimetric MEMS sensors fabrication process and optimization

Micro sensors are produced on 3 inches wafers characterized by a (100) crystal plane. The fabrication process, presented by Ghouila-Houri et al. [64] of the micro sensors is based on the succession of several micro machining steps depicted in Figure 6.1.

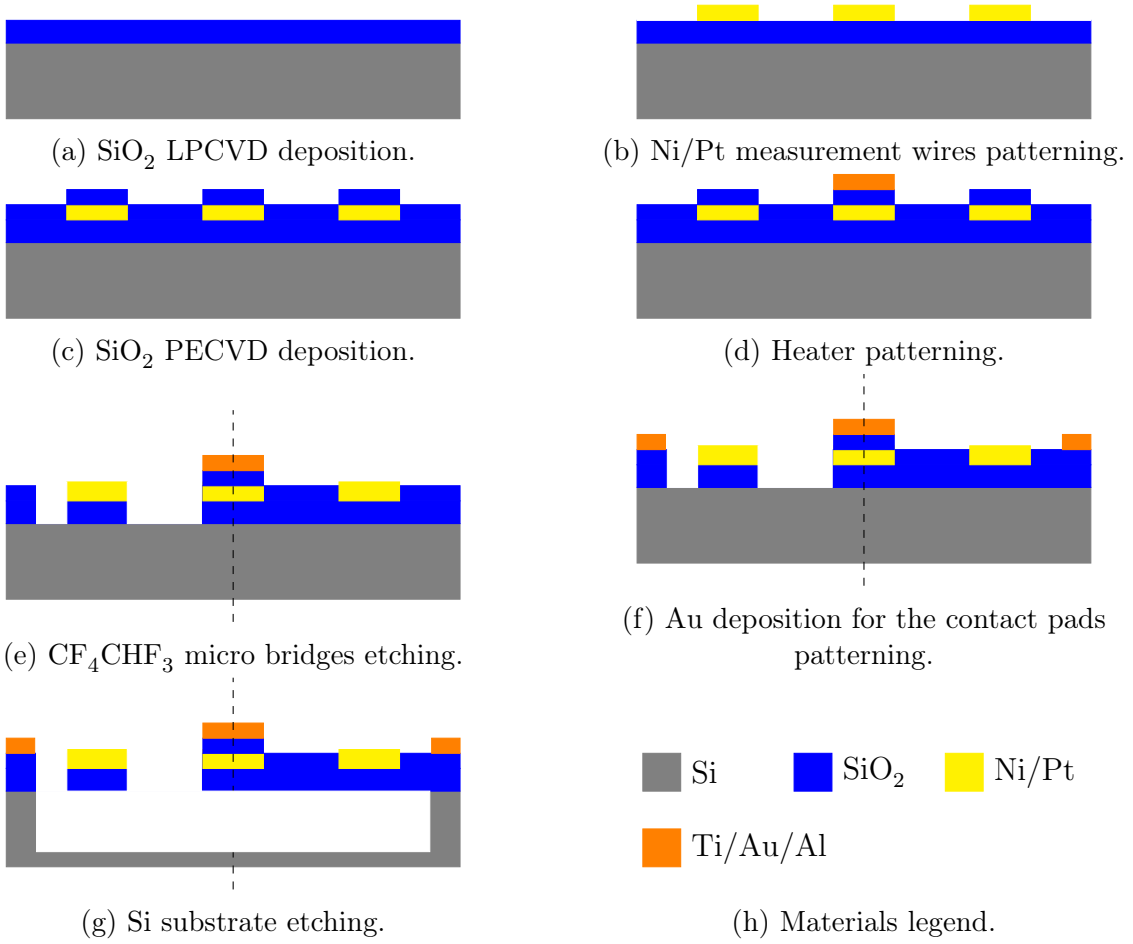

(a) SiO_2 LPCVD deposition.
(b) Ni/Pt measurement wires patterning.
(c) SiO_2 PECVD deposition.
(d) Heater patterning.
(e) CF_4CHF_3 micro bridges etching.
(f) Au deposition for the contact pads patterning.
(g) Si substrate etching.
(h) Materials legend.

Figure 6.1: Fabrication steps of the calorimetric micro sensors (inspired from Ghouila-Houri [180]).

a A SiO_2 layer is deposited by LPCVD (Low Pressure Chemical Vapor Deposition). This technique enables the deposition of a thin layer of pure material, based on the

use of gaseous precursors. The wafer substrate is exposed to one or several gases which react and decompose themselves on the substrate surface. For the SiO_2 layer, a wet deposition process is considered such that the chemical reaction is achieved between Si and super-heated steam (800°C), as described by Equation (6.1):

$$Si \ + \ 2H_2O \rightarrow \ SiO_2 \ + \ 2H_2 \tag{6.1}$$

b Measurement wires are patterned by photolithography and metal deposition. The photolithography process consists in transferring designs from a mask to a photosensitive resin. The resin is firstly spin coated on the wafer. It is then exposed to UV through the mask on which the wire patterns are defined. The exposed resin to UV is removed in a chemical solution and the patterns footprint remain on the wafer. Then, a multi layer Ni/Pt metal deposition is performed. Finally, the remaining undesired resin is removed by lift-off. Figure 6.2 provide details on the steps of the photolithography process.

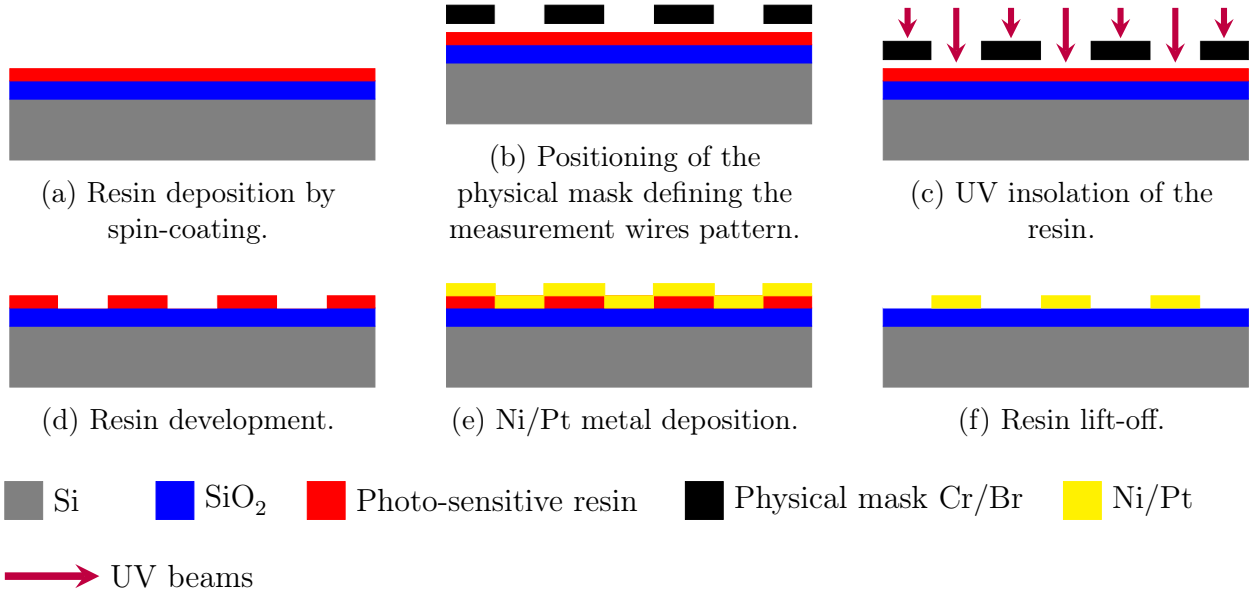

Figure 6.2: Photolithography process for the patterning of measurement wires (inspired from Ghouila-Houri [180]).

c A new SiO_2 layer is deposited by PECVD in order to isolate the measurement wires from the heating wire. Using plasma as a catalyzer of the reaction described by Equation (6.2), this deposition method is performed at a temperature of 300°C, avoiding the previous metallic layer to melt.

$$SiH_4 \ + \ 2N_2O \rightarrow \ SiO_2 \ + \ 2N_2 \ + \ 2H_2 \tag{6.2}$$

d The heating wire fabrication step is similar to the one of the measurement wires. The heater consists in a metallic multilayer composed of Ti/Au/Al. The Ti is used as an adhesion layer between SiO_2 and Au, while the Al layer is used to protect the Au layer during the following etching step.

e To create the suspended structure of the calorimetric micro sensors an etching step is required. This etching step relies firstly on a photolithography phase to define micro bridges patterns. The patterns are then etched by a plasma composed of CF_4 and CHF_3. This plasma solution guarantees an an-isotropic etching.

f Contact pads on the micro sensor chips are obtained by the deposition of Au on the substrate. These pads are necessary for the interconnection of chips with their electronics.

g Chips produced on the wafer are then separated from each other, before the final step consisting in an etching phase releasing the wires from the substrate. The substrate is etched by plasma using XeF_2, in order to have an isotropic etching.

This plasma etching phase based on the use of XeF_2 leads to repeatability issues, damaging of the electrical pads in Au. The optimization proposed aims at solving these issues by using an hybrid RIE process, etching both physically and chemically the silicon substrate. The plasma considered in the optimized process is composed of SF_6/N_2. The SF_6 plasma induces an isotropic etching. However, it damages the thin layers of Au and must therefore be coupled with the non-reactive N_2 gas to preserve the Au pads. The optimization process is performed using a 4 variables Doehlert [189] design of experiment in order to determine a relationship between the etching parameters and the lateral etch rate, while minimizing the number of experiments.

The optimization study is performed on a silicon wafer (100) patterned with a 500 nm thick SiO_2 layer consisting of equal lines and spaces of 20μm width, as depicted in Figure 6.3a.

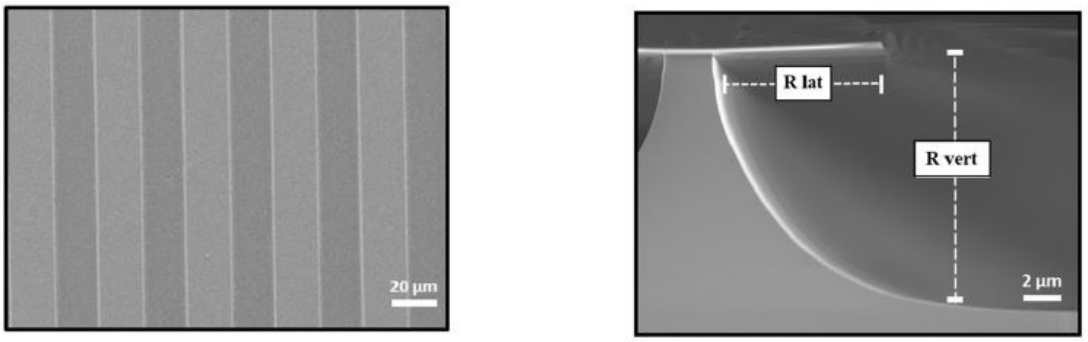

(a) SEM top view. (b) SEM side view.

Figure 6.3: SEM top (a) and side (b) view of the wafer on which the optimization process is investigated.

The four variables considered are the mass flow rate (sccm), ratio of SF_6/N_2, pressure (mTorr) and power (W). Their respective ranges and values are defined in Table 6.1. The number of experiments is determined according to Equation (6.3):

$$N = F^2 + F + N_0, \tag{6.3}$$

where F is the number of variables and N_0 the number of experiments at the central point. With $F = 4$ and $N_0 = 1$, the total number of experiments is $N = 21$. Etching experiments

are carried out in the OIPT Plasmalab 80 RIE frame in the IEMN clean room with an etching time of 7 min.

Table 6.1: Design of experiments variables and predicted lateral etching rates.

Optimization variables Range	Mass flow rate (sccm) 20-50	Gases ratio (N_2/SF_6) 0.1-0.6	Pressure (mTorr) 80-150	Power (W) 80-150	R_{lat} (exp.) (μm/min)	R_{lat} (pred.) (μm/min)
1	35	0.35	115	115	1.12	1.13
2	35	0.60	115	115	1.01	1.05
3	35	0.10	115	115	1.19	1.20
4	48	0.48	115	115	1.10	1.13
5	22	0.23	115	115	1.35	1.35
6	22	0.48	115	115	1.23	1.28
7	48	0.23	115	115	1.25	1.20
8	39	0.48	143	115	1.14	1.09
9	31	0.23	86	115	1.27	1.27
10	31	0.48	86	115	1.15	1.12
11	44	0.35	86	115	1.18	1.16
12	39	0.23	143	115	1.05	1.08
13	26	0.35	143	115	1.21	1.20
14	39	0.48	122	142	1.37	1.37
15	31	0.23	107	87	1.12	1.11
16	31	0.48	107	87	1.07	1.01
17	44	0.35	107	87	0.98	1.02
18	35	0.35	136	87	0.96	0.99
19	39	0.23	122	142	1.44	1.42
20	26	0.35	122	142	1.57	1.51
21	35	0.35	93	142	1.41	1.44

The influence of etching parameters on the lateral Si etching rate is investigated with a response surface methodology in order to obtain a predictive model. The lateral etch rate, defined as the ratio between the lateral length of etching with the etching time of Si is determined by cross-sectional SEM analysis, as illustrated in Figure 6.3b. Based on the measurements presented in Table 6.1, the 21 values are used to derive a linear and quadratic equation of the effects of the different factors on the lateral etching rate R_{lat}:

$$\begin{aligned} R_{lat} = {} & 3.556 - 1.633Y_1 - 0.05148Y_2 - 0.00508Y3 \\ & - 0.02024Y_4 + 0.01158Y_3 + 0.0006531{Y_2}^2 + 0.0001203{Y_4}^2, \end{aligned} \tag{6.4}$$

where Y_1, Y_2, Y_3 and Y_4 respectively denote the gases ratio, the mass flow rate, the pressure and the power. The coefficient of determination $r^2 = 0.972$ indicates a reliable model for the derivation of the etch rate. Figure 6.4 presents the response surface plots derived from Equation (6.4) providing the relationship between the rate and each parameter. Effects of power and ratio variations in Figure 6.4a are described for the mass flow rate and pressure set at their center point, respectively of 35 sccm and 114.5 mTorr. The power tends to increase the lateral etching rate by raising the ion energy and the F-atom density. On the contrary, increasing the ratio lowers the lateral etching rate, because of the SF_6 dilution, as observed by Pinto et al. [190].

Effects of the mass flow rate and pressure, fixing the power and ratio at their center values respectively of 114.5 W and 0.35, are illustrated in Figure 6.4b. An increase in the pressure induces a linear decrease in the lateral etching rate. Evolution of the R_{lat} is quadratic against the mass flow rate, reaching a minimum value for a mass flow rate of 41 sccm.

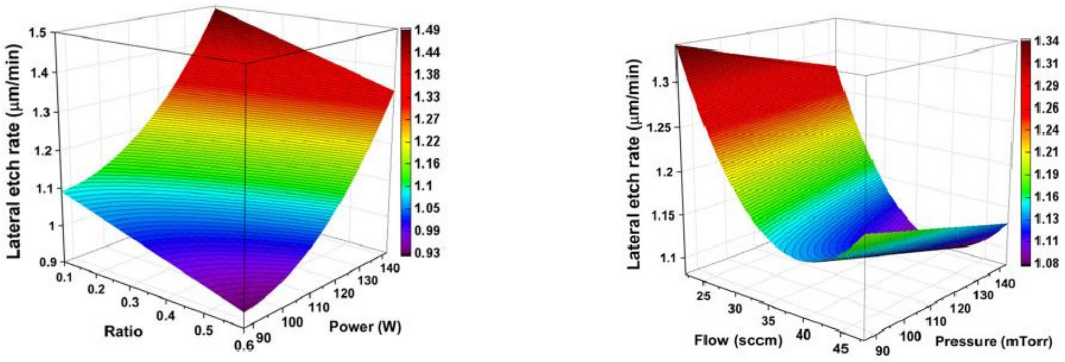

(a) Lateral etching rate against gases ratio and power.

(b) Lateral etching rate against the mass flow rate and the pressure

Figure 6.4: Three dimensional surface plots of the lateral etching rate against the gases ratio and the power (a) and against the mass flow rate and the pressure (b).

Based on Equation (6.4), the optimized value of the four parameters are derived for a maximal lateral rate of 1.8 μm/min, yielding a mass flow rate of 22 sccm, a ratio of 0.1, a pressure of 86 mTorr and a power of 143 W. These parameters were experimentally validated reaching $R_{lat} = 1.79$ μm/min. Furthermore, the N_2 protects the Ti/Au layers contrary to the first employed etching process.

6.1.2 Sensor copper traversing vias

The connection between the micro sensors and their packaging, as it is the case in Chapter 3, was previously performed using the wire bonding technique. It consists in soldering a metallic wire (Au, Al or Cu) of few micrometers in diameters on one hand, on the micro sensor chip and on the other hand on the packaging. However, this technique does not enable the use of the micro sensors in harsh environmental conditions, as vibrations or shocks could break the wires. It is therefore considered to build the micro sensors with traversing vias, enabling the electrical contact on the rear side of the chip. Hence, the micro sensors can be flush mounted on any type of surface using the BGA (Ball Grid Array) technology illustrated in Figure 6.5.

(a) Chip front side.

(b) Chip rear side.

Figure 6.5: Illustration of the Ball Grid Array principle on the calorimetric micro sensor for both front and rear (a) sides (b).

The traversing copper vias have to meet several criteria to be functioning. They have to be electrically isolated from each other, be characterized by a low electrical resistance and by

a high weld-ability. The process of vias fabrication, sketched in Figure 6.6, is carried out before the fabrication process presented in Figure 6.1. The main steps of traversing vias fabrication are summarized in the following:

a Holes in the silicon wafer are drilled with the Bosch process by DRIE.

b The electrical isolation of the vias with the intrinsic semi-conductor wafer is ensured by the deposition of thermal oxide SiO_2;

c Cr/Au metal is deposited on the wafer by pulverization. This layer serves as an adhesion layer for the later growth of the Cu metal composing the vias. It also has an adhesion layer role on the plating electrode from which the Cu growth is performed. At the end of this step, indium is also evaporated on the wafer in order to anticipate the next process step.

d The wafer is sealed on a polyimide membrane necessary for the Cu growth step;

e Vias holes are filled with copper thanks to an electrolysis optimized by the PPRP deposition process, presented in the following. The electrolysis solution is composed of $CuSO_4$ (0.5 mol/L) and H_2SO_4;

f Finally, the wafer is separated from the polyimide membrane.

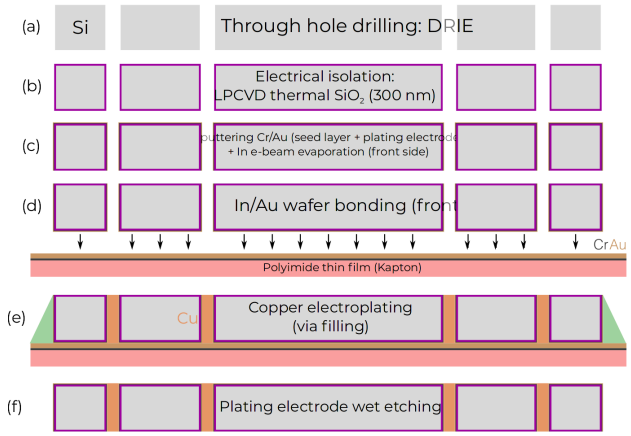

Figure 6.6: Sketch of the traversing vias fabrication process developed on a 3 inches silicon wafer.

Wafer front and rear sides at the end of this process are presented in Figure 6.7. Traversing vias are obtained with an homogeneous copper deposition leaving the wafer front side smooth enough to perform the rest of the micro sensor fabrication steps. In order to have an homogeneous growth of Cu in the vias, the PPRP process is employed. This process consist in applying a current density J between the cathode, from which Cu is grown, and an anode made of Pt. Based on the Faraday law, the mass of Cu deposited is proportional to J. On the contrary to usual electrolysis based on an average current density constantly applied, the PPRP process cyclically alternates deposition phases, characterized by a cathodic current J_F, and etching phases, characterized by an anodic current J_R. This process, schematically presented in Figure 6.8, provides an homogeneous deposition of Cu in the traversing vias.

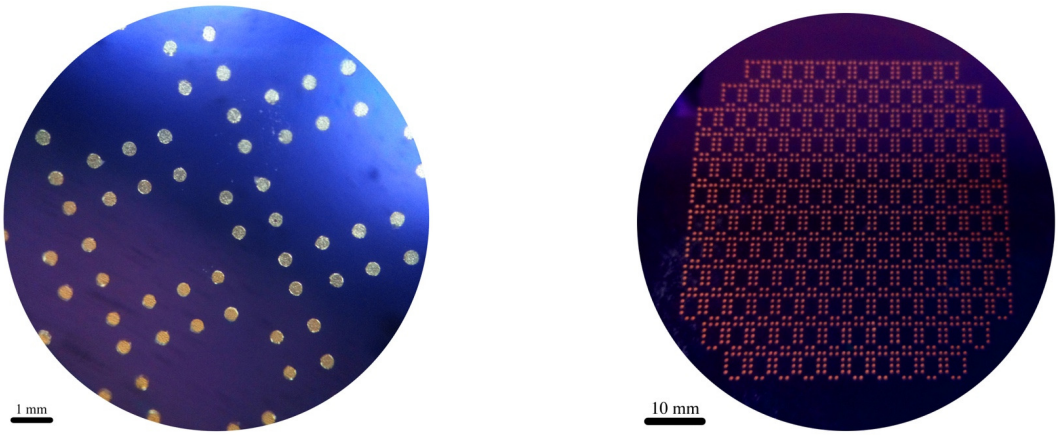

(a) Wafer front side. (b) Wafer rear side.

Figure 6.7: Pictures of a wafer front and rear (a) sides (b) after the traversing vias process.

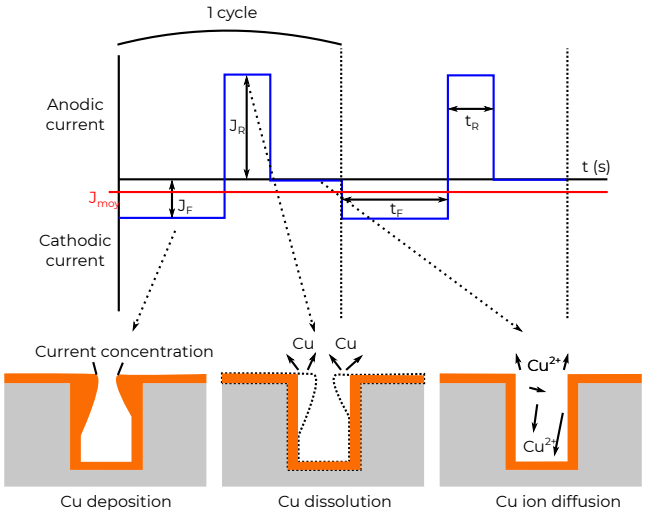

Figure 6.8: Illustration of the PPRP principle.

During the deposition phase, Cu^{2+} ions preferentially agglomerate in highly electrically polarized areas, such as the vias salient angles. Therefore, an aggregation of Cu is formed at the vias openings, leading to the sealing of the empty vias if nothing is done. Hence, an etching phase is required to remove these aggregations and homogenize the Cu deposition. The third phase characterized by a null current density helps regenerate the quantity of Cu^{2+} ions available for the formation of Cu during the following cycle. Optimizing the PPRP process therefore consists in determining the optimal values of the deposition time t_F, the etching time t_R, the pausing time t_{off} and of J_F and J_R the cathodic and anodic density currents, in order to obtain an homogeneous formation of Cu. This optimization process also depends on the traversing vias aspect ratio of 0.79, in the considered case. Values retained after optimization are $t_F = 475$ ms, $t_R = 50$ ms, $t_{off} = 475$ ms, $J_{avg} = -4$ mA/cm^2 and $J_R = -4J_F$. Pictures of the traversing copper vias obtained during the fabrication process of calorimetric sensors are presented in Figure 6.9.

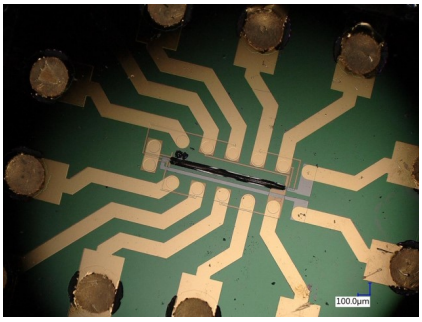

(a) Picture of a calorimetric sensor with traversing vias.

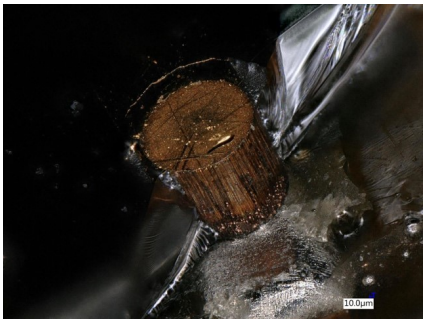

(b) Sectional view of a traversing copper via.

Figure 6.9: Pictures (a) and sectional view (b) of a calorimetric sensor with copper traversing vias.

6.1.3 Dynamical wall shear stress measurements

Real flight tests measurements are performed with a Flight Design CTSW microlight aircraft. The airplane is equipped with a 3 blades propeller and a Rotax 912s engine, characterized by a gear box ratio of 1/2.43. PODs are installed on the airplane landing gear and are instrumented with one calorimetric micro sensor each, as illustrated in Figure 6.10.

(a) Flight design CTSW microlight aircraft.

(b) POD installation on the microlight aircraft landing gear.

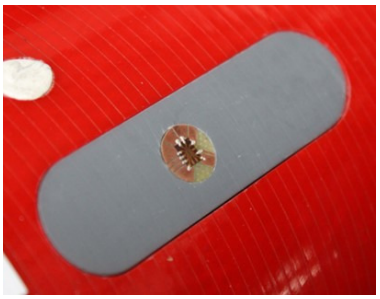

(c) Calorimetric micro sensor integration on the right side POD.

Figure 6.10: Pictures of the microlight aircraft (a), POD installation on the landing gear (b) and of the calorimetric micro sensor integration (c)).

The following points are assessed through different flights:

- Validate the robustness of the micro-sensor towards real flight conditions;
- Assess the effects of airspeed on the measurements;
- Assess the effects of altitude on the measurements;
- Detect the stall of the airplane;
- Detect the propeller signature depending on the engine regimes.

To assess the effects of both airspeed and altitude on the measurements, the airplane is flown at the different velocities and altitudes presented in Table 6.2. The data time series of a

micro sensor are presented in Figure 6.11 and compared to measurements performed in a turbulent boundary layer wind tunnel.

Table 6.2: Airspeeds and altitudes of the airplane for the different in-flight measurements.

Airspeeds and altitude combinations				
Airspeeds (km/h)	100	150	200	250
Altitudes (ft)	1000	1500	2000	

Figure 6.11 left, presents the evolution of the wall shear stress calibration curve of the micro sensor as a function of the wind tunnel freestream velocity. This calibration curve is presented simultaneously with the evolution of the flight measurements. Figure 6.11 right, is

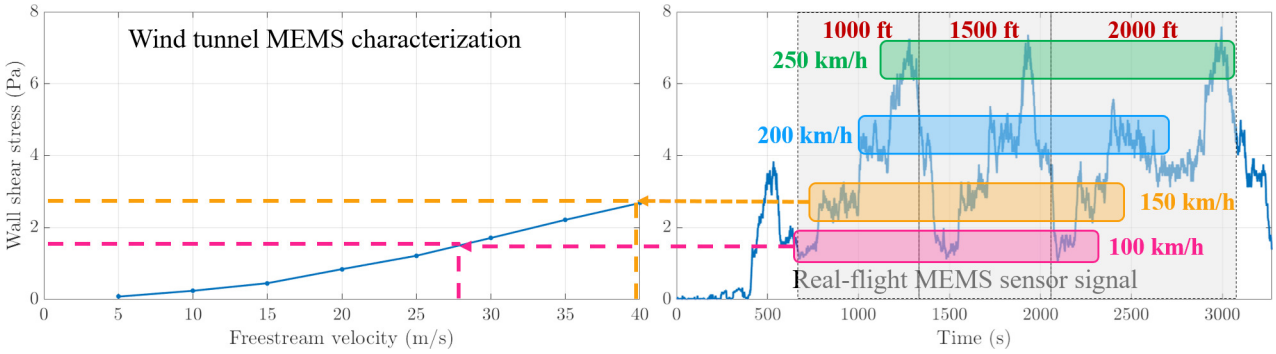

Figure 6.11: Comparison of the response of a calorimetric wall shear stress sensor in the turbulent boundary layer wind tunnel (left) with the flight measurements for different altitudes and airspeeds (right).

composed of several phases. The first phase up to 600 s corresponds to the airplane taxiing and taking off. The second phase highlights the velocity steps at the different altitudes from 100 km/h to 250 km/h at 1000 ft, 1500 ft and 2000 ft. Velocities of 100 km/h and 150 km/h yield similar wall shear stress measurements as the one obtained during the sensor calibration for the same velocities, pointing out the reliability of the sensor in uncontrolled flow conditions. Oscillations in the measurements come from the turbulent air conditions and their influence on the airplane velocity during the flight. Also, based on the pilot feedback, maintaining the velocity of 250 km/h was difficult because of these turbulent air conditions and because of the airplane inherent velocity limits. Therefore, velocity steps at 250 km/h are less visible than the others. Moreover, effects of the altitude can not be observed in these measurements as the altitude variations are only of 1000 ft, yielding in the standard atmospheric conditions a variation of 1.98°C. Effects of the temperature may be seen during future measurements to be carried out on a fighter aircraft.

A frequency analysis of the data is carried out to complete the previous observations. Figure 6.12 presents the PSD for the different airspeeds considered during the flights. The blue curve corresponds to the spectrum derived from the measurements when the airplane is at rest. Other curves correspond to the spectra at the different velocities and indicate fundamental frequencies of 76 Hz, 87.5 Hz, 92 Hz and 106 Hz respectively for 100 km/h, 150 km/h,

200 km/h and 250 km/h. These frequencies are in agreement with the engine constructor documentation. Harmonics of these frequencies can also be observed in the spectra.

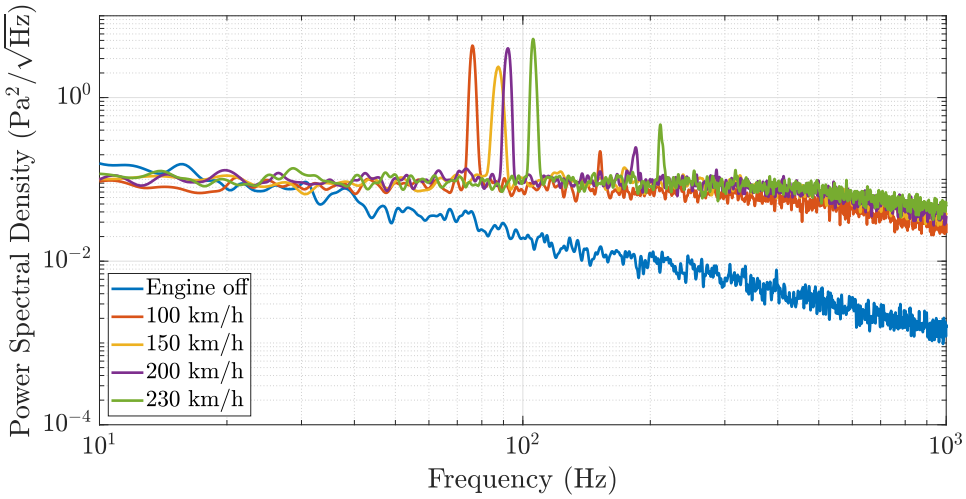

Figure 6.12: Spectra of the micro sensor measurements during the different flight phases.

Further measurements are carried out during a stall manoeuvre of the airplane. Both the wall shear stress evolution and the spectrogram derived from these measurements are presented in Figure 6.13. During the 60 first seconds the pilot prepares the manoeuvre. During the next 15 seconds, the pilots reduces the throttle and pulls up to maintain a constant altitude. The airplane loses velocity and therefore lift resulting in the decrease of the wall shear stress measurements. Once the stall angle of attack is reached, the airplane nose dives. The

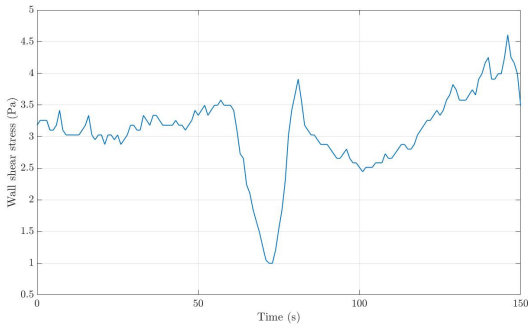

(a) Wall shear stress evolution with time.

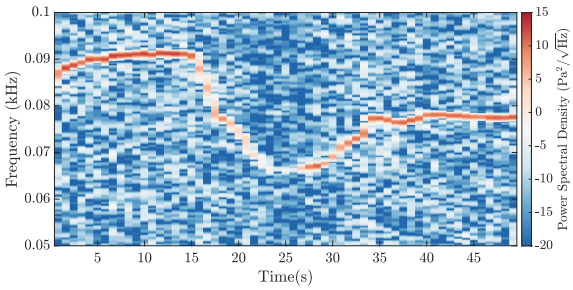

(b) Spectrogram of the wall shear stress during stall.

Figure 6.13: Wall shear stress evolution with time (a) and spectrum (b) during the airplane stall manoeuvre.

airplane recovers speed and lift, therefore the wall shear stress increases again. This phase corresponds to times between 75 s and 80 s. Then the pilot stabilizes the airplane altitude converting the accumulated velocity into altitude. When the desired altitude is reached, the pilot progressively increases the throttle. This phase corresponds to the end of Figure 6.13a. Figure 6.13b corresponds to the spectrogram derived from data framed in the time serie. As previously described, the frequency, corresponding to engine signature through the propeller, decreases, reaches a minimum and increases again. The constant frequency between 33 s and

50 s is lower than the one between 0 s and 15 s because of the kinematic energy accumulated during the stall.

Analysis of the spectra derived during the take-off and landing phases also highlight the evolution of the propeller rotations per minute. Figure 6.14 presents the spectra of these phases. During take off, the frequency increases progressively and reaches a nominal value - in agreement with the engine documentation - of 99 Hz. In the spectrogram, sub-harmonics, which progressively disappear, can be observed. They might be due to the vortices detaching from the propeller tips as already observed by Kitaplioglu [191]. Considering the landing phase, the spectrogram indicates a progressive decrease in the frequency, corresponding to the pilot reducing the throttle down to the engine stop, as asked during the manoeuvre.

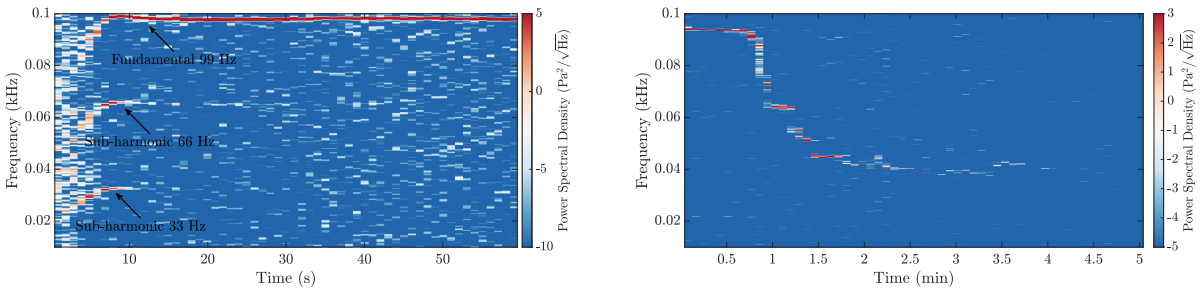

(a) Take-off spectrogram.

(b) Landing spectrogram.

Figure 6.14: Spectrograms of the airplane take-off (a) and landing (b).

The flight measurements carried out on a microlight aircraft prove the micro sensor robustness and reliability. Similar results to those obtained in wind tunnel are retrieved regarding both the wall shear stress time series and spectrum analyses. Despite effects of temperature on the measurements could not be observed, these initial results will be completed by flight testings to be carried out on a MB-339 fighter aircraft.

6.2 Integration of MEMS sensors into a microvalve

Further sensor developments focus on the integration of a micro-processed hot film inside the channel of a microvalve. Open-loop measurements are carried out in order to characterize the inside actuator transfer function. Based on this identified transfer function, the aim is to implement the closed-loop control of the actuator, in order to flatten the gain curve. A L-DDC approach is considered for the closed-loop implementation, similarly to the strategy employed in Chapter 3.

6.2.1 Sensor fabrication process and integration

A micro sensor adapted to the microvalve channel is designed and mircomachined. It consists in a hot film placed in the microvalve microchannel. The following steps describe the fabrication process, schematically presented in Figure 6.15.

a Firstly, a SiO_2 layer is deposited by LPCVD.

b Secondly, the measurement wire is patterned by photolithography and Pd/Pt metal is deposited by evaporation.

c Thirdly, micro-bridges are etched by plasma to create the suspended structure. The plasma is composed of CF_4 and CHF_3.

d Finally, the substrate is etched by XeF_2, to create the suspended structure.

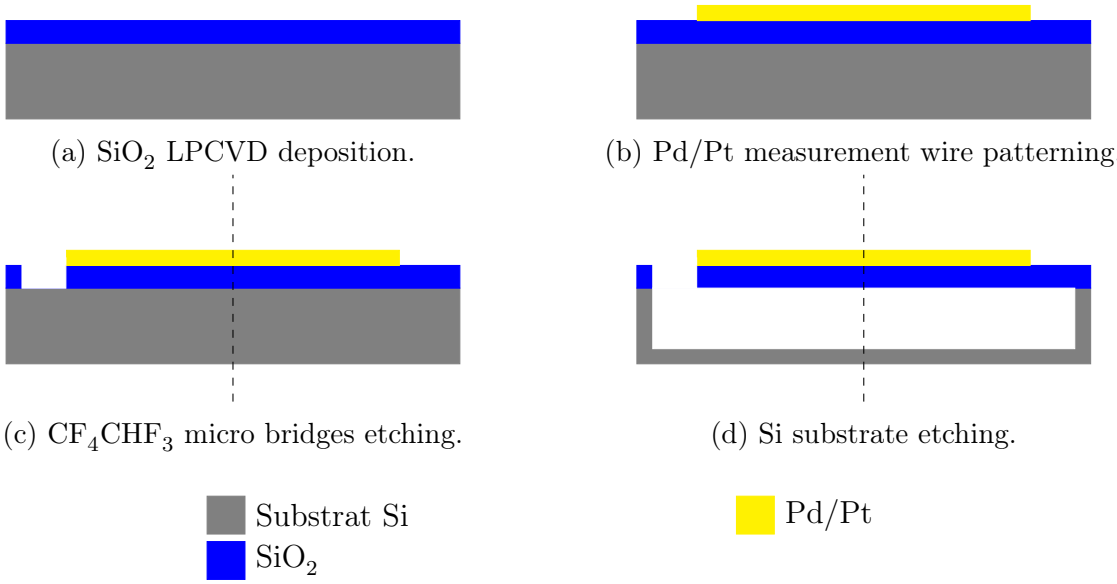

(a) SiO_2 LPCVD deposition.

(b) Pd/Pt measurement wire patterning.

(c) CF_4CHF_3 micro bridges etching.

(d) Si substrate etching.

(e) Materials legend.

Figure 6.15: Fabrication steps of the MEMS hot film to be integrated inside a microvalve.

The micro sensors are processed on a 3 inches wafer presented in Figure 6.16a, alongside with one chip, after the wafer is sliced. Gold pads, seen at the bottom of Figure 6.16b ensure the electrical contact between the sensor and the supply electronics, consisting in a constant temperature anemometer electronics. Unlike the microvalves presented in Chapter 2, for an easier integration of the micro sensor inside the actuator, the microchannel is built in a PCB plate of depth 350 μm, as depicted in Figure 6.16c. The sensor chip and the PCB microchannel are soldered together and the microvalve is assembled. Once integrated, open and closed-loop measurements are carried out on the new microvalve design.

6.2.2 Open-loop measurements

The microvalve is fixed on a support and supplied with both pressurized air and an electrical driving signal. As previously described, the micro sensor is integrated inside the microvalve, providing information on the flow inside the microchannel. A hot wire Dantec 55P11 probe is placed at the actuator outlet, yielding information on the outlet flow. As the purpose of the measurements is to demonstrate the possibility to flatten the actuator gain curve through closed-loop control, no calibration of the hot wire probe or the inside sensor is effected. Recorded voltages are therefore considered as representative of the velocity observed by the different sensors. The acquisition of data is performed with a Dspace MicroLabBox with

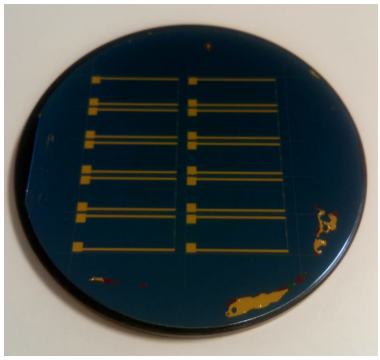

(a) Wafer used during the fabrication process.

(b) Micro sensor chip.

(c) Microvalve PCB microchannel.

Figure 6.16: Pictures the 3 inches wafer on which the micro sensors are fabricated (a), of a micro sensor chip with the Au pads (b) and of the microvalve microchannel (c).

a sampling frequency $f_s = 20$ kHz. First measurements focus on characterizing the inside sensor behavior. Examples of measurements are presented in Figure 6.17. The microvalve is driven with either a sine wave or a square excitation signal of frequency 10 Hz and amplitude 2 V. In each case, the blue curve corresponds to the excitation signal while the red one corresponds to the inside sensor response and exhibit the ability of the sensor to follow the pulsed flow response to the excitation signal.

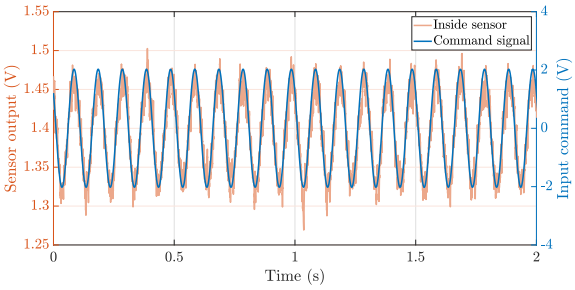

(a) Sensor response to a sine wave.

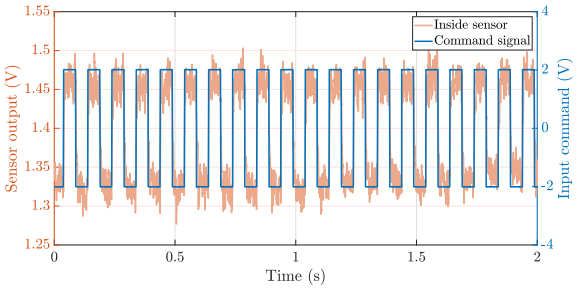

(b) Sensor response to a square wave.

Figure 6.17: Response of the inside sensor to a sine wave (a) and to a triangle (b) of frequency 10 Hz and amplitude 2V exciting the microvalve.

For a dynamical characterization of the microvalve with the inside actuator, a logarithmic frequency sweep of 300 s between 20 Hz and 380 Hz is employed for a similar calculation of the system transfer function as the one presented in Chapter 4. In this case, the transfer function is define as the ratio between the inside sensor output and the excitation signal. Figure 6.18 illustrates both the driving signal and inside sensor measurement spectrograms. The transfer function defined in this case as the ratio between the sensor output and the driving signal input is presented in Figure 6.19. Similarly to Figure 4.6, the transfer function gain curve exhibits two anti-resonances respectively at 100 Hz and 300 Hz.
Aim of the closed-loop strategy is to flatten the gain curve and eliminate the first anti-resonance. Considering the L-DDC strategy, previously described in Chapter 3, data pre-

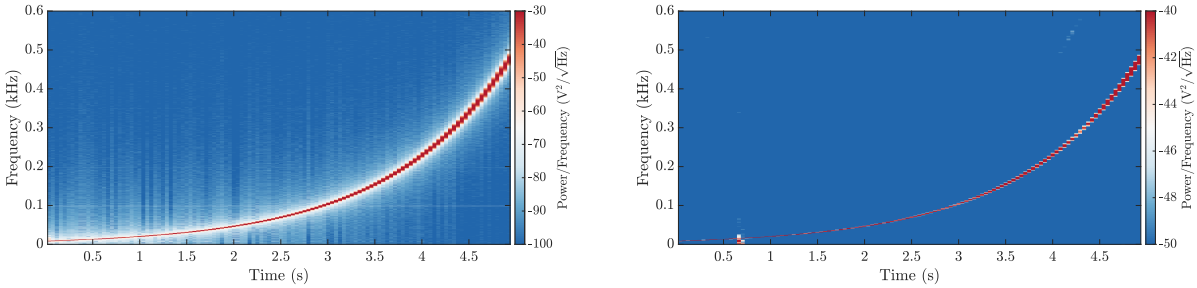

(a) Input sweep spectrogram.

(b) Sensor output spectrogram.

Figure 6.18: Spectrograms of the logarithmic sweep input (a) and inside sensor measurements (b).

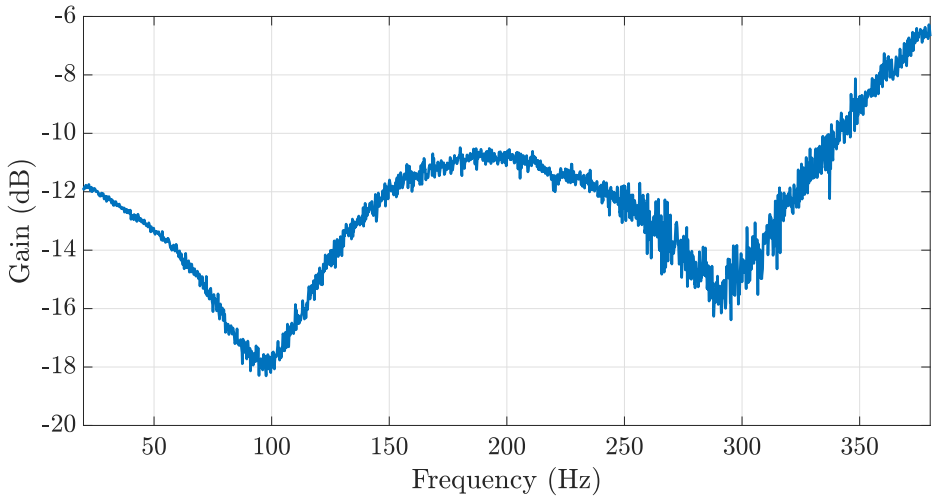

Figure 6.19: Gain of the microvalve transfer function based on the inside micro sensor.

sented in Figure 6.19 constitute the raw data:

$$\{z_k, \boldsymbol{\Phi}_k\}_{k=1}^{N}, \tag{6.5}$$

required for the finding of an appropriate linear controller.

The objective closed-loop transfer function $\mathbf{M}$ is defined as a constant $\mathbf{M}(\mathbf{s}) = \mathbf{0.2512}$, such that the closed-loop transfer function of the microvalve would be characterized by a flat gain curve of gain -12 dB for frequencies between 20 Hz and 200 Hz. The ideal controller $\mathbf{K}^\star$, defined in Equation (3.2), is computed. The reduced order controller $\mathbf{K}_r$ is computed for an order $r = 6$. Figure 6.20 illustrates the controller gain after time-domain discretization with a frequency of 10 kHz.

6.2.3 Closed-loop control of a microvalve

Once designed, the controller is implemented in the real-time controller Dspace MicroLab-Box. The aim is to maintain a given amplitude, varying with time, on the inside sensor

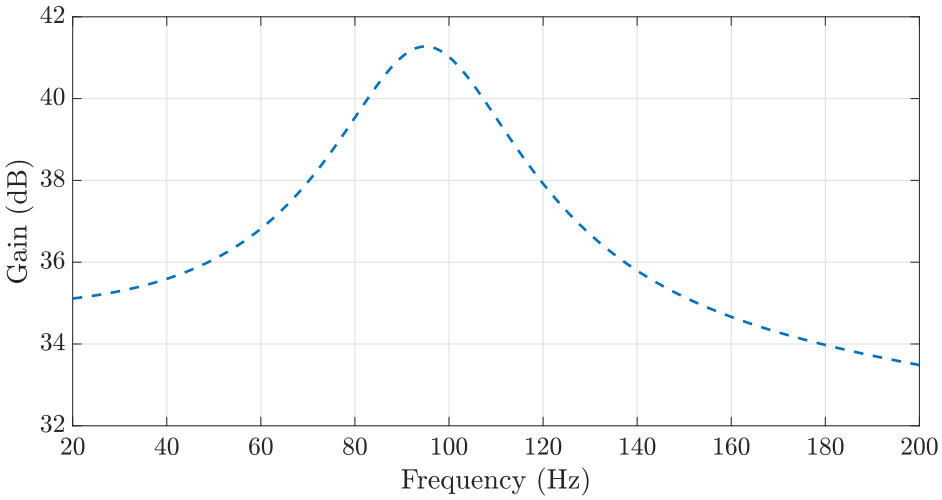

Figure 6.20: Gain of the discretized controller designed based on the inside controller measurements.

output. For a fixed driving signal amplitude and for sine waves of 20 Hz and 100 Hz, the controller command signals are compared in Figure 6.21.

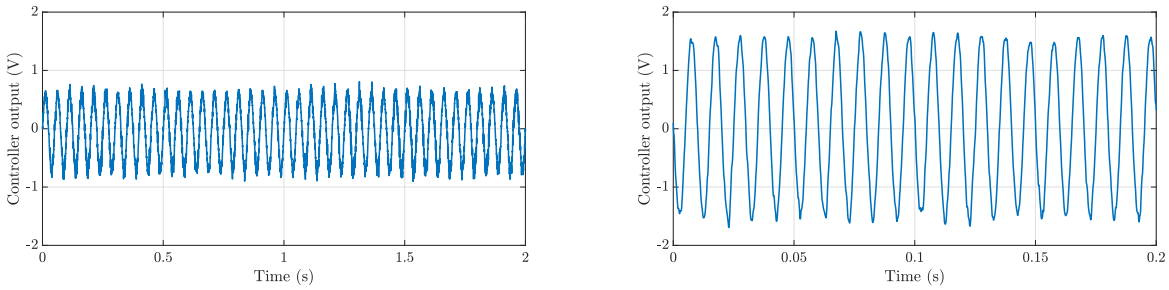

(a) Controller output command signal: sine wave of frequency 20 Hz.

(b) Controller output command signal: sine wave of frequency 100 Hz.

Figure 6.21: Comparison of the controller output command signals for sine wave driving signals of frequency 20 Hz (a) and 100 Hz (b).

As expected, the command signal amplitude is higher for an excitation signal of 100 Hz. To completely characterize the closed loop system, its transfer function is computed based on the use of a logarithmic sweep excitation signal, similar to the one used for the system open loop identification. A comparison of the open and closed loop transfer functions is presented in Figure 6.22a for both the inside sensor. As observed, the anti-resonance at 100 Hz is reduced and the maximum difference in the gain for frequencies between 20 Hz and 200 Hz is of 2 dB, instead of 8 dB in the open-loop case. Regarding the hot wire transfer functions comparison in Figure 6.22b, the gain curve from 20 Hz to 200 Hz is flattened around a gain of 13 dB. Also, the controller compensates too much around 80 Hz for a completely flat gain curve, as observed in the gain bump of 1 dB around this frequency. For further improvements of the microvalve, a generalized controller could aim at damping both anti-resonances at 100 Hz and 300 Hz.

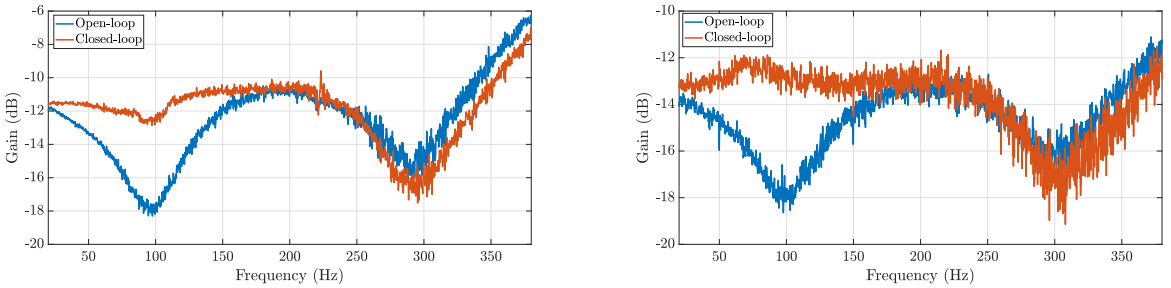

(a) Open and closed loop transfer functions gain computed with the inside micro sensor.

(b) Open and closed loop transfer functions gain computed with the outside hot wire.

Figure 6.22: Instrumented microvalve transfer function gain for the inside sensor (a) and the outside hot wire (b).

Conclusion

This 6th chapter presented developments carried out on the IEMN micro sensors and micro actuators technologies. Improvement of the micro sensors fabrication process is proposed through the optimization of the last etching phase, consisting in releasing the suspended structure. The robustness of the micro sensors is also proved through real-flight testing performed on a microlight aircraft. Regarding the microvalve, a sensor is integrated to the actuator design to carry out inside measurements. Based on these measurements, a controller is designed in order to flatten the gain curve around the first anti-resonance.

Further improvements of the microvalve design could on one part focus on the application of a controller flattening the entire actuator gain curve and on a second part, focus on increasing the microvalve velocity performances. To do so, for a microvalve supplied with a given inlet pressure, a counter pressure could be applied at the back of the pad, such that the pad reaches the same equilibrium position when no inlet pressure is applied. Therefore, no matter the inlet pressure used, the pad would always oscillate around the same equilibrium position. Coupling this design with the inner closed-loop control of the microvalve, the pulsed jets generated by the microvalve would have the same modulation depth on the entire actuator bandwith, whatever the supply pressure is.

Conclusion

The work presented in this manuscript aimed at the implementation of closed-loop control strategies on two canonical flow configurations: the control of flow separation/separated flow and the control of an open-cavity flow. Regarding the first application, contributions of this work consisted in the application of two control approaches over a plain flap with conventional actuators and sensors. Further contributions related to the use of MMMS microvalves consisted in the implementation of closed-loop control of an open-cavity flow with linear controllers.

Therefore, in Chapter 2, the two flow configurations on which experiments are carried out are presented. Regarding the control of flow separation and separated flow, experiments are conducted on a NACA 4412 plain flap. The motorized flap is instrumented with hot films integrated along the flap chord and with Festo valves on the flap leading edge. Because of the large mass flow rates required to control the flow, MEMS actuators could not be used on this configuration. The MEMS actuators are therefore integrated on an other flow configuration, the open-cavity, on which control of the flow instabilities is performed.

Chapter 3 focuses on the closed-loop test campaign carried out on the plain flap in the ONERA L1 wind tunnel. On the NACA 4412 configuration equipped with conventional actuators and sensors, two simple but yet efficient control approaches are considered: one data driven leading to the synthesis of a linear integral controller and a second one being a phenomenological/model-driven approach (derived from the biological domain), leading to a non-linear positive integral control law. Tracking of a reference value defined with respect to the hot films measurements with both controllers lead to the delay of flow separation and once the flow was partially separated, the recirculation bubble size growth was limited by the controllers.

In Chapter 4, the MMMS microvalves are integrated to the open-cavity in the ONERA S19 wind tunnel, for open-loop flow control experiments, the first step towards the closed-loop control implementation. Effects of both quasi-steady and pulsed jets have been investigated. It was demonstrated that quasi-steady jets could reduce the cavity fundamental oscillation amplitude down by 20 dB for a freestream velocity of 20 m/s and for a global mass flow rate of 25 L/min. Regarding pulsed jets, a locking phenomenon was highlighted for harmonic forcing frequencies close to the cavity resonant frequency. It was outlined that the capture bandwith on which the cavity resonant frequency is shifted towards the actuators frequency depends on the forcing driving pressure ΔP and on the amplitude of the electrical driving signal. Nevertheless, the capture bandwidth only spreads over few Hz, showing the authority limit of the pulsed jet on the flow in open-loop experiments. Harmonic forcings with actu-

ation frequencies away from the cavity resonant frequency were only able to further reduce the cavity resonant frequency amplitude by few dB. Effects of the pulsed jets do not enable to perform open-loop flow control experiments on the open-cavity flow as actuators do not show enough authority to trigger non-linearities in the flow, such that these non-linearities have effects on the flow dynamics fundamental frequency. However, the actuators may be efficient during closed-loop control experiments as less power is required to control the flow, as the oscillatory flow dynamics fall into the controllable bandwith of the actuators and as the actuators can be driven with any type of signals.

Chapter 5 focuses on the closed-loop implementation of the open-cavity flow with the MMMS microvalves. Flow control was performed for flow regimes characterized by low frequency oscillations in the actuators bandwith. The first step consisted in the identification of a transfer function between the actuators and the sensors. The open-cavity was forced with small amplitudes forcings, ensuring a linear response. To obtain the frequency response of the open-cavity flow, measurements are performed with multi-frequency signals consisting in frequency linear sweeps. Variability in these measurements is low because the frequency in these input signals varies at a quasi-static rate and at any given time, the flow is considered as forced by a purely harmonic input. This type of signal is therefore ideal for identification because the entire frequency range $120 - 240$ Hz may be identified using less than 10 realizations to converge the mean response to a good precision. This is indeed much more economical than using purely harmonic forcings. Then, a structured H_∞ loop-shaping approach is employed to synthesize a linear controller. For a freestream velocity of 20 m/s and for a forcing mass flow rate of 10 L/min, the cavity resonant frequency amplitude was reduced down by 9 dB compared to the open-loop case for the same forcing mass flow rate. Further experiments show the controller robustness towards modification of the freestream velocity by $\pm 5\%$ and indicate that a reduced number of microvalves can be used to reach the same reduction in the open-cavity resonance SPL. This study shows the straightforward use of the MMMS microvalves (with the ability to be driven with any type of signal, as required in closed-loop) in the closed-loop control of a periodic open-cavity flow and constitutes a first step towards the closed-loop control of more complex flows such as quasi-periodic open-cavity flows or the control of different flow configurations such as the jet flows, as will be considered in future studies.

In Chapter 6, the focus is brought onto the TRL increase from 4 to 5-6 of the disruptive MEMS sensors technologies developed at the IEMN, designed for flow applications. The robustness of the micro sensors is notably proved through real-flight testing performed on a microlight aircraft. For a demonstration of the TRL increase of actuators technologies, an in-situ monitoring of a microvalve is proposed through the integration of a MEMS calorimetric sensor. The closed-loop control is implemented thanks to the data driven approach considered on the plain flap configuration.

Further improvements of the microvalve design could focus on increasing the microvalve velocity outlet without modifying its modulation ability. To do so, for a microvalve supplied with a given inlet pressure, a counter pressure could be applied at the back of the pad, such that the pad reaches the same equilibrium position when no inlet pressure is applied. Therefore, no matter the inlet pressure used, the pad would always oscillate around the

same equilibrium position. Such an improvement of the MMMS microvalves would benefit the flow control applications, as these actuators could on one side address the large mass flow rates required for the control of separated flow and on another side help implementing the closed-loop control of more complex flow configurations.

Bibliography

[1] ACARE. Adisory council for aviation research and innovation in europe, 2022. URL `https://www.acare4europe.org/`.

[2] Clean Aviation. Clean aviation joint undertaking, 2022. URL `https://www.clean-aviation.eu/about-us/who-we-are`.

[3] Mohamed Gad-el Hak. *Flow control: passive, active, and reactive flow management*. Cambridge University Press, Cambridge, 2000. OCLC: 247967659.

[4] Mark Sheplak, Catherine B McGinley, Eric F Spina, Ralph Stephens, Purnell Hopson, and Vincent Cruz. Micro-Sensor Thin-Film Anemometer, 1996.

[5] Mark Sheplak, John Seiner, Kenneth Breuer, and Martin Schmidt. A MEMS microphone for aeroacoustics measurements. In *37th Aerospace Sciences Meeting and Exhibit*, Reno,NV,U.S.A., January 1999. American Institute of Aeronautics and Astronautics.

[6] A. Padmanabhan, M. Sheplak, K.S. Breuer, and M.A. Schmidt. Micromachined sensors for static and dynamic shear-stress measurements in aerodynamic flows. In *Proceedings of International Solid State Sensors and Actuators Conference (Transducers '97)*, volume 1, pages 137–140, Chicago, IL, USA, 1997. IEEE.

[7] T. Nishida, L. Cattafest, M. Sheplak, and D. Arnold. MEMS-based acoustic array technology. In *40th AIAA Aerospace Sciences Meeting & Exhibit*, Reno,NV,U.S.A., 2002. American Institute of Aeronautics and Astronautics.

[8] Clyde Warsop. AEROMEMS-II: A European Research Effort to Develop MEMS Based Flow Control Technologies. In *2nd AIAA Flow Control Conference*, Portland, Oregon, June 2004. American Institute of Aeronautics and Astronautics.

[9] International Energy Agency. Fossil fuel demand in the Stated Policies Scenario 1900-2050, 2022. URL `https://www.iea.org/data-and-statistics/charts/fossil-fuel-demand-in-the-stated-policies-scenario-1900-2050`. IEA. Licence: CC BY 4.0.

[10] G MacMynowski, D and D Williams. Flow Control Terminology, Fundamentals and Applications of Modern Flow Control. *AIAA Journal*, pages 59–71, 2009.

[11] Walter Tollmien, Hermann Schlichting, Henry Görtler, and F. W. Riegels. Über Flüssigkeitsbewegung bei sehr kleiner Reibung. In F. W. Riegels, editor, *Ludwig Prandtl*

Gesammelte Abhandlungen, pages 575–584. Springer Berlin Heidelberg, Berlin, Heidelberg, 1961.

[12] P. W. Bearman and J. K. Harvey. Control of circular cylinder flow by the use of dimples. *AIAA Journal*, 31(10):1753–1756, October 1993.

[13] J. Reuther, A. Jameson, J. Farmer, L. Martinelli, and D. Saunders. Aerodynamic shape optimization of complex aircraft configurations via an adjoint formulation. In *34th Aerospace Sciences Meeting and Exhibit*, Reno,NV,U.S.A., January 1996. American Institute of Aeronautics and Astronautics.

[14] E. M. Papoutsis-Kiachagias, V. G. Asouti, K. C. Giannakoglou, K. Gkagkas, S. Shimokawa, and E. Itakura. Multi-point aerodynamic shape optimization of cars based on continuous adjoint. *Structural and Multidisciplinary Optimization*, 59(2): 675–694, February 2019.

[15] John C Lin. Review of research on low-profile vortex generators to control boundary-layer separation. *Progress in Aerospace Sciences*, 38(4-5):389–420, May 2002.

[16] Roy Myose, Michael Papadakis, and Ismael Heron. Gurney Flap Experiments on Airfoils, Wings, and Reflection Plane Model. *Journal of Aircraft*, 35(2):206–211, March 1998.

[17] Kevin Garry. Introduction to Flow Control Techniques. *Part of lecture given at Cranfield University on Technology for Sustainable Aviation*, 2019.

[18] Louis N. Cattafesta and Mark Sheplak. Actuators for Active Flow Control. *Annual Review of Fluid Mechanics*, 43(1):247–272, January 2011.

[19] Sven Grundmann and Cameron Tropea. Active cancellation of artificially introduced Tollmien–Schlichting waves using plasma actuators. *Experiments in Fluids*, 44(5):795–806, May 2008.

[20] Ercan Atam, Lionel Mathelin, and Laurent Cordier. Identification-Based Closed-Loop Control Strategies for a Cylinder Wake Flow. *IEEE Transactions on Control Systems Technology*, 25(4):1488–1495, July 2017.

[21] Colin Leclercq, Fabrice Demourant, Charles Poussot-Vassal, and Denis Sipp. Linear iterative method for closed-loop control of quasiperiodic flows. *Journal of Fluid Mechanics*, 868:26–65, June 2019.

[22] Steven L. Brunton and Bernd R. Noack. Closed-Loop Turbulence Control: Progress and Challenges. *Applied Mechanics Reviews*, 67(5):050801, September 2015.

[23] Mark Pastoor, Lars Henning, Bernd R. Noack, Rudibert King, and Gilead Tadmor. Feedback shear layer control for bluff body drag reduction. *Journal of Fluid Mechanics*, 608:161–196, August 2008.

[24] Jean-François Beaudoin, Olivier Cadot, Jean-Luc Aider, and José-Eduardo Wesfreid. Drag reduction of a bluff body using adaptive control methods. *Physics of Fluids*, 18 (8):085107, August 2006.

[25] Louis N. Cattafesta, Qi Song, David R. Williams, Clarence W. Rowley, and Farrukh S. Alvi. Active control of flow-induced cavity oscillations. *Progress in Aerospace Sciences*, 44(7-8):479–502, October 2008.

[26] P. Yan, Hitay Ozbay, Onder Efe, Mo Samimy, Edgar Caraballo, Jim DeBonis, M. Debiasi, X. Yuan, R. Camphouse, J. Myatt, A. Serrani, and J. Malone. Controller Design for Active Closed-Loop Control of Cavity Flows. In *42nd AIAA Aerospace Sciences Meeting and Exhibit*, Reno, Nevada, January 2004. American Institute of Aeronautics and Astronautics.

[27] Miroslav Krstic, Ashish Krupadanam, and Clas Jacobson. Self-Tuning Control of a Nonlinear Model of Combustion Instabilities. *IEEE TRANSACTIONS ON CONTROL SYSTEMS TECHNOLOGY*, 7(4):13, 1999.

[28] Nick Killingsworth and Miroslav Krstic. PID tuning using extremum seeking: online, model-free performance optimization. *IEEE Control Systems*, 26(1):70–79, February 2006.

[29] Pierre-Yves Passaggia, Asamaning Quansah, Nicolas Mazellier, Guy Y. Cornejo Maceda, and Azeddine Kourta. Real-time feedback stall control of an airfoil at large Reynolds numbers using linear genetic programming. *Physics of Fluids*, 34(4):045108, April 2022.

[30] Guy Cornejo Maceda and Yiqing Li. Gradient-Enriched Machine Learning Control Fer Shear Flow Stabilization. *12th International Sumposium on Turbulence and Shear Flow Phenomena (TSFP12)*, 2022.

[31] N. Gautier, J.-L. Aider, T. Duriez, B. R. Noack, M. Segond, and M. Abel. Closed-loop separation control using machine learning. *Journal of Fluid Mechanics*, 770:442–457, May 2015.

[32] Antoine Debien, Kai A. F. F. von Krbek, Nicolas Mazellier, Thomas Duriez, Laurent Cordier, Bernd R. Noack, Markus W. Abel, and Azeddine Kourta. Closed-loop separation control over a sharp edge ramp using genetic programming. *Experiments in Fluids*, 57(3):40, March 2016.

[33] M Efe, Marco Debiasi, Peng Yan, Hitay Ozbay, and Mo Samimy. Control of Subsonic Cavity Flows by Neural Networks - Analytical Models and Experimental Validation. In *43rd AIAA Aerospace Sciences Meeting and Exhibit*, Reno, Nevada, January 2005. American Institute of Aeronautics and Astronautics.

[34] Denis Sipp and Peter J. Schmid. Linear Closed-Loop Control of Fluid Instabilities and Noise-Induced Perturbations: A Review of Approaches and Tools1. *Applied Mechanics Reviews*, 68(2):020801, March 2016.

[35] Kimon Roussopoulos and Peter A. Monkewitz. Nonlinear modelling of vortex shedding control in cylinder wakes. *Physica D: Nonlinear Phenomena*, 97(1-3):264–273, October 1996.

[36] Eric Lauga and Thomas R. Bewley. Performance of a linear robust control strategy on a nonlinear model of spatially developing flows. *Journal of Fluid Mechanics*, 512, August 2004.

[37] Jeremy A. Dahan, A. S. Morgans, and S. Lardeau. Feedback control for form-drag reduction on a bluff body with a blunt trailing edge. *Journal of Fluid Mechanics*, 704: 360–387, August 2012.

[38] Colin Leclercq and Denis Sipp. Mean resolvent operator of statistically steady flows. Technical Report arXiv:2210.07104, arXiv, October 2022. arXiv:2210.07104 [physics] type: article.

[39] Sanjay S. Joshi, Jason L. Speyer, and John Kim. A systems theory approach to the feedback stabilization of infinitesimal and finite-amplitude disturbances in plane Poiseuille flow. *Journal of Fluid Mechanics*, 332:157–184, February 1997.

[40] Miroslav Krstic and Andrzej Banaszuk. Multivariable adaptive control of instabilities arising in jet engines. *Control Engineering Practice*, 14(7):833–842, July 2006.

[41] Kenzo Sasaki, Pierluigi Morra, Nicoló Fabbiane, André V. G. Cavalieri, Ardeshir Hanifi, and Dan S. Henningson. On the wave-cancelling nature of boundary layer flow control. *Theoretical and Computational Fluid Dynamics*, 32(5):593–616, October 2018.

[42] J. Doyle. Guaranteed margins for LQG regulators. *IEEE Transactions on Automatic Control*, 23(4):756–757, 1978.

[43] Lennart Löfdahl and Mohamed Gad-el Hak. MEMS applications in turbulence and flow control. *Progress in Aerospace Sciences*, 35(2):101–203, February 1999.

[44] Nicolas Benard, Eric Moreau, John Griffin, and Louis N. Cattafesta III. Slope seeking for autonomous lift improvement by plasma surface discharge. *Experiments in Fluids*, 48(5):791–808, May 2010.

[45] Ye Tian, Louis Cattafesta, and Rajat Mittal. Adaptive Control of Separated Flow. In *44th AIAA Aerospace Sciences Meeting and Exhibit*, Reno, Nevada, January 2006. American Institute of Aeronautics and Astronautics.

[46] Leonard Shaw. Active control for cavity acoustics. In *4th AIAA/CEAS Aeroacoustics Conference*, Toulouse,France, June 1998. American Institute of Aeronautics and Astronautics.

[47] Jonathan Poggie, Carl P. Tilmann, Peter M. Flick, Joseph S. Silkey, Bradley A. Osbourne, Gregory Ervin, Dragan Maric, Siva Mangalam, and Arun Mangalam. Closed-Loop Stall Control System. *Journal of Aircraft*, 47(5):1747–1755, September 2010.

[48] A. Berns, U. Buder, E. Obermeier, A. Wolter, and A. Leder. AeroMEMS sensor array for high-resolution wall pressure measurements. *Sensors and Actuators A: Physical*, 132(1):104–111, November 2006.

[49] Susumu Sugiyama, Mitsuharu Takigawa, and Isemi Igarashi. Integrated piezoresistive pressure sensor with both voltage and frequency output. *Sensors and Actuators*, 4: 113–120, January 1983.

[50] Liang Lou, Songsong Zhang, Woo-Tae Park, J M Tsai, Dim-Lee Kwong, and Chengkuo Lee. Optimization of NEMS pressure sensors with a multilayered diaphragm using silicon nanowires as piezoresistive sensing elements. *Journal of Micromechanics and Microengineering*, 22(5):055012, May 2012.

[51] Shou-En Zhu, Murali Krishna Ghatkesar, Chao Zhang, and G. C. A. M. Janssen. Graphene based piezoresistive pressure sensor. *Applied Physics Letters*, 102(16): 161904, April 2013.

[52] M. Zagnoni, A. Golfarelli, S. Callegari, A. Talamelli, V. Bonora, E. Sangiorgi, and M. Tartagni. A non-invasive capacitive sensor strip for aerodynamic pressure measurement. *Sensors and Actuators A: Physical*, 123-124:240–248, September 2005.

[53] A.D. Sundararajan and S.M. Rezaul Hasan. Release etching and characterization of MEMS capacitive pressure sensors integrated on a standard 8-metal 130 nm CMOS process. *Sensors and Actuators A: Physical*, 212:68–79, June 2014.

[54] Hyungdae Bae, David Yun, Haijun Liu, Douglas A. Olson, and Miao Yu. Hybrid Miniature Fabry–Perot Sensor with Dual Optical Cavities for Simultaneous Pressure and Temperature Measurements. *Journal of Lightwave Technology*, 32(8):1585–1593, April 2014.

[55] Jonghyun Eom, Chang-Ju Park, Byeong Ha Lee, Jong-Hyun Lee, Il-Bum Kwon, and Euiheon Chung. Fiber optic Fabry–Perot pressure sensor based on lensed fiber and polymeric diaphragm. *Sensors and Actuators A: Physical*, 225:25–32, April 2015.

[56] Wook Choi, Junwoo Lee, Yong Kyoung Yoo, Sungchul Kang, Jinseok Kim, and Jeong Hoon Lee. Enhanced sensitivity of piezoelectric pressure sensor with microstructured polydimethylsiloxane layer. *Applied Physics Letters*, 104(12):123701, March 2014.

[57] Stephen Horowitz, Toshikazu Nishida, Louis Cattafesta, and Mark Sheplak. Development of a micromachined piezoelectric microphone for aeroacoustics applications. *The Journal of the Acoustical Society of America*, 122(6):3428–3436, December 2007.

[58] Vijay Chandrasekharan, Jeremy Sells, Jessica Meloy, David P. Arnold, and Mark Sheplak. A Microscale Differential Capacitive Direct Wall-Shear-Stress Sensor. *Journal of Microelectromechanical Systems*, 20(3):622–635, June 2011.

[59] Nicolas André, Bertrand Rue, Gilles Scheen, Denis Flandre, Laurent A. Francis, and Jean-Pierre Raskin. Out-of-plane MEMS-based mechanical airflow sensor co-integrated in SOI CMOS technology. *Sensors and Actuators A: Physical*, 206:67–74, February 2014.

[60] Tilmann Von Papen, Ulrich Buder, Ha Duong Ngo, and Ernst Obermeier. A second generation MEMS surface fence sensor for high resolution wall shear stress measurement. *Sensors and Actuators A: Physical*, 113(2):151–155, July 2004.

[61] Sebastian Grosse and Wolfgang Schröder. Dynamic wall-shear stress measurements in turbulent pipe flow using the micro-pillar sensor MPS3. *International Journal of Heat and Fluid Flow*, 29(3):830–840, June 2008.

[62] Dantec Dynamics. Dantec hot film. Technical report, Dantec Dynamics, 2022.

[63] C. Ghouila-Houri, J. Claudel, J.-C. Gerbedoen, Q. Gallas, E. Garnier, A. Merlen, R. Viard, A. Talbi, and P. Pernod. High temperature gradient micro-sensor for wall shear stress and flow direction measurements. *Applied Physics Letters*, 109(24):241905, December 2016.

[64] Cécile Ghouila-Houri, Quentin Gallas, Eric Garnier, Alain Merlen, Romain Viard, Abdelkrim Talbi, and Philippe Pernod. High temperature gradient calorimetric wall shear stress micro-sensor for flow separation detection. *Sensors and Actuators A: Physical*, 266:232–241, October 2017.

[65] Cécile Ghouila-Houri, Abdelkrim Talbi, Romain Viard, Quentin Gallas, Eric Garnier, Alain Merlen, and Philippe Pernod. High temperature gradient micro-sensors array for flow separation detection and control. *Smart Materials and Structures*, 28(12):125003, December 2019.

[66] Ibraheem Haneef, John D. Coull, Syed Zeeshan Ali, Florin Udrea, and Howard P. Hodson. Laminar to turbulent flow transition measurements using an array of SOI-CMOS MEMS wall shear stress sensors. In *2008 IEEE Sensors*, pages 57–61, Lecce, Italy, October 2008. IEEE.

[67] A Seifert, S Eliahu, D Greenblatt, and I Wygnanski. Use of Piezoelectric Actuators for Airfoil Separation Control. *AIAA JOURNAL*, 36(8):4, 1998.

[68] R. L. Sarno and M. E. Franke. Suppression of flow-induced pressure oscillations in cavities. *Journal of Aircraft*, 31(1):90–96, January 1994.

[69] W. P. Jeon and R. F. Blackwelder. Perturbations in the wall region using flush mounted piezoceramic actuators. *Experiments in Fluids*, 28(6):485–496, June 2000.

[70] Jose Mathew, Qi Song, Bhavani V. Sankar, Mark Sheplak, and Louis N. Cattafesta. Optimized Design of Piezoelectric Flap Actuators for Active Flow Control. *AIAA Journal*, 44(12):2919–2928, December 2006.

[71] Louis Cattafesta, Sanjay Garg, and Deepak Shukla. Development of Piezoelectric Actuators for Active Flow Control. *AIAA Journal*, page 7, 2001.

[72] Thomas C. Corke, Martiqua L. Post, and Dmitry M. Orlov. SDBD plasma enhanced aerodynamics: concepts, optimization and applications. *Progress in Aerospace Sciences*, 43(7-8):193–217, October 2007.

[73] Ryan Durscher and Subrata Roy. Novel Multi-Barrier Plasma Actuators for Increased Thrust. In *48th AIAA Aerospace Sciences Meeting Including the New Horizons Forum and Aerospace Exposition*, Orlando, Florida, January 2010. American Institute of Aeronautics and Astronautics.

[74] A Kurz, S Grundmann, C Tropea, M Forte, A Seraudie, O Vermeersch, D Arnal, R Goldin, and R King. Boundary Layer Transition Control using DBD Plasma Actuators. *Aerospace Lab Journal*, page 9, 2013.

[75] Chris Rethmel, Jesse Little, Keisuke Takashima, Aniruddha Sinha, Igor Adamovich, and Mo Samimy. Flow Separation Control Using Nanosecond Pulse Driven DBD Plasma Actuators. *International Journal of Flow Control*, 3(4):213–232, December 2011.

[76] Roman Seele, Philipp Tewes, René Woszidlo, Michael A. McVeigh, Nathaniel J. Lucas, and Israel J. Wygnanski. Discrete Sweeping Jets as Tools for Improving the Performance of the V-22. *Journal of Aircraft*, 46(6):2098–2106, November 2009.

[77] Edward A. Whalen, Doug S. Lacy, John C. Lin, Marlyn Y. Andino, Anthony E. Washburn, Emilio C. Graff, and Israel J. Wygnanski. Performance Enhancement of a Full-Scale Vertical Tail Model Equipped with Active Flow Control. In *53rd AIAA Aerospace Sciences Meeting*, Kissimmee, Florida, January 2015. American Institute of Aeronautics and Astronautics.

[78] D. McCormick. Boundary layer separation control with directed synthetic jets. In *38th Aerospace Sciences Meeting and Exhibit*, Reno,NV,U.S.A., January 2000. American Institute of Aeronautics and Astronautics.

[79] Hassan Nagib, John Kiedaisch, Israel J Wygnanski, Aaron Stalker, Tom Wood, and Michael McVeigh. First-In-Flight Full-Scale Application of Active Flow Control: The XV-15 Tiltrotor Download Reduction. *NATO Report*, 2004.

[80] C. Chovet, M. Lippert, L. Keirsbulck, and J.-M. Foucaut. Dynamic characterization of piezoelectric micro-blowers for separation flow control. *Sensors and Actuators A: Physical*, 249:122–130, October 2016.

[81] L Gimeno, A Talbi, R Viard, A Merlen, P Pernod, and V Preobrazhensky. Synthetic jets based on micro magneto mechanical systems for aerodynamic flow control. *Journal of Micromechanics and Microengineering*, 20(7):075004, July 2010.

[82] Azeddine Kourta and Cédric Leclerc. Characterization of synthetic jet actuation with application to Ahmed body wake. *Sensors and Actuators A: Physical*, 192:13–26, April 2013.

[83] Jeffrey P. Bons, Rolf Sondergaard, and Richard B. Rivir. The Fluid Dynamics of LPT Blade Separation Control Using Pulsed Jets. *Journal of Turbomachinery*, 124(1): 77–85, January 2002.

[84] Huadong Lou, Farrukh S. Alvi, and Chiang Shih. Active and Adaptive Control of Supersonic Impinging Jets. *AIAA Journal*, 44(1):58–66, January 2006.

[85] F. S. Alvi, C. Shih, R. Elavarasan, G. Garg, and A. Krothapalli. Control of Supersonic Impinging Jet Flows Using Supersonic Microjets. *AIAA Journal*, 41(7):1347–1355, July 2003.

[86] Clyde Warsop, Martyn Hucker, Andrew J. Press, and Paul Dawson. Pulsed Air-jet Actuators for Flow Separation Control. *Flow, Turbulence and Combustion*, 78(3-4): 255–281, May 2007.

[87] Brian G. Kilberg, Daniel S. Contreras, Joseph Greenspun, and Kristofer S. J. Pister. MEMS aerodynamic control surfaces for millimeter-scale rockets. In *2017 International Conference on Manipulation, Automation and Robotics at Small Scales (MARSS)*, pages 1–5, Montreal, QC, July 2017. IEEE.

[88] Pedro Garcia Eijo, Roberto Sosa, Jean-Luc Aider, and Juan Martin Cabaleiro. Control of air micro-jets by the use of dielectric barrier discharges. *Sensors and Actuators A: Physical*, 305:111937, April 2020.

[89] Jean-Claude Gerbedoen, Abdelkrim Talbi, Romain Viard, Vladimir Preobrazhensky, Alain Merlen, Philippe Pernod, and Joint International Laboratory LIA LICS. Elaboration of Compact Synthetic Micro-jets Based on Micro Magneto-mechanical Systems for Aerodynamic Flow Control. *Procedia Engineering*, 120:740–743, 2015.

[90] Romain Viard, Abdelkrim Talbi, Cécile Ghouila-Houri, Azeddine Kourta, Alain Merlen, and Philippe Pernod. Magneto-mechanical micro-valve for active flow control. *Sensors and Actuators A: Physical*, 316:112387, December 2020.

[91] P. Pernod, V. Preobrazhensky, A. Merlen, O. Ducloux, A. Talbi, L. Gimeno, R. Viard, and N. Tiercelin. MEMS magneto-mechanical microvalves (MMMS) for aerodynamic active flow control. *Journal of Magnetism and Magnetic Materials*, 322(9-12):1642–1646, May 2010.

[92] Mohammed K. Ibrahim, Ryoji Kunimura, and Yoshiaki Nakamura. Mixing Enhancement of Compressible Jets by Using Unsteady Microjets as Actuators. *AIAA Journal*, 40(4):681–688, April 2002.

[93] Joshua Hogue, John Solomon, Michael Hays, Farrukh Alvi, and William Oates. Broadband pulsed flow using piezoelectric microjets. In *SPIE*, San Diego, California, USA, March 2010.

[94] Norman Schaeffler, Timothy Hepner, Gregory Jones, and Michael Kegerise. Overview of Active Flow Control Actuator Development at NASA Langley Research Center. In *1st Flow Control Conference*, St. Louis, Missouri, June 2002. American Institute of Aeronautics and Astronautics.

[95] Keith McManus, Hartmut Legner, and Steven Davis. Pulsed vortex generator jets for active control of flow separation. In *Fluid Dynamics Conference*, Colorado Springs,CO,U.S.A., June 1994. American Institute of Aeronautics and Astronautics.

[96] G. Godard and M. Stanislas. Control of a decelerating boundary layer. Part 3: Optimization of round jets vortex generators. *Aerospace Science and Technology*, 10(6): 455–464, September 2006.

[97] J.-R. Frutos, D. Vernier, F. Bastien, M. de Labachelerie, and Y. Bailly. An Electrostatically Actuated Valve for Turbulent Boundary Layer Control. In *IEEE Sensors, 2005.*, pages 82–88, Irvine, CA, USA, 2005. IEEE.

[98] Olivier Ducloux. *Microsystèmes Magnéto-Mécaniques (MMMS) pour le contrôle actif d'écoulements aérauliques.* PhD thesis, Ecole Centrale de Lille, 2006.

[99] Ducloux Olivier, Talbi Abdelkrim, Deblock Yves, Gimeno Leticia, Tiercelin Nicolas, Pernod Philippe, Preobrazhensky Vladimir, and Merlen Alain. Magnetically actuated microvalve for active flow control. *Journal of Physics: Conference Series*, 34:631–636, April 2006.

[100] Olivier Ducloux, Abdelkrim Talbi, Leticia Gimeno, Romain Viard, Philippe Pernod, Vladimir Preobrazhensky, and Alain Merlen. Self-oscillation mode due to fluid-structure interaction in a micromechanical valve. *Applied Physics Letters*, 91(3): 034101, July 2007.

[101] Eric Garnier, Marc Pruvost, Olivier Ducloux, Abdelkrim Talbi, Laeticia Gimeno, Philippe Pernod, R. Viard, A. Merlen, and V. Preobrazhensky. Pulsed-Jet Micro-Actuators Evaluation for Flow Separation Control. In *4th Flow Control Conference*, Seattle, Washington, June 2008. American Institute of Aeronautics and Astronautics.

[102] O Ducloux, R Viard, A Talbi, L Gimeno, Y Deblock, P Pernod, V Preobrazhensky, and A Merlen. A magnetically actuated, high momentum rate MEMS pulsed microjet for active flow control. *Journal of Micromechanics and Microengineering*, 19(11):115031, November 2009.

[103] F Lu and D Jensen. Potential Viability of a Fast-Acting Micro-Solenoid Valve for Pulsed Detonation Fuel Injection. In *41st Aerospace Sciences Meeting and Exhibit*, Reno, Nevada, January 2003. American Institute of Aeronautics and Astronautics.

[104] J. Kostas, J. M. Foucaut, and M. Stanislas. The Flow Structure Produced by Pulsed-jet Vortex Generators in a Turbulent Boundary Layer in an Adverse Pressure Gradient. *Flow, Turbulence and Combustion*, 78(3-4):331–363, June 2007.

[105] Vikas Kumar and Farrukh S. Alvi. Use of High-Speed Microjets for Active Separation Control in Diffusers. *AIAA Journal*, 44(2):273–281, February 2006.

[106] Jean-Luc Aider, Pierric Joseph, Tony Ruiz, Philippe Gilotte, Yoann Eulalie, Christophe Edouard, and Xavier Amandolese. Active flow control using pulsed micro-jets on a full-scale production car. *International Journal of Flow Control*, 6(1):1–20, March 2014.

[107] Sighard. F. Hoerner. *Fluid-Dynamics Lift: Practical Information on Aerodynamic and Hydrodynamics Lift.* Brick Town, N.J., Hoerner, 1985.

[108] Jie-Zhi Wu, Xi-Yun Lu, Andrew G. Denny, Meng Fan, and Jain-Ming Wu. Post-stall flow control on an airfoil by local unsteady forcing. *Journal of Fluid Mechanics*, 371: 21–58, September 1998.

[109] Philipp Tewes, Israel Wygnanski, and Anthony E. Washburn. Feedback-Controlled Forcefully Attached Flow on a Stalled Airfoil. *Journal of Aircraft*, 48(3):940–951, May 2011.

[110] N. Benard, L. N. Cattafesta, E. Moreau, J. Griffin, and J. P. Bonnet. On the benefits of hysteresis effects for closed-loop separation control using plasma actuation. *Physics of Fluids*, 23(8):083601, August 2011.

[111] Nathan Packard and Jeffrey Bons. Closed-Loop Separation Control of Unsteady Flow on an Airfoil at Low Reynolds Number. In *50th AIAA Aerospace Sciences Meeting including the New Horizons Forum and Aerospace Exposition*, Nashville, Tennessee, January 2012. American Institute of Aeronautics and Astronautics.

[112] Andrew J. Lombardi, Patrick O. Bowles, and Thomas C. Corke. Closed-Loop Dynamic Stall Control Using a Plasma Actuator. *AIAA Journal*, 51(5):1130–1141, May 2013.

[113] T. Shaqarin, C. Braud, S. Coudert, and M. Stanislas. Open and closed-loop experiments to identify the separated flow dynamics of a thick turbulent boundary layer. *Experiments in Fluids*, 54(2):1448, February 2013.

[114] Brian Allan, Jer-Nan Juang, David Raney, Avi Seifert, Latunia Pack, and Donald Brown. Closed-loop separation control using oscillatory flow excitation. Technical report 2000-32, NASA, 2000.

[115] Victor Troshin and Avraham Seifert. Performance recovery of a thick turbulent airfoil using a distributed closed-loop flow control system. *Experiments in Fluids*, 54(1):1443, January 2013.

[116] Byunghyun Lee, Minhee Kim, Byounghun Choi, Chongam Kim, H Jin Kim, and Kyoung Jin Jung. Closed-loop Active Flow Control of Stall Separation using Synthetic Jets. In *31st AIAA Applied Aerodynamics Conference*, San Diego, CA, June 2013. American Institute of Aeronautics and Astronautics.

[117] Jeremy T. Pinier, Julie M. Ausseur, Mark N. Glauser, and Hiroshi Higuchi. Proportional Closed-Loop Feedback Control of Flow Separation. *AIAA Journal*, 45(1): 181–190, January 2007.

[118] M. Garwon, L. H. Darmadi, F. Urzynicok, G. Barwolff, and R. King. Adaptive control of separated flows. In *2003 European Control Conference (ECC)*, pages 3231–3236, Cambridge, UK, September 2003. IEEE.

[119] Timothée Chabert, Julien Dandois, and Eric Garnier. Experimental closed-loop control of flow separation over a plain flap using slope seeking. *Experiments in Fluids*, 55(8): 1797, August 2014.

[120] Maxime Feingesicht, Andrey Polyakov, Franck Kerhervé, and Jean-Pierre Richard. Sliding Mode Control for Turbulent Flows. *IFAC-PapersOnLine*, 50(1):2690–2695, July 2017.

[121] Ralf Becker, Rudibert King, Ralf Petz, and Wolfgang Nitsche. Adaptive Closed-Loop Separation Control on a High-Lift Configuration Using Extremum Seeking. *AIAA Journal*, 45(6):1382–1392, June 2007.

[122] Ye Tian, Louis Cattafesta, and Rajat Mittal. Adaptive Control of Separated Flow. In *44th AIAA Aerospace Sciences Meeting and Exhibit*, Reno, Nevada, January 2006. American Institute of Aeronautics and Astronautics.

[123] Lars Henning and Rudibert King. Robust Multivariable Closed-Loop Control of a Turbulent Backward-Facing Step Flow. *Journal of Aircraft*, 44(1):201–208, January 2007.

[124] Rudibert King, Notger Heinz, Matthias Bauer, Thomas Grund, and Wolfgang Nitsche. Flight and Wind-Tunnel Tests of Closed-Loop Active Flow Control. *Journal of Aircraft*, 50(5):1605–1614, September 2013.

[125] Satoshi Shimomura, Satoshi Sekimoto, Akira Oyama, Kozo Fujii, and Hiroyuki Nishida. Experimental Study on Application of Distributed Deep Reinforcement Learning to Closed-loop Flow separation Control over an Airfoil. In *AIAA Scitech 2020 Forum*, Orlando, FL, January 2020. American Institute of Aeronautics and Astronautics.

[126] J Dandois and P Y Pamart. NARX Modeling and Extremum-Seeking Control of a Separation. *Journal Aerospace Lab*, 6(6):14, 2013.

[127] Timothée Chabert. *Contrôle expérimental en boucle fermée du décollement sur un volet.* PhD thesis, Université Pierre et Marie Curie, 2014.

[128] Ralf Becker, Maiko Garwon, and Rudibert King. Development of model-based sensors and their use for closed-loop control of separated shear flows. In *2003 European Control Conference (ECC)*, pages 3237–3242, Cambridge, UK, September 2003. IEEE.

[129] Clarence W. Rowley and David R. Williams. Dynamics and control of high-reynolds-number flow over open cavities. *Annual Review of Fluid Mechanics*, 38(1):251–276, January 2006.

[130] Anatol Roshko. Some Measurements of Flow in a Rectangular Cutout. Technical report, National Advisory Committee for Aeronautics, 1955.

[131] Krishnamurty. *Krishnamurty_k_1956.pdf.* PhD thesis, California Institue of Technology, Passadena, Californie, 1956.

[132] Plumblee, Gibson, and Lassiter. A theoretical and experimental investigation of the acoustic response of cavities in an aerodynamic flow. Technical report WADD-61-75, Defense Technical Information Center, Marietta, Georgie, 1962.

[133] J. E. Rossiter. Wind tunnel experiments on the flow over rectangular cavities at subsonic and transonic speeds. *RAE Technical Report No. 64037*, 1964.

[134] D. Rockwell and E. Naudascher. Review—Self-Sustaining Oscillations of Flow Past Cavities. *Journal of Fluids Engineering*, 100(2):152–165, June 1978.

[135] D. Rockwell. Prediction of Oscillation Frequencies for Unstable Flow Past Cavities. *Journal of Fluids Engineering*, 99(2):294–299, June 1977.

[136] D Rockwell and E Naudascher. Self-Sustained Oscillations of Impinging Free Shear Layers. *Annual Review of Fluid Mechanics*, 11(1):67–94, January 1979.

[137] L.F. East. Aerodynamically induced resonance in rectangular cavities. *Journal of Sound and Vibration*, 3(3):277–287, May 1966.

[138] Sami Yamouni, Denis Sipp, and Laurent Jacquin. Interaction between feedback aeroacoustic and acoustic resonance mechanisms in a cavity flow: a global stability analysis. *Journal of Fluid Mechanics*, 717:134–165, February 2013.

[139] Ahmad D. Vakili and Christian Gauthier. Control of cavity flow by upstream mass-injection. *Journal of Aircraft*, 31(1):169–174, January 1994.

[140] Lawrence Ukeiley, Michael Sheehan, Francois Coiffet, Farrukh Alvi, Srinivasan Arunajatesan, and Bernard Jansen. Control of Pressure Loads in Geometrically Complex Cavities. *Journal of Aircraft*, 45(3):1014–1024, May 2008.

[141] Michael Stanek, Ganesh Raman, Valdis Kibens, John Ross, Jessaji Odedra, and James Peto. Control of cavity resonance through very high frequency forcing. In *6th Aeroacoustics Conference and Exhibit*. American Institute of Aeronautics and Astronautics, 2000.

[142] L. Cattafesta, III, S. Garg, M. Choudhari, F. Li, L. Cattafesta, III, S. Garg, M. Choudhari, and F. Li. Active control of flow-induced cavity resonance. In *28th Fluid Dynamics Conference*, Snowmass Village,CO,U.S.A., June 1997. American Institute of Aeronautics and Astronautics.

[143] M Gharib. Response of the Cavity Shear Layer Oscillations to External Forcing. In *AIAA journal*, volume 25. American Institute of Aeronautics and Astronautics, 1987.

[144] Leonard Shaw and Stephen Northcraft. Closed loop active control for cavity acoustics. In *5th AIAA/CEAS Aeroacoustics Conference and Exhibit*, Bellevue,WA,U.S.A., May 1999. American Institute of Aeronautics and Astronautics.

[145] Philippe Micheau, Ludovic Chatellier, Janick Laumonier, and Yves Gervais. Active Control of a Self-sustained Pressure Fluctuation due to Flow over a Cavity. In *10th AIAA/CEAS Aeroacoustics Conference*, Manchester, GREAT BRITAIN, May 2004. American Institute of Aeronautics and Astronautics.

[146] M. Debiasi and M. Samimy. Logic-Based Active Control of Subsonic Cavity Flow Resonance. *AIAA Journal*, 42(9):1901–1909, September 2004.

[147] Tim Kestens and Franck Nicoud. Active control of an unsteady flow over a rectangular cavity. In *4th AIAA/CEAS Aeroacoustics Conference*, Toulouse,France, June 1998. American Institute of Aeronautics and Astronautics.

[148] Michael Kegerise, Louis Cattafesta, and Chung-Soo Ha. Adaptive Identification and Control of Flow-Induced Cavity Oscillations. In *1st Flow Control Conference*, St. Louis, Missouri, June 2002. American Institute of Aeronautics and Astronautics.

[149] David Williams and Julie Morrow. Adaptive control of multiple acoustic modes in cavities. In *15th AIAA Computational Fluid Dynamics Conference*, Anaheim,CA,U.S.A., June 2001. American Institute of Aeronautics and Astronautics.

[150] David Williams, Drazen Fabris, Ken Iwanski, and Julie Morrow. Closed-loop control in cavities with unsteady bleed forcing. In *38th Aerospace Sciences Meeting and Exhibit*, Reno,NV,U.S.A., January 2000. American Institute of Aeronautics and Astronautics.

[151] C. Rowley, D. Williams, T. Colonius, R. Murray, D. MacMartin, and D. Fabris. Model-based control of cavity oscillations. II - System identification and analysis. In *40th AIAA Aerospace Sciences Meeting & Exhibit*, Reno,NV,U.S.A., January 2002. American Institute of Aeronautics and Astronautics.

[152] M.A. Kegerise, R.H. Cabell, and L.N. Cattafesta III. Real-time feedback control of flow-induced cavity tones—Part 1: Fixed-gain control. *Journal of Sound and Vibration*, 307(3-5):906–923, November 2007.

[153] M.A. Kegerise, R.H. Cabell, and L.N. Cattafesta. Real-time feedback control of flow-induced cavity tones—Part 2: Adaptive control. *Journal of Sound and Vibration*, 307 (3-5):924–940, November 2007.

[154] L. Cattafesta, III, D. Shukla, S. Garg, and J. Ross. Development of an adaptive weapons-bay suppression system. In *5th AIAA/CEAS Aeroacoustics Conference and Exhibit*, Bellevue,WA,U.S.A., May 1999. American Institute of Aeronautics and Astronautics.

[155] Clarence Rowley, Vejapong Juttijudata, and David Williams. Cavity Flow Control Simulations and Experiments. In *43rd AIAA Aerospace Sciences Meeting and Exhibit*, Reno, Nevada, January 2005. American Institute of Aeronautics and Astronautics.

[156] Randolph H. Cabell, Michael A. Kegerise, David E. Cox, and Gary P. Gibbs. Experimental Feedback Control of Flow-Induced Cavity Tones. *AIAA Journal*, 44(8): 1807–1816, August 2006.

[157] Alexandre Barbagallo, Denis Sipp, and Peter J. Schmid. Closed-loop control of an open cavity flow using reduced-order models. *Journal of Fluid Mechanics*, 641:1–50, December 2009.

[158] Simon J. Illingworth, Aimee S. Morgans, and Clarence W. Rowley. Feedback control of cavity flow oscillations using simple linear models. *Journal of Fluid Mechanics*, 709: 223–248, October 2012.

[159] M. Samimy, M. Debiasi, E. Caraballo, A. Serrani, X. Yuan, J. Little, and J. H. Myatt. Feedback control of subsonic cavity flows using reduced-order models. *Journal of Fluid Mechanics*, 579:315–346, May 2007.

[160] P. Yan, M. Debiasi, X. Yuan, J. Little, H. Ozbay, and M. Samimy. Experimental Study of Linear Closed-Loop Control of Subsonic Cavity Flow. *AIAA Journal*, 44(5): 929–938, May 2006.

[161] Guy Y. Cornejo Maceda, Eliott Varon, François Lusseyran, and Bernd R. Noack. Stabilization of a multi-frequency open cavity flow with gradient-enriched machine learning control. *arXiv:2202.01686 [physics]*, February 2022. arXiv: 2202.01686.

[162] Simon J. Illingworth, Aimee S. Morgans, and Clarence W. Rowley. Feedback control of cavity flow oscillations using simple linear models. *Journal of Fluid Mechanics*, 709: 223–248, October 2012.

[163] L. Mongeau, H. Kook, and M. Franchek. Active control of flow-induced cavity resonance. In *4th AIAA/CEAS Aeroacoustics Conference*, Toulouse,France, June 1998. American Institute of Aeronautics and Astronautics.

[164] David Greenblatt and Israel J Wygnanski. The control of #ow separation by periodic excitation. *Progress in Aerospace Sciences*, page 59, 2000.

[165] Timothée Chabert, Julien Dandois, Eric Garnier, and Laurent Jacquin. Experimental detection of flow separation over a plain flap by wall shear stress analysis with and without steady blowing. *Comptes Rendus Mécanique*, 342(6-7):389–402, June 2014.

[166] P. Kergus. *Data-driven model reference control in the frequency-domain From model reference selection to controller validation.* Ph.D. thesis, Onera, ISAE, Toulouse University, Toulouse, France, Octobre 2019.

[167] C. Briat. A Biology-Inspired Approach to the Positive Integral Control of Positive Systems: The Antithetic, Exponential, and Logistic Integral Controllers. *SIAM Journal on Applied Dynamical Systems*, 19(1):619–664, 2020.

[168] J.G. Ziegler and N.B. Nichols. Optimum settings for automatic controllers. *Transactions of the ASME*, 64:759–768, 1942.

[169] K.J. Åström. Self-Tuning Regulators - Design Principles And Applications. In *Applications of Adaptive Control*, pages 1–68. Elsevier, 1980.

[170] A J. Mayo and A C. Antoulas. A framework for the solution of the generalized realization problem. *Linear Algebra and its Applications*, 425(2):634–662, 2007.

[171] I.V. Gosea, C. Poussot-Vassal, and A.C. Antoulas. On Loewner data-driven control for infinite-dimensional systems. In *Proceedings of the IEEE European Control Conference*, Virtual, June 2021.

[172] P. Vuillemin, P. Kergus, and C. Poussot-Vassal. Hybrid Loewner Data Driven Control. In *Proceedings of the IFAC World Congress*, Berlin, Germany, July 2020.

[173] C. Poussot-Vassal, P. Kergus, F. Kerhervé, D. Sipp, and L. Cordier. Interpolatory-based data-driven pulsed fluidic actuator control design and experimental validation. *IEEE transactions on Control Systems Technology*, 2021.

[174] L. Farina and S. Rinaldi. *Positive Linear Systems: Theory and Applications.* John Wiley & Sons, 2000.

[175] C. Briat. Robust stability and stabilization of uncertain linear positive systems via integral linear constraints - L_1- and L_∞-gains characterizations. *International Journal of Robust and Nonlinear Control*, 23(17):1932–1954, 2013.

[176] Y. Ebihara, D. Peaucelle, and D. Arzelier. L_1 gain analysis of linear positive systems and its applications. In *50th Conference on Decision and Control, Orlando, Florida, USA*, pages 4029–4034, 2011.

[177] W. M. Haddad, V. Chellaboina, and Q. Hui. *Nonnegative and compartmental dynamical systems*. Princeton University Press, 41 William Street, Princeton, USA, 2010.

[178] C. Briat, A. Gupta, and M. Khammash. Antithetic Integral Feedback Ensures Robust Perfect Adaptation in Noisy Biomolecular Networks. *Cell Systems*, 2(1):15–26, 2016.

[179] C. Poussot-Vassal, P. Kergus, and P. Vuillemin. *Realization and Model Reduction of Dynamical Systems, A Festschrift in Honor of the 70th Birthday of Thanos Antoulas (eds. C. Beattie, P. Benner, M. Embree, S. Gugercin and S. Lefteriu)*, chapter Interpolation-based irrational model control design and stability analysis, pages 353–371. Springer, 2022.

[180] Ghouila-Houri. *Développement de micro-capteurs de frottement pariétal et de pression pour les mesures en écoulement turbulents et le contrôle de décollement*. PhD thesis, Ecole Centrale de Lille, 2018.

[181] H.H. Fernholz and P.J. Finleyt. The incompressible zero-pressure-gradient turbulent boundary layer: An assessment of the data. *Progress in Aerospace Sciences*, 32(4): 245–311, August 1996.

[182] Jérémy Basley. *An Experimental Investigation on Waves and Coherent Structures in a Three-Dimensional Open Cavity Flow*. PhD thesis, Université Paris Sud - Paris XI, Monash University (Melbourne, Australie), 2012.

[183] Ganesh Raman and Surya Raghu. Cavity Resonance Suppression Using Miniature Fluidic Oscillators. *AIAA Journal*, 42(12):2608–2612, December 2004.

[184] P. Bueno, O. Unalmis, N. Clemens, and D. Dolling. The effects of upstream mass injection on a Mach 2 cavity flow. In *40th AIAA Aerospace Sciences Meeting & Exhibit*. American Institute of Aeronautics and Astronautics, 2002.

[185] Ning Zhuang, Farrukh Alvi, and Chiang Shih. Another Look at Supersonic Cavity Flows and Their Control. In *11th AIAA/CEAS Aeroacoustics Conference*, Monterey, California, May 2005. American Institute of Aeronautics and Astronautics.

[186] Denis Sipp. Open-loop control of cavity oscillations with harmonic forcings. *Journal of Fluid Mechanics*, 708:439–468, October 2012.

[187] Larry K. B. Li and Matthew P. Juniper. Lock-in and quasiperiodicity in a forced hydrodynamically self-excited jet. *Journal of Fluid Mechanics*, 726:624–655, July 2013.

[188] Clarence W. Rowley, David R. Williams, Tim Colonius, Richard M. Murray, and Douglas G. Macmynowski. Linear models for control of cavity flow oscillations. *Journal of Fluid Mechanics*, 547(-1):317, January 2006.

[189] David H. Doehlert. Uniform Shell Designs. *Applied Statistics*, 19(3):231, 1970.

[190] R. Pinto, K. V. Ramanathan, and R. S. Babu. Reactive Ion Etching in SF 6 Gas Mixtures. *Journal of The Electrochemical Society*, 134(1):165, January 1987.

[191] Cahit Kitaplioglu. Analysis of a Small-Scale Rotor Hover Performance Data. Technical Report 102271, NASA, March 1990.

Titre : Contrôle en boucle fermée d'un écoulement décollé et de l'écoulement sur une cavité ouverte à l'aide de technologies MEMS

Résumé : Dans ce mémoire, une revue sur le contrôle en boucle fermée d'écoulements est proposé. Celle-ci se concentre sur deux configurations typiques d'écoulements: le contrôle des écoulements décollés et le contrôle des écoulements sur cavité ouverte.
Concernant le contrôle des écoulements séparés, le contrôle en boucle fermée est mis en place sur un volet plein de type NACA 4412, à l'aide d'actionneurs et de capteurs conventionnels, respectivement des vannes Festo et des films chauds. Deux lois de contrôle sont appliquées: l'une basée données, menant à un contrôleur intégral linéaire et la seconde étant une loi phénoménologique/basée modèle, menant à la synthèse d'un contrôleur non linéaire, intégral positif. Ces lois permettent la mise en place simple et rapide du contrôle d'un écoulement décollé.
Le contrôle de l'écoulement sur une cavité ouverte, favorable à l'utilisation d'actionneurs MEMS, est réalisé à l'aide de microvalves MMMS (Micro Magneto Mechanical Systems) intégrées à la paroi amont de la cavité. Des essais de contrôle en boucle ouverte et fermée sont menés. Pour le contrôle en boucle fermée, des contrôleurs linéaires sont conçus par une synthèse structurée H_∞ permettant l'amortissement des oscillations de la cavité ouverte.
Dans une dernière partie, des développements technologiques sont proposés à la fois sur des capteurs et actionneurs MEMS en vue de futurs essais de contrôle d'écoulements sur des configurations encore plus ambitieuses.

Mots clés : Contrôle d'écoulements, boucle fermée, actionneurs MEMS, capteurs, MEMS

Title : Experimental closed-loop feedback control of separated and open-cavity flows with MEMS technologies

Abstract : This thesis starts with a literature review on aerodynamic closed-loop flow control. Focus is brought onto two canonical applications studied in the present work: control of separated flows and control of open-cavity flows.
Considering the control of separated flows, closed-loop control is implemented on a NACA 4412 plain flap model with conventional actuators and sensors technologies respectively solenoid Festo valves and hot films. Two control laws are considered: a data-driven control law, leading to a linear integral controller and a second one being a phenomenological/model-driven approach, leading to a non-linear positive integral control law. These approaches constitute a generic but yet simple approach to design flow separation feedback control laws.
Regarding the control of an open-cavity flow, favorable for the use of MEMS actuators, MMMS (Micro Magneto Mechanical Systems) microvalves are integrated as a linear array to perform both open and closed-loop flow control experiments. Closed-loop tests are performed using linear controllers designed thanks to a structured H_∞ synthesis design technique, successfully damping the open-cavity flow oscillations.
Finally, development on both MEMS sensors and actuators technologies are initiated for future closed-loop flow control experiments on more challenging configuration.

Keywords : Flow control, closed-loop, MEMS actuators, MEMS sensors